



**Selective Recovery of Valuable Cobalt-Nickel Alloys and Inorganic Compounds
from Spent Lithium Ion Battery Cathodes for Open and Closed Loop Recycling**

By

TENDAI TAWONEZVI

Thesis submitted in fulfilment of the requirements for the Degree

Doctor of Engineering in Chemical Engineering

in the Faculty of Engineering

At the Cape Peninsula University of Technology

Supervisors

Dr Myalelo Nomnqa

Dr Dorcas Zide

Prof Leslie Petrik

External Supervisors

Prof Bernard Bladergroen (ESIL-UWC)

Bellville Campus


August 2024

CPUT Copyright Information

The thesis may not be published either in part (in scholarly, scientific or technical journals) or as a whole (as a monograph) unless permission has been obtained from the university.

Declaration

I, Tendai Tawonezvi, declare that the contents of this thesis represent my own unaided work and that the thesis has not previously been submitted for academic examination towards any qualification. Furthermore, it represents my own opinions and not necessarily those of either Cape Peninsula University of Technology or the South African Institute of Advanced Materials Chemistry.



06/07/2024

Signed

Date

Abstract

Lithium-ion batteries (Li-ionBs) have been extensively deployed as the primary electrochemical power source for many applications, and their demand has increased significantly over the past decade, with the market projected to reach 116 billion United States dollars (USD) by 2030. Consequently, a considerable amount of end-of-life Li-ionBs are disposed of as waste annually. The current processes utilized for recycling spent Li-ionBs involve high-cost, energy-intensive, and eco-hazardous processes and materials. This has resulted in only a mere 5% of the spent Li-ionBs currently being recycled. Therefore, the development of an effective, low-cost, low-energy-intensive, and eco-friendly recycling process route for recovering valuable metals (i.e., lithium [Li], cobalt [Co], nickel [Ni], and manganese [Mn]) is imperative and imminent.

The cathode, in this study composed of Lithium Nickel Manganese Cobalt Oxide ($\text{LiNi}_x\text{Mn}_y\text{Co}_z\text{O}_2$, or NMC) material, is a key determinant of a NMC Li-ionB's cost and performance. While NMC is one of the predominant cathode chemistries used in Li-ionBs due to its favourable balance of performance, stability, and cost, other types of cathode materials are also widely employed in various applications. NMC cathode combines the valuable metals Ni, Co, and Mn in varying ratios (x, y, z in $\text{LiNi}_x\text{Mn}_y\text{Co}_z\text{O}_2$) for optimal performance, stability, and cost. For example, NMC 532, used in this study, has a Ni:Mn:Co ratio of 5:3:2, corresponding to the formulation $\text{LiNi}_{0.5}\text{Mn}_{0.3}\text{Co}_{0.2}\text{O}_2$. Conventional pure metal recovery, from Li-ionB waste, processes include solvent extraction, ion exchange, and selective precipitation, followed by galvanostatic electrowinning to obtain solid metal deposits. In this work, valuable Ni-Co alloys from spent Li-ionBs were selectively recovered from multi-ion (Ni^{2+} , Co^{2+} , Mn^{2+} , and Li^+) NMC 532 leachate solutions through potentiostatic electrowinning. Since the post-electrowinning spent liquor still contains traces of Ni and Co and significant amounts of Li and Mn, an additional sodium (Na)-based chemical precipitation unit operation was added to recover the nickel hydroxide ($\text{Ni}(\text{OH})_2$), manganese hydroxide ($\text{Mn}(\text{OH})_2$) and cobalt hydroxide ($\text{Co}(\text{OH})_2$) composite mixture ($0.6[\text{Ni}(\text{OH})_2].0.3[\text{Mn}(\text{OH})_2].0.1[\text{Co}(\text{OH})_2]$), $\text{Mn}(\text{OH})_2$, and lithium carbonate (Li_2CO_3) materials.

The rationale of this research was based on the elimination of cost and energy-intensive hydrometallurgical intermediate processes like solvent extraction, ion exchange, and selective precipitation (to extract Ni and Co selectively), utilization of potentiostatic techniques (instead of conventional galvanostatic techniques) to selectively extract specific metals and enhance

purity, integration of rotating cathodes to increase the deposition rate, and utilization of Platinum (Pt)-coated Titanium (Ti) dimensionally stable anodes (DSA) to reduce deposit contamination and consequently levelize the cost of operation. It is believed that by applying a constant potential suitable for Co and Ni reduction reactions (potentiostatic electrowinning), valuable Ni and Co can be selectively deposited and separated from less valuable Li and Mn. Recovered Ni-Co alloys can be used as feedstock for Lithium Nickel Manganese Cobalt Oxide (NMC) cathode production processes. Ni-Co alloys can also be used in the production of magnetic films, electrocatalysis materials, and other various technological applications.

In the first experimental phase, this research demonstrated the applicability of inorganic acid-reductant leachant-based leaching of NMC 532 to effectively leach and recover all valuable metals in the cathode material. This approach provides quantitative recovery data for each element of the entire particle population at different operational parameters: reductant and inorganic acid concentration, solid-to-liquid (S/L) ratio, reaction time, and temperature. The quantification of elemental recovery data was done through Inductively Coupled Plasma Optical Emission Spectroscopy (ICP-OES) and Energy Dispersive Spectroscopy (EDS). Phase composition was assessed through X-ray Diffraction (XRD) analysis. Morphology and particle size were analysed using High-Resolution Scanning Electron Microscopy (HR-SEM). By utilising optimised leaching parameters, aluminium (Al) foil and carbon (C) flakes were freed from the cathode matrix and peak leaching recovery efficiencies of 98.9% for Li, 97.1% for Co, 96.9% for Ni, and 95.7% for Mn were attained.

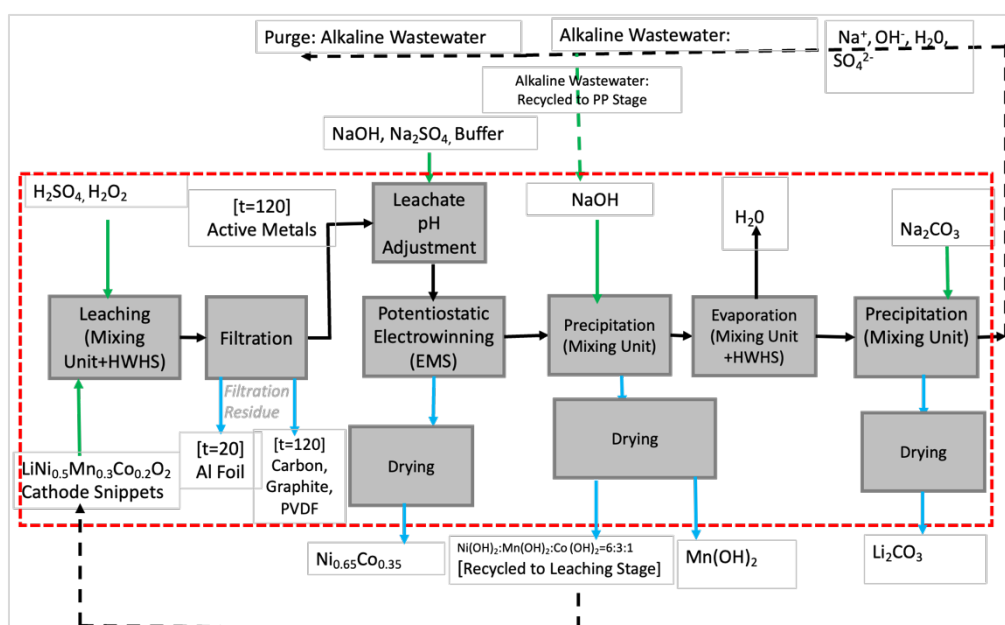
In the second experimental phase, the effects of key electrowinning parameters were quantified and studied, and alternative electrodes were tested to suppress the extent of scaling, electrode resistivity, operational and capital costs, and life cycle duration limitations. This optimisation study was conducted using synthetic Ni, Co, Mn, and Li sulphate solutions mimicking the NMC 532 ratio of elements. The optimised electrowinning parameters such as applied potential, temperature, pH, Co-Ni, Na_2SO_4 and buffer dosage, and electrode distance and active area were then utilised to recover $\text{Ni}_{0.65}\text{Co}_{0.35}$ alloy from real NMC leachate at a minimum rate of $0.06 \text{ g/cm}^2\cdot\text{hr}$ with 88% current efficiency. 90% of the Co and 77% of the Ni in the leachate were recovered in a 3-hour electrowinning run.

In the last phase of the experiments, the metals remaining in the post-electrowinning electrolyte from the electrowinning were recovered through multi-stage precipitation to recover $\text{Mn}(\text{OH})_2$ and Li_2CO_3 , and a hydroxide composite formulation of Ni, Mn, and Co

($0.6[\text{Ni}(\text{OH})_2].0.3[\text{Mn}(\text{OH})_2].0.1[\text{Co}(\text{OH})_2]$) at over 99% precipitation efficiency. Approximately 19% of Ni, 7.5% of Co, and 95% of Li were recovered during multi-stage precipitation. The varied and optimized key parameters for pH-based precipitation were temperature, reactants ratio, and pH. The semi-closed loop recycling cost (R/kg) of the cathode was calculated to be R 153/kg, which is at least 50% lower than R 360/kg, R 308/kg, and R 258/kg recycling costs for direct recycling, pyrometallurgical, and hydrometallurgical processes, respectively.

A significant fraction of the process resultant solution from the whole process can be recycled for use in the leachate pH adjustment stage, while the minority portion will need further treatment (to remove sulphate (SO_4^{2-}) and sodium (Na^+) before being discarded per National Environmental Protection Agency (NEPA) regulations since it contains negligible and environmentally tolerant metal concentrations of Mn, Li, Ni and Co. The obtained results demonstrate the feasibility of a semi-closed loop spent Li-ionB cathode recycling process comprising battery pre-treatment, single-stage leaching, single-compartment electrowinning cell, and Na-based precipitation. The main objective of this work, high purity $\text{Ni}_{0.65}\text{Co}_{0.35}$ alloy recovery, was successfully achieved. The recovered $\text{Ni}_{0.65}\text{Co}_{0.35}$ alloy, Li_2CO_3 , $\text{Mn}(\text{OH})_2$, and $0.6[\text{Ni}(\text{OH})_2].0.3[\text{Mn}(\text{OH})_2].0.1[\text{Co}(\text{OH})_2]$ are versatile compounds with applications ranging from the production of Li-ionBs to medicine and material production, among other applications.

Keywords: Spent Li-ion batteries, Leaching, Metal Recovery, Electrowinning, Cobalt, Nickel, Open and Closed Loop Recycling



Graphical abstract of the valuable Ni-Co and metallic by products recovery process

Acknowledgements

I wish to express my gratitude to:

- My cherished blossom, my dearest mother, **Placedes Ranga**, your endless prayers and unwavering support have been the foundation of all that I have achieved. From the very beginning, your love has been my guiding star, and your wise words of encouragement have lifted me through every challenge. I am forever indebted to you, not just for your sacrifices, but for the warmth and strength you've given me throughout this journey. With all my heart, thank you, Mom.
- My supervisor, **Prof B.J. Bladergroen**, for believing in me from the very beginning. His constant guidance and encouragement throughout this journey ensured this project was successful. It was an honour to be a student of such a prominent Professor. He has assisted me not only as my supervisor for this project but also granted me adequate opportunities to extend my knowledge related to this project.
- My supervisor, **Prof Leslie Petrik**, for her constructive remarks, suggestions, and comments. Her contribution to my research work ensured that it reached its full potential.
- My supervisor, **Dr Dorcas Zide**, for her remarkable insights and invaluable contributions throughout the research process. Her guidance has exceeded the role of a typical supervisor, and I am deeply grateful for her support.
- My supervisor, **Dr Myalelo Nomnqa**, for his exceptional supervision and insightful contribution throughout the research and administrative processing. He has been my role model for building my personality as a researcher. I am greatly indebted to him.
- **Energy Storage Innovation Lab (ESIL) and Council for Scientific and Industrial Research (CSIR)** for the financial support provided throughout the course of the study. For their assistance, encouragement, support and all the interactions that made my master's journey exciting.
- My light bearer, **Natali Nyabanga**, the love of my life, from the first step to the final page, your steadfast love and support have been my anchor. Your endless encouragement, patience, and dedication have given every word purpose. This work, at its core, belongs to you as much

as it does to me. Thank you for being not just my muse, but the very soul of this entire endeavour.

- My mentor, **Dr Innocentia “Zulu Princess” Erdogan** for her support, care, guidance and insightful remarks and suggestions. Her contributions could not go unmentioned.
- My siblings, **Tracy, Takudzwa and Tatenda Tawonezvi**, for their support, love and motivation throughout this journey, it meant a lot.
- My best friends, **Tendai Pfavai and Wesley Tafadzwa Guzha**, for their constant wise words of encouragement and relentless support. I am forever grateful for their unwavering support and love.
- My **friends and family** for their love and support.

Dedication

This research work is dedicated to:

My Flower, Placsedes Ranga

I owe my journey to your buoyant support, unequivocal love and endless sacrifices that have shaped my path toward a brighter future. Your nurturing spirit has been my greatest strength, and I am forever grateful for everything you've done.

Mom, I love you dearly.

Research Outputs

Conferences

1. Tawonezvi, T., Petrik, L., Nomnqa, M., Zide, D. & Bladergroen, B.J. Battery Waste Management: Recovery of Valuable Metals from NMC 532 Battery Cathodes using Electrowinning. *2023 Green Talk: Batteries Edition Symposium 2023*. Madrid, Spain, 19-21 October 2023.
2. Tawonezvi, T., Madondo, M., Zide, D., Nomnqa, M., Petrik, L. & Bladergroen, B.J. Recovery of valuable metals from NMC 532 battery cathodes using chemical-based precipitation for closed-loop recycling. *2023 Chemistry Symposium*. 2023. Bellville, South Africa, 22-23 November 2023.
3. Tawonezvi, T., Dyonashe, N., Zide, D., Nomnqa, M., Petrik, L. & Bladergroen, B.J. Leaching of valuable metals from NMC 532 battery cathodes using organic acids. *2023 Chemistry Symposium*. 2023. Bellville, South Africa, 22-23 November 2023.

Journal Articles

1. Tawonezvi, T., Nomnqa, M., Petrik, L. & Bladergroen, B.J. 2023. Recovery and Recycling of Valuable Metals from Spent Lithium-Ion Batteries: A Comprehensive Review and Analysis. *Journal of Energies (MDPI)*, 16(3): 1365. **Status: Published**
2. Tawonezvi, T., Nomnqa, M., Zide, D., Petrik, L. & Bladergroen, B.J. 2023. Selective electrodeposition of Co-Ni alloys from synthetic quasi LiB NMC 532 cathode sulphate solutions using rotating plate potentiostatic electrowinning. *Chemical Engineering Journal Advances (Elsevier)*. 17: 100582. **Status: Published**
3. Tawonezvi, T., Zide, D., Nomnqa, M., Madondo, M., Petrik, L. & Bladergroen, B.J. 2023. Recovery of $\text{Ni}_x\text{Mn}_y\text{Co}_z(\text{OH})_2$ and Li_2CO_3 from Spent Lithium-Ion Battery Cathodes through Non-Na Precipitant-Based Chemical Precipitation for Sustainable Recycling. *Chemical Engineering Journal Advances (Elsevier)*. 17: 100579. **Status: Published**

Table of Contents

Declaration	i
Abstract	ii
Acknowledgements	v
Research Outputs	ii
List of Figures	ix
List of Tables	xv
List of Symbols-Scientific	i
List of Symbols-Chemical Species	i
List of Abbreviations	iii
Chapter 1: Introduction and Background	5
1.1 Background	5
1.1.1 Li-ion Battery Application Trends.....	5
1.1.2 Li-ion Battery Economic, Production and Disposal Trends	6
1.1.3 Li-ion Battery Conventional Recycling and Future Technologies.....	9
1.1.4 Rationale of This Work	11
1.2 Research Problem Statement	13
1.3 Research Aim and Objectives	13
1.4 Research Questions	14
1.5 Delineation	15
1.6 Novelty of Study	15
1.7 Significance of Research	15
1.8 Thesis Layout	17
Chapter 2: Literature Review	22
2.1 Overview	22
2.2 Lithium Ion Battery	22

2.2.1	Historic Review	22
2.2.2	Lithium-ion Battery Components.....	23
2.2.3	Working Mechanism	23
2.2.4	Anode Material.....	25
2.2.5	Cathode Material.....	32
2.2.6	Electrolyte Solution.....	48
2.2.7	Separator	48
2.3	Summated Lithium-Ion Battery Commercial Cathode Development over the Years	49
2.4	Why Recycle Lithium-Ion Batteries?	51
2.5	Conventional Recycling Methodologies	54
2.5.1	Overview	54
2.5.2	Pre-treatment Process	56
2.5.3	Metal Extraction Processes	64
2.5.4	Chemical Processes.....	67
2.5.5	Product Recovery.....	80
2.5.6	Product Preparation	80
2.5.7	Industrial Developed Processes.....	81
2.6	Electrometallurgy	85
2.6.1	Overview	85
2.6.2	Electrowinning Working Principle.....	86
2.6.3	Faraday Law	87
2.6.4	Current Efficiency.....	87
2.6.5	Electrode Potential and Nernst's Equation.....	88
2.6.6	Cell Voltage and Energy Consumption.....	89
2.6.7	Metal Electrodeposition.....	89
2.6.8	Electrowinning of Co and Ni	91

2.7	Summary of Review	97
Chapter 3: Experimental Methodology		99
3.1	Chapter Overview	99
3.2	Methodology Overview	99
3.3	Recovery Process Setup	105
3.3.1	Material and Chemicals.....	105
3.3.2	Equipment.....	106
3.3.3	Battery Pre-Treatment.....	109
3.3.4	Test Cell Assembly	111
3.3.5	Leaching Process Optimisation.....	112
3.3.6	Cyclic Voltammetry.....	117
3.4	Electrowinning Optimisation Using Synthetic Quasi NMC 532 Solutions	118
3.4.1	Methodology Overview	118
3.4.2	Electrowinning Optimisation Experimental Design.....	119
3.4.3	Investigation of the Effect of Co/Ni Ratio on Current Efficiency and Deposit Composition.....	120
3.4.4	Investigation of the Effect of Applied Potential	121
3.4.5	Investigation of the Effect of pH.....	122
3.4.6	Investigation of the Effect of Temperature	123
3.4.7	Investigation of the Effect of Co-Ni Concentration	123
3.4.8	Investigation of the Effect of Distance Between Electrodes.....	124
3.4.9	Investigation of the Effect of Electro-Active Area.....	125
3.4.10	Investigation of the Effect of Monosodium Phosphate on pH as a Function of Time	125
3.4.11	Investigation of the Effect of Na ₂ SO ₄ Concentration	126
3.4.12	Investigation of the Effect of the Rotating Cathode Speed.....	127
3.5	Electrowinning Experiments Using Synthetic Ni, Co Sulphate Solution	127

3.5.1	Anode Selection and Fabrication	128
3.6	Electrowinning Experiment Using Leached Cathode Solutions.....	128
3.7	Recovery of Mn(OH)₂ and 0.6[Ni(OH)₂].0.3[Mn(OH)₂].0.1[Co(OH)₂] Precipitates.....	130
3.8	Recovery of Li₂CO₃ Precipitates	133
3.9	Material Characterization	135
3.9.1	X-Ray Diffraction.....	135
3.9.1	Scanning Electron Microscopy	136
3.9.1	Inductively Coupled Plasma-Optical Emission Spectroscopy (ICP-OES)	137
3.10	Electrochemical Characterization	138
3.10.1	Cycling Voltammetry.....	138
3.10.2	Potentiostatic Electrochemical Operation	143
Chapter 4: Inorganic Acid-Reductant Leaching of Valuable Metals from NMC 532		
Cathodes.....		147
4.1	Overview.....	147
4.2	NMC Material Characterisation and Analysis.....	147
4.3	Leaching Process Optimization	150
4.3.1	NMC 532 Composition Analysis.....	150
4.3.2	Effect of H ₂ O ₂ on Leaching Efficiency	150
4.3.3	Effect of S/L Ratio on Leaching Recovery Efficiency.....	154
4.3.4	Effect of H ₂ SO ₄ Acid Concentration on Leaching Recovery Efficiency.....	156
4.3.5	Effect of Leaching Temperature on Leaching Recovery Efficiency.....	158
4.3.6	Effect of Leaching Reaction time on Leaching Recovery Efficiency.....	159
4.3.7	Leaching Kinetics	161
Chapter 5: Electrowinning Optimization Using Synthetic Quasi NMC 532 Solutions 167		
5.1	Overview.....	167
5.2	Cyclic Voltammetry (For Co and Ni Deposition).....	168

5.3	Effect of Co/Ni Ratio on Current Efficiency and Deposit Composition	171
5.4	Effect of Applied Potential on Current Efficiency and Rate of Deposition	174
5.5	Effect of pH on Current Efficiency	179
5.6	Effect of Temperature on Current Efficiency	181
5.7	Effect of Concentration on Co-Ni Concentration on Current Efficiency	184
5.8	Effect of Inter-Electrode Distance on Developed Current	186
5.9	Effect of Electrode Active Area on the Developed Current	188
5.10	Effect of Monosodium Phosphate on pH Fluctuation	189
5.11	Effect of Na₂SO₄ on the Current Efficiency	192
5.12	Effect of Rotating Cathode Speed on Current Efficiency and Current	193
5.13	Cobalt/Nickel Electrowinning Using Synthetic Solution	195
Chapter 6: Electrowinning Cell Voltage Optimization		203
6.1	Overview	203
6.2	Cell Voltage Optimisation	203
Chapter 7: Co-Ni Electrowinning using Real NMC Leachate Electrolyte		210
7.1	Overview	210
7.2	Co-Ni Electrowinning using real NMC Leachate Electrolyte	210
Chapter 8: Recovery of Mn(OH)₂, Li₂CO₃ and 0.6[Ni(OH)₂].0.3[Mn(OH)₂].0.1[Co(OH)₂] Precipitates		218
8.1	Overview	218
8.2	Spent Electrowinning Electrolyte Analysis	219
8.3	Mn(OH)₂ and 0.6[Ni(OH)₂].0.3[Mn(OH)₂].0.1[Co(OH)₂] Precipitates Recovery: Effect of pH and Temperature on the Elemental Recovery	220
8.4	Recovery of the Li₂CO₃ Precipitate	225
8.4.1	Effect of CO ₃ ²⁻ :Li ⁺ Ratio on the Lithium Recovery Efficiency (Li ₂ CO ₃ Recovery) 225	
8.4.2	Effect of Temp on the Elemental Recovery Efficiency (Li ₂ CO ₃ Recovery).....	227

8.4.3	Effect of pH on the Elemental Recovery Efficiency (Li ₂ CO ₃ Recovery)	228
Chapter 9:	Process Flow Mass Balance.....	231
9.1	Overview	231
9.2	Process Flow and Material Balance	232
9.3	Environmental Pseudo-Assessment	240
Chapter 10:	Conclusion and Recommendations	242
10.1	Conclusion	242
10.2	The Novelty of the Study	245
10.3	Recommendations	245
References.....		247
Appendix A-Process Cost Estimation.....		278
A.1	Overview	278
A.3	Material Production Cost of a Lab Scale Pilot Plant with Capacity of 4500 kgs of Ni-Co Composite/Year	278
A-4	Cash Flow of a Plant Capacity of 4500 kg (Ni-Co)/Year	286
Appendix B-Cash Flow Statement (4500 kg Ni-Co Production Plant)		288

List of Figures

Figure 1-1: The demand-led market growth of Li-ion batteries (Data derived from (ESMAP 2022)).....	6
Figure 1-2: Rechargeable Li-ionB market size (data derived from (Phuc Anh LE 2019)).....	7
Figure 2-1: Li-ionB schematic structure.....	23
Figure 2-2: Working mechanism of a Li-ionB (Tycoron 2021).....	24
Figure 2-3: Crystal structures of (a) lithiated graphite anode material, (b) lithium titanate anode material (LTO), (c) silicon anode material during lithiation and d) charge–discharge profiles at low C-rates, showing voltage hysteresis (reproduced by Nitta et al. (2015) with Permission Copyright (2014) American Chemical Society) (Figure Adapted from (Nitta et al., 2015)).....	26
Figure 2-4: Approximate range of average specific capacity and discharge potentials for some of the most prevalent conversion-type anode materials (Figure Adapted from (Nitta et al., 2015)).....	27
Figure 2-5: Typical voltage profiles of conversion-based anode materials after the first cycle, showing voltage hysteresis (Kim et al. 2022).	31
Figure 2-6: Crystal structures of the most prevalent intercalation cathode materials: structure of (a) layered (LiCoO_2), (b) spinel (LiMn_2O_4), (c) olivine (LiFePO_4), and (d) tavorite (LiFeSO_4F) (Figure Adapted from Nitta et al, (2015)).	33
Figure 2-7: Typical discharge profiles of the most prevalent intercalation cathode materials (Figure adapted from (Liu et al. 2016)).	34
Figure 2-8: Transformations annotated in selected conversion-type cathode materials: (a) propagation of lithiation reaction front through a single FeF_2 particle; (b) polysulphides shuttle accompanying charge and discharge of a S particle and (c) typical discharge profiles of the most prevalent conversion type cathode materials (Figure adapted from (Wang et al. (2011)).....	43
Figure 2-9: Approximate range of average specific capacity and discharge potentials for some of the most prevalent conversion-type cathodes (Figure adapted from (Wu & Yushin, 2017)).....	43
Figure 2-10: Global market size and total battery spent estimation of Li-ionBs over the years (Data derived from (AL Shaqsi et al. 2020; CSIRO 2022; ESMAP 2022)).....	51

Figure 2-11: Global demand for battery technologies by application from 2015 to 2030 (Data from (Global Battery Alliance 2020)).....	52
Figure 2-12: Typical Li-ionB composition (data derived from (Werner et al. 2020; Chandran et al. 2021; Piątek et al. 2021)).....	53
Figure 2-13: Conventional recycling stages for spent Li-ionBs.....	55
Figure 2-14: Recycling mythologies for spent Li-ionBs.....	56
Figure 2-15: Process flow chart of a conventional mechanical recycling process (constituting pyrolysis, crushing and sieving) (Figure based on work described by (Shin et al. 2005)).....	63
Figure 2-16: Conventional pyrometallurgical processes for spent Li-ionBs.....	65
Figure 2-17: Conventional hydrometallurgical recycling and recovering processes for spent Li-ionBs (Partial data derived from (Chandran et al. 2021)).....	66
Figure 2-18: (a) Correlation between equilibrium aqueous metal ion concentration (at 25 °C) and pH ; (b) Potential (E vs SHE) and pH diagram for the Ni-H ₂ O and Co-H ₂ O systems (at 25 °C, Co=Ni = 0.2 mol/L) (Figure Adapted from (Lv et al. 2018)).....	68
Figure 2-19: Spider chart for a relative evaluation index of leaching spent Li-ionBs with various conventional leaching reagents (Data from (Lv et al. 2018)).....	72
Figure 2-20: Effect of pH on the solvent extraction of Cu, Ni and Co using different extraction reagents (at 25°C and A:O = 1, except for Mextral 5640H (A:O = 2)) (Date derived from (Lv et al. 2018)).....	75
Figure 2-21: Process flow diagram for the Umicore process.....	81
Figure 2-22: Toxco process flow diagram (Jinyue Yan 2015).....	83
Figure 2-23: Schematic of the simplest electrowinning circuit.....	86
Figure 3-1: Single-compartment cell used in the different electrowinning tests.....	101
Figure 3-2: The complete hydro-electrometallurgy experimental design of the recovery of Ni-Co composite from spent Li-ionBs.....	104
Figure 3-3: Schematic diagram of the leaching set-up.....	106
Figure 3-4: The oven employed during material synthesis.....	107
Figure 3-5: a) Electrowinning lab set-up b) schematic of the electrowinning set-up.....	107
Figure 3-6: Overhead mixer.....	108
Figure 3-7: Electrochemical management setup.....	108
Figure 3-8: Experimental set-up for battery pre-treatment process.....	111

Figure 3-9: a) Electrowinning lab set-up b) 2D conception of the electrowinning cell with three electrodes.....	112
Figure 3-10: The schematic representation of the 3-electrode Autolab system.....	117
Figure 3-11: Single-compartment cell used in the different electrowinning tests.....	129
Figure 3-12: Schematic diagram of a SEM machine (Figure derived from (Suryanarayana 2016)).....	137
Figure 3-13: Potential-time profiles generated during the linear sweep and cyclic voltammetry (concept adapted from (Figure derived from (Figure derived from (Davies et al., 2005))).	139
Figure 3-14: Cyclic voltammogram (Figure derived from (Davies et al., 2005)).	140
Figure 3-15: Experimental testing configuration for conventional cycling voltammetry (Figure adapted from (Tawonezvi, 2020)).....	140
Figure 3-16: Schematic representation of the on-ground test environment.....	142
Figure 3-17: Schematic representation of the on-ground test environment (Top view).....	142
Figure 3-18: Constant current and constant voltage charging (concept adapted from (Pyun et al., 2012)).	144
Figure 3-19: Front panel of the metrohm autolab electrochemical testing station.....	144
Figure 4-1: The X-ray diffraction (XRD) pattern of spent lithium nickel manganese cobalt oxide (NMC 532) cathode materials.....	148
Figure 4-2: (a) The scanning electron microscopy (SEM) analysis of cathode materials; (b) the energy-dispersive X-ray spectroscopy (EDS) analysis of NMC cathode materials.....	149
Figure 4-3: Effect of H ₂ O ₂ concentration on leaching recovery efficiency at a) S/L=25 g/L and b) 45 g/L (H ₂ SO ₄ =3M, Time=3 hrs, T=70 °C, IS=350 rpm).....	152
Figure 4-4: Effect of solid-to-liquid ratio on the leaching recovery efficiency at different acid concentrations a) 1 M and b) 3M (6 % v/v H ₂ O ₂ , t=180 min, T=70 °C, IS=350 rpm).	155
Figure 4-5: Effect of H ₂ SO ₄ acid concentration on leaching recovery efficiency at different temperatures a) 50 °C and b) 70 °C (6 % v/v H ₂ O ₂ , t =180 min, S:L=75 g/L, IS=350 rpm).	157
Figure 4-6: Effect of temperature on leaching recovery efficiency at different S/L ratios a) 75 g/L and b) 45 g/L (6 % v/v H ₂ O ₂ , H ₂ SO ₄ =2M, S/L=75 g/L, Time=180 mins, IS=350 rpm).	159
Figure 4-7: Effect of time on leaching recovery efficiency (6 % v/v H ₂ O ₂ , H ₂ SO ₄ =2M, S/L=75 g/L, T=60 °C, IS=350 rpm).	160
Figure 4-8: Experimental fit for Model I: Spherical particles under reaction control.....	163

Figure 4-9: Experimental fit for Model II: Spherical particles under product layer diffusion control.	163
Figure 4-10: Experimental fit for Model III: Avrami model.....	164
Figure 4-11: Arrhenius plot for leaching of metals from Li-ionBs.....	165
Figure 5-1: Voltammograms of a) Co and Ni deposition on Al alloy cathode in 15 g/L metal ion solution at pH= 4 and 50 °C and b) Co-Ni deposition on Al cathode in 47.5 g/L $Ni^{2+}_{0.25}Co^{2+}_{0.1}Mn^{2+}_{0.15}Li^{+}_{0.5}$ solution at pH= 4.....	169
Figure 5-2: the effect of Co/Ni ratio on current efficiency and deposit composition (-0.95 V, pH =4, 60 °C, 47.5 g/L $Ni^{2+}_xCo^{2+}_yMn^{2+}_{0.15}Li^{+}_{0.5}$ (where $x+y=0.35$), Cathodic Active Area/Electrolyte Volume (AA/EV) of 2 cm ² /250 cm ³).....	172
Figure 5-3: Effect of applied potential on the current as a function of time (tests done in 47.5 g/L of $Ni^{2+}_{0.25}Co^{2+}_{0.1}Mn^{2+}_{0.15}Li^{+}_{0.5}$ solution at pH=5, 60 °C and 2 cm ² /250 cm ³ AA/EV).	175
Figure 5-4: Effect of applied potential on a) the mean current and rate of deposition b) current efficiency and Co/Ni ratio and c) current efficiency and % Li and Mn impurity (tests done at pH=5, 60 °C and 2 cm ² /250 cm ³ AA/EV in 47.5 g/L $Ni^{2+}_{0.25}Co^{2+}_{0.1}Mn^{2+}_{0.15}Li^{+}_{0.5}$	176
Figure 5-5: SEM images of cathode surface after applying different potentials a) 0 V (Fresh electrode), b) -1.15 V, c) -1.25 V, d) -1.35 V, e) and f) -1.45 V vs Ag/AgCl (Deposit obtained in 47.5 g/L of $Ni^{2+}_{0.25}Co^{2+}_{0.1}Mn^{2+}_{0.15}Li^{+}_{0.5}$ solutions at pH=5, 60 °C and 2 cm ² /250 cm ³ AA/EV).	178
Figure 5-6: Influence of pH of the electrolyte on Co-Ni electro-deposition at different temperatures (47.5 g/L of $Ni^{2+}_{0.25}Co^{2+}_{0.1}Mn^{2+}_{0.15}Li^{+}_{0.5}$, 50 °C and 60 °C and , -1,15 V vs Ag/AgCl and AA/E of 2 cm ² /250 cm ³).....	180
Figure 5-7: The effect of temperature on the current efficiency at an applied potential of -1.15 V, pH=3, 4 5 and 6 using an electrolyte composition of 47.5 g/L [$Ni^{2+}_{0.25}Co^{2+}_{0.1}Mn^{2+}_{0.15}Li^{+}_{0.5}$] and AA/EV of 2 cm ² /250 cm ³	182
Figure 5-8: SEM images of cathode surface (with Ni-Co alloy) after electrowinning in an electrolyte solution containing a) pure 30 g/L of $Co^{2+}_{0.3}Ni^{2+}_{0.7}$ and b) 47.5 g/L $Ni^{2+}_{0.25}Co^{2+}_{0.1}Mn^{2+}_{0.15}Li^{+}_{0.5}$ (tests done at 1.15 V vs Ag/AgCl, 50 °C, pH = 4.5 for 180 minutes).	184
Figure 5-9: Effect of Co-Ni concentration [$Co^{2+}_{0.25}Ni^{2+}_{0.1}$] in a multi-ion [$Co^{2+}_{0.25}Ni^{2+}_{0.1}Mn^{2+}_{0.15}Li^{+}_{0.5}$] solution on the current efficiency at -1.15 V vs Ag/AgCl, pH=4.5,	

Temperatures=40 °C, 50 °C, 60 °C and 70 °C using a varied electrolyte composition up to 30 g/L [Co ²⁺ _{0.25} Ni ²⁺ _{0.1}] solution and AA/EV of 2 cm ² /250 cm ³	185
Figure 5-10: The effect of distance between electrodes on the developed current density at -1.15 V vs Ag/AgCl, 47.5 g/L [Ni ²⁺ _{0.25} Co ²⁺ _{0.1} Mn ²⁺ _{0.15} Li ⁺ _{0.5}], pH=4.5, 50 °C and AA/EV of 2 cm ² /250 cm ³	187
Figure 5-11: Effect of Electrode-active Area on the developed Current density at -1.15 V vs Ag/AgCl, 47.5 g/L [Ni ²⁺ _{0.25} Co ²⁺ _{0.1} Mn ²⁺ _{0.15} Li ⁺ _{0.5}], pH=4.5, 50 °C and AA/EV of 2 cm ² /250 cm ³	188
Figure 5-12: a) pH variation with time at different buffer dosages and effect of buffer dosage on the current efficiency in the electrowinning set-up at -1.15 V vs Ag/AgCl, 47.5 g/L [Ni ²⁺ _{0.25} Co ²⁺ _{0.1} Mn ²⁺ _{0.15} Li ⁺ _{0.5}], Starting pH=4.5, 50 °C and AA/EV of 2 cm ² /250 cm ³	190
Figure 5-13: Effect of Na ₂ SO ₄ in an electrowinning set-up (-1.15 V, pH =4.5, 15 g/L of buffer, 50 °C, 47.5 g/L of Ni ²⁺ _{0.25} Co ²⁺ _{0.1} Mn ²⁺ _{0.15} Li ⁺ _{0.5} , AA/EV of 2 cm ² /250 cm ³).	192
Figure 5-14: Current as a function of rotating cathode speed (-1.15 V, pH =4.5, 15 g/L of buffer, 15 g/L Na ₂ SO ₄ , 50 °C, 47.5 g/L of Ni ²⁺ _{0.25} Co ²⁺ _{0.1} Mn ²⁺ _{0.15} Li ⁺ _{0.5} , AA/EV of 2 cm ² /250 cm ³).	193
Figure 5-15: a) The Levich plot analysis and b) the effect of cathode rotational speed on current efficiency and (-1.15 V, pH =4.5, 50 °C, 47.5 g/L of Ni ²⁺ _{0.25} Co ²⁺ _{0.1} Mn ²⁺ _{0.15} Li ⁺ _{0.5} , AA/E of 2 cm ² /250 cm ³).	194
Figure 5-16: Composition of deposit from constant current electrowinning (CE) vs constant potential electrowinning (PE) (PE=>-1.15 V vs Ag/AgCl, CE=> 0.035 A/cm ² , 180 minutes, 2cm ² /250 cm ³ AA/EV in 47.5 Ni ²⁺ _{0.25} Co ²⁺ _{0.1} Mn ²⁺ _{0.15} Li ⁺ _{0.5} Solution).	196
Figure 5-17: Expected mass deposited vs actual mass deposited over a 120 minute period (-1.15 V, pH =4.5, 50 °C, 47.5 g/L of Ni ²⁺ _{0.25} Co ²⁺ _{0.1} Mn ²⁺ _{0.15} Li ⁺ _{0.5} , AA/E of 2 cm ² /250 cm ³).	197
Figure 5-18: a) Concentration variation of a 30 g/L [Co ²⁺ _{0.3} Ni ²⁺ _{0.7}] mixture within a multi-ion synthetic solution (47.5 g/L of Ni ²⁺ _{0.25} Co ²⁺ _{0.1} Mn ²⁺ _{0.15} Li ⁺ _{0.5}) over 250 minutes of electrowinning and b) kinetics of Co-Ni electrodeposition during the first 120 minutes (at -1.15 V, pH 4.5 and 50 °C in 30 g/L [Co ²⁺ _{0.3} Ni ²⁺ _{0.7}]).	198
Figure 5-19: a) Micrograph of the deposit morphology, deposit obtained from the synthetic solution electrowinning and b) EDX spectrum of the deposit (47.5 g/L of Ni ²⁺ _{0.25} Co ²⁺ _{0.1} Mn ²⁺ _{0.15} Li ⁺ _{0.5} , -1.15 V vs Ag/AgCl, 50 °C, 15 g/L of buffer, 15 g/L Na ₂ SO ₄ , pH 4.5, AA/E of 2 cm ² /250 cm ³).	200

Figure 6-1: Anodic overvoltage for Pt, C, GC, Ti and Pb (0.035 A/cm ² , pH =4.5, 50 °C, 47.5 g/L of Ni ²⁺ _{0.25} Co ²⁺ _{0.1} Mn ²⁺ _{0.15} Li ⁺ _{0.5}).....	204
Figure 6-2: Comprehensive performance analysis of pure Pb, Ti, Pt, C and GC electrodes based on anode overvoltage, cost, service life and corrosion factor (mass lost during operation) (Partial Data derived from ref (Moradi et al. 2020; Bloomberg 2022)).	205
Figure 6-3: Anodic voltage of Ti and Pt Coated Ti (at 0.035 A/cm ² , pH =4.5, 50 °C in 47.5 g/L of Ni ²⁺ _{0.25} Co ²⁺ _{0.1} Mn ²⁺ _{0.15} Li ⁺ _{0.5}).....	205
Figure 6-4: Cell potential vs energy consumption and current density for the electrowinning of Co-Ni deposits.....	208
Figure 7-1: a) Micrograph of the deposit obtained from the cathode leachate solution electrowinning, b) EDX spectrum of the electrowon deposit and c) EDS mapping of the electrowon deposit (-1.15 V vs Ag/AgCl, 50 °C, 15 g/L of buffer solution, 15 g/L Na ₂ SO ₄ , pH 4, AA/E of 2 cm ² /250 cm ³).	214
Figure 8-1: Concentration of the Li, Ni, Co and Mn metals at different pH levels (a) Temperature = 20 °C b) Temperature = 40 °C.....	221
Figure 8-2: Recovery efficiency of the NMC metals at different pH levels (Temp=20 °C).	222
Figure 8-3: Photo (a) and XRD pattern (b) of 0.6[Ni(OH) ₂].0.3[Mn(OH) ₂].0.1[Co(OH) ₂]material obtained by precipitation.	225
Figure 8-4: The effect of CO ²⁻ ₃ :2Li ⁺ molar ratio on Li ⁺ recovery efficiency (reaction time=1hr).	226
Figure 8-5: The effect of temperature on Li ⁺ recovery efficiency.	227
Figure 8-6: The effect of pH on Li ⁺ recovery efficiency over time.....	228
Figure 8-7: a) Photo and b) XRD pattern of Li ₂ CO ₃ material recovered through precipitation.	229
Figure 9-1: Summated process flow diagram (with numbered streams) of the novel process reported in this work.	235
Figure 9-2: Comprehensive metal recovery material balance block flow diagram.....	239
Figure A-0-1: Cash flow of a plant with a capacity of 4500 kgs/year.	286

List of Tables

Table 2-1: Characteristics of the prevalently employed intercalation cathode compounds; crystal structure, theoretical/experimental/commercial specific and volumetric capacities, average operation voltages, and level of development.	35
Table 2-2: Approximate value for main components in a typical Li-ion cell (April 2022) (data from (Bloomberg 2022))......	54
Table 2-3: Advantages and disadvantages of conventional pre-treatment methods (Kim et al. 2021; Zhang et al. 2021)......	64
Table 2-4: Summative review of leaching spent Li-ionBs using different leaching reagents....	70
Table 3-1: Materials and chemicals utilised during the course of this research.....	105
Table 3-2: Compilation of all the small equipment used in this project.	109
Table 3-3: Leaching experimental design specifying the high and low values for each variable.	113
Table 3-4: leaching conditions at different H ₂ O ₂ concentration levels.	114
Table 3-5: Leaching conditions at different solid/liquid ratios.	115
Table 3-6: Leaching conditions at acid concentrations.....	115
Table 3-7: leaching conditions at different temperature levels.	116
Table 3-8: leaching conditions at different time levels.	117
Table 3-9: Electrowinning experimental design.....	120
Table 3-10: Electrowinning conditions at different Co/Ni ratios.....	121
Table 3-11: Electrowinning conditions at different potential levels.....	122
Table 3-12: Electrowinning conditions at different pH levels.....	122
Table 3-13: Electrowinning conditions at different temperature levels.....	123
Table 3-14: Electrowinning conditions at different Ni-Co concentrations.	124
Table 3-15: Electrowinning conditions at different electrode distance levels.....	124
Table 3-16: Electrowinning conditions at different electro-active area levels.	125
Table 3-17: Electrowinning conditions at different buffer concentrations.....	126
Table 3-18: Electrowinning conditions at different Na ₂ SO ₄ concentrations.	126
Table 3-19: Electrowinning conditions at different rotating anode speeds.....	127
Table 3-20: Composition of the solutions employed in the electrowinning tests.....	127
Table 3-21: Precipitation conditions at different pH levels (20 °C).....	132

Table 3-22: Precipitation conditions at different pH levels (40 °C).....	132
Table 3-23: Precipitation conditions at different $\text{CO}_3^{2-}:\text{Li}^+$ Ratios.....	134
Table 3-24: Precipitation conditions at different temperature levels.	134
Table 3-25: Precipitation conditions at different pH levels.	135
Table 4-1: Characterization of the sample using ICP-OES obtained after pre-treatment of the NMC battery cathode used for the acid leaching tests.	150
Table 4-2: Leaching yields obtained using a 75 g/L S/L, 2M H_2SO_4 + 6 H_2O_2 v/v % solution, at 60 °C for 2h.....	161
Table 4-3: Kinetic parameters for leaching of Li, Co, Ni, and Mn under different temperature Model I, Model II and by Avrami model.	164
Table 5-1: Chemical composition, determined by ICP-OES, of the Ni-Co deposit obtained in the electrowinning process (47.5 g/L of $\text{Ni}^{2+}_{0.25}\text{Co}^{2+}_{0.1}\text{Mn}^{2+}_{0.15}\text{Li}^{+}_{0.5}$, -1.15 V vs Ag/AgCl, 50 °C, 15 g/L of buffer, 15 g/L of Na_2SO_4 , pH 4.5, 40 rpm).....	199
Table 5-2: Chemical composition, determined by EDS, of the deposit obtained in the electrowinning (47.5 g/L of $\text{Ni}^{2+}_{0.25}\text{Co}^{2+}_{0.1}\text{Mn}^{2+}_{0.15}\text{Li}^{+}_{0.5}$, -1.15 V vs Ag/AgCl, 50 °C, 15 g/L of buffer, 15 g/L Na_2SO_4 , pH 4.5, AA/E of 30 $\text{cm}^2/250 \text{cm}^3$).	201
Table 6-1: Cell voltage contributions from anode potential, cathode potential, solution voltage and contact voltage.	208
Table 7-1: Current efficiency obtained using different synthetic solution compositions electrowinning (-1.15 V vs Ag/AgCl, 50 °C, 15 g/L of buffer, 15 g/L Na_2SO_4 , pH 4.5).	211
Table 7-2: Composition of the cathode before electrowinning, and EW Ni-Co deposit after the electrowinning process as determined by ICP-OES (-1.15 V vs Ag/AgCl, 50 °C, 15 g/L of buffer, 15 g/L Na_2SO_4 , pH 4.5).....	212
Table 7-3: Chemical composition of Ni-Co deposit, determined by EDS, of the deposit obtained in the electrowinning (-1.15 V vs Ag/AgCl, 50 °C, 15 g/L of buffer, 15 g/L Na_2SO_4 , pH 4.5)...	215
Table 8-1: Composition of the leachate before and after the electrowinning process using ICP-OES.....	219
Table 8-2: ICP-OES analysis of the resultant precipitate at pH 7.85.	224
Table 8-3: ICP-OES analysis of the resultant precipitate at pH 12.85.....	224
Table 8-4: ICP-OES analysis of the resultant solution after electrowinning and multistage precipitation.	230
Table 9-1: Detailed mass balance of the novel recovery process reported in this work.....	238

Table A-0-1: Raw materials cost estimation to produce 5.8 g of Ni-Co composite material.	279
Table A-0-2: Cost of major equipment utilised in the production of Ni-Co (4500 kgs/year).	280
Table A-0-3: Energy consumed (kWh/day) per each major unit involved in the recovery process.	281
Table A-0-4: Estimation cost of the plant utilities per year (plant with capacity 4500 kgs Ni-Co/year).	282
Table A-0-5: Operating labour cost for 1300 hours per year using a plant capacity for Ni-Co composite material at a rate of 4500 kgs Ni-Co/year.	283
Table A-0-6: Manufacturing cost estimation for production of Ni-Co composite material (4500 kgs/year).	284
Table B-0-1: Cash Flow Statement (4500 kg Ni-Co Production Plant).....	288

List of Symbols-Scientific

Scientific Symbols

Symbol	Description	Units
E_a	Activation Energy	J/mol
θ	Angle	°
V_x	Bulk Volume	ml
X_c	Conversion	%
I	Current	A
η_c	Current efficiency	%
D	Diameter	m
E	Energy	J
η	Energy Efficiency	%
De	Equivalent Diameter	m
F	Faraday Constant	V
Q	Flowrate	m ³ /hr
G	Free Energy	J
n	Impeller Effective Diameter	m
μ_K	Kinematic Viscosity	m ² /s
η_l	Leaching efficiency	%
m	Mass	kg
M_r	Molar Mass	g/mol
N	Moles	mol
η_x	Overpotential	V
E	Potential	V
P	Power	W
η_p	Precipitation efficiency	%

k	Rate Constant	
X_i	Reaction Conversion Factor	%
X	Recovery Efficiency	%
R	Resistance	W
Re	Reynolds Number	
W	Specific Energy	J/kg
E_C	Specific Energy Capacity	mAh/g
ρ_{sg}	Specific gravity	
E^0	Standard Potential	V
v	Stoichiometry Coefficient	
t	Time	hrs
R	Universal Gas Constant	J/mol. K
$\pm n$	Valence of a metal	
V	Voltage	V
λ	Wavelength	m

List of Symbols-Chemical Species

Specie	Description
CO ₂	Carbon Dioxide
Co	Cobalt
Co(OH) ₂	Cobalt Hydroxide
CoSO ₄	Cobalt Sulphate
Cu	Copper
F	Fluorine
HCl	Hydrochloric Acid
H ₂	Hydrogen
Fe	Iron
Pb	Lead
Li	Lithium
Li ₂ CO ₃	Lithium Carbonate
LiCoO ₂	Lithium Cobalt Oxide
LiOH	Lithium Hydroxide
Li ₂ SO ₄	Lithium Sulphate
Li ₂ S	Lithium Sulphide
Mn	Manganese
Mn(OH) ₂	Manganese Hydroxide
MnSO ₄	Manganese Sulphate
NaH ₂ PO ₄	Monosodium Phosphate
Ni	Nickel
Ni(OH) ₂	Nickel Hydroxide
NiSO ₄	Nickel Sulphate
HNO ₃	Nitric Acid

H_2PtCl_6	Platinic Acid
Pt	Platinum
Se	Selenium
Ag	Silver
Ag/AgCl	Silver/Silver Chloride
NaOH	Sodium Hydroxide
Na_2SO_4	Sodium Sulphate
S	Sulphur
H_2SO_4	Sulphuric Acid
Te	Tellurium
Ti	Titanium
H_2O	Water

List of Abbreviations

BMS	Battery Management System
BTS	Battery Testing Station
CB	Carbon Black
CS	Cathode Rotational Speed
AA/EV	Cathodic Surface Area to Electrolyte Volume Ratio
CSIRO	Commonwealth Scientific and Industrial Research Organisation
CE	Constant Current Electrowinning
PE	Constant Potential Electrowinning
CV	Cyclic Voltammetry
DOE	Department of Energy (United States)
DC-AC	Direct Current-Alternating Current
EPRI	Electric Power Research Institute
ES	Energy Storage
FCC	Face Centred Cubic
GF/CNT	Graphene Foam-Carbon Nano-Tubes
C	Graphite
HCP	Hexagonal Close Packed
IREA	International Renewable Energy Agency (USA)
LCO	Lithium Cobalt Oxide
LFP	Lithium Iron Phosphate
NCA	Lithium Nickel Cobalt Aluminium Oxide
NCM	Lithium Nickel Cobalt Manganese Oxide
NMC	Lithium Nickel Manganese Cobalt
LTO	Lithium Titanium Oxide

Li-ionB	Lithium-Ion Battery
MCI	Metal Chlorides
MF	Metal Fluorides
NPV	Net Present Value
NiCd	Nickel Cadmium
NiMH	Nickel Metal Hydride
OCV	Open Circuit Voltage
PCM	Phase Change Material
PDI	Polydispersity Index
PVDF	Polyvinylidene Fluoride
PEM	Proton Exchange Membrane
SEM	Scanning Electron Microscopy
SEI	Solid Electrolyte Interphase
TEM	Transmission Electron Microscopy
XRD	X-Ray Diffraction

Chapter 1: Introduction and Background

1.1 Background

1.1.1 Li-ion Battery Application Trends

In the last decade, the world has initiated a global trend focused on environmental conservation to achieve sustainability across ecological, economic, and social dimensions. Due to their non-renewable nature, fossil fuels, which have long met our society's energy needs, are gradually exhibiting various detrimental effects on the environment and energy security. As a result, many organizations and countries worldwide are actively devoting resources that could replace traditional internal combustion engines with electric cars and equipment powered by renewable energy storage sources. Ultimately, this shift aims to overcome the challenges associated with the utilization of fossil fuels. Consequently, the demand for portable electronic devices, such as smartphones, tablets, notebooks, radios, laptops, and other devices powered by electric storage systems (i.e., batteries), has experienced a significant surge in recent years. These trends have spurred the development and widespread application of portable electrochemical energy storage technologies, including nickel-metal hydride batteries (NiMH), lithium-ion batteries (Li-ionB), conventional lead-acid batteries (Pb-acid), and nickel-cadmium batteries (NiCd) (AL Shaqsi et al. 2020).

Li-ionBs stand as the most widely adopted and utilized battery technology within the realm of renewable energy storage devices. This dominance is attributed to their exceptional electrochemical performance, boasting superior power density, energy density, and enduring stability. Government initiatives and policies advocating for clean energy and electric mobility have significantly contributed to the escalating market demand for these batteries. Furthermore, the increased global focus on sustainability, coupled with advancements in battery technology that amplify the efficiency and performance of Li-ionBs, has spurred a notable surge in their demand. As industries and consumers prioritize environmentally friendly solutions, the Li-ionB market is expected to continue its upward trajectory, fostering innovation and economies of scale in producing and deploying these energy storage devices. Moreover, there is an anticipation that the use of Li-ionBs in the automotive industry will continue to expand, further increasing their demands.

1.1.2 Li-ion Battery Economic, Production and Disposal Trends

The demand-led market growth of Li-ionBs and the rechargeable Li-ionB market size are shown in Figure 1-1 and Figure 1-2, respectively. The global demand for Li-ionBs is projected to reach nearly 700 GWh by 2030, with prices expected to drop to as low as USD \$100/kWh (Phuc Anh LE 2019). The Energy Sector Management Assistance Program (ESMAP) (2022) reported that the Li-ionB market grew from 5 billion US \$ in 2005 to approximately 35 billion US \$ in 2020, with a significant proportion of applications in electronic devices. The Li-ionB market is projected to reach over 75 billion US dollars in 2025, accounting for 70% of the market for rechargeable batteries, as indicated in Figure 1-2 (Phuc Anh LE 2019; ESMAP 2022). Figure 1-2 illustrates the shift in the electrochemical battery energy storage market from 2015 to 2025, highlighting the transition from Pb-acid batteries dominated market to a Li-ionBs dominated market. As highlighted, the market is shifting from fully recyclable Pb-acid battery technology to Li-ionB technology, which is currently not being recycled as effectively. The shift underscores the growing need for recycling of Li-ionBs to manage the increasing volume of spent batteries generated by the expanding user market.

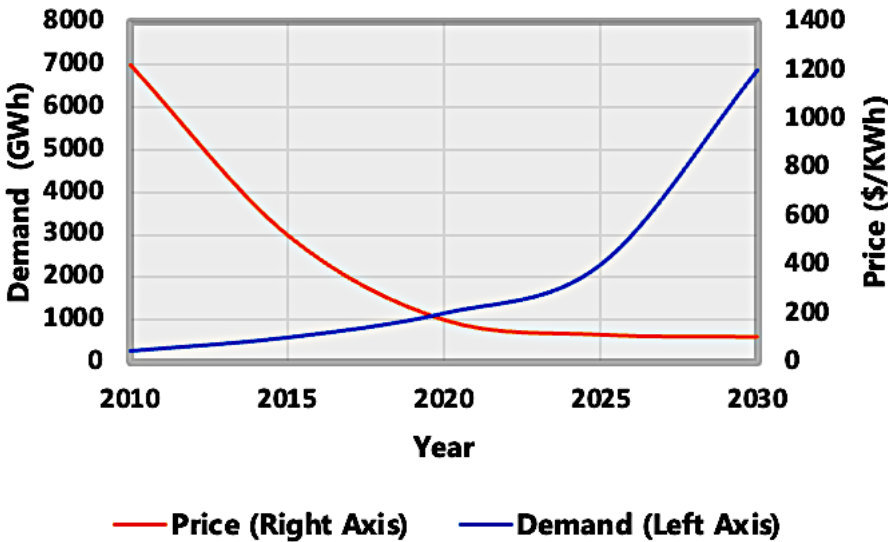


Figure 1-1: The demand-led market growth of Li-ion batteries (Data derived from (ESMAP 2022)).

The upsurge of Li-ionB production and deployment is currently hampered by a lack of sufficient raw materials and environmental pollution accumulated from spent Li-ionBs. Landfilling is the traditional method of disposing of spent Li-ionBs; however, the heavy metals and organic electrolytes present in spent Li-ionBs will possibly leak and spill into the surrounding

environment, ultimately posing a severe threat to the environment and human health. The anticipated substantial increase in the consumption of Li-ionBs to meet rising demand in the future is poised to create challenges that demand prompt and effective resolutions. This is particularly crucial due to the significant accumulation of spent Li-ionBs in landfills, necessitating immediate attention to address potential environmental and waste management concerns.

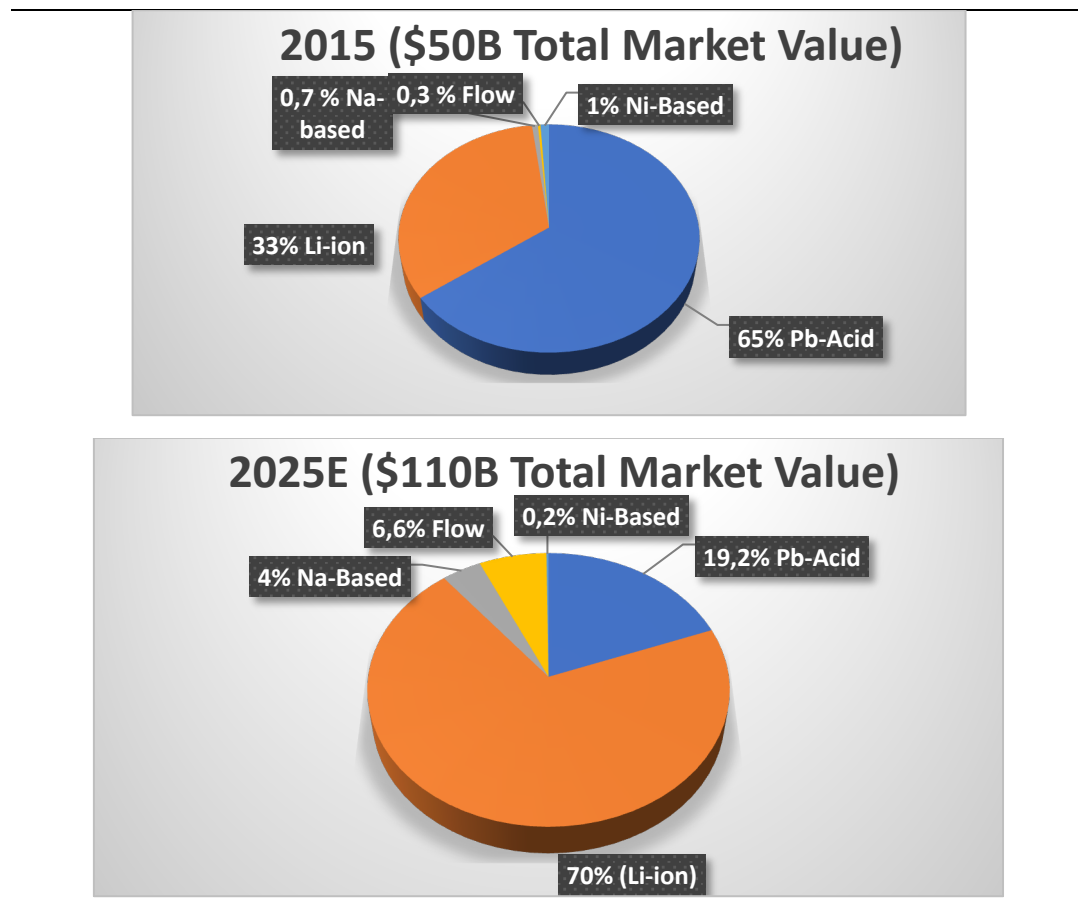


Figure 1-2: Rechargeable Li-ionB market size (data derived from (Phuc Anh LE 2019)).

In an attempt to avoid the apparent inevitable consequences associated with disposing of batteries in landfills, countries and economic unions are introducing bills and laws aimed at reducing e-waste in landfills. In particular, the EU introduced Directive 2006/66/EC of The European Parliament to address the waste of old electric and electronic devices and batteries. The measures aim to curb the presence of spent batteries in landfill sites (European Union 2006). This means end-user consumers and companies must submit e-waste for recycling by taking it to a licensed electric and electronic waste equipment recycler.

In the South African context, the Consumer Protection Act (CPA) 68 of 2008 regulates the recycling of lithium-ion batteries by enforcing safe disposal obligations, mandating take-back programs, and promoting extended producer responsibility, in alignment with the National Environmental Management: Waste Act 107 of 1998 (South African Government 1999, 2009). Suppliers must accept returns of Li-ionBs from consumers without charge, ensuring responsible disposal and preventing environmental harm. Additionally, manufacturers, importers, and distributors are required to manage the recycling of these batteries, while the CPA also prohibits misleading claims about recyclability and encourages consumer education on proper disposal practices.

The widespread and continuously escalating consumption levels of Li-ionBs result in substantial quantities of spent batteries that need to be recycled using eco-friendly and economically viable process routes. Closed and open loop recycling process routes should ideally provide sufficient materials for manufacturing new Li-ionBs. It is evident that recycling, recovering, and reusing Li-ionBs will be a crucial initiative in assisting countries (both developed and developing) to make a rapid and sustainable transition to clean energy generation. If recycling and reuse practices are implemented effectively on a large scale, greenhouse gas (i.e., CO₂, CH₄, NO_x) emissions and environmental damage should be curtailed.

Li-ionBs constitute significant amounts of valuable metals such as copper (Cu) aluminium (Al), lithium (Li), cobalt (Co), manganese (Mn), and nickel (Ni), with Co being the most valuable (Zheng et al. 2018). Assuming that the valuable metal content in Li-ionB cathodes can be effectively recovered in its pure metallic form, approximately a combined US\$ 20 000 monetary value of Co and Ni present in 1 metric ton of spent Li-ionBs (de Oliveira Demarco et al. 2019; Bloomberg 2022). The market value of Li is significantly lower, on average US\$ 6500 per ton, but has increased steadily since 2010, reaching US\$ 40000 a ton in Jan 2022 (Bloomberg 2022). As a result, the recovery of these valuable metals has a significant economic influence on the development of the Li-ionB recycling process (de Oliveira Demarco et al. 2019; Bloomberg 2022).

1.1.3 Li-ion Battery Conventional Recycling and Future Technologies

In light of the environmental and economic concerns, it is necessary and imperative to separate, reuse, and recycle all components of Li-ionBs to circumvent problems accrued from spent Li-ionB disposal (Zheng et al., 2018; Halli et al., 2020). Considering the complexity of raw materials, it is challenging to design and successfully run a single-stage recycling process that is both economical and environmentally friendly. Therefore, recycling spent Li-ionBs using a multistage combination of physical and chemical methods is standard practice. Physical dismantling, crushing, sieving, heating, and mechanochemical treatment are traditional physical techniques that enhance recycling efficiency (Werner et al. 2020; Chandran et al. 2021). Pyrometallurgy and hydrometallurgy are two major subsets of the chemical recycling process routes. Hydrometallurgical processes edge pyrometallurgical processes, which are often carried out at high temperatures due to more environmentally friendly process pathways, milder reaction conditions, and higher valuable metals recovery efficiency, especially Li (Georgi-Maschler et al. 2012; Zheng et al. 2018; Chandran et al. 2021). These advantages mark hydrometallurgical processes as preferable and ideally promising for processing and recycling spent Li-ionBs.

Conventionally, In order to recover valuable metals (Co, Ni, and Li) from spent Li-ionB waste, the process often starts with acid-based leaching. The leaching solution typically constitutes an acid plus added reducing agent additive. This process oxidizes the metals to more soluble states (ions) (Georgi-Maschler et al. 2012; Kim et al. 2021). More than 99% (by mass) of Co, Ni, and Li metals can be leached when a sufficiently strong acidic solution is utilized. The metals in leachate solution of battery metals are selectively separated using either ion exchange membranes, selective precipitation or solvent extraction (Georgi-Maschler et al. 2012; Zheng et al. 2018; Chandran et al. 2021). The pure metal solutions can undergo chemical or electrochemical (electrochemical reduction to produce pure metal forms such as metal salts, oxides or electrolytic metal.

To date, many technologies based on pyrometallurgical, hydrometallurgical, and electrometallurgical processes have been developed commercially for the recycling of spent Li-ionBs. Pyrometallurgical processes have been commercialized and exploited by some companies (Umicore, SONY, OnTo, Accurec, Inmetco, Xstrata, etc.) (Tawonezvi et al. 2023). The pyrometallurgical processes are often coordinated with hydrometallurgical processes to

recycle the valuable metals. In pyrometallurgical processes, the acetylene black, organic electrolyte, and binder in the spent Li-ionBs are usually burnt off, which causes high energy consumption and emission of hazardous gases (Makuza et al. 2021a).

Consequently, these elements are prone to oxidation during the smelting process, leading them to enter the slag in the form of their respective oxides. Electrometallurgy uses electrical current to extract metals from their ore solutions (Zeng et al. 2014; Chandran et al. 2021). It is usually the last stage in valuable metal extraction and is, therefore, preceded conventionally by pyrometallurgical or hydrometallurgical operations (Tawonezvi et al. 2023). The electrometallurgy process entails low energy consumption, minimal emissions, and high product purity (Tawonezvi et al. 2023). By contrast, hydrometallurgical and electrometallurgy processes entail some attractive advantages, such as high metal recovery rates, high product purity, moderate energy consumption, and minimal gas emission. Therefore, hydrometallurgical processes are considered more suitable for recycling spent Li-ionBs, and many studies based on hydrometallurgical processes have been reported in recent years.

Closed-loop recycling has been demonstrated to effectively reduce cost and energy consumption; however, since recovered materials are of low elemental purity, they cannot be repurposed, unlike open-loop recycling, which allows for materials repurposing after recovery although the recycling route entails high cost and high energy consumption (Chen, Zheng, et al. 2019; Yang et al. 2023). In addition to the above, it is worth noting that most recycling work up to date is open-loop recycling since most of the valuable metals will be repurposed for multiple and broad applications. As highlighted previously, owing to the great increase in spent Li-ionBs waste generation, the recovery and recycling of the valuable metals constituted in Li-ionBs should be investigated to avoid the disposal of tons of dangerous waste (Zeng et al. 2014). The goal of waste minimization, combined with the economic value of metals such as Ni and Co, requires the development of cost and energy-efficient recycling processes. Therefore, recycling spent battery waste, besides the apparent anti-environmental pollution benefit, can also accrue economic benefits.

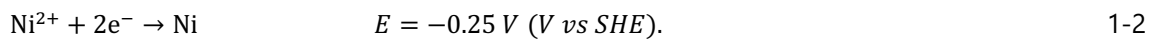
1.1.4 Rationale of This Work

The cathode of Li-ionBs is the most determinant component for the battery's electrochemical performance. The NMC cathode is also the most valuable component in a typical NMC Li-ionB because it typically contains significant amounts of precious metals such as Li, Co, Ni, and Mn. Notably, Ni and Co are significantly more valuable than Li and Mn. Conventionally, battery metals (Ni, Co, Li and Mn) are selectively recovered as their pure metal solutions from complex multi-ion leachate solutions by using solvent extraction, ion exchange, and selective precipitation (to extract Li, Mn Ni and Co selectively). The produced pure metal ion rich solutions still need to go through reduction stage to reduce the metal ions to their metallic state or metallic oxides using galvanostatic electrowinning (electrochemical reduction).

Although there are many types of cathode materials, such as NMC, LFP, and NCA, NMC is currently the most dominant chemistry, accounting for 60% of the Li-ion battery market (Kamran 2023). In light of the expanding Li-ion battery market, NMC is expected to be the most prevalent chemistry in typical Li-ion battery waste (Kim et al. 2021; Islam and Iyer-Raniga 2022). Therefore, NMC has been selected as the focus of this research. In this work, Ni-Co alloys from spent Li-ionBs were selectively recovered from NMC leachate solutions that contain Li, Mn, Co and Ni ions through potentiostatic electrowinning since, besides application in cathode production, Ni-Co composites and alloys can also be used in production of magnetic films, electrocatalysis, electronic chips, anti-corrosion systems, micro and nanogears among other various technological applications (Tian et al. 2011; Karimzadeh et al. 2019). Since the post electrowinning spent liquor still constitute low traces of Ni and Co and significant amounts of Li and Mn, additional Na-based multi-stage chemical precipitation unit operation was added to selectively recover pure $0.6[\text{Ni}(\text{OH})_2].0.3[\text{Mn}(\text{OH})_2].0.1[\text{Co}(\text{OH})_2]$, $\text{Mn}(\text{OH})_2$ and Li_2CO_3 materials.

The rationale of this research is hinged on the elimination of cost and energy-intensive hydrometallurgy intermediate processes like solvent extraction, ion exchange, and selective precipitation (to extract Ni and Co selectively), utilization of potentiostatic techniques (instead of conventional galvanostatic method) to selectively extract specific valuable metals (Ni and Co) from less valuable metals (Mn and Li) and enhance the purity, integration of rotating cathodes to increase deposition rate and utilization of Pt coated Ti dimensionally stable anodes

(DSA) to reduce deposit contamination and consequently levelized cost of operation. The selective separation of valuable Ni and Co from less valuable Li and Mn can be achieved by applying constant potential (-0.24 to -0.30 V vs SHE) suitable for Co and Ni reduction reactions, specifically through potentiostatic electrowinning. The reduction potentials of the metals present in the cathode leachates are listed as follows:



The elimination of intermediate purification stages is based on the fact that the Co and Ni salts or pure Ni and Co compounds are introduced to the cathode synthesis or production process as a mixture; therefore, there is no need to separate them beforehand. The Ni-Co alloys recovered from spent Li-ionBs was targeted for closed and open loop recycling since besides Li-ionB cathode production, they can also be used in magnetic films, electrocatalysis, electronic chips, anti-corrosion systems, micro, and nanogears among other various technological applications. The recovered Li_2CO_3 is a versatile compound with applications ranging from producing Li-ionBs and stabilizing mood in pharmaceuticals to enhancing properties in glass and ceramics, aluminium production, metallurgical processes, chemical synthesis, and absorption refrigeration systems for air conditioning. The recovered $\text{Mn}(\text{OH})_2$ can be employed as a coagulant in water treatment, a cathode material in alkaline batteries, and a micronutrient supplement in agriculture, showcasing its versatility across applications. Lastly, the recovered hydroxide composite formulation of Ni, Mn, and Co ($0.6[\text{Ni}(\text{OH})_2].0.3[\text{Mn}(\text{OH})_2].0.1[\text{Co}(\text{OH})_2]$) ought to be used solely for Li-ionB cathode production. The integrated hydro-electrometallurgy process route of extracting Ni-Co alloys was explored and thoroughly assessed. This work demonstrates the technical viability of recovering Ni-Co alloys and metallic by-products through the optimized hydro-electrometallurgy process.

1.2 Research Problem Statement

Battery recycling emerges as a critical facilitator for achieving the “Net Zero Scenario” owing to the cumulative demand for Co and Ni that are projected to surpass current known reserves by 2050 (Zheng et al. 2018). A 'Net Zero Scenario', in the context of battery waste, refers to a situation where the amount of critical elements (Ni and Co) disposed of as Li-ion battery waste is balanced by the amount recovered through recycling, resulting in no net increase in the levels of these elements in the environment. With universal battery recycling, primary Co and Ni demand will remain below known reserves, and there is also the prospect of a fully functional circular battery industry. In addition, battery waste poses an environmental and safety hazard, which makes it more complex and expensive to sort and reprocess. Spent batteries contain toxic and flammable components, and negligent disposal of batteries in landfills carries a high risk of soil and groundwater contamination and explosions (Werner et al. 2020; Zhao et al. 2021a). The cost and energy consumption of conventional recycling processes is enormous.

Based on the exploration of the literature, it is clear galvanostatic electrowinning has been conventionally used to reduce metals at the latter stages of recycling processes that include costly and energy intensive methods like solvent extraction, ion exchange and selective precipitation (Wang 2006; Zeng et al. 2014; Lv et al. 2018; Zhou et al. 2020; Ali et al. 2022; Baum et al. 2022; Du et al. 2022). It is also clear and evident that potentiostatic electrowinning, a different mode of electrowinning, was never explored to selectively recover metals from multi metal specie battery metal solutions. In this work, a cost and energy-optimised potentiostatic electrowinning recovery process is explored thoroughly. Solvent extraction, ion exchange, selective precipitation and any other Co and Ni selective purification process are eliminated from a conventional electrometallurgy recycling process to reduce capital and operating costs. Selective recovery of Ni and Co from solutions containing Li, Mn, Mn and Co is attained using potentiostatic electrowinning after leaching.

1.3 Research Aim and Objectives

The aim of this study is to recover Ni-Co alloys at industrial-grade purity using an optimised hydro-electrometallurgy process.

To achieve the aim as stipulated above, the objectives of this research are as follows:

- a) To optimise leaching by varying solid-to-liquid (S/L) ratio, leaching reaction time, leachant concentration, and the additive H_2O_2 concentration.
- b) Perform cyclic voltammetry using simulated solutions to establish Co and Ni deposition potential.
- c) Establish a comparison of the selectivity for Ni-Co deposition in a Li, Mn, Co, and Ni electrolyte solution between potentiostatic and galvanostatic electrowinning methods.
- d) Optimise electrowinning of Co-Ni alloys using simulated solutions and modified electrodes (electroless platinum-plated titanium and aluminium alloy electrodes) by varying metal concentration, deposition potential, temperature, pH, anode rotation speed, electrode distance, and area.
- e) Recover Co-Ni alloy from a leachate solution, obtained from NMC cathode material, using an optimized electrowinning process.
- f) Optimise the Na-based chemical precipitation using the electrowinning spent liquor by varying reactants ratio, pH, and temperature.
- g) Recover $\text{Mn}(\text{OH})_2$, Li_2CO_3 , and $0.6[\text{Ni}(\text{OH})_2].0.3[\text{Mn}(\text{OH})_2].0.1[\text{Co}(\text{OH})_2]$ from the electrowinning spent liquor (post electrowinning liquor) using Na-based chemical precipitation.
- h) Perform a cost evaluation of the Ni-Co production at pilot scale using the optimized electrowinning and Na-based chemical precipitation processes.

1.4 Research Questions

- What is the optimum solid-to-liquid ratio (S/L), leaching reaction time, leachant concentration, and reductant H_2O_2 concentration to effectively leach valuable metals from NMC 532 cathode?
- What is the Co and Ni deposition potential in a simulated Co-Ni solution using potentiostatic electrowinning?
- Is the potentiostatic electrowinning selective towards Ni-Co in a Li, Mn, Co and Ni electrolyte solution than galvanostatic electrowinning?
- What is the optimum metal concentration, deposition potential, temperature, pH, Na_2SO_4 concentration, NaH_2PO_4 buffer dosage, cathode rotation speed, and, cathode formulation, electrode distance and area to effectively recover valuable Ni-Co alloys from simulated NMC 532 cathode solutions?

- What is the deposition rate and purity of the recovered Ni-Co composite metals from the leachate solution when recovered using an optimised electrowinning process?
- What is the optimal pH, temperature, and reactants ratio to efficiently recover and extract Mn(OH)_2 , Li_2CO_3 , and $0.6[\text{Ni(OH)}_2].0.3[\text{Mn(OH)}_2].0.1[\text{Co(OH)}_2]$ selectively from electrowinning spent liquor (post electrowinning liquor)?
- What is the production cost of the Ni-Co alloy production at pilot scale and recycling cost of the NMC cathode using the optimised hydro-electrometallurgy process from this work?
- How does the optimised hydro-electrometallurgy process compare to other conventional processes used to extract valuable metals?

1.5 Delineation

This research will mainly focus on the recovery of Ni-Co alloys from spent Lithium-ion battery cathode (NMC 532) leachates through an electrowinning process that utilises Pt-plated titanium and aluminium electrodes without the need for pre-purification processes. Additionally, the research will touch upon the recovery of Mn(OH)_2 , Li_2CO_3 , and $0.6[\text{Ni(OH)}_2].0.3[\text{Mn(OH)}_2].0.1[\text{Co(OH)}_2]$ from the electrowinning liquor through an optimised Na-based chemical precipitation process.

1.6 Novelty of Study

- The presented valuable *metal recovery process* of NMC 532 Li-ionB cathode.
- The utilisation of *rotating plate batch potentiostatic electrowinning* to selectively recover pure (98 % pure) Ni-Co alloys from Mn^{2+} , Li^+ , Co^{2+} and Ni^{2+} multi-ion solution.
- The utilisation of Pt-plated titanium plate and aluminium plate electrodes and rotating anode mechanism.
- The elimination of conventional pre-purification separation stages (e.g., solvent extraction, ion exchange, and selective precipitation).

1.7 Significance of Research

The retrieval of valuable materials during the recycling process is pivotal for producing new batteries and, consequently, reducing the overall manufacturing costs. Approximately half of a

battery's cost is attributed to cathode materials (United States Geological Survey 2020; ESMAP 2022). The prices of two common cathode metals, cobalt, and nickel, the most expensive components, have fluctuated substantially in recent years. Notably, the prices of crucial cathode metals, particularly cobalt, and nickel, have experienced significant fluctuations in recent years, with current market prices at roughly \$27,500 per metric ton for Co and \$12,600 per ton for Ni (United States Geological Survey, 2020). The concentrations of these metals, along with those of lithium and manganese, in many Li-ionBs exceed the concentrations in natural ores, making spent batteries akin to highly enriched ore. If more economical than extracting from natural ore, successful large-scale recovery of these metals from used batteries holds the potential to drive down the price of batteries and electric vehicles.

In addition to potential economic benefits, recycling could reduce the material going into landfills. Cobalt, nickel, manganese, and other metals found in batteries can readily leak from the casing of buried batteries and contaminate soil and groundwater, threatening ecosystems and human health. The same is true of lithium fluoride salts (LiPF_6 is common) in organic solvents used in a battery's electrolyte. Batteries can have adverse environmental effects at the end of their lives and long before they are manufactured. As Gaines (2012) pointed out, more recycling means less mining of virgin material and less of the associated environmental harm. For example, mining for some battery metals requires processing metal-sulphide ore, which is energy-intensive and emits SO_x that can lead to acid rain (Gaines 2012). Less reliance on mining for battery materials could also slow the depletion of these raw materials. Xu et al. (2020) used computational methods to model how growing battery production could affect the geological reserves of several metals through 2050. Acknowledging that these predictions are "complicated and uncertain," the researchers found that world reserves of lithium and nickel are adequate to sustain the rapid growth of battery production. However, battery manufacturing could decrease global cobalt reserves by more than 10% (Xu et al. 2020).

There are also political costs and downsides that recycling Li-ionBs could help address. According to a CSIRO (2022) report 50% of the world's production of cobalt comes from the Democratic Republic of the Congo and is tied to armed conflict, illegal mining, human rights abuses, and harmful environmental practices (CSIRO 2022). Recycling batteries and formulating cathodes with a reduced concentration of cobalt could help lower the dependence on such problematic foreign sources and raise the security of the supply chain.

The Ni-Co composite recovered from spent Li-ionBs will be targeted for closed and open loop recycling since besides Li-ionB cathode production, which is the main target use for the Ni-Co composite, Ni-Co alloys and alloys can be used in magnetic films, electrocatalysis, electronic chips, anti-corrosion systems, micro and nanogears among other various technological applications. The recovered Li_2CO_3 is a versatile compound with applications ranging from production of Li-ionBs, stabilizing mood in pharmaceuticals to enhancing properties in glass and ceramics, aluminium production, metallurgical processes, chemical synthesis, and absorption refrigeration systems for air conditioning. The recovered $\text{Mn}(\text{OH})_2$ can be employed as a coagulant in water treatment, a cathode material in alkaline batteries, and a micronutrient supplement in agriculture, showcasing its versatility across applications. Lastly, the recovered hydroxide composite formulation of Ni, Mn, and Co ($0.6[\text{Ni}(\text{OH})_2].0.3[\text{Mn}(\text{OH})_2].0.1[\text{Co}(\text{OH})_2]$) is to be used solely for Li-ionB cathode production. The integrated hydro-electrometallurgy process route of extracting Ni-Co alloys was explored and thoroughly assessed. This work demonstrate the technical viability of recovering Ni-Co and metallic by-products through the optimised hydro-electrometallurgy process.

1.8 Thesis Layout

The outline structure of this thesis is briefly described under each of the chapter headings that follow:

Chapter 1 - Introduction:

This introductory chapter provides insight into the research with background information on Lithium-ion battery recycling and an overview of the potential and current functional recycling technologies that are currently under investigation. A brief background into the hub of the research in Lithium-ion batteries is also provided. The application, justification and value of this research for recycling Li-ionBs using leaching-**electrowinning**-chemical precipitation process are discussed. The overall aim and research objectives are also identified and explained in this chapter.

Chapter 2 - Literature Review:

The literature review shelters all the theoretical background required to gain an in-depth understanding of the fundamental engineering principles that are applied in this research. The review is extensive and covers most of the theory, directly and indirectly, related to the research to ensure that the review is sufficiently holistic for a range of engineers, regardless of discipline, to comprehend the theories and implicated practical work presented here. Recovery of valuable metals from spent Li-ionBs using hydrometallurgical and electrometallurgical processes is the primary focus of the literature review; however, other sections related to Li-ionB recycling have also been featured briefly to facilitate easy connections to the overarching concept. Fundamental understandings of Li-ionB design, deliberations and theories and conventional recycling methods have also been included as the foundation of the research topic. The testing standards required to validate this study have also been covered and presented.

Chapter 3 – Experimental Methods:

This chapter describes the materials and experimental methodologies used in this research. All the techniques, programs and equipment are well-detailed and presented to elucidate how the literature information was employed in practice to solve the research problem.

Chapter 4: Results and Discussion- Results and Discussion-Leaching of Valuable Metals from NMC 532 Cathodes:

This chapter focuses on the leaching of the NMC 532 cathode material and subsequently, the results presented in this chapter are the outcomes of numerous experiments that were conducted within the scope of the laid objectives. Several investigations were carried out, in order, involving NMC cathode composition analysis and acid leaching. The leaching parameters such as solid/liquid ratio, temperature, acid and reductant concentration and leaching time were successfully optimized to recover effectively the valuable metals (Ni, Co, Mn, Li) from $\text{LiN}_{0.5}\text{Mn}_{0.3}\text{Co}_{0.2}\text{O}_2$ (NMC 532) cathode material. The examinations and discussions of the results also cover the comparisons of the various numerical and empirical datasets. Based on these discussions and examinations, concluding statements are connected to the primary objectives of the research set out in Chapter 1.

Chapter 5: Results and Discussion-Electrowinning Optimization Using Synthetic Quasi NMC 532 Solutions

This chapter focuses on research that is centred on the recovery of Ni and Co from synthetic Ni, Co, Mn and Li sulphate solutions mimicking the NMC 532 ratio of elements using a hydro-electrometallurgy process route that integrates hydrometallurgy and potentiostatic electrometallurgy techniques. This quasi-model is done to elucidate the effect of multiple influencing parameters, through isolation and varying, on the selective electrodeposition of Co-Ni from multi-ion (Li, Ni, Mn and Co) complex solutions before applying it using real cathode leachates. The selective potentiostatic electrowinning metal recovery process route is a cost-effective alternative to the energy, cost and material-intensive hydrometallurgy intermediate purification processes such as solvent extraction, selective precipitation, and ion-exchange, processes that produces metal rich solutions still requires integration of additional reduction process like galvanostatic electrowinning. The study delves into the effects of various electrowinning parameters, including applied potential, temperature, pH, Co, Ni, Na₂SO₄, NaH₂PO₄ buffer concentration, and cathode rotational speed. These parameters were thoroughly investigated and effectively optimised to achieve the high recovery efficiency and rate of Ni_{0.65}Co_{0.35} at optimal current efficiency. The examinations and discussions also cover the comparisons of the various numerical and empirical datasets. Based on these discussions and examinations, concluding statements are connected to the primary objectives of the research set out in Chapter 1.

Chapter 6: Results and Discussion- Electrowinning Cell Voltage Optimization

This chapter focuses on the optimisation of electrowinning cell voltage. The energy-associated cost is of paramount importance, as it exerts a substantial impact on the economic feasibility of the overall production process. This chapter delves into a rigorous exploration of the intricate network of factors influencing the energy-associated cost dynamics inherent to Co and Ni production. This chapter focuses on reducing the overall voltage consequently reducing the overall energy consumption. The examinations and discussions also cover the comparisons of the various numerical and empirical datasets. Based on these discussions and examinations, concluding statements are connected to the primary objectives of the research set out in Chapter 1.

Chapter 7: Results and Discussion-Cobalt/Nickel Electrowinning Using NMC Leachate Electrolyte

This chapter is centred on the recovery of Ni and Co from real NMC 532 leachate solutions using a hydro-electrometallurgy process route that integrates hydrometallurgy and potentiostatic electrometallurgy techniques. This real model utilises the optimised leaching and electrowinning parameters from the previous chapters. The study delves into the deposit composition, impurities composition and reaction kinetics. The composition of the electrowon deposit was meticulously quantified using Inductively Coupled Plasma (ICP). The examinations and discussions also cover the comparisons of the various numerical and empirical datasets. Based on these discussions and examinations, concluding statements are connected to the primary objectives of the research set out in Chapter 1.

Chapter 8: Results and Discussion-Recovery of Mn(OH)_2 , Li_2CO_3 and $0.6[\text{Ni(OH)}_2].0.3[\text{Mn(OH)}_2].0.1[\text{Co(OH)}_2]$ Precipitates

Following the successful recovery of Ni-Co from spent NMC 532 battery leachates, the valuable by-products such as Li_2CO_3 and Mn(OH)_2 and $0.6[\text{Ni(OH)}_2].0.3[\text{Mn(OH)}_2].0.1[\text{Co(OH)}_2]$ composite were recovered from spent electrolytes through chemical precipitation. This chapter focuses on the recovery of valuable metals from the electrowinning resultant leachate. The resultant leachate was treated with NaOH to specific pH levels to selectively recover mixed Ni, Mn and Co hydroxides ($0.6[\text{Ni(OH)}_2].0.3[\text{Mn(OH)}_2].0.1[\text{Co(OH)}_2]$) and Mn(OH)_2 . The resultant electrolyte is followed up by Na_2CO_3 chemical-based precipitation to recover Li_2CO_3 through filtration. The combination of pH-based and chemical precipitation was utilised to analyse the separation and recovery performance of Ni, Co Mn Li in metal sulphate solutions as NMC hydroxides and Mn(OH)_2 respectively. The recovered NMC hydroxides and Li_2CO_3 are synthesised to be used as precursors in the NMC cathode production facilities. The examinations and discussions also cover the comparisons of the various numerical and empirical datasets. Based on these discussions and examinations, concluding statements are connected to the primary objectives of the research set out in Chapter 1.

Chapter 9: Material Balance

The primary purpose of this chapter is to examine and discuss the collated material and component balance data. The material balance examinations and discussions also cover the comparisons of the various numerical and empirical datasets. Based on these discussions and examinations, concluding statements are connected to the primary objectives of the research set out in Chapter 1.

Chapter 10: Conclusion and Recommendations:

Following chapters 4-10, chapter 11 summarises all the key points in relation to the addressing of the research problem and objectives. Key points are meticulously investigated and evaluated. Furthermore, the consequences and implications of the study are discussed. Following the conclusion, a summary of various changes and alterations that could be implemented should a research budget or any other limitations allow for it is presented. Over and above research limitations, various recommendations for concerns discovered during the research, are deliberated in terms of future research work in this area of Lithium-ion battery recycling. This proposes new insights and creative approaches for framing and contextualizing the research problem based on the results garnered in this study.

Appendix A: Process Cost Evaluation

While the contents of this chapter are self-explanatory, the primary purpose of this chapter is to estimate, examine and discuss the collated process cost evaluation data. The examinations and discussions also cover the comparisons of the various numerical and empirical datasets. Based on these discussions and examinations, concluding statements are connected to the primary objectives of the research set out in Chapter 1.

Chapter 2: Literature Review

2.1 Overview

Before initiating a laboratory scheme for recycling the spent Li-ionBs, a comprehensive review of the Li-ionB landscape is necessary to highlight the historical development, the current chemistries of battery components as well as market trends of the Li-ionBs. In addition, a brief overview in terms of laboratory and industrial spent Li-ionBs recycling is also crucial to provide a basic understanding, and direction for forming step-by-step treatment and recycling of spent Li-ionBs in this thesis. Last but not least, comprehensive literature regarding analytical techniques, which are used in this spent Li-ionBs recycling study, are also briefly introduced. These contents are all covered in this Literature Review as providing initial understandings and basis for the subsequent engineering aspects and contents with regard to recycling spent Li-ionBs.

2.2 Lithium Ion Battery

2.2.1 Historic Review

In the 1970s, Michael Stanley Whittingham pioneered the construction of the first lithium batteries, utilizing lithium and titanium sulphide as battery electrodes (Whittingham, 2004). While this initial chemistry discovery was not immediately practical, it laid the foundation for subsequent advancements. The next generation of reversible intercalation electrode batteries was pioneered by Jürgen Otto Besenhard (Ramanan 2019; Manthiram 2020).. Following this, Samar Basu identified lithium electrochemical intercalation in graphite (Manthiram 2020). Rachid Yazami then addressed the challenge of the rapid deterioration of battery cells assembled at that time through his research on the reversible intercalation of lithium-ion in graphite in the early 1980s (Ramanan 2019; Manthiram 2020).

Subsequently, various academic groups initiated extensive research efforts to advance Li-ionBs, with a particular focus on cathode materials (Georgi-Maschler et al. 2012; Zheng et al. 2018; Kim et al. 2019). In 1991, Li-ionBs achieved their first commercial breakthrough spearheaded by the Sony Corporation, initially used to power handheld video cameras. This milestone

marked the onset of rapid development and the expansive application of this battery type up to recent times (Ramanan 2019).

2.2.2 Lithium-ion Battery Components

A standard Li-ionB comprises four primary components: cathode, anode, electrolyte, and separator. The variation or alteration of materials in these components significantly influences essential characteristics affecting the performance of a Li-ion battery, including energy density, durability, cycle life, and safety. The basic Li-ion cell schematic structure is depicted below in Figure 2-1.

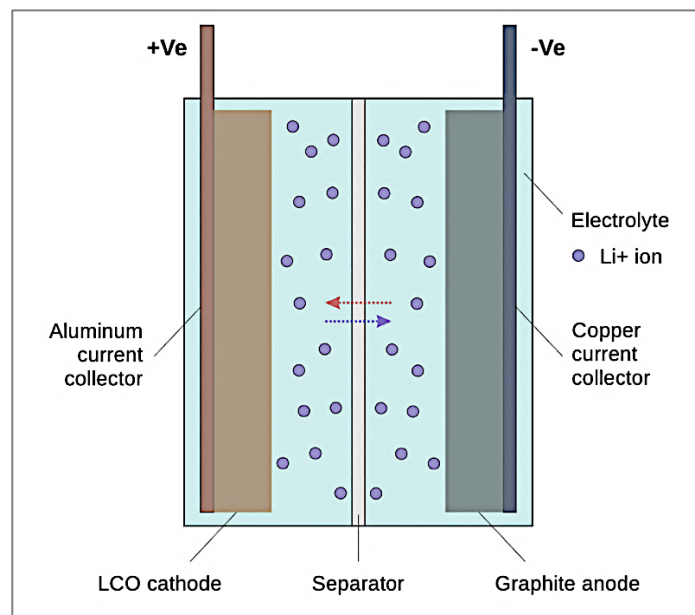


Figure 2-1: Li-ionB schematic structure.

2.2.3 Working Mechanism

The electrochemical charging and discharging processes of a standard Li-ionB are driven by the intercalation and deintercalation reactions of lithium ions between the anode and the cathode electrodes (de Oliveira Demarco et al. 2019; Phuc Anh LE 2019). The intercalation reaction occurs when an ion or molecule is included or inserted into a crystal lattice or layered structure. In a Li-ionB system, two electrodes (cathode and anode) function as solid host networks capable of storing and releasing lithium ions and electrons during battery discharging and charging processes. During the discharging phase, lithium ions are deintercalated, moving the electrons from the anode electrode to the cathode electrode. The flow

of electrons through an external circuit generates electric current and ultimately electrical power. Subsequently, these transferred particles – lithium ions and electrons – are intercalated into the layered structure of the cathode material. These electrochemical reactions are reversible, allowing for a reverse process to occur when applying an external electric current to a Li-ionB. Figure 2-2 schematically depicts the electrochemical reactions of an LCO-graphite Li-ionB during its operation.

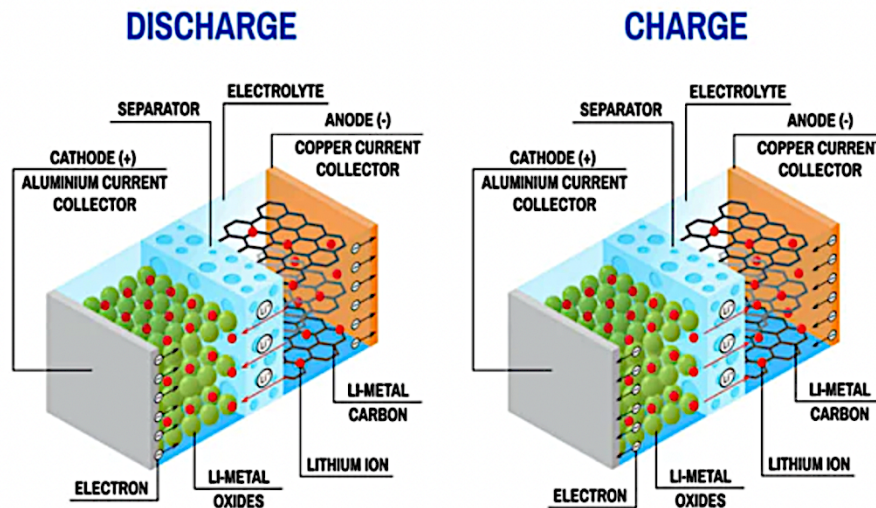
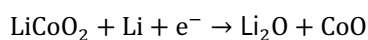


Figure 2-2: Working mechanism of a Li-ionB (Tycorun 2021).

Overcharging a Li-ionB can lead to battery destruction (disintegration of active material) due to the saturation of the active cathode material with electrons. The chemical reaction of this phenomenon is shown below (Nitta et al. 2015; Kim et al. 2019; Phuc Anh LE 2019).



2-1

The release, absorption, and arrangement of charged sub particles in the electrode structures is greatly influenced by the charging and discharging voltage. Consequently, the charging and discharging voltage significantly influence the capacity and charging duration of a Li-ionB. Charging at a lower rate yields a higher capacity but necessitates an extended charging time, whereas a higher charging rate reduces the charging time at the expense of diminished battery capacity. Additionally, charging the battery at an elevated cut-off voltage may diminish its cycle life and compromise safety. This is attributed to the destabilization of the cathode crystal

structure and the occurrence of adverse side reactions involving the cathode and electrolyte solution (Whittingham 2004; Nitta et al. 2015).

2.2.4 Anode Material

The manufacturing process for the anode mirrors that of its counterpart, the cathode, with the anode material, typically carbon based, being applied to a copper current collector foil. Since the commencement of commercial Li-ionB production in the 1990s, both graphite and hard carbon have been employed as anode materials. Despite the existence of hard carbon, graphite continues to dominate the anode market over time, owing to its superior discharge profile (Yu et al. 2014; Ma, Chen, et al. 2019). Firstly, it essentially attains its near-optimal theoretical specific capacity, approximately 375 mAh/g, equivalent to roughly 150 Wh/kg energy density. However, this falls short of meeting the energy density demand for electric vehicles, which is set at 200 Wh/kg (Lee et al., 2014).

Moreover, graphite anode material exhibits an inherent irreversibility that contributes to the growth of lithium dendrites when Li-ionBs undergo cycling at high C-rates (Liu et al. 2014). For the abovementioned reasons, numerous manufacturers of Li-ionBs have initiated research into alternative non-graphite anodes, such as tin, silicon, or spinel lithium titanate ($\text{Li}_4\text{Ti}_5\text{O}_{12}$ – LTO) (Lee et al. 2014; Liu et al. 2014; Nitta et al. 2015). The electrochemical properties of LTO anode material can be easily enhanced and adjusted by fine-tuning its nanostructure (Song, Kim, et al. 2014; Nasara et al. 2021).

2.2.4.1 Graphitic and Hard Carbons

Over two decades ago, the utilization of carbon anodes played a pivotal role in making Li-ionBs economically feasible, and to this day, they continue to be the preferred and optimal choice for anodes (Asenbauer et al. 2020). The electrochemical activity in carbon stems from the intercalation of Li between the graphene planes, providing excellent two-dimensional mechanical stability, electrical conductivity, and Li transport (Figure 2-3). This mechanism allows for the storage of up to 1 Li atom per 6 C units (Nitta et al. 2015; Asenbauer et al. 2020).

Carbon possesses a combination of advantageous properties, including low cost, widespread availability, a low delithiation potential vs Li, high Li diffusivity, excellent electrical conductivity,

and relatively low volumetric expansion during lithiation/delithiation (Figure 2-3). Consequently, carbon exhibits an appealing balance of relatively low cost, abundance, moderate energy density, power density, and cycle life compared to other intercalation-type anode materials. While carbon's gravimetric energy density surpasses that of most cathode materials (Figure 2-4), the volumetric capacity of commercial graphite electrodes remains limited (320–440 mAh/cm³).

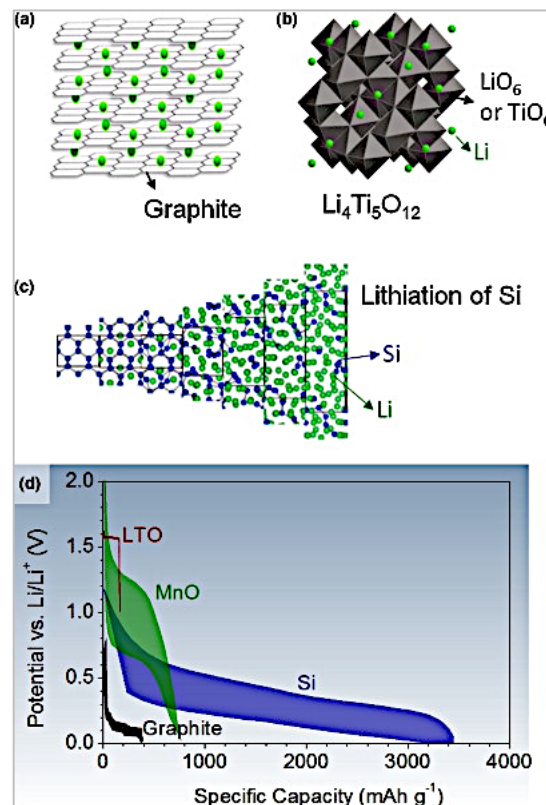


Figure 2-3: Crystal structures of (a) lithiated graphite anode material, (b) lithium titanate anode material (LTO), (c) silicon anode material during lithiation and d) charge–discharge profiles at low C-rates, showing voltage hysteresis (reproduced by Nitta et al. (2015) with Permission Copyright (2014) American Chemical Society) (Figure Adapted from (Nitta et al., 2015)).

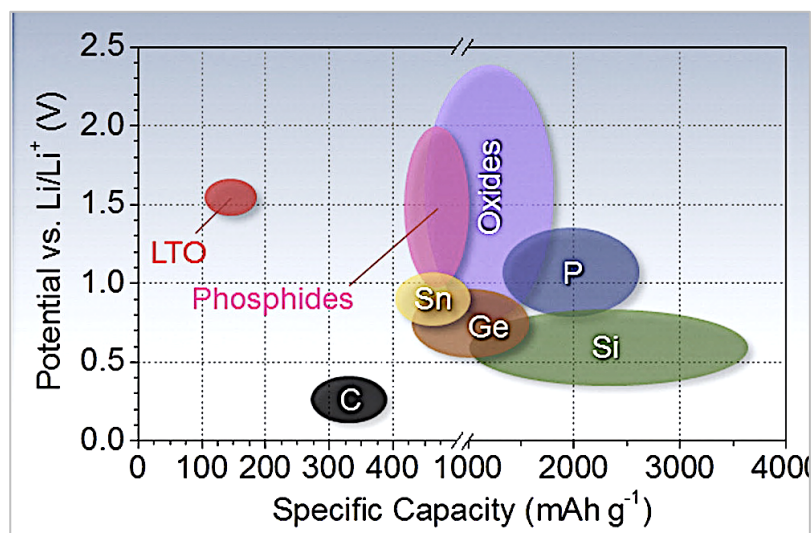


Figure 2-4: Approximate range of average specific capacity and discharge potentials for some of the most prevalent conversion-type anode materials (Figure Adapted from (Nitta et al., 2015)).

Commercial carbon anodes can be broadly categorized into two types. Graphitic carbons, characterized by large graphite grains, can approach the theoretical charge capacity. However, these carbons face challenges when paired with propylene carbonate (PC)-based electrolytes, preferred for their low melting point and rapid Li transport. The issue arises from PC intercalating alongside Li^+ between the graphitic planes, leading to graphite exfoliation and capacity loss (Aurbach et al. 1999). Even in the absence of solvent intercalation, Li intercalation takes place at the basal planes, resulting in the preferential formation of the solid electrolyte interphase (SEI) on these planes (Nitta et al. 2015). The process of Li intercalation induces a significant uniaxial 10% strain along the edge planes of single crystalline graphitic particles, potentially causing SEI damage and reducing the cell's cycle life (Qi et al. 2010). To address these issues, a recent approach involves coating graphitic carbons with a thin layer of amorphous carbon, serving as a protective barrier for the susceptible edge planes against electrolytes and enhancing coulombic efficiency.

Hard carbons possess diminutive graphitic grains characterized by disordered orientation, making them significantly less prone to exfoliation. These grains feature nanovoids in between, leading to diminished and isotropic volume expansion. Additionally, the nanovoids and defects contribute to excess gravimetric energy density, enabling a capacity surpassing the theoretical limit of 372 mAh/g (Nitta et al. 2015). Collectively, these characteristics establish hard carbons as an electrode material with high capacity and extended cycle life. Nevertheless, the elevated

fraction of exposed edge planes leads to the formation of a higher quantity of solid electrolyte interface (SEI), thereby diminishing coulombic efficiency in the initial cycles. Considering the limited lithium inventory in a full Li-ion cell, this poses a notable drawback in terms of attainable capacity. Additionally, the presence of void spaces substantially lowers the particle density, further reducing the volumetric capacity.

Ultimately, impurities like hydrogen atoms can yield additional capacity in anodes based on carbon (Kiciński and Dyjak 2020). Nevertheless, these electrodes experience greater voltage hysteresis, increased irreversible capacity loss, and even diminished volumetric capacity. Consequently, their commercial viability is near unlikely (Borah et al. 2020).

2.2.4.2 Lithium Titanium Oxide ($\text{Li}_4\text{Ti}_5\text{O}_{12}$ /LTO)

Lithium titanium oxide (LTO) has attained successful commercialization due to its ability to combine superior thermal stability, high rate capability, relatively high volumetric capacity, and extended cycle life. Despite the higher cost associated with titanium, as well as a reduced cell voltage and lower specific capacity (175 mAh/g & 600 mAh/cm³ theoretical) (Peter E Roth and Doughty Dan 2012), LTO demonstrates high rate and stability, stemming from a "zero strain" intercalation mechanism and a high lithiation potential. The term "zero strain" is attributed to the minimal volume change (0.2%) during the phase change caused by lithiation/delithiation (Wagemaker et al. 2006; Colin et al. 2010).

Electrochemically, this characteristic is reflected in a small voltage hysteresis in the charge–discharge profile (Figure 2-7). Moreover, the high equilibrium potential (~1.55 V vs. Li/Li+) allows LTO to operate in a potential window above 1 V, effectively avoiding the formation and growth of the anode solid electrolyte interface (SEI). This circumvention is crucial, as it prevents delays in Li insertion and mitigates Li losses in graphite anodes. Even if an SEI is formed, the minimal volume change enhances its stability. The absence of SEI impedance concerns enables the use of LTO nanoparticles, similar to intercalation cathode material, enhancing rate performance at the expense of slightly lower volumetric capacity (Jung et al. 2011; Wu et al. 2012). Additionally, LTO is deemed extremely safe due to its high potential, preventing Li dendrite formation, even at high rates. While LTO may not exhibit particularly high Li diffusivity

or electrical conductivity compared to other anode materials, it remains an ideal choice for lower energy, high-power, and high-cycle-life Li-ion batteries (Goutam et al. 2017).

Regrettably, surface reactions remain unavoidable with LTO anodes. Severe gassing occurs due to a reaction between the organic electrolyte and the LTO active material (Nitta et al. 2015). Although carbon coating can suppress this reaction, it also has the potential to catalyse and expedite electrolyte decomposition during SEI formation, particularly at temperatures exceeding 45 °C (He et al. 2013; Song, Kim, et al. 2014). Nevertheless, LTO anodes exhibit impressive longevity, lasting for tens of thousands of cycles, providing a distinct advantage over most other anode materials for high-power applications (Miao et al. 2019).

2.2.4.3 Conversion Materials – Alloying Materials (Type B)

In this context, the term 'alloying materials' pertains to elements that undergo electrochemical alloying, forming compound phases with Li, specifically falling into the category of Type B conversion materials at low potential (preferably below 1 V). While alloying materials can exhibit exceptionally high volumetric and gravimetric energy density, they are known for their substantial volume expansion, increasing to several times the original volume during lithiation. (Figure 2-3c illustrates how this occurs for Si). This can lead to particle fracturing and the loss of electrical contact (Wang et al. 2014). In the case of anodes, volume change has the potential to disrupt the protective layer of the solid electrolyte interface (SEI), leading to continuous electrolyte decomposition, depletion of lithium inventory, and an increase in cell impedance. Consequently, alloying anodes often experience a shortened cycle life due to active material loss and escalating cell impedance, particularly at high mass loadings (Chan et al. 2008; Oumellal et al. 2008).

As a general approach, successful strategies involve the creation of a carbon composite wherein the alloying material particles have sufficiently small dimensions to ensure mechanical stability, electron transport, and lithium transport, while maintaining Li diffusion paths within the electrode. Achieving this often necessitates a hierarchical structure, as depicted in Figure 2-3. To enhance SEI stability, the active material can be enclosed in a carbon shell with ample void space to accommodate volume expansion (Figure 2-3) (Park et al. 2013). This

encapsulation, in principle, can stabilize the SEI, prevent particle sintering into larger particles, and enable a high cycle life even at high mass loadings (Chen et al. 2012).

Further stabilization of the SEI and extension of cycle life can be achieved through electrolyte additives. Binders that bond to the active material, possess high stiffness, and exhibit minimal swelling in electrolytes can provide additional mechanical stability, especially if a carbon shell is not employed. Nevertheless, high mass loading electrodes with volumetric energy capacity exceeding 400 mAh/cm³ and reasonable cycle life (2x10³⁺ cycles) in full Li-ionB cells have been demonstrated (Ma, Sung, et al. 2019; Chen et al. 2021). Nanoparticles inherently present a challenge due to their high surface area, leading to significant SEI formation and substantial irreversible capacity loss during the initial cycles.

Si has garnered significant attention among alloying materials due to its relatively low average delithiation potential, extremely high volumetric and gravimetric energy capacity, abundance, low cost, chemical stability, and non-toxicity. Sn has also attracted interest, sharing similar properties with Si but featuring lower gravimetric energy density, slightly lower cell voltage, and higher electrical conductivity (Figure 2-3). However, Sn appears prone to delicate fracturing even when reduced to the 10 nm range (Nitta et al. 2015). Ge maintains structural integrity even at larger particle sizes, but its cost renders it impractical for most applications. Ga possesses the intriguing characteristic of being in a liquid state near room temperature, yet its expense limits widespread practical use (Nitta et al. 2015; Kitsche et al. 2020).

Among cost-effective lithium alloying metals, Zn, Cd, and Pb exhibit substantial volumetric capacity; however, they contend with the limitation of low gravimetric energy density. Al, another cost effective metal, metal also suffers from severe fracturing, even with nano dimensions, as confirmed by in situ transmission electron microscopy (TEM) (Liu et al. 2011). Elements like P and Sb have gained attention recently, with both displaying high capacity. Electrodes with well-rounded electrochemical performance have been constructed by ball-milling the P and Sb material with carbon. However, both elements are toxic, possess relatively high delithiation potentials, and, additionally, Sb is not abundant (Darwiche et al. 2012; Qian et al. 2012). Moreover, phosphorus is particularly dangerous due to its potential to form phosphine (Nitta et al. 2015; Wei et al. 2023).

2.2.4.4 Conversion Materials – other (Type A)

Historically, a prevalent strategy for developing conversion materials involved utilizing oxides wherein Li_2O is generated during the initial charging of the battery. Li_2O serves as a bonding agent, holding together particles of the alloying material (e.g., Si or Sn), while simultaneously mitigating overall volume changes within the particles (Nitta et al. 2015). Nevertheless, Li_2O exhibits low electrical conductivity, leading to substantial irreversible capacity and a significant voltage hysteresis, meaning a high discrepancy between the voltage at which the electrode material charges versus discharges (Kim et al. 2022). Figure 2-5 shows the typical voltage profiles of conversion-based anode materials after the first cycle, showing voltage hysteresis.

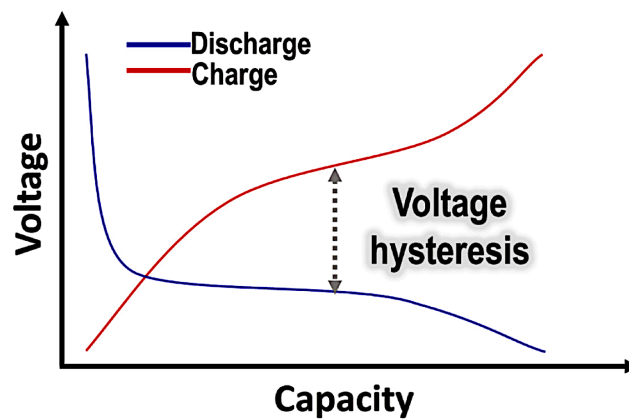


Figure 2-5: Typical voltage profiles of conversion-based anode materials after the first cycle, showing voltage hysteresis (Kim et al. 2022).

This issue persists even at extremely slow rates (Reddy et al. 2013). An alternative approach involves utilizing Li_2O itself as an active material, provided the voltage range is considerably widened. This allows for the use of non-alloying transition metals (such as Manganese(II)Oxide), presenting the challenge of further reducing the potential difference with the cathode. Additionally, if the Li_2O phase is consumed, nanoparticles of active alloying materials may sinter into larger particles, consequently increasing their ohmic and mass transfer resistance (Zheng, Sun, et al. 2012). This process also typically results in significant volume changes, posing challenges akin to those encountered with alloying anodes. Among various Type A conversion anode materials, $\text{Li}_{1.07}\text{V}_{0.93}\text{O}_2$ and MgH_2 stand out due to their relatively moderate voltage hysteresis and delithiation potentials, albeit at low current density operations (low C-rates) (Oumellal et al. 2008; Armstrong et al. 2011). However, studies have yet to establish the viability

of these cathode materials at higher C-rates (higher current density operations), and the demonstrated electrochemical cycle life is also limited. Similarly, certain phosphide and nitride electrodes have shown relatively low voltage hysteresis, but only at low C-rates (low charge/discharge current densities) for several cycles (Cabana et al. 2010).

2.2.5 Cathode Material

The production of a cathode for a Li-ionB involves coating the aluminium current collector foil with the active cathode material. The cathode holds significant importance in commercial Li-ion batteries due to its inclusion of valuable metals (e.g., Co, Li, Mn) which play a decisive role in determining battery properties and performance. Consequently, commercial lithium-ion batteries are commonly identified by their active cathode material, serving as the lithium-ion donor in the battery (Manthiram 2020).

This review compares and contrasts the electrochemical performance characteristics, existing limitations, and recent advancements and breakthroughs in the development of commercial intercalation cathode active materials, including lithium nickel cobalt manganese oxide (NMC), lithium cobalt oxide (LCO), lithium nickel cobalt aluminium oxide (NCA), lithium titanium oxide (LTO), lithium iron phosphate (LFP) and others, with that of conversion materials such as alloying anodes (Sn, Ge, Si etc.), chalcogenides (S, Te, Se), and metal halides (Br, Cl, I) (Nitta et al. 2015; Manthiram 2020). Notably, lithium nickel manganese cobalt (NMC) emerges as the most widely deployed active material for cathodes, this trend is witnessed with a gradual increase in market proportion over the years due to its higher energy and power density, relatively higher safety rating, and lower cost compared to other competing electrodes (Kim et al. 2019; Phuc Anh LE 2019; CSIRO 2022; Islam and Iyer-Raniga 2022; Tawonezvi et al. 2023).

2.2.5.1 Intercalation Cathode Materials

An intercalation cathode serves as a solid host network capable of storing guest ions, allowing for and facilitating their reversible insertion and removal from the host network. In the context of Li-ion batteries (Li-ionBs), Li^+ acts as the guest ion, while the host network compounds encompass polyanion compounds, metal chalcogenides and transition metal oxides. These intercalation compounds exhibit various crystal structures, such as layered, spinel, olivine, and tavorite (as depicted in Figure 2-6).

The layered structure represents the earliest form of intercalation compound used in cathode materials for Li-ion batteries. Metal chalcogenides like TiS_3 and NbSe_3 were investigated more than half a century ago as potential intercalating cathode materials (Murphy and Trumbore 1976; Nitta et al. 2015). While TiS_3 exhibited only partial reversibility due to an irreversible structural shift from trigonal prismatic to octahedral coordination upon lithiation, NbSe_3 displayed reversible electrochemical behaviour. Among various chalcogenides, LiTiS_2 (LTS) garnered significant attention due to its high specific energy density, extended cycle life (surpassing 1200 cycles), and eventual commercialization by the company Exxon (Whittingham 2004). However, the bulk of current intercalation cathode research focuses on transition metal oxides and polyanion compounds due to their higher operating voltage and consequent surge in energy storage capacity (Murphy and Trumbore 1976). Typically, intercalation cathodes demonstrate a specific capacity ranging from 100 to 200 mAh/g and an average operating voltage of 3 to 5 V vs. Li/Li^+ (refer to Figure 2-6 and Figure 2-7) (Murphy and Trumbore 1976; Nitta et al. 2015).

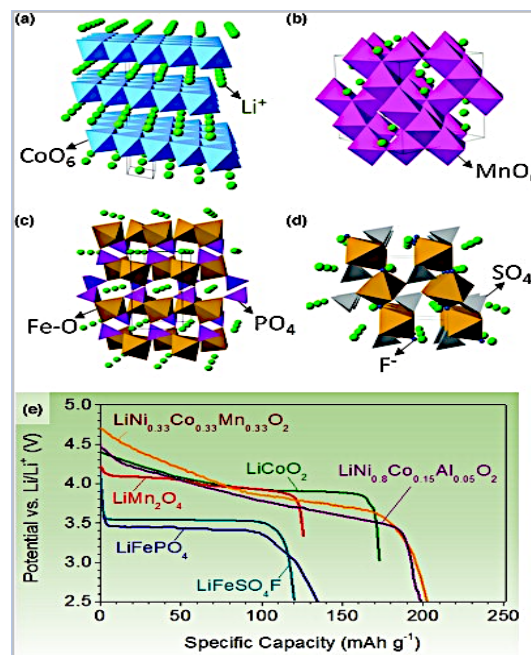


Figure 2-6: Crystal structures of the most prevalent intercalation cathode materials: structure of (a) layered (LiCoO_2), (b) spinel (LiMn_2O_4), (c) olivine (LiFePO_4), and (d) tavorite (LiFeSO_4F) (Figure Adapted from Nitta et al, (2015)).

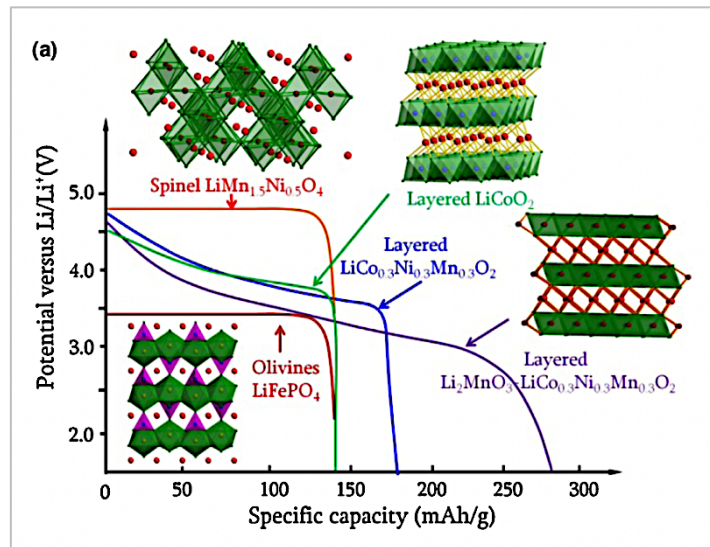


Figure 2-7: Typical discharge profiles of the most prevalent intercalation cathode materials (Figure adapted from (Liu et al. 2016)).

A comprehensive review of the characteristics of the prevalently employed intercalation cathode compounds; crystal structure, theoretical/experimental/commercial specific and volumetric capacities, average operational voltages, and level of development is tabulated in Table 2-1.

Table 2-1: Characteristics of the prevalently employed intercalation cathode compounds; crystal structure, theoretical/experimental/commercial specific and volumetric capacities, average operation voltages, and level of development.

Crystal structure	Compound	Specific capacity; Theoretical/ Exp./ Typical commercial cells (mAh/g)	Vol. capacity Theoretical/ typical commercial cells (mAh/cm³)	Average voltage (V)	Status of development	Reference
Layered	LiCoO ₂	274/190 /180	1363/550	3.9	Commercialized	(Lyu et al. 2021)
	LiNiO ₂	278/160	1280	3.8	Research	(Mesnier and Manthiram 2020)
	LiMnO ₂	285/140	1148	3.3	Research	(Zhu et al. 2021)
	LiNi _{0.33} Mn _{0.33} Co _{0.33} O ₂	280/165/170	1333/600	3.7	Commercialized	(Cheng et al. 2017)
	LiNi _{0.8} Co _{0.15} Al _{0.05} O ₂	279/205/200	1284/700	3.7	Commercialized	(Martha et al. 2011; Chen, Zhu, et al. 2019)
	Li ₂ MnO ₃	458/180	1708	3.8	Research	(Wang et al. 2013; Guerrini et al. 2020)
Spinel	LiMn ₂ O ₄	148/110	596	4.1	Commercialized	(Thackeray and Amine 2021)
	LiCo ₂ O ₄	142/84	704	4.0	Research	(Choi and Manthiram 2012)
Olivine	LiFePO ₄	170/164	589	3.4	Commercialized	(Wang et al. 2018; Li and Ma 2019)
	LiMnPO ₄	171/168	567	3.8	Research	(Wang et al., 2018)
	LiCoPO ₄	167/125	510	4.2	Research	(Kim et al. 2015; Zhang et al. 2018)
Tavorite	LiFeSO ₄ F	151/120	487	3.7	Research	(Kim et al. 2015)
	LiVPO ₄ F	156/129	484	4.2	Research	(Xue et al. 2020)

2.2.5.2 Transition Metal Oxide

LiCoO₂ (LCO), pioneered by Goodenough, stands as the first and most commercially prosperous form of layered transition metal oxide cathodes (Ramanan 2019; Lyu et al. 2021). Initially brought into commercial space by SONY, this electrode material continues to be employed in the majority of commercial Li-ionBs. Co and Li, situated in octahedral sites, occupy alternating layers, creating a hexagonal symmetry (Figure 2-6 a). LCO stands out as a highly commercially viable cathode material, attributed to its relatively high theoretical specific capacity of 276 mAh/g, substantial theoretical volumetric capacity of 1365 mAh/cm³, minimal self-discharge, elevated discharge voltage, and commendable cycling performance (Nitta et al. 2015; Lyu et al. 2021).

The primary challenges associated with LCO include its high cost, limited thermal stability, and rapid capacity degradation, particularly at high current rates or during extended cycling. The elevated cost of LCO cathodes is mainly due to the substantial cost of Co (Nitta et al., 2015). Low material thermal stability denotes the exothermic liberation of oxygen when a lithium metal oxide cathode is heated beyond a specific threshold, potentially triggering a runaway reaction leading to the ignition of the cell (Dahn et al. 1994; Du Pasquier et al. 2003). The occurrence of thermal runaway poses a significant concern in the utilization of Li-ionBs, exemplified by the grounding of all Boeing 787 airplanes in 2013 (Williard et al. 2013). Although this problem is common among transition metal oxide intercalation cathodes, LCO exhibits the lowest thermal stability compared to any other commercially available cathode material (Nitta et al. 2015). While thermal stability is also influenced by non-material factors such as cell design and size, LCO batteries typically undergoes thermal runaway beyond approximately 200°C. This is a consequence of an exothermic reaction between the liberated oxygen and organic materials. (Choi and Manthiram 2012; Lyu et al. 2021).

Subjecting the battery to deep cycling (delithiation beyond 4.2 V, equivalent to around 50% or more lithium extraction) leads to lattice distortion, shifting from hexagonal to monoclinic symmetry. This transformation adversely affects cycling performance. Various metals, including Mn, Al, Fe, and Cr, have been investigated as dopants or partial substitutes for Co, showing

promise but with performance limitations (Nitta et al., 2015). The utilization of coatings containing diverse metal oxides (Al_2O_3 , B_2O_3 , TiO_2 , ZrO_2) has proven more effective in enhancing the stability and performance characteristics of LCO, particularly during deep cycling. This efficacy is attributed to the mechanically and chemically stable nature of oxide materials, which can alleviate structural changes in LCO and minimize side reactions with the electrolyte (Lyu et al., 2021; Scott et al., 2011).

LiNiO_2 (LNO) shares an identical crystal structure with LiCoO_2 and exhibits a comparable theoretical specific capacity of 280 mAh/g (Ohzuku et al. 1993; Mesnier and Manthiram 2020). The ongoing extensive research on LNO cathode compounds is primarily driven by its relatively high energy density and lower cost compared to Co-based materials (Mesnier and Manthiram 2020). Pure LNO cathodes are unfavourable due to Ni^{2+} ions tendency of clogging the Li^+ sites during synthesis and delithiation, ultimately impeding the Li^+ diffusion and transfer (Rougier et al., 1996). Thermal instability of LNO surpasses that of LCO as Ni^{3+} in LNO is more readily reduced than Co^{3+} in LCO (Mesnier and Manthiram 2020). Effective reduction of cationic disorder involves partial substitution of Ni with Co (Hebert and McCalla 2021).

Insufficient thermal stability during high SOC prompted improvements through Mg doping, while adding a minute amount of Al enhanced both the thermal stability and electrochemical performance (Cormier et al. 2019). Consequently, the $\text{LiNi}_{0.8}\text{Co}_{0.15}\text{Al}_{0.05}\text{O}_2$ (NCA) cathode has achieved widespread commercial deployment, notably in Panasonic Li-ionBs for Tesla electric vehicles (EVs) (Nitta et al., 2015). NCA exhibits a high usable discharge capacity (approximately 220 mAh/g) and prolonged storage calendar life compared to conventional Co-based oxide cathode compounds. However, reports indicate potential severe capacity fade at elevated temperatures (50–80°C) due to solid electrolyte interface (SEI) growth and micro-crack development at grain boundaries (Bloom et al. 2003; Chen et al. 2004).

Despite advancements in anhydrous and stoichiometric layered LMO cathode compounds almost two decades ago, enhancing prior aqueous methods with induced impurities, varied stoichiometries, poor crystallinity, and undesirable structural changes during cycling (Bruce et al. 1999; Zheng et al. 2012; Gowda et al. 2014; Vu et al. 2021; Zhu et al. 2021), the cycling performance of LMO remains unsatisfactory. This is attributed to the tendency of the layered

structure to shift into a spinel structure during Li^+ ion extraction and the leaching of Mn during charge/discharge electrochemical cycling (Zhu et al. 2021).

Dissolution of Mn during leaching occurs when Mn^{3+} ions undergo a disproportionation reaction, forming Mn^{2+} and Mn^{4+} , observed in all cathodes containing Mn (Knight et al. 2015). Mn^{2+} is believed to be soluble in the electrolyte, potentially destabilizing the anode SEI. The increase in Mn concentration in the electrolyte and anode SEI with aging is noted for Mn-containing cathodes. Additionally, anode impedance is observed to rise with Mn dissolution on carbon anodes but not on LTO (which has a negligible SEI) (Bruce et al. 1999; Zheng et al. 2012; Gowda et al. 2014). Despite experimental and theoretical attempts at cationic doping to stabilize LMO, poor cycle stability, especially at elevated temperatures, has hindered widespread commercialization (Nitta et al. 2015).

Continuous research efforts to develop cathode active materials less costly than LCO led to the formulation of $(\text{Li}(\text{Ni}_x\text{Mn}_y)\text{O}_2)$, where $x=0.5$ and $y=0.5$ (NMO) cathode compounds (Nitta et al. 2015; Manthiram 2020). NMO compounds offers great potential as cathode materials due to their ability to exhibit similar energy density to mainstream LCO compounds while reducing costs through utilisation of lower-cost transition metals. The presence of Ni in the NMO structure allows for higher Li^+ extraction capacity. Nevertheless, the mixing of cations, during synthesis of NMO cathode compounds, may limit and compromise Li^+ diffusivity, consequently leading to a limited rate capability of the electrodes during cycling. Recent Ab Initio computational modelling forecasts that low-valence transition metal cations (Ni^{2+}) offer high-rate pathways and minimal strain, pivotal elements for attaining high-rate capability in layered cathodes. Kang et al. (2006) synthesized NMO through an ion exchange method and the material exhibited a remarkably low concentration of defects, exhibiting a specific capacity as high as approximately 190 mAh/g, even under very high C-rates (discharge rates) of 6C (Kang et al. 2006).

Incorporating the high cost transition metal Co into the NMO $(\text{Li}(\text{Ni}_x\text{Mn}_y)\text{O}_2)$, where $x=0.5$ and $y=0.5$ cathode material structure further enhances structural stability and integrity (Yabuuchi and Ohzuku 2003). $\text{LiNi}_x\text{Co}_y\text{Mn}_z\text{O}_2$ (NMC, aka NCM) cathode material compounds exhibits similar or higher usable specific capacity than LCO cathode material compounds, with

comparable operating voltage and lower cost since the Co content is reduced. $\text{LiNi}_{0.33}\text{Co}_{0.33}\text{Mn}_{0.33}\text{O}_2$, once a prevalent form of the NMC cathode material family, is still widely used in the Li-ion battery market. Recent advancements, such as the synthesis of macroporous NMC compounds, have demonstrated reversible specific capacity as high as 270 mAh/g (at 4.65 cut-off voltage) and excellent cycle stability even at elevated temperatures of 50 °C (Divakaran et al. 2021).

Li_2MnO_3 stabilized LiMO_2 (where M = Ni, Co, Mn) can reach high specific energy capacity (>230 mAh/g) when cycled at high voltages (4.6–3.2 V) (Vu et al. 2021). Li_2MnO_3 is activated at operating voltages >4.6 V, releasing Li_2O on the first discharge-charge cycle, providing extra Li^+ ions. The remaining Li_2MnO_3 facilitates Li diffusion and acts as a Li^+ ion reservoir. This active cathode material phase is termed as Li^+ -rich layered oxide compound due to its surplus Li^+ -ion compared to the conventional layered structure. Sun et al. (2009) synthesized a cathode material with an average composition of $\text{LiNi}_{0.68}\text{Co}_{0.18}\text{Mn}_{0.18}\text{O}_2$, which incorporates a bulk material consisting of a nickel-rich layered oxide ($\text{LiNi}_{0.8}\text{Co}_{0.1}\text{Mn}_{0.1}\text{O}_2$) to enhance energy/power density, and an outer layer comprising Mn and Co substituted NMC ($\text{LiNi}_{0.46}\text{Co}_{0.23}\text{Mn}_{0.31}\text{O}_2$) to improve cycle life and safety. It is suggested that the stability of this material may stem from the presence of stable Mn^{4+} in the surface layer, thereby delaying gas evolution resulting from the reaction between Ni^{2+} ions and the electrolyte (Sun et al. 2009; Wang et al. 2013).

Spinel $\text{Li}_2\text{Mn}_2\text{O}_4$, also known as LMO, derives advantages from the plentiful availability, cost-effectiveness, and environmentally friendly characteristics of Mn^+ (Wang et al. 2013; Nitta et al. 2015). Li^+ ions occupies tetrahedral 8a sites whilst Mn is located in octahedral 16d sites in a ccp array of oxygen anions (Figure 2-6). Li^+ ions have the ability to permeate through unoccupied tetrahedral and octahedral interstitial sites within the three-dimensional framework. The inadequate long-term cyclability is thought to stem from irreversible side reactions with the electrolyte, loss of oxygen from the de-lithiated LiMn_2O_4 , dissolution of Mn, and the creation of tetragonal $\text{Li}_2\text{Mn}_2\text{O}_4$ on the surface, particularly under high C-rates (high charge-discharge rates) (Thackeray and Amine 2021).

Through utilisation of active material nanoparticles, the rate performance can be enormously improved due to shorter Li^+ diffusion lengths and improved electron kinetics. Numerous

different researchers have synthesized LMO nanowires and mesoporous LMO, showing promising results (Sun et al. 2003; Jiao and Bruce 2007; Kim et al. 2008; Hosono et al. 2009; Thackeray and Amine 2021). While diminished diffusion lengths contribute to the aggravation of the dissolution problem, it can be mitigated through various means, including the application of a surface coating containing ZnO, the incorporation of a Mn-rich layered structure, metal doping, adjustment of oxygen stoichiometry, blending with alternative cathode materials, and the establishment of a stable cathode SEI layer (Sun et al. 2003; Jiao and Bruce 2007; Lee et al. 2010; Thackeray and Amine 2021). Jiao et al. (2008) presented a novel ordered mesoporous lithium-rich $\text{Li}_{1.12}\text{Mn}_{1.88}\text{O}_4$ spinel which was demonstrated to exhibit improved electrochemical performance compared to bulk spinel (Jiao et al. 2008).

2.2.5.3 Polyanion Compounds

In exploring new cathode active materials, researchers developed a new class of compounds called polyanions. Large $(\text{XO}_4)^{3-}$ ($\text{X} = \text{W}, \text{S}, \text{P}, \text{As}, \text{Si}, \text{Mo}, \text{V}$) polyanions occupy lattice positions and increase cathode redox potential while also stabilizing their structure (Nanjundaswamy et al., 1996). LiFePO_4 (LFP) stands as the archetypal material exhibiting the olivine structure, renowned for its thermal stability and robust power capabilities (Li and Ma 2019). In the LFP configuration, Li^+ and Fe^{2+} occupy octahedral sites, while P resides in tetrahedral sites within a slightly distorted hexagonal close-packed (HCP) oxygen arrangement (Figure 2-6 c). Despite its merits, the LiFePO_4 cathode material grapples with certain electrochemical and physicochemical weaknesses, including its relatively low average potential (Figure 2-7) and diminished electrical and ionic conductivity. A decade of intensive research has yielded noteworthy advancements in both the performance and mechanistic comprehension of the LFP cathode formulation.

Efficient enhancement of rate performance was achieved through a combination of reducing particle size, employing carbon coating, and incorporating cationic doping (Li and Ma 2019). It is crucial to underscore that relatively high electrochemical performance can also be attained without carbon coating when particles are uniformly nano-sized, and conductive nanocarbons are integrated into the cathodes (Delacourt et al. 2006; Nitta et al. 2015). Notable examples, such as the virus-templated amorphous anhydrous FP/CNT composite, have exhibited

promising outcomes (Lee et al. 2009). Reports indicate that the facile redox reaction in non-conductive LFP may be attributed to a curved one-dimensional lithium diffusion path through the [0 1 0] direction (Nishimura et al. 2008). However, the inherent low density of nanostructured LFP electrodes, coupled with their low average potential, imposes constraints on the energy density of LFP cells. Notably, a recent introduction of a novel non-olivine allaudite LFP has demonstrated fundamentally different electrochemical behaviour compared to conventional olivine LFP (Kim et al. 2013).

Various olivine structures, including LiMnPO_4 (LMP), offer an approximately 0.4 V higher average voltage than olivine LFP (Figure 2-6), translating to higher specific energy but at the expense of lower conductivity. Additionally, LiCoPO_4 , $\text{LiNi}_{0.5}\text{Co}_{0.5}\text{PO}_4$, and $\text{LiMn}_{0.33}\text{Fe}_{0.33}\text{Co}_{0.33}\text{PO}_4$ (LCP, NCP, MFCP) have shown promising results, yet further strides are required in power, stability, and energy density (Nitta et al. 2015). The novel $\text{Li}_3\text{V}_2(\text{PO}_4)_3$ (LVP) exhibits a relatively high operating voltage (4.0 V) and commendable capacity (197 mAh/g) (Huang et al. 2002). Remarkably, the LVP/C nanocomposite has demonstrated 95% theoretical capacity at a high rate of 5 C, despite the low electronic conductivity of LVP (similar to LFP) (Delacourt et al. 2006).

LiFeSO_4F (LFSF) emerges as another intriguing cathode material due to its elevated cell operation voltage and reasonably moderate specific capacity (160 mAh/g) (Recham et al. 2010). Fortunately, LFSF boasts better ionic/electronic conductivity, mitigating the imperative need for carbon coating and/or nanoparticles. Moreover, LFSF presents economic viability as it can be prepared with abundant resources. Structurally, LFSF consists of two slightly distorted $\text{Fe}^{2+}\text{O}_4\text{F}_2$ oxyfluoride octahedra connected by F vertices in the trans position, forming chains along the c-axis, and the Li^+ is situated along the (1 0 0), (0 1 0), and (1 0 1) directions (Figure 2-6d). Simulation-based evaluations of tavorite-structured cathode materials have indicated the fluorosulphate and fluorophosphate families as the most promising, while the oxysulphate family lags behind (Mueller et al. 2011).

Tavorite-structured materials, featuring one dimensional diffusion channels, are posited to exhibit low activation energies, facilitating charge and discharge of $\text{Fe}(\text{SO}_4)\text{F}$ and $\text{V}(\text{PO}_4)\text{F}$ at remarkably high rates, akin to those observed in small olivine $\text{Fe}(\text{PO}_4)$ particles. While the vanadium-containing material, LiVPO_4F , displays efficient cycling with high voltage and

capacity, concerns persist regarding its toxicity and environmental impact (Barker et al. 2003; Nitta et al. 2015). Interestingly, Li^+ intercalation at approximately 1.85 V showcases the versatility of the material, rendering it suitable for utilisation in both the anode ($\text{Li}_{1+x}\text{VPO}_4$ where $x = 0-1$) and cathode ($\text{Li}_{1-x}\text{VPO}_4$ where $x = 0-1$) configurations. For comprehensive and in-depth details on material synthesis methods, physicochemical properties, and structural and reaction mechanisms, specialized reviews are available elsewhere (Masquelier and Croguennec 2013; Sergio and Stefania 2021).

2.2.5.4 Conversion Cathode Materials

Conversion electrode materials undergo a solid-state redox reaction during the processes of lithiation and delithiation. This involves a transformation in the crystalline structure, accompanied by the breaking and recombining of chemical bonds (Yu et al. 2018). The full reversible electrochemical reaction for conversion electrode materials is generally as follows:

Type A



Type B



Concerning cathodes, the Type A classification (Eq. 2-2) encompasses metal halides that involve high-valence metal ions (2 or more) to achieve elevated theoretical capacities. The process is exemplified in Figure 2-8 (a) using FeF_2 particles. F ions, exhibiting heightened mobility, diffuse out of the FeF_2 structure, leading to the formation of LiF, while nanoscale phases of Fe materialize subsequently (Wang, Robert, et al. 2011). Consequently, metal nanoparticles become dispersed within a 'sea' of LiF (expressed as $\text{Li}_{(y/z)}X$ in Eq. (2-3)). It is noteworthy that this mechanism is applicable, to varying degrees, across all Type A active materials, although certain instances may involve the creation of an intermediate Li insertion phase.

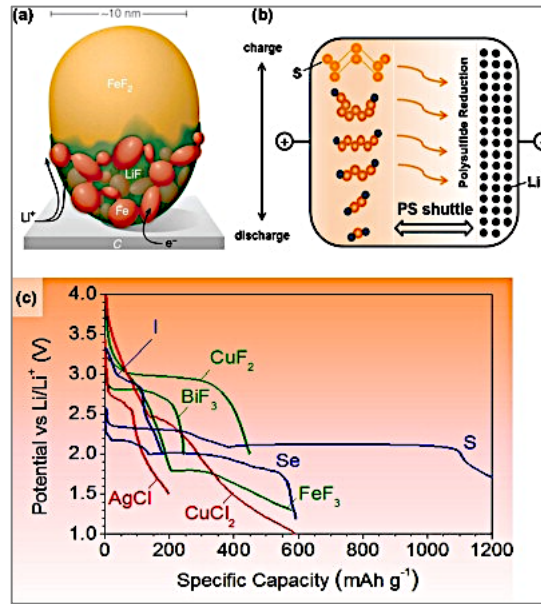


Figure 2-8: Transformations annotated in selected conversion-type cathode materials: (a) propagation of lithiation reaction front through a single FeF₂ particle; (b) polysulphides shuttle accompanying charge and discharge of a S particle and (c) typical discharge profiles of the most prevalent conversion type cathode materials (Figure adapted from (Wang et al. (2011))).

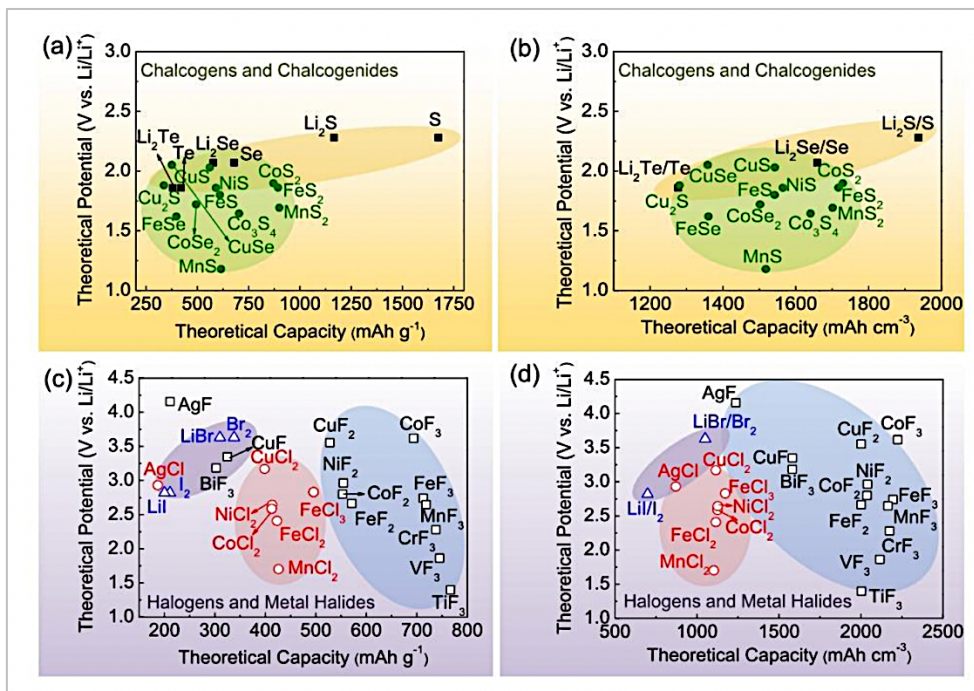


Figure 2-9: Approximate range of average specific capacity and discharge potentials for some of the most prevalent conversion-type cathodes (Figure adapted from (Wu & Yushin, 2017)).

S, Se, Te, and I adhere to the Type B reaction (Eq. 2-2,2-3). Among these elements, S has garnered the most extensive attention due to its high theoretical specific capacity (1680 mAh/g), cost-effectiveness, and abundance in the Earth's crust. It is crucial to note that oxygen is also classified as a Type B cathode in lithium-air batteries; however, it introduces fundamentally different technological challenges as it exists in a gaseous state. The inclusion of ambient air in such systems further complicates the matter. Consequently, lithium-air batteries are not within the scope of this review.

Figure 2-8 (b) illustrates the intermediate steps involved in the complete S conversion reaction, featuring intermediate polysulphides that are soluble in organic electrolytes. Additionally, Figure 2-9 (c) presents the typical discharge curves for conversion cathode materials. Notably, CuF_2 and BiF_3 exhibit a well pronounced and promising discharge profiles characterized by high-voltage plateaus. In contrast, Li_2S , Se, and S display a notably flat and extended voltage plateaus, indicating favourable kinetics in the reaction between two solid phases (Wang, Robert, et al. 2011; Nitta et al. 2015; Yu et al. 2018).

2.2.5.5 Fluorine and Chlorine Compounds

Recent attention has been devoted to metal fluorides (MF) and chlorides (MCl) owing to their relatively moderate operation potentials and high theoretical specific and volumetric capacities. However, these cathode materials exhibit unfavourable characteristics such as poor conductivity, substantial voltage hysteresis, high volume expansion, dissolution of active material and unwanted side reactions (Nitta et al. 2015). Most MF, especially FeF_3 and FeF_2 , are renowned for their limited electroconductivity attributable to their large band gap resulting from the highly ionic nature of the metal-halogen bond. Despite this, their open spatial structures can facilitate robust ionic movement and transfer therefore giving rise to high ionic conductivity environment (Zheng et al. 2012; Yu et al. 2014). Similarly, metal chlorides also suffer from inadequate electroconductivity for analogous reasons. Notably, all reported MF and MCl materials exhibit pronounced voltage hysteresis, a consequence of factors such as poor electronic mobility (poor electroconductivity) and ionic mobility (poor ionic conductivity) (Yu et al. 2014).

Moreover, Type A conversion materials lead to the formation of metal nanoparticles at their fully lithiated state. BiF_3 and FeF_2 have been identified as catalysts for the decomposition of cyclic carbonates at relatively high voltages, thereby compromising cycle life (Gmitter et al. 2010). On the other hand, Cu nanoparticles can undergo electrochemical conversion to Cu^{1+} , which subsequently dissolves into the electrolyte (Nitta et al. 2015). Even in the absence of such undesired side reactions, the coalescence of metal nanoparticles over numerous cycles can exacerbate voltage hysteresis (Liu et al. 2012).

Many ionic compounds, including certain fluorides, are soluble in polar solvents (Fu et al. 2005). Metal chlorides, including LiCl, are even more prone to dissolution in various solvents, including those commonly used in Li-ionB electrolytes (Wang, Robert, et al. 2011). Meanwhile, the empirically calculated volume expansions of MCl and MF, based on room temperature densities before and after lithiation, are relatively moderate (Wang, Robert, et al. 2011; Nitta et al. 2015). The extensively studied MF and MCl materials generally exhibit volume expansions ranging from 2% to 25%. Although not as substantial as observed in Type B conversion cathode materials and conversion/alloying anode materials (discussed in subsequent sections), issues such as fracturing, and loss of electrical contact remain possible.

To address their respective low electro and ionic conductivities, the synthesis of nanoparticles for conversion cathode materials becomes crucial to shorten the transfer pathways for ions and electrons. For MF and MCl, active materials are often dispersed onto or enveloped in conductive matrix materials to create alloys with enhanced conductivity, exemplified by FeF_3 /graphene, FeF_3 /CNT, BiF_3 / MoS_2 /CNT and AgCl/acetylene black (Nitta et al. 2015).

2.2.5.6 Sulphur and Lithium Sulphide

Sulphur boasts an exceptionally high theoretical specific capacity of 1675 mAh/g, coupled with its cost-effectiveness and relative abundance in the Earth's crust. Nonetheless, cathodes based on sulphur encounter challenges, including a low potential versus Li/Li^+ , poor electrical conductivity, dissolution of intermediate reaction products (polysulphides) in the electrolyte, and, in the case of pure sulphur, an exceedingly low vaporization temperature, leading to sulphur loss during electrode drying under vacuum. Sulphur also undergoes an approximate

80% volume change, posing a risk of disrupting electrical contact in standard carbon composite electrodes (Du Pasquier et al. 2003; Yu et al. 2014). To address the effects of both dissolution and volume expansion, sulphur can be encapsulated within a hollow structure with excess internal void space. Various materials, such as polyvinyl pyrrolidone polymer, carbon, and TiO₂ capsules, have been impregnated with sulphur through infiltration and chemical precipitation. Tested in half cells with thin electrode configurations, these alloys demonstrate cycle life, at times, approaching 1000 cycles (Du Pasquier et al. 2003; Yu et al. 2014).

To circumvent the adverse effects of volume expansion, prevent sulphur evaporation during drying, and establish full cells with Li-free (and consequently safer) anodes, electrode materials have also been devised in the form of Li₂S (Du Pasquier et al. 2003; Nitta et al. 2015). Unlike S, Li₂S is less readily infiltrated into a host network because of its higher melting point. However, the substantial solubility of Li₂S in environmentally friendly solvents like glycerol, acetic acid and ethanol presents an opportunity to fabricate various Li₂S-based nanocomposites, such as Li₂S nanoparticles embedded within conductive carbon matrices (Su et al. 2014). Given that fully lithiated Li₂S does not undergo further volume expansion, the need for void spaces is eliminated. In fact, carbon-coated Li₂S exhibits little to no change in morphology after 350 charge/discharge cycles (Nan et al. 2014).

Electrolyte modification stands as the conventional approach to alleviate polysulphide dissolution, with additives like LiNO₃ and P₂S₅ forming a robust solid electrolyte interface (SEI) on the Li metal surface, thereby preventing the reduction and subsequent precipitation of polysulphides (Lin et al. 2013a; Nitta et al. 2015). Additionally, the introduction of lithium polysulphides can temporarily decrease cathode dissolution (Lin et al. 2013b). Several studies have also employed higher molarity electrolytes, significantly reducing polysulphide solubility (Lee et al., 2013; Suo et al., 2013). Lastly, solid-state electrolytes offer a means to prevent polysulphide dissolution while concurrently enhancing cell safety by averting Li dendrite short-circuiting (Hassoun and Scrosati 2010; Lin et al. 2013b; Nitta et al. 2015).

2.2.5.7 Selenium and Tellurium

Recently, Se and Te have garnered attention due to their higher electroconductivities compared to S and substantial theoretical volumetric capacities of 1700 mAh/cm³ and 1300 mAh/cm³, respectively, in their fully lithiated state. Owing to their superior electroconductivity, Se and Te often exhibit enhanced utilization of active materials and higher rate capability than S. However, akin to S, Se-based cathodes face challenges related to the dissolution of high-order polyselenides, leading to rapid capacity loss, suboptimal cycle performance, and reduced coulombic efficiency (Luo et al. 2013). As of the recent date of publication, no reports have surfaced regarding the dissolution of polytelluride. Elemental Se and Te are also susceptible to considerable volume changes during cycling (Nitta et al. 2015). Fortunately, both Se and Te share the characteristic of having low melting points. Researchers have successfully infiltrated these materials into diverse porous carbon hosts and dispersed or enveloped them in conductive matrices to enhance their performance. It is essential to note, however, that Te's impractical cost prohibits its widespread use. Moreover, Se and Te, akin to Ag and Au, exhibit limited abundance, making them unlikely candidates for mass production (Yang et al. 2013; Nitta et al. 2015).

2.2.5.8 Iodine

The lithium-iodine (LiI) primary battery technology employs LiI as a solid electrolyte (with a conductivity of 10⁻⁹ S/cm), resulting in a low self-discharge rate and high energy density. Consequently, this configuration serves as a crucial power source for implantable cardiac pacemaker applications (Nitta et al. 2015). During discharge, the cathodic iodine undergoes a reduction process, first forming the tri-iodide ion (I³⁻) and then further reducing to the iodide ion (I⁻). While suitable for implantable cardiac pacemakers, this chemistry presents challenges in other applications due to its low power capability. Additionally, in standard organic electrolytes, iodine, triiodide, and lithium iodide exhibit solubility (Wang, Sun, et al. 2011). Given the high solubility of LiI in organic solvents, iodine ions have been considered for utilization in lithium-flow batteries. Recent advancements involve the infiltration of active iodine into the pores of porous carbon, facilitated by its low melting point of 113°C (Kang et al. 2020). The resulting iodine-conductive carbon black composite demonstrates a high discharge voltage

plateau, commendable cycle performance, and excellent rate capability. These improvements are attributed to enhanced electronic conductivity and the suppression of active material dissolution (Wang et al., 2011; Nitta et al., 2015).

Moreover, electrolyte modifications play a crucial role in minimizing unfavourable reactions between the electrolyte and active material during various stages of charge and discharge (Yu et al. 2014; Nitta et al. 2015; Phuc Anh LE 2019).

2.2.6 Electrolyte Solution

The electrolyte solution plays a crucial role in the operation of any electrochemical cell, as it enables the movement of ions (such as lithium ions in Li-ionBs) between electrodes, generating electric current. In the case of Li-ionBs, the electrolyte consists of a blend of organic solvents and lithium salts. Typical organic solvents include dimethyl carbonate, ethyl methyl carbonate, propylene carbonate (PC), dimethyl sulphoxide (DMSO), and diethyl carbonate (DEC) (Younesi et al. 2015). lithium-perchlorate (LiClO_4), Lithium-hexafluoroarsenate (LiAsF_6), Lithium tetrafluoroborate (LiBF_4) and lithium-hexafluorophosphate (LiPF_6) are popular lithium salts (Younesi et al. 2015).

2.2.7 Separator

The separator in Li-ionBs, typically made from polyolefin, constitutes a microporous membrane (Othman et al. 2020). The separator, immersed in the electrolyte solution, is positioned between the anode and cathode, serving as a safety barrier to prevent short-circuiting in case of direct contact between the two electrodes. The lithium-ion permeability of the membrane ensures the exclusive flow of charged particles, specifically lithium ions, between the two electrodes, thereby ensuring the battery's normal operation.

Separators in Li-ionBs can be either multi-layered or single-layered and are crafted from materials such as polypropylene (PP) or polyethylene (PE) (Nitta et al. 2015; Phadke et al. 2018). Collectively, each of these components plays a crucial role in influencing battery performance and properties. Modifying any of these components has the potential to enhance

electrochemical properties and overall operation of the Li-ionB. Notably, electrodes, particularly the cathode, hold exceptional significance as they directly impact various characteristics of Li-ionBs, including safety, charging time, depth of discharge, capacity, and more. Consequently, efforts aimed at optimizing and recycling have been initiated to comprehensively understand and develop the potential of Li-ionBs effectively and sustainably, especially concerning their cycle life.

2.3 Summated Lithium-Ion Battery Commercial Cathode Development over the Years

The first commercial rechargeable Li-ionBs were prototyped by SONY in the early 1990s and consisted of a LiCoO_2 (LCO) cathode and a carbonaceous anode (Nishi 2001; Reddy et al. 2020). Since its commercial inception, Li-ionBs have been viewed as the most promising "green battery" due to their high energy and power density, exceptional design flexibility, and prolonged lifespan when compared to other battery technologies (Piątek et al. 2021). Lithium manganese oxide (LMO), LMO-based rich layered materials (LMR, NMC), Lithium cobalt oxide (LCO), lithium nitrate oxide (LNO), lithium iron phosphate (LFP), lithium nickel manganese cobalt oxide (NMC), and lithium nickel cobalt aluminium (NCA) are some of the novel types of Li-ionBs that have been intensively researched in recent years to meet the exponentially growing need for creating battery-powered gadgets (Werner et al. 2020).

The market value, circulability (cm) and supply risk of several Li-ion cathode active materials are quantified and evaluated using correlations from Bloomberg Precious and Industrial Markets, as guided by Lv et al. (Lv et al. 2018). The data correlations demonstrate that recycling LCO and NCM is slightly more imperative, feasible, and profitable than recycling other cathode active material formulations due to the high Co content nature of their respective formulations. In the last decade, low-circulability and high-cost metals (in cathode active materials) with high supply risks have been gradually replaced by high-circulability and low-cost metals with lower supply risks. It is consequently necessary to improve Co circulability and research new cathode active materials in order to alleviate supply risk pressure.

The McKensie battery manufacturing model (2020) predicts that the production of Li-ionBs will continue to grow rapidly between 2010 and 2030. The model extrapolated the production to reach 7500 GWh in 2030 (AL Shaqsi et al. 2020; CSIRO 2022; ESMAP 2022). One driving factor is the rapid development and production of electric vehicles, whose sales have remained booming vastly in recent years. As NCM, NCA, and LiFePO₄ become more crucial cathode active materials for power batteries, the amount of valuable metals like Li, Ni, and Co that must be recycled through the recycling streams will increase proportionately (Werner et al. 2020; Chandran et al. 2021; Piątek et al. 2021). The spent Li-ionB waste stream will become significantly complex if processed without effective classification and management (Werner et al. 2020; Chandran et al. 2021; Piątek et al. 2021).

Nevertheless, data from ESMAP (2022) indicated that less than 25 % of the spent batteries available for recycling were recycled in 2020. Meanwhile, CSIRO (2022) reported that less than 2% of Li from spent Li-ionBs was recycled in the world in the same year despite the amount of spent Li-ionBs surging from 180000 metric tonnes in 2014 to 600000 metric tonnes in 2020. Contrasting this trend to Figure 2-10, which depicts the global growth in the amount of spent Li-ionBs and the market size of Li-ionBs in the global market from 2008 to 2030, it is evident that there is a positive correlation between the amount of spent Li-ionBs and the market size of Li-ionBs. Therefore, from the market revenue of Li-ionBs, the consumption and demand trends of spent Li-ionBs could be extrapolated (Lv et al. 2018; Zhao et al. 2021b). The recycling processes of spent Li-ionBs need to be studied and developed further urgently to establish industrial process routes that are more cost-effective and environmentally friendly than current processes.

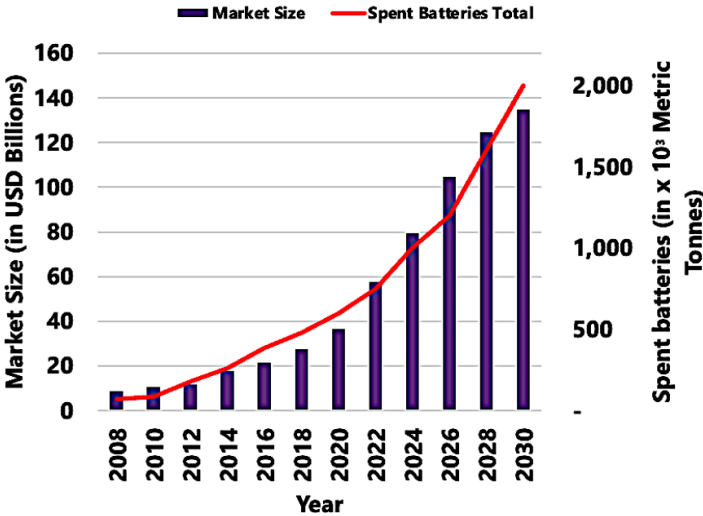


Figure 2-10: Global market size and total battery spent estimation of Li-ionBs over the years (Data derived from (AL Shaqsi et al. 2020; CSIRO 2022; ESMAP 2022)).

2.4 Why Recycle Lithium-Ion Batteries?

Figure 2-11 depicts the rechargeable battery global demand surge by battery application over the years (Global Battery Alliance 2020; Zhao et al. 2021b). Up to date, portable electronics like cell phones and note PCs have accounted for the majority of the Li-ionB demand. It is anticipated that demand for such tiny gadgets will exponentially rise over time. After a succession of advancements, the market for Li-ionBs will prosper with the aid of various Li-ionB applications, including solar panel systems, electrical power tools, smart grids, and especially electric automobiles. According to extrapolations (Figure 2-11), the market for rechargeable batteries for electric vehicles will surpass 7000 GWh in 2030, while the overall market for batteries will top 10000 GWh.

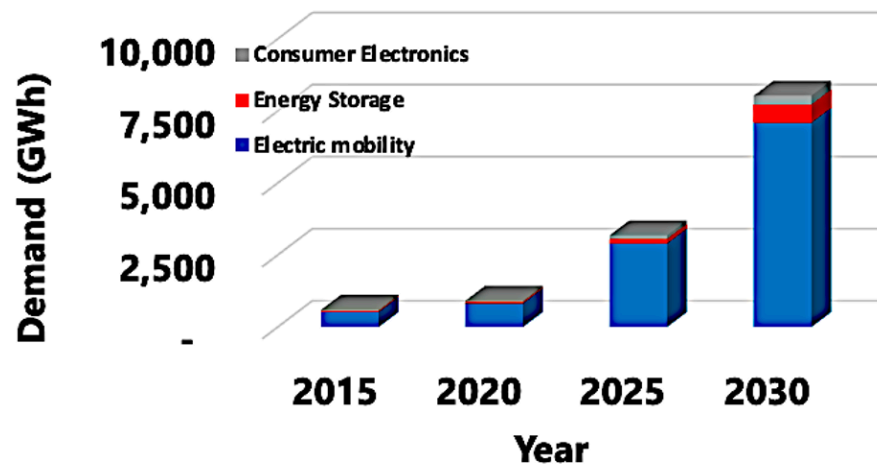


Figure 2-11: Global demand for battery technologies by application from 2015 to 2030 (Data from (Global Battery Alliance 2020)).

The typical lifespan of Li-ionBs is 3–4 years. As deposits in the electrolyte created during charging hinder ion transit over time, the capacity of the cell declines. Age and cycling both result in an increase in internal resistance, which lowers the cell's capacity to conduct current. Additionally, as internal resistance increases, the terminal voltage decreases. Older batteries, therefore, don't charge as quickly as new ones (the charging time required decreases proportionally). Li-ionBs will inevitably contribute significantly to solid waste, which must not be disregarded (Zhao et al. 2021b; Du et al. 2022).

Since Li-ionBs don't contain any substances that are hazardous to the environment on their own, they are harmless and deemed suitable for landfill disposal. However, if Li-ionB materials in a landfill leak and eventually come into contact with water, hazardous materials will be produced that will seep into the groundwater, making the landfill hazardous to the environment. Poisonous HF can be emitted when LiPF_6 in the electrolyte decomposes and reacts with water: $\text{LiPF}_6 + \text{H}_2\text{O} \rightarrow \text{POF}_3 + 2\text{HF} + \text{LiF}$ (Werner et al. 2020; Zhao et al. 2021b). Additionally, internal short circuits during decomposition can generate significant heat and oxygen, potentially causing explosions. Li-ion batteries contain elements like cobalt, copper, nickel, and iron, which can leach into the environment and present serious health risks to both animals and humans. These toxic elements may lead to chronic diseases and can be fatal if ingested or otherwise introduced into the body. Additionally, discarding the batteries

necessitates the extraction or mining of new metals, which has a considerably greater negative impact on the environment than simple recycling. Although Li-ionBs are partially recycled, a substantial amount still ends up in landfills each year, taking up space that could otherwise be conserved (ESMAP 2022).

While Li-ionBs are NOT extensively and effectively recycled, Pb-acid batteries are recycled to a degree of 97%, and more than 50% of the lead supply originates from recycled batteries (Global Battery Alliance 2020). Despite the enormous increase in Li demand, the study of the geological resource base for Li reveals that not enough Li is present in the Earth's crust to support the production of electric vehicles in the requisite quantities using only Li-ionBs (CSIRO 2022). Recycling can significantly lower the amount of Li needed. Having a recycling system in place will allay worries that the adoption of Li-ionB-powered vehicles will result in a shortage of lithium carbonate and a reliance on nations like China, Russia, and Bolivia, who hold the majority of the world's Li reserves (ESMAP 2022).

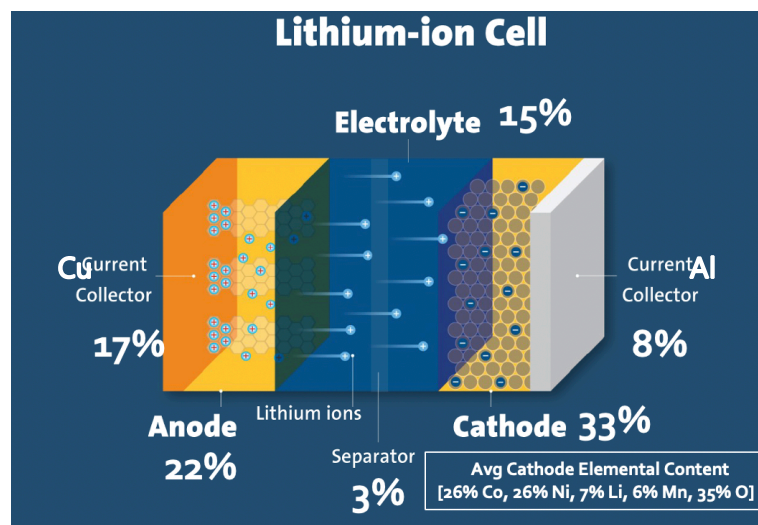


Figure 2-12: Typical Li-ionB composition (data derived from (Werner et al. 2020; Chandran et al. 2021; Piątek et al. 2021).

Conventional electrochemical Li-ionBs constitute valuable metallic elements such as Co, Mn, Fe, and Ni. Figure 2-12 depicts a typical composition of a Li-ionB. Table 2-2 shows the approximate value per metric ton (in the year 2022) for the key valuable components in a standard Li-ionB technology (Bloomberg 2022). Large-scale economic and non-complex Li-ionB recycling will undoubtedly benefit the environment and the economy as more and more

Li-ionBs are produced and consumed (Steward et al. 2019; Du et al. 2022; Wu et al. 2023). As noted, Cathode active materials contribute the largest share in the overall cost of the battery, hence the emphasis of recycling should be primarily focused on the cathode component.

Table 2-2: Approximate value for main components in a typical Li-ion cell (April 2022) (data from (Bloomberg 2022)).

Component	Approximate Value (US\$/Ton)
Cobalt	87,633
Aluminium	2,753
Nickel	28,370
Manganese	2,000
Iron	300
Electrolyte	1,500
Copper	9,219
Lithium	59,720

2.5 Conventional Recycling Methodologies

2.5.1 Overview

Spent Li-ionBs constitute mainly valuable metallic components such as Ni, Co, and Li and less valuable elemental components such as P, Al and Fe (Nitta et al. 2015; Zheng et al. 2018; Du et al. 2022; Wu et al. 2023). The recovery of highly valuable metals like Li, Ni, and Co from cathode active materials is the primary objective of recycling spent Li-ionBs, an initiative largely driven by environmental and economic concerns as highlighted in prior sections.

Spent Li-ionBs are conventionally recycled by employing hydrometallurgy, pyrometallurgy, bio metallurgy or electrometallurgy or a combination of all or some of them at the industrial and pilot scale (Phadke et al. 2018; Harper et al. 2019; Makuza et al. 2021b; Du et al. 2022). Figure 2-13 depicts a schematic representation of a typical recycling scheme, which typically entails

four primary steps: pre-treatment, metal extraction, product and component refining, and battery production. which typically entails four primary steps: pre-treatment, metal extraction, product and component refining, and battery production.

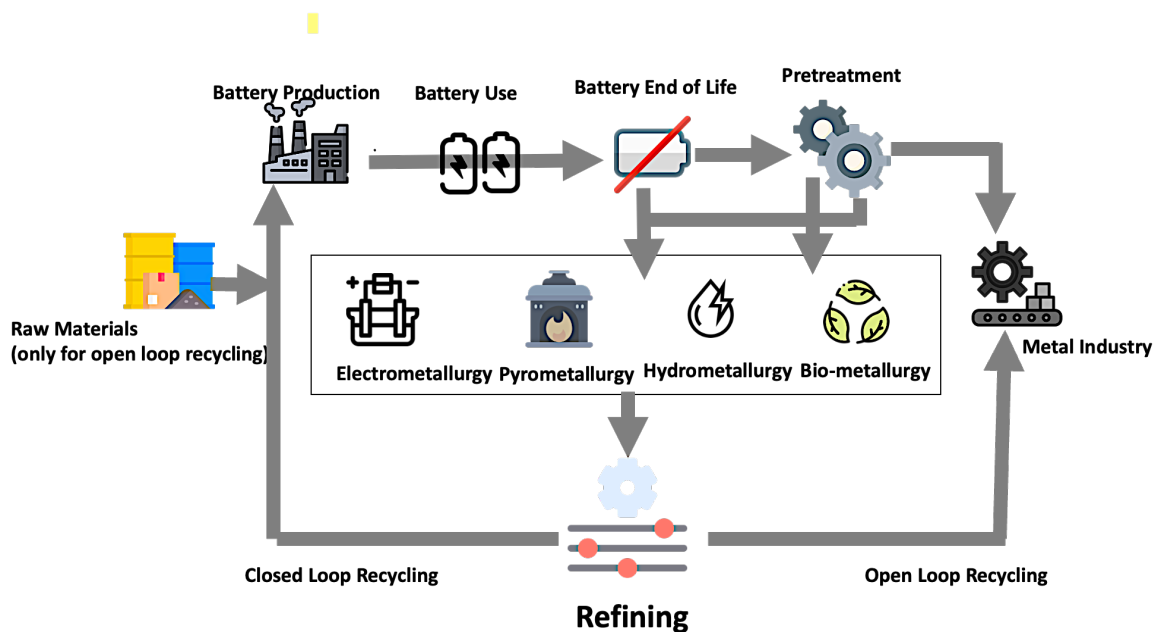


Figure 2-13: Conventional recycling stages for spent Li-ionBs.

Figure 2-14 lists all the conventional processes involved in each stage of recycling spent Li-ion batteries, the stages include pretreatment, physical processes, chemical processes, and product preparation processes. To avoid runaway spontaneous combustion of battery elements or short-circuiting during the subsequent disassembling or dismantling step, spent Li-ionBs are typically first fully discharged to empty all the remaining power. To discharge spent Li-ionBs, they are usually immersed in a salt solution (Georgi-Maschler et al. 2012; Zheng et al. 2018; Phuc Anh LE 2019). Following the discharging step, the fully discharged spent Li-ionBs are processed through mechanical separation and automated or manual dismantling. The goal of this step is to remove the plastic or metal casings and separate the internal components of spent Li-ionBs (i.e., anode, cathode and separator) for further recycling processing. Following the disassembling step, the active cathode material is separated from the current collector through chemical, thermal or physical treatment processes (e.g., thermal treatment method, manual scraping method, NaOH dissolution method, solvent dissolution method, ultrasonic-

assisted separation, or mechanical method) (Georgi-Maschler et al. 2012). The recovered cathode active material is then channelled to the next stage for further processing.

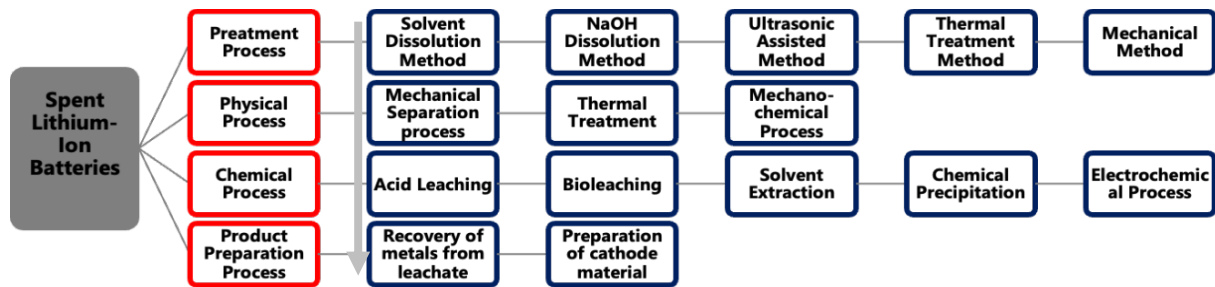


Figure 2-14: Recycling methodologies for spent Li-ionBs.

2.5.2 Pre-treatment Process

The various waste battery streams are often subjected to either a mechanical or chemical pre-treatment procedure in order to prepare them for later processing. Pre-treatment also increases the efficiency of the overall battery recycling process. The subsequent processes will be more fluid if thorough pre-treatment is administered. Dismantling, crushing, screening, heat treatment, mechanochemical technique, dissolving, and other pre-treatment procedures are the primary pre-treatment processes. Due to their vastly differing physical qualities, several valuable metals, components or materials, such as Cu, Al, and carbonaceous anode, are simple to recover and recycle through pre-treatment. Pre-treatment processing plays a significant role in separating and recovering cathode active materials and organic binders from the current collector as it makes subsequent process execution much less energy and time-intensive (Shuguang Zhu et al. 2011).

Shin et al. (2005) described a single-stage pre-treatment process in which the spent Li-ionBs were directly crushed to an appropriate size, followed by fine crushing and sieving to remove aluminium foil which would affect the leaching process (Shin et al. 2005). At the end stream, metallic material was collected using magnetic separation. The pre-treatment technique requires the removal of the organic binder, which is crucial. Thermal treatment, ultrasonic cleaning, and organic reagent dissolving are the ideal processes to undertake such a task (Shin et al. 2005; Granata et al. 2012; Song, Wang, et al. 2014; He et al. 2017a).

To separate different materials, Granata et al. (2012) utilised a splitter and a two-rotor crusher. Thermal processing at 300 °C for two hours removed the organic binder (Granata et al. 2012). However, the breakdown of organic materials like PVDF resulted in the production of harmful and poisonous fumes like HF and exhaust that have been contaminated with heavy metals. As a result, it seems necessary to use a system that includes a cooler, a condensation chamber, bag filters and carbon filters as tail gas processes to dispose of harmful gases. Researchers experimented with organic dissolution reagents to dissolve the organic binder in light of the drawbacks entailed by the heat treatment. For instance, the dissolution reagent used to dissolve PVDF is a mixture of N, N-dimethylformamide (DMF) and N-methyl pyrrolidone (NMP) or ethanol, although the dissolution reagent (solvent) itself is typically referred to as a toxicant (Song, Wang, et al. 2014). Citrus fruit juice (CFJ) was ascribed by Pant and Dolker (Pant and Dolker 2017) as a green, non-toxic, and eco-friendly solvent to make up for the drawback of utilizing a hazardous solvent as a dissolution reagent. To accomplish successful dissolution, the CFJ procedure is often carried out under extreme temperature conditions (typically over 90 °C) (Pant and Dolker 2017; Lv et al. 2018).

The mechanochemical process, in addition to mechanical processing methods, is an imperative process that alters raw materials mechanically to affect their physicochemical properties through the utilisation of high-energy ball milling (Saeki et al. 2004; Wang et al. 2016; Guan et al. 2017; Yang et al. 2017). The grinding and rubbing of particles could also unintentionally activate various chemical reactions. The activity of the materials will subsequently be improved following the mechanochemical conversion. In light of this, mechanochemical technology is frequently utilized in pre-treatment operations of spent Li-ionB cathode active particles to alter, modify or disrupt their respective crystal structure in order to enhance the leaching efficiency (Yang et al. 2017). Even though pre-treatment processes have been the subject of a lot of research, there are still certain practical challenges that must be addressed for the developed processes to be viable. The practical challenges faced by the pre-treatment processes are summarized in Table 2-3. Furthermore, the adoption of various pre-treatment techniques is still hampered by the disorganized and less effective classification of Li-ion spent batteries, complex disassembly and dismantling processes, and inefficient valuable metal extraction (i.e. Co, Ni and Li) (Kim et al. 2021; Zhang et al. 2021). Pre-treatment processes must therefore be

utilised in conjunction with other physicochemical procedures to achieve the goal of efficiently recycling all valuable materials or metals in spent Li-ionBs.

Effective separation of the cathode active material from the foil is achieved via solvent dissolution, ultrasonic-assisted separation, sodium hydroxide (NaOH) dissolution, thermal treatment and mechanical separation methods (Lv et al. 2018). The methods are discussed in detail in the following sections.

2.5.2.1 Solvent Dissolution Method

The solvent dissolution process weakens the bond between the substrate and cathode active material by dissolving the binder material. Selecting the most effective organic solvent to dissolve, consequently weakening, the binder is the key step in the solvent dissolution process. The organic solvent N-methyl pyrrolidone has been widely utilised to extensively dissolve the PVDF binder (Lv et al. 2018). Zhou et al. (2010) proposed utilising dimethylformamide (DMF) to dissolve the binder PVDF. The solubility of PVDF in DMF was found to be 175 g/L at 60 °C. The PVDF-based cathode active material was compatible with DMF solvent (Zhou et al. 2010). However, the PTFE-based cathode active material was not appropriately suitable for dissolution in DMF (Lv et al. 2018; Zhang et al. 2021).

Zhang et al. (2014) effectively extracted the Li-ionB cathode active material from the Al foil current collector using the trifluoroacetate (TFA) solvent (Zhang et al. 2014). The cathode active material from the Al foil current collector can be successfully extracted using the solvent dissolution process, according to numerous research. For PVDF-based cathode active material, the majority of studies had achieved success, but for PTFE-based cathode active material (Zhang et al. 2021), it had been very challenging to remove the cathode active material from the Al substrate. The solution used in this procedure is often costly and hazardous to human and environmental health (Lv et al. 2018; Zhang et al. 2021).

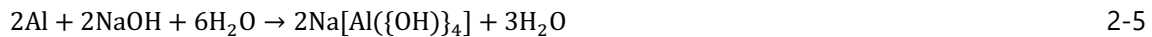
The latest developments in Li-ionB pre-treatment processes were discussed by Zhang et al. (2021). The substrate (aluminium foil) dissolution method was employed to dissolve the foil from the electrode-substrate matrix by employing alkaline solutions (Zhang et al. 2021). The method entails the selective dissolution of the foil without dissolving the cathode-active

materials (Lv et al. 2018; Zhang et al. 2021). In addition to the aforementioned methodologies, a high-temperature process is also utilized, but because it disintegrates the electrode materials and ultimately dissolves them, the method is not ideally feasible. The electrode materials that were recovered after removing the battery casing were heated with an N-methyl pyrrolidone (NMP) solution at approximately 100 °C in the pilot process for recycling Li-ionBs that Zhou et al. (2010) described. Graphite and LiCoO₂ were successfully extracted from the collector using this process while Al and Cu were still in their metallic state (Zhou et al. 2010).

Triethyl phosphate was utilised by Bai et al. (2021) to extract Li-ionB cathode active material (e.g. NMC, LCO etc) by dissolving the PVDF binder (Bai et al. 2021). Through a solvent-based separation process, electrochemically active components were removed from cathode scraps gathered during the manufacturing process of electrodes without altering their physicochemical properties, electrochemical characteristics, and crystallography. The aluminium foils that were recovered were spotless and exhibited no signs of corrosion after PVDF dissolution. The polymer-based binder can also be recovered using wet phase inversion (a non-solvent-induced phase separation technique) (Bai et al. 2021).

2.5.2.2 NaOH Dissolution Method

Numerous proposed methods for separating or isolating the Li-ion cathode active materials from the aluminium foil substrate included leaching the cathode using a NaOH solution. Ideally, the components can be separated using the amphoteric properties of aluminium (Dong et al. 2018). The separation of cathode active material from aluminium foil substrate was accomplished by utilizing a 10 wt.% NaOH solution for 300 min at ambient temperature (Nan et al. 2005). The process effectively dissolved over 97% of the aluminium foil substrate. The aluminium oxide protective layer covering the substrate surface dissolves [Eq. 2-4] along with the aluminium foil [Eq. 2-5] when a NaOH solution solvent targeting substrate is used (Dong et al. 2018; Lv et al. 2018).



Advantages of this technology include high separation efficiency, ease of operation and effective separation. However, the effective recovery of Al is hampered due to its existence in ionic form. Furthermore, the NaOH alkali wastewater (is hazardous to environmental and human health.

2.5.2.3 Ultrasonic-Assisted Separation

Since the polymeric binders have high adhesive strength, it is relatively challenging to remove cathode active material from the aluminium foil current. The ultrasonic treatment process is regarded to be an ideal practical process for eliminating cathode active material from the Al foil substrate due to the cavitation effect generated by ultrasonic sound waves. Li et al. (Li et al. 2014) put forth the ground-breaking idea of recycling used Li-ionBs by integrating crushing and ultrasonic washing to recover the Co compound. The alternate approach enhances the Co recovery efficiency while lowering energy consumption and environmental pollution. In order to separate the electrode materials from their support substrate, Li-ionBs were crushed through a 12 mm aperture screen before being processed into an ultrasonic washing vessel. A 2 mm aperture screen was utilised to filter the cleaned materials in order to obtain the underflow items, specifically the recovered electrode material. The cathode active material remains adhered to the substrate surface when utilizing solely the mechanical approach, and only the components phase matrixes (not elemental or chemical components) are separated when employing the ultrasonic washing method (Lv et al. 2018).

Li et al. (2014) investigated how the cavitation effect (from ultrasonic treatment) and agitation affected the separation of cathode active materials (Li et al. 2014). The study established that when mechanical agitation alone was applied, the majority of the cathode active materials remained adherent to the surface of the Al substrate. Only a portion of the cathode active materials was separated when the ultrasonic-assisted separation method was utilized independently. However, practically all of the cathode active materials could be effectively removed from the Al substrates when both techniques were applied concurrently. This effect

is attributed to the cavitation effect generated during ultrasonic treatment, which can produce more pressure to liquefy and scatter insoluble contaminants. The mechanical agitation's washing effect further enhances the separation of cathode-active materials from the substrate (Li et al. 2009).

He et al. (2015) iterated that the separation of cathode active materials from Al foil substrate by ultrasonic treatment is a functional result of the binder dissolution and the cavitation effect induced by the ultrasonic waves (He et al. 2015). Based on this mechanism, when NMP was employed as the cleaning solution, the stripping efficiency of the cathode active material was over 99% at a temperature of 70 °C, and ultrasonic power of 240 W, for 90 minutes of continuous ultrasonic treatment. The cathode active material exhibited low aggregation after being removed from the Al foil substrate by ultrasonic treatment, which facilitated the subsequent cathode active material dissolution process (leaching process) (He et al. 2015; Lv et al. 2018).

2.5.2.4 Thermal Treatment Method

Vacuum pyrolysis is a straightforward method for extracting cathode active material. The pyrolysis process evaporates or breaks down the electrolyte and binder, which in turn weakens the cathode active material matrix-substrate bond (Sun and Qiu 2011; Hanisch et al. 2015; Yang, Huang, Xu, et al. 2016). The thermal treatment approach employs high temperatures to break down the binder, weakening the foil substrate-cathode active material bond. The cathode active materials can subsequently be effectively removed via physical separation processes (such as sieving, magnetic separation, crushing etc) (Yang, Huang, Xu, et al. 2016).

Although some materials, such as acetylene black, conductive carbon, etc., oxidize beyond 350 °C and generally decompose above 600 °C, PVDF binder is typically reported to decompose above 350 °C (Li et al. 2014; Yang, Huang, Xu, et al. 2016). Vacuum pyrolysis has been proposed by Sun and Qiu (Sun and Qiu 2011) as a novel process for effectively separating cathode active material from the current collector (Al foil). Pyrolysis weakens the adhesion between the cathode active material and the current collector by evaporating or decomposing the electrolyte and binder. The cathode active materials only disintegrated from the collectors

when the pyrolysis temperature was more than 450 °C. When the pyrolysis temperature was below 450 °C, the cathode active materials remained bonded to the current collectors. The extent and effectiveness of separation improved with temperature nominally between 500 and 600 °C. Since the aluminium foil remained brittle at temperatures above 600 °C, it was difficult to remove the cathode active material from the collector. The cathode active materials from the Al collectors are separated by employing heat treatment in a reducing atmosphere (Hanisch et al. 2015). It was demonstrated that it is feasible to effectively separate the cathode active materials from the current collectors by adjusting the temperature of the reducing atmosphere (Yang, Huang, Xu, et al. 2016). Additionally, the molecular structure of the active cathode materials is altered during this process, which makes it easier to leach cathode metals during the leaching phases. Thermal treatment has several benefits, including ease of use and high separation efficiency. The binder and additives are thermally treated; however, this process by-products hazardous gases.

2.5.2.5 Mechanical Method

Mechanical pre-treatment processes, such as sieving, crushing, magnetic separation, and other similar processes, are widely recognized as useful in the context of recycling spent Li-ionBs. Zhang et al. (2014) investigated the process, mechanical and chemical mineralogical characterizations of spent Li-ionBs waste by integrating several analytical methods in order to give fundamental information pertaining to mechanical separation processes (Zhang et al. 2014). It was discovered that used Li-ionBs exhibited good selective crushing characteristics during processing. Three components make up the crushing by-products of wasted Li-ionBs: an Al-enriched fraction (> 2 mm), an Al- and Cu (AL Shaqsi et al. 2020; CSIRO 2022; ESMAP 2022)-enriched fraction (0.25-2 mm), and a Co- and a graphite-enriched fraction (0.25 mm). The cathode active materials derived from a fraction of less than 0.25 mm in terms of mineral phase and chemical state were found to have kept their original crystalline structure and chemical state in Li-ionBs. However, these powders included a coating of hydrocarbons on their surface that made flotation operations problematic.

Shin et al. (2005) developed a mechanical recycling process that integrated pyrolysis, crushing and sieving to recover valuable active mass from the wasted Li-ionBs. The developed process

is illustrated in Figure 2-15. After a variety of mechanical processes, including crushing, sieving, and magnetic separation, enriched LiCoO_2 particles were produced. These particles were then finely ground to separate the LiCoO_2 from tiny fragments of aluminium foil. Prior to the metal-leaching process, mechanical separation can increase the efficiency of the targeted metal recovery (Shin et al. 2005). The main drawback of mechanical procedures is that the components of used Li-ionBs cannot be entirely separated from one another. In addition, the environment is put in danger because of the disintegration of LiPF_6 , DEC, and PC during mechanical processes (Xu et al. 2014).

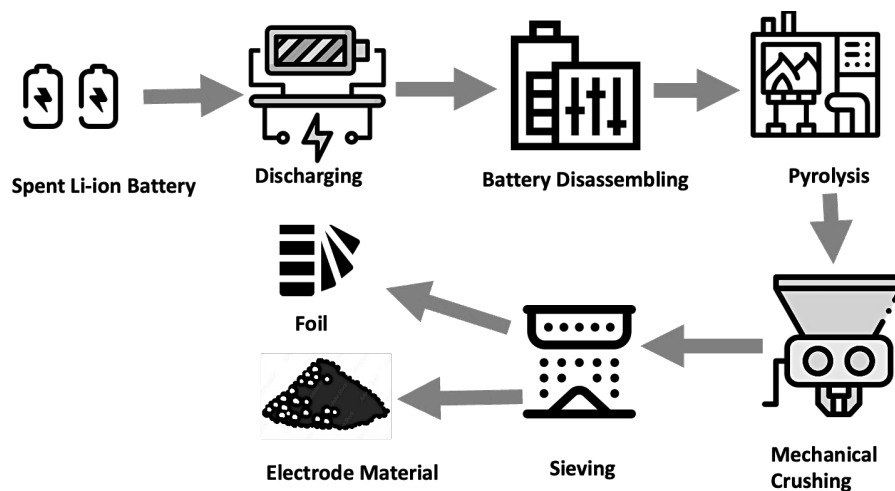


Figure 2-15: Process flow chart of a conventional mechanical recycling process (constituting pyrolysis, crushing and sieving) (Figure based on work described by (Shin et al. 2005)).

There are still existing challenges with the pre-treatment processing of spent Li-ionBs despite the fact that numerous pre-treatment technologies have been established by researchers. A summary of the benefits and drawbacks of various pre-treatment techniques is summated in Table 2-3.

Table 2-3: Advantages and disadvantages of conventional pre-treatment methods (Kim et al. 2021; Zhang et al. 2021).

Method	Advantages	Disadvantages
Solvent Dissolution method	High separation efficiency	The costlier the solution, the higher the degree of toxicity
NaOH method	Simple operation with high separation efficiency	Alkali wastewater is harmful to the ecosystem, and Al extraction is challenging since it is in an ionic state
Ultrasonic assisted separation	The operation method is simple with no hazardous or toxic traits	High capital cost, noise pollution
Thermal treatment	Simple operation, high-efficiency process	Capital cost is the high, high toxic gas emission
Mechanical methods	Operation method that is simple to employ	High levels of hazardous gas emissions and incomplete metal removal from spent Li-ionBs

2.5.3 Metal Extraction Processes

2.5.3.1 Pyrometallurgical Process

A subset of extractive metallurgy, pyrometallurgy employs heat to physically and chemically modify ore and concentrates in order to recover valuable metals (Harper et al. 2019; Makuza et al. 2021a). In order to recover heavy metals (such as Cd, Pb, Cu, Zn etc) from depleted Ni-Cd batteries, Ni-Fe or Zn-Mn dry batteries, pyrometallurgical methods have been extensively researched (Espinosa et al. 2004; Lv et al. 2018). In pyrometallurgical operations, smelt slags are frequently utilised to segregate metals, with certain metals going to the slag and the target metals becoming alloys. Most pyrometallurgical processes, with the exception of the Umicore technology, require pre-treatment processing (Sun and Qiu 2011; Meshram et al. 2014, 2015a; Makuza et al. 2021b). By incorporating CaO+SiO₂, pyrolusite, and minute amounts of Al shells into the processing of spent Li-ionBs, Ren et al. (2016) presented a novel slag system of MnO-

$\text{SiO}_2\text{-Al}_2\text{O}_3$. The mixture was then heated for 30 minutes at 1475 °C. This innovative technique produced a high-purity metallic alloy with Ni (99%), Co (99%), and Cu (99%) as well as enhanced slag with MnO (46%) and Li_2O (2,5%) (Ren et al. 2016; Lv et al. 2018).

Li-ions are usually trapped in the slag phase in a standard pyrometallurgical process, which has to be further processed to be extracted in pure form (Sun et al. 2017). Recently, attention has been directed to the carbothermal reduction process as a low-cost, non-complex, and consistently repeatable pyrometallurgical route to recycle Li, Co, and other valuable metals (Makuza et al. 2021a). The mixed spent Li-ionBs can be converted into lithium carbonate, metal oxide, or pure metal through this carbothermal reduction process. Water leaches lithium carbonate in one step, whereas the carbon (from graphite) in the leachate slag burns to carbon dioxide and leaves metal oxide as the remaining residue (Xiao et al. 2017; Makuza et al. 2021a). The following stage involves wet magnetic separation to further separate lithium carbonate, graphite, and pure metal (Li et al. 2016). Pyrometallurgical technologies, however, now confront challenges in lowering energy consumption and meeting the strict and rigorous specified requirements for modern treatment processes. The pyrometallurgical process, which primarily entails pyrolysis, is comprehensively summarized in Figure 2-16.

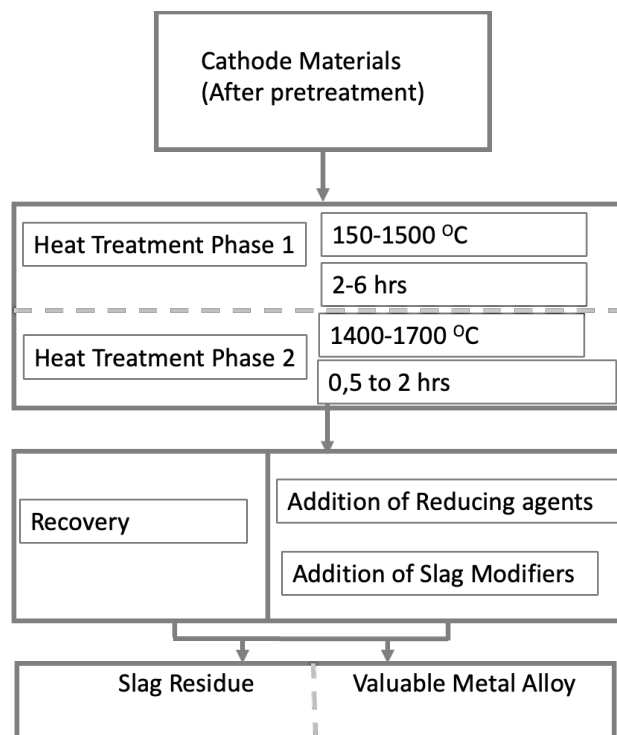


Figure 2-16: Conventional pyrometallurgical processes for spent Li-ionBs.

2.5.3.2 Hydrometallurgical Process

Leaching and extraction constitute most of a typical hydrometallurgical process. In comparison to the pyrometallurgical process, it entails numerous added advantages, including high valuable metal extraction efficiency, low energy intensive, less harmful gas emission, and low capital and production cost. Commercialization of hydrometallurgy has enormous possibilities. However, when it comes to disposing of waste materials, the process entails considerable challenges. The hydrometallurgical process, which primarily entails leaching, solvent (liquid-liquid) extraction, chemical precipitation, and electroreduction process, is comprehensively summarized in Figure 2-17. Among these, a relatively small portion of the research is reported on the recovery and recycling of spent Li-ionBs by the electrochemical process because of its high energy-intensive nature, even though past research does imply its viability for recovering Co-based compounds and pure Co metal (Garcia et al. 2008, 2011, 2012; Chandran et al. 2021).

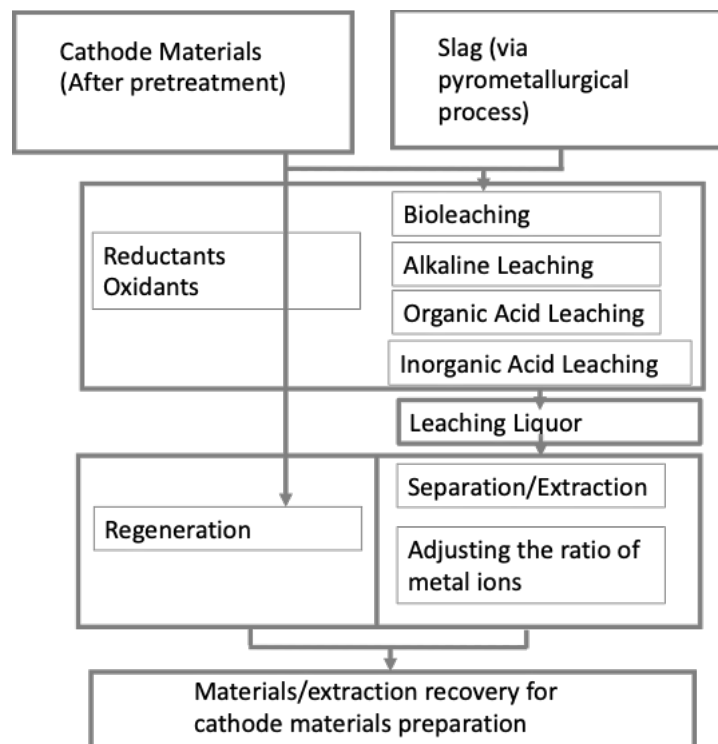
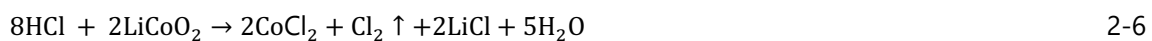


Figure 2-17: Conventional hydrometallurgical recycling and recovering processes for spent Li-ionBs (Partial data derived from (Chandran et al. 2021)).

2.5.4 Chemical Processes

2.5.4.1 Conventional Leaching

The primary phases of the recycling of spent Li-ionBs, akin to most metallurgical processes, include the dissolution of the cathode active materials in leachants (leaching reagents), followed by reduction, separation, and extraction. In earlier research studies, in-organic acid reagents, such as nitric acid (HNO₃), hydrochloric acid (HCl), and sulphuric acid (H₂SO₄), were conventionally utilised as leaching agents and proved to be practically successful and effective, but drawbacks, such as the by-production of secondary pollutants and the complexity of extractive separation and purification processes, also surfaced (Ferreira et al. 2009a; Sun and Qiu 2011; Granata et al. 2012). The chemical reaction of the leaching process using HCl as the leaching agent can be annotated as:



Similar reactions occur when different monoprotic acids or polyprotic acids are used for leaching. In the absence of reductants, the leaching efficiency of Co proceeds in the following order: HCl > HNO₃ ≈ H₂SO₄. The relatively higher leaching efficiency of HCl is mostly caused by the reducibility nature of HCl (Joulié et al. 2014). Therefore, unless H₂O₂ or other reductants are added, the leaching efficiency of the majority of reagents would be limited. The leaching + reduction reaction mechanism can be annotated (using LiCoO₂ as an example):

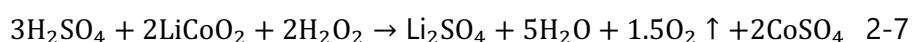


Figure 2-18 (a) shows how reductants like H₂O₂ or ascorbic acid can enhance the leaching properties of leaching reagents. At normal temperatures, Co²⁺ is much more easily dissolved than Co³⁺, yet Co³⁺ is primarily substantial in spent Li-ion cathode active materials. Therefore, the leaching efficiency and reaction kinetics will undoubtedly be enhanced when the Co³⁺ is transformed into Co²⁺. Moreover, because Co³⁺ has a significantly different solubility constant from Mn²⁺, Cu²⁺ and other metal ions, the shadow in Figure 2-17 (a) would be an ideal region to isolate Co³⁺ from these metal ions and other metal ions. Leaching efficiency and reaction rate would initially rise in line with an increase in reductant concentrations, and then they would plateau, where they would not fluctuate noticeably (Nayaka, Pai, Santhosh, et al. 2016c).

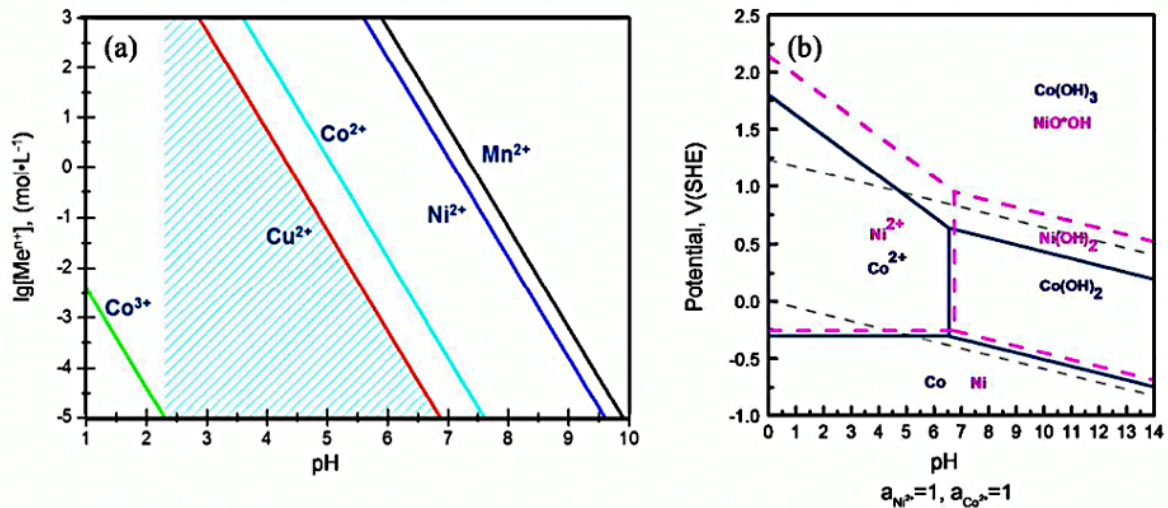


Figure 2-18: (a) Correlation between equilibrium aqueous metal ion concentration (at 25 °C) and pH ; (b) Potential (E vs SHE) and pH diagram for the Ni-H₂O and Co-H₂O systems (at 25 °C, Co=Ni = 0.2 mol/L) (Figure Adapted from (Lv et al. 2018)).

Numerous organic leaching reagents, such as oxalic acid, citric acid, malic acid, ascorbic acid, aspartic acid, and glycine, are intensively explored to address the issues that arise when employing the inorganic leaching reagents (Li et al. 2013; Zeng et al. 2015a; Nayaka, Pai, Manjanna, et al. 2016; Nayaka, Pai, Santhosh, et al. 2016c).

Li et al. (2014) iterated that while the leaching efficiency of Li is consistently steady throughout those various leaching media, the leaching efficiency of Co is higher when employing citric acid compared to HCl or H₂SO₄. Most organic acids have a similar reaction mechanism to citric acid, with a few exceptions like acid (Li et al. 2014; Nayaka, Pai, Manjanna, et al. 2016; Nayaka, Pai, Santhosh, et al. 2016d, 2016c). Oxalic acid may serve as both a reductant (by replacing H₂O₂ in equation 2-17) and a leachant (by oxidising the metal), consequently, Co and Li leaching could attain leaching efficiencies of more than 97% (Nayaka, Pai, Manjanna, et al. 2016; Nayaka, Pai, Santhosh, et al. 2016c).

An alkaline-based leaching system, like NH₃, has also been researched in addition to the acid-based leaching system. An NH₃-(NH₄)₂SO₄ system with high metal selectivity during leaching was demonstrated by Zheng et al. (2017). A similar leaching system, containing NH₃, (NH₄)₂SO₄ and (NH₄)₂CO₃ was employed by Ku et al. (2016). In spent Li-ionBs, Co and Ni have a high

valence state which makes them difficult to dissolve, whereas Cu was easily separated from Co and Ni in the NH_3 -based system (Ku et al. 2016a; Zheng et al. 2017). $\text{NH}_4)_2\text{CO}_3$ served as a pH buffer to maintain a stable leaching solution's pH while $(\text{NH}_4)_2\text{SO}_4$ was added as a reductant to upsurge the leaching efficiencies of Ni and Co.

Additionally, the supercritical fluid used in metal extraction processes offers an ideal leachant alternative. Bertuol et al. (2016) effectively leached cobalt from spent Li-ionB cathode active material using supercritical CO_2 extraction using H_2SO_4 (as cosolvent) and H_2O_2 (as reductant additive). The results indicated that 95% leaching efficiency could be attained by reducing the reduction process duration and H_2O_2 consumption from 60 min to 5 min and 8 vol% to 4 vol%, respectively (Bertuol et al. 2016; Lv et al. 2018). Liu and Zhang (2016) synthesized the acid leachant for the leaching process through the dechlorination of PVC using subcritical water as the catalyst. At 350 °C temperature, PVC/LCO ratio of 3:1 and 16:1 S/L ratio, approximately 96% of Co and nearly 99% of Li were leached from the base cathode active material (Liu and Zhang 2016). However, the operation is complex and entails high capital costs due to the rigorous equipment requirements, high-pressure and high-temperature environment. All of the economic and technical challenges highlighted above have dampened interest in utilising supercritical fluid in battery recycling (Liu and Zhang 2016; Lv et al. 2018).

Table 2-4 provides a summated overview of the Li-ionB cathode active material leaching processes over the years. Though there are numerous reports on Li-ionB cathode active material leaching processes, only a small proportion focuses on detailing the leaching process mechanism at the molecular or atomic level based on the crystallographic method. Takacova et al. (2016) explored the change of spent Li-ionB cathode active sub-particles in the HCl and H_2SO_4 leaching mediums. The work also detailed the influence of temperature on Li and Co extraction from cathode active mass, a case for both leaching reagents, through kinetics (activation energy) and thermodynamics studies. Such studies foster further investigations on the cathode active material leaching process in the future. The more the leaching process mechanisms are understood, the more opportunities arise for enhancing the efficiency of the leaching process (Wang et al. 2012; Takacova et al. 2016).

Table 2-4: Summative review of leaching spent Li-ionBs using different leaching reagents.

Type of leaching and source	Reagent	T	Time	Leaching efficiency (%)		Ref
		(°C)	(min)	Co	Li	
Inorganic Acid Leaching						
Spent Li-ionBs	1.75 mol/L HCl	50	90	99.0	100	(Barik et al. 2017a)
Spent Li-ionBs (LiCoO ₂)	4 mol/L HCl	80	30	90.6	93.1	(Zhang et al. 1998)
LiFePO ₄ and LiMn ₂ O ₄	6.5 mol/L HCl + 5 vol % H ₂ O ₂	30	60		74.1	(Huang et al. 2016)
Li-ionBs industry waste (LiCoO ₂)	2 mol/L H ₂ SO ₄ + 5 vol % H ₂ O ₂	75	30	94.0	95.0	(Swain et al. 2007)
Lini _x mnyco _z o compounds	4 mol/L H ₂ SO ₄ + 5 vol % H ₂ O ₂	65–70	120	96.0		(Gratz et al. 2014)
Spent Li-ionBs (mixture)	1 mol/L H ₂ SO ₄ + 0.075 M NaHSO ₃	95	240	91.6	96.7	(Meshram et al. 2015a)
Spent Li-ionBs (LiCoO ₂) (from laptops)	2 mol/L H ₂ SO ₄ + 5 vol % H ₂ O ₂	75	60	70.0	99.1	(Jha et al. 2013)
Spent Li-ionBs (LiCoO ₂) (cell phones)	2% H ₃ PO ₄ + 2 vol % H ₂ O ₂	90	60	99.0	88.0	(Pinna et al. 2017a)
Spent Li-ionBs (LiCoO ₂)	0.7 mol/L H ₃ PO ₄ + 4 vol % H ₂ O ₂	40	60	99.0	100.0	(Chen, Ma, et al. 2017)
Spent Li-ionBs (LiCoO ₂)	1 mol/L HNO ₃ + 1.7 vol % H ₂ O ₂	75	60	95.0	95.0	(Lee and Rhee 2002)
Alkaline Leaching						
Spent Li-ionBs (Li(Ni _{1/3} Co _{1/3} Mn _{1/3})O ₂)	4 mol/L NH ₃ -1.5 mol/L (NH ₄) ₂ SO ₄ + 0.5 M Na ₂ SO ₄	80	300	80.7	95.3	(Zheng et al. 2017)
Organic Acid Leaching						
Spent Li-ionBs (LiCoO ₂)	0.4 mol/L Tartaric acid + 0.02 mol/L Ascorbic acid	80	60	93.0	95.0	(Nayaka, Pai, Santhosh, et al. 2016c)
Spent LiCoO ₂ and CoO	1 mol/L Oxalate + 5 vol % H ₂ O ₂	80	120	96.7		(Sun and Qiu 2012)
Spent Li-ionBs (LiCoO ₂)	2 mol/L Citric acid + 0.6 g/g H ₂ O ₂ (H ₂ O ₂ /Spent Li-ionBs)	70	80	96.0	98.0	(Chen et al. 2015)
Spent Li-ionBs (LiCoO ₂)	1 mol/L Oxalic acid	95	150	97.0	98.0	(Zeng et al. 2015a)
Spent Li-ionBs (LiCoO ₂)	1 mol/L Iminodiacetic acid + 0.02 M Ascorbic acid	80	120	99.0	90.0	(Nayaka, Pai, Manjanna, et al. 2016)
Spent Li-ionBs (LiCoO ₂)	1 mol/L Maleic acid + 0.02 M Ascorbic acid	80	120	99.0	96.0	(Nayaka, Pai, Manjanna, et al. 2016)
Spent Li-ionBs (LiCoO ₂)	0.5 mol/L Glycine + 0.02 M Ascorbic acid	80	120	91.0		(Nayaka, Pai, Santhosh, et al. 2016d)
Spent Li-ionBs (LiCoO ₂)	1.5 mol/L Succinic acid + 4 vol % H ₂ O ₂	70	40	100.0	96.0	(Li et al. 2015a)
Spent Li-ionBs, LiCoO ₂ & LiNi _{0.5} Co _{0.2} Mn _{0.3} O ₂	2 mol/L L-Tartaric acid + 4 vol % H ₂ O ₂	70	30	98.6	99.1	(He et al. 2017a)

In this section, quantitative methods for leaching rates of Li and Co are proposed for gaining a magnified visualization of the advantages and disadvantages entailed by using various leaching reagents. The metal leaching rate is annotated as:

$$r_M = W_M \times a \times R/t \quad 2-8$$

where r_M denotes the metal leaching rate, W_M (w/w %) denotes the weight or mass percentage of metal in spent Li-ionBs cathode active materials a (%) denotes the metal leaching efficiency, R (g/L) denotes the solids to liquid ratio, and t denotes the leaching time. This equation quantifies leaching efficiencies for different leaching reagents for comparison. The leaching efficiency of valuable metals typically exceeds 90%. However, to reach high leaching efficiencies, some of the processes utilise a low R or long leaching time. To analyse recycling, greenhouse gas (GHG) emissions, energy consumption, and operational cost were quantified using stoichiometric consumption of materials under the assumption that 1 kg of Co is leached from spent Li-ionB cathode active material by various leaching processes (Lv et al. 2018).

Lv et al. (2008) further stated that additional relative evaluation index data was acquired from the GREET (**G**reenhouse gases, **R**egulated **E**missions, and **E**nergy use in **T**ransportation) model developed by Argonne National Laboratory. The energy consumption, greenhouse gas emissions (GHG), and cost of organic chemicals are considerably higher, and their leaching rate is notably lower compared to inorganic reagents, as indicated in Figure 2-19. However, considering the biodegradability nature of organic leaching reagents and reduced flue gas emission from the processing, the advantages accrued from utilising organic reagents in leaching processes are quite significant in the context of environment conservation (Li et al. 2013; Lv et al. 2018). Moreover, the relevant data for H_2SO_4 about GHG emissions and energy consumption was not presented. H_2SO_4 has a substantially higher rate of valuable metal leaching than other presented reagents for a high S/L and short leaching reaction time. In addition, H_2SO_4 is usually produced as a by-product of other chemical processes in many chemical plants, i.e., copper smelting (Lv et al. 2018).

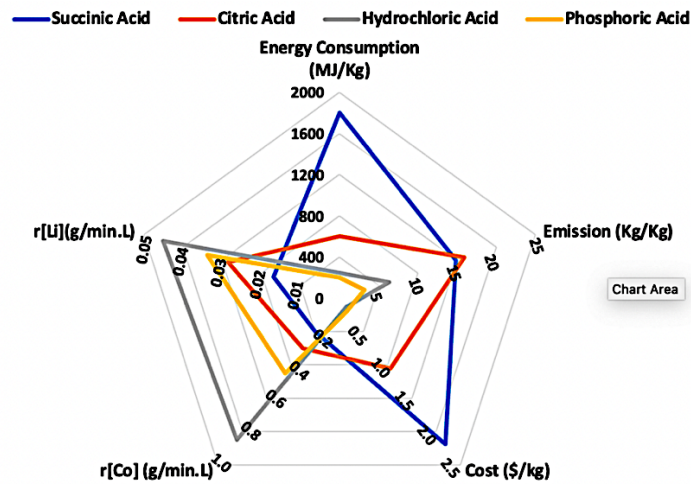


Figure 2-19: Spider chart for a relative evaluation index of leaching spent Li-ionBs with various conventional leaching reagents (Data from (Lv et al. 2018)).

In summation, the leaching performance was shown to be primarily influenced by the temperature, leaching time, solid-to-liquid ratio (S/L), agitation speed, and leachant and reductant concentration. The leaching rate and efficiency both decrease as the solid-liquid ratio (S/L) increases. However, the leaching rate and efficiency would be increased by increasing leaching time, temperature, agitation speed and concentrations of leachant and reductant (Wang et al. 2012). It should be noted that the leaching rate and efficiency would stagnate when a certain max quantity value of these factors is reached. These figures (leaching rates for each respective leachant) will guide future efforts to optimize the leaching process when processing various chemistries of Li-ionBs with different leachants.

2.5.4.2 Bio-metallurgical Process

The bio-metallurgy process utilizes microorganisms (bacteria) to treat and recover metals. The ability of microorganisms (or microbes) to transform insoluble solid materials into soluble and extractable forms is the driving factor influencing the effectiveness of a typical bio-metallurgical process (Ijadi Bajestani et al. 2014; Dominguez-Benetton et al. 2018; Biswal and Balasubramanian 2023). (*Acidithiobacillus ferrooxidans*, a chemolithotrophic and acidophilic bacteria, was employed by Mishra et al. (2008) as a leaching bacterium. The reaction operates optimally at 30 °C and a pH level of 2.5, however even with a long leaching duration with added Fe^{2+} acting as a catalyst, the leaching efficiencies of Co and Li both were rather low (Mishra et

al. 2008; Ren et al. 2009; Ijadi Bajestani et al. 2014). The Co leaching efficiency could, however, reach more than 98 % in just 7 days in an *Acidithiobacillus ferrooxidans* leaching system with 0.02 g/L of Ag⁺ as a catalyst, according to data by (Zeng et al. 2013) and Chen et al. (Chen and Lin 2009). Cu²⁺ can be employed similarly as the catalyst for the *Acidithiobacillus ferrooxidans* leaching systems. Combining diverse bacteria cultures in one system was trialled, such as acidophilic sulphate-oxidizing bacteria and iron-oxidizing bacteria systems (Xin et al. 2009, 2016). Fungal leaching has numerous advantages over bacterial leaching, including the ability to thrive across a wide pH range, tolerance for hazardous and toxic chemicals, and the ability to conduct at a high leaching rate (Ren et al. 2009; Horeh et al. 2016; Bahaloo-Horeh and Mousavi 2017). To accomplish the leaching process, various organic acids found in fungus metabolites have been employed (Ren et al. 2009; Horeh et al. 2016; Bahaloo-Horeh and Mousavi 2017; Biswal and Balasubramanian 2023).

Bio-metallurgical processes utilise less energy consumption routes under mild conditions compared to conventional processes, making them ideal environmentally friendly processes (Horeh et al. 2016). The bio-metallurgical process, however, has fatal flaws when applied in industrial production, this is due to its slow kinetics and poor pulp density. In one investigation, the pulp density went up from 1 to 4%, which resulted in a drastic fall in bioleaching efficiency for Co and Li of 52 to 10% and 80 to 37%, respectively (Niu et al. 2014). The bio-metallurgical processes are still very time-intensive even though high pulp concentration can be utilised to obtain high Co and Li leaching efficiencies by regulating leaching reaction temperature, upping the dose of mixed energy substrates, and altering the pH (Niu et al. 2014; Biswal and Balasubramanian 2023). The bio-metallurgical processes for recycling spent Li-ionBs are thus still a long way from being applied in industry, despite the fact that they offer significant energy-saving processing routes.

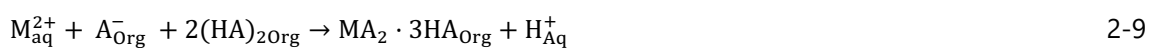
2.5.4.3 Solvent Extraction

The primary objective of the battery recycling process is the extraction of pure metal or metal-based compounds. The recycling of pure metal or metal complexes will be necessarily hampered by the coexistence of different metal ions in the leachate. Additionally, the attempt at single-step precipitation is ineffective for producing pure metals due to the overlap of the

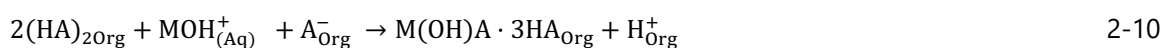
precipitation pH range of several metals. Therefore, in order to attain acceptable levels of purity, the leaching solution must go through several separations and extraction stages, such as selective precipitation, solvent extraction and electrochemical processes.

The solvent extraction process, also known as the liquid-liquid extraction process, leverages the disparity in relative solubilities of compounds in two immiscible liquids, usually polar and non-polar solvents, to separate the compounds from one another (Lv et al. 2018). Despite the challenges encountered in the separation of substances exhibiting similar functional groups, the process has proven to be reliable and robust, consequently, it is widely utilised in the extraction metallurgy sector (e.g Cobalt, Nickel, Copper, Molybdenum, Tungsten extraction and purification) and refining processes (e.g nuclear materials processing, organic compounds synthesis) (Nguyen and Lee 2016; Whitworth et al. 2022).

In solvent extraction, the equilibrium pH has a considerable effect on the selective extraction of specific metals. The di(2-Ethylhexyl)phosphoric acid (D2EHPA), for instance, is effective in extracting Cu and Mn ions but has poor selectivity for Co extraction at a pH range of 2.2–3.0 (Wang et al. 2016). The extraction of Co with the cationic extractant D2EHPA is more effective at high pH (the higher the PH the higher the extraction efficiency) (Shakibania et al. 2022). The metal extraction reaction imitates the below-highlighted mechanism (Zhao et al. 2011; Granata et al. 2012):



or



Where:

$2(HA)_{2org} + A_{org}^{-}$ represents the saponification reaction as:



At pH 4.5, the extractant PC-88A can effectively extract Ni and Co ions from a pool of numerous metal ions, however, at pH levels lower than 3, it is ineffective (Wang et al. 2016). Due to its

remarkable selectivity, Cyanex272 has received much research attention as an extractant. Swain et al. (2007) extracted 85.42% Co from the leachate at pH 5 using Cyanex 272, 5 vol% tributyl phosphate (TBP) as a phase modifier, and paraffin (kerosene) as diluents. A similar system was designed by Jha et al. (2013), although isodecanol was utilized as a phase modifier. At pH 5.0, Co extraction efficiency at over 99.9% was attained (Jha et al. 2013).

The optimal pH scales of numerous extraction reagents are summarized in Figure 2-20 (Zhang et al. 1998; Darvishi et al. 2005; Joo, Shin, Oh, Wang, and Shin 2016; Joo, Shin, Oh, Wang, Senanayake, et al. 2016; Virolainen et al. 2017). It is evident that some reagents effectively extract Ni and Co in the pH range of 3 to 5, however, the reactor must be corrosion-resistant to withstand such conditions. Cynaex 272 and P507 may be an ideal additive as it possesses the ability to alter the optimal pH for solvent extraction. For example, in Figure 2-20, the ideal pH, when the PC-88A is utilised solely to selectively extract Co, falls between 3.2 and 4.2. However, Ni extraction efficiency is low in this pH range. The addition of trioctylamine (TOA) as a phase modifier will shift and expand the ideal pH range from 3-4 to 3.5 and 5, which provides more room for adjustment of operational parameters since its greater than the previous range.

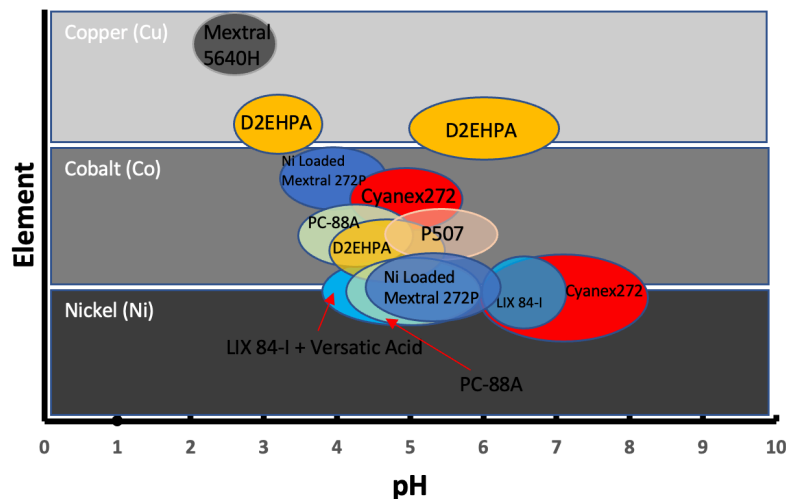


Figure 2-20: Effect of pH on the solvent extraction of Cu, Ni and Co using different extraction reagents (at 25°C and A:O = 1, except for Mextral 5640H (A:O = 2)) (Date derived from (Lv et al. 2018)).

2.5.4.4 Chemical Precipitation

In order to effectively recover specific metals from complex multi-metal solutions, through selective precipitation, a single-stage chemical method, has been extensively studied and employed. However, often, it is challenging to precipitate only one ion from a multi-metal ion solution. As indicated in the E-pH diagram depicted in Figure 2-18 (band Co^{2+}), Co^{2+} and Ni^{2+} are prone to coprecipitating via a neutralizing reaction because the stable regions of $\text{Co}(\text{OH})_2$ and $\text{Ni}(\text{OH})_2$ overlap vastly. However, Figure 2-18 (b) also demonstrates a minor overlap between the stable regions of Ni^{2+} and $\text{Co}(\text{OH})_3$. Therefore, one feasible route is to convert Co^{2+} to Co^{3+} in order to accomplish selective precipitation of Co^{3+} in this small region. Joulié et al. (2014) demonstrated the viability and efficacy of this process route. The Ni and Co recovery efficiencies both exceeded 99% when sodium hypochlorite (NaClO) was used as a reductant (Joulié et al. 2014). The reaction mechanism can be annotated as:



It should be highlighted that no Mn is present in the oxidation-precipitation process system as outlined by Joulié et al. (2014). If Mn is present, at pH 2 the Mn^{2+} is oxidized to Mn^{4+} yielding MnO_2 or $\text{Mn}(\text{OH})_4$ hydroxide according to the reaction:



In order to chemically precipitate Ni^{2+} as a nickel dimethylglyoxime chelating precipitate from mixed multi-metal solutions of Mn, Ni and Co, the dimethylglyoxime reagent (DMG, $\text{C}_4\text{H}_8\text{N}_2\text{O}_2$) is extensively employed. When DMG reagent is utilised, nearly 95% of Ni^{2+} may precipitate at ambient temperature within 20 minutes, as reported by Chen et al. (2015). The pK_{sp} values for Li^+ , Ni^{2+} and Co^{2+} are on the order of $\text{NiC}_2\text{O}_4 \approx \text{CoC}_2\text{O}_4 \gg \text{Li}_2\text{C}_2\text{O}_4$ (Pant and Dolker 2017). The predominant metal ion in leachate after Co^{2+} and Ni^{2+} are precipitated is Li^+ , which can precipitate effectively as Li_3PO_4 or Li_2CO_3 (Chen, Fan, et al. 2016).

2.5.4.5 Leaching Cathode Resynthesis

Solvent extraction (liquid-liquid extraction), chemical precipitation, and ion exchange, the conventional extraction and separation processes, are frequently not economically viable to use in industrial production due to their significant drawbacks, such as convoluted recycling routes, and high waste production and high chemical reagent consumption. Therefore, it is necessary and imperative to conduct research into less time-consuming and effective processes for recycling spent Li-ionBs. Recent research has focused on material synthesis technologies that achieve one-step recovery of metals from leachate to regenerate materials, such as the leaching-resynthesis process or direct physical process, in order to shorten the route, avoid the challenges accrued from separating metal ions from one another, reduce secondary pollution, and improve the recycling efficiencies of valuable metals (Sa et al. 2015; Yang, Huang, Xie, et al. 2016; Yang, Huang, Xu, et al. 2016). The leaching-resynthesis process, which is a subset of regeneration processes, resynthesizes the electrode materials in fewer steps through sol-gel or coprecipitation process routes.

In one study, Sa et al. (2015) employed leachate solution as raw liquor and a conventional coprecipitation process to regenerate NMC ($\text{LiNi}_{1/3}\text{Mn}_{1/3}\text{Co}_{1/3}\text{O}_2$) in an N_2 atmosphere at ambient temperature. The specific capacity of the regenerated cathode active material falls to 80% (120 mAh/g) after 50 cycles. Li et al. (2012) used ascorbic acid for leaching and adjusted the pH and metal ion ratio of the leachate to produce regenerated cathode active material $\text{LiCo}_{0.33}\text{Ni}_{0.33}\text{Mn}_{0.33}\text{O}_2$ through a sol-gel process (Li et al. 2012). A similar method was employed by Zou et al. (2013) to recover and recycle spent cathode active materials and produce high electrochemical performance regenerated cathode active materials. The regenerated cathode active materials exhibited electrochemical similarities to those of commercial batteries in terms of rate capacity and cycle life, which should be underlined (Zou et al. 2013; Yao et al. 2016). Among these, the regenerated cathode active materials recovered through ascorbic acid leaching processing exhibit much better electrochemical characteristics than their respective counterparts synthesized from other processes (Yao et al. 2016; Lv et al. 2018). Other than that, the research data indicates that cathode-active material from various leachates exhibits few electrochemical property differences (Lv et al. 2018).

An alternative ideal process route that has been extensively developed by numerous researchers is the synthesis of various reactive materials from the Li-ionB waste in addition to regenerated cathode active materials. To synthesize sintered or hydrothermal cobalt ferrite (CoFe_2O_4) precursor, Yao et al. (2016) demonstrated a straightforward process route that comprised pre-treatment, H_2SO_4 leaching, filtering, sol-gel, and calcination methods (S- CoFe_2O_4 or H- CoFe_2O_4). The reactive materials produced exhibit superior physicochemical properties in terms of train derivative coefficient ($1.69 \times 10^{-9} \text{ 1/A}$) and magnetostriction coefficient (158.5 ppm) (Yao et al. 2016). The low train derivative coefficient indicates a high degree of stability and less sensitivity to current fluctuations and the relatively moderate magnetostriction coefficient indicates the material's ability to undergo mechanical deformation in response to magnetic fields.

Direct recovery is a process of recovering valuable components from spent Li-ionBs without using complex chemical processes (Dunn et al. 2012; Yang et al. 2018). Prior to processing spent Li-ionBs, they were disassembled into multiple individual cells. After that, supercritical CO_2 was used to treat the individual cells, and the electrolytes were drained and stored. It is possible to extract CO_2 from the electrolyte by reducing the pressure and temperature thereby regenerating the electrolyte. The cells were then broken apart, sorted, and disassembled. In the end, the cathode active material was gathered, cleaned and repurposed (Huang et al. 2018; Zhang et al. 2019; Zhou et al. 2020).

Chen J et al. (2016) reported a process route to directly regenerate LFP from spent soft-pack Li-ionBs. In the case of no recovery of electrolyte, the spent Li-ionBs were disassembled, crushed and cleaned in the sealed box. The residual PVDF binder and material decomposition after thousands of charge and discharge cycles lower the energy density of recovered LFP material and its electrochemical performance. The electrochemical performance of the regenerated electrode was enhanced after heat treatment at 650°C , discharging nearly the same nominal capacity and energy density as the starting novel cathode active material (Chen, Li, et al. 2016).

Song et al (1999) sintered the spent cathode active materials with fresh cathode active materials to regenerate LFP electrode materials from spent Li-ionBs. The electrochemical performance of the regenerated LFP battery cathode active material is nearly equal to that of

a fresh LFP cathode active material . (Song et al. 1999). Zhang et al. (2019) recorded a recovery efficiency of cathode active materials of 98.2% when recovery was executed through direct pyrolysis and physical recovery. The advantages of a direct physical recovery process are primarily minimal energy use, quick recovery pathways, environmental friendliness, and a high recovery rate. However, it is unclear whether the recovered cathode active material will match the long-term properties of a typical fresh active cathode material (Zhang et al. 2019).

2.5.4.6 Electrochemical Process

Myoung et al. (2002) potentiostatically reduced Co ions, from waste LCO by using a HNO₃ leachant solution, into Co(OH)₂ on a titanium cathode in an electrochemical set-up (Myoung et al. 2002). CoO was subsequently precipitated via a dehydration process. When subjected to ideal pH circumstances and accurate CoO heat application, island-shaped Co(OH)₂ particles were produced on a titanium (Ti) material (Hanisch et al. 2015; Chandran et al. 2021). Swain et al. (2007) recovered cobalt from spent Li-ionBs by employing H₂SO₄ leaching and electroreduction (Swain et al. 2007). Over 98% of Cobalt was dissolved in an acid leachant with a concentration of 10 M at 70 °C for 60 mins. The leachate liquor was purified by the hydrolysed deposition processed at the interval between pH 2.0 and 3.0 at 90 °C.

Lowering dissolved oxygen and nitrate ions could raise the local electrode pH. Therefore, with the optimum pH circumstances, Co(OH)₂ material can precipitate. Hence, this process provides an ideal route to improve LiCoO₂ production from cobalt oxide. Co-remediation by electro-winning and sulphuric acid leaching was studied and demonstrated by Sharma et al. (Sharma and Das 2019). Approximately 99% of the cobalt in the spent Li-ionBs was dissolved at a temperature of 70 °C for 60 mins with a 10 mol/L H₂SO₄ concentration. In the pH range of 2.0-3.0 and at 90 °C, hydrolysed deposition cleans the leachant. Cobalt cathode was effectively deposited at a current density of 235 A/m² (Jeffrey et al. 2000a; Sharma et al. 2005a; Mulaudzi and Kotze 2013).

This electrochemical methodological approach is deemed feasible and viable for the industry scale-up. The electroreduction mechanism is worthy of exploring due to the relatively high recovery of pure cobalt from spent Li-ionBs. It does not add specific stimulants and it removes impurities in comparison to several hydrometallurgical processes for metal recovery from spent

Li-ionBs (Ordoñez et al. 2016). Nevertheless, this approach has the drawback of being extremely energy-intensive.

2.5.5 Product Recovery

The final product stream, after the metal dissolution process, constitutes metal ions (i.e. Co^{2+} , Li^+ , Ni^{2+} , Mn^{2+}). The successful recovery and separation of these valuable metals, therefore, require a product recovery phase. Chemical precipitation, also known as selective precipitation, and solvent extraction (liquid-liquid extraction), are two often widely separation and recovery processes (Zheng et al. 2018; Phuc Anh LE 2019; ESI-Africa 2021). Notably, the by-products of the hydro or bio-metallurgical processes are essentially leachate, whereas the by-products of the pyrometallurgical process are subjected to acidic dissolution so as to be converted to leachate.

Liquid-Liquid extraction, also known as solvent extraction, is a methodology that separates metallic compounds based on the difference of their relative solubilities in two immiscible liquids while chemical or selective precipitation employs a specific reagent that can precipitate specific metal ions while leaving impurities or undesirable compounds in the aqueous solution (Nayaka, Pai, Santhosh, et al. 2016a; de Oliveira Demarco et al. 2019; Othman et al. 2020). In order to effectively recover Ni, Co, and Li, there have been numerous studies and reports targeting the recycling of spent Li-ionBs. To effectively recover metals from leachate solution after metal dissolution, regulation of the pH of the leachate and employing various precipitants (e.g. NH_4OH , NaOH and Na_2CO_3) is necessary for optimising selective precipitation. NaOH is still the widely utilised precipitant, though several organic solvent systems are being used to study solvent extraction (e.g. Cyanex 272, PC-88A, saponified P507, etc.). The target metals were recovered with an overall recovery efficiency of 85% and a minimum leaching efficiency of 90% (Othman et al. 2020).

2.5.6 Product Preparation

Purification and preparation of recovered products for subsequent steps are the main goals of this step (e.g., commercial sales as construction materials, synthesis of new active cathode materials etc.). Purification, crystallization, dewatering, and oxidation stages are then employed

to formulate a stable solid-state from the products obtained through the product recovery steps (Georgi-Maschler et al. 2012; Zheng et al. 2018; ESI-Africa 2021). Following the recovery and preparation processes, they are categorized for various reasons. Valuable components can be used for the synthesis of new active cathode materials (e.g., NMC, LFP, LCO etc) or commercial sales for other applications (e.g., pure Li, pure Ni, pure Co etc). The recovered materials can also be used in the steel industry or building materials (Ordoñez et al. 2016; Sun et al. 2017).

2.5.7 Industrial Developed Processes

Umicore Process

One of the most widely applied industrial recycling techniques for spent Li-ionBs and NiMH batteries is the Umicore battery recycling process. The process doesn't entail any pre-treatment for spent batteries. The Umicore process combines hydrometallurgical and pyrometallurgical unit activities (Jinyue Yan 2015; ESMAP 2022). The primary goal of this recycling process is to recover alloys of Co, Ni and Cu. The slag portion of the process is used to recycle Li and rare earth elements. The simplified flow chart below (Figure 2-21) illustrates the Umicore recycling process.

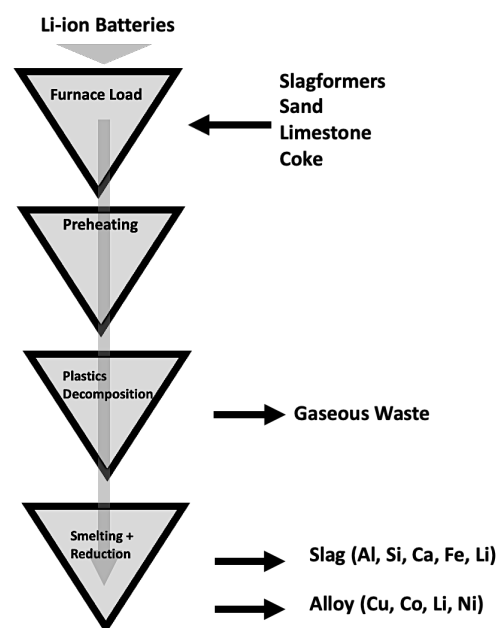


Figure 2-21: Process flow diagram for the Umicore process.

The Isa Smelt furnace technology is used in this process route to lessen the need for mechanical pre-treatment of spent batteries. There are three distinct temperature zones in the furnace when it is in use:

The top pre-heating zone: In order to evaporate battery electrolytes, the temperature in this zone must be kept below 300 °C. Explosion risks from dangerous compounds in electrolytes are reduced by gradual heating to the desired temperature.

The middle pyrolyzing zone: A temperature of roughly 700 °C is maintained in this zone to remove plastic from spent batteries. This exothermic removal process also supplies heat energy to the top zone.

The bottom smelting zone: The purpose of this zone, which has a temperature range of 1,200–1,450 °C, is to separate the remaining battery components through the alloy and slag phases. The alloy phase is made up of cobalt, copper, nickel, and iron, whereas the slag also contains various metal oxides including Li oxides.

The alloy goes through several hydrometallurgical operations, and the removed slag is sold for use in construction. Ni, Co, Zn, Cu, and Fe are then dissolved and precipitated to help the material transition out of the alloy phase. Ni and Co are recovered as nickel hydroxide (Ni(OH)₂) and cobalt chloride (CoCl₂), respectively. The fresh LiCoO₃ cathode active material can then be made by oxidizing CoCl₂ and burning it with LiCoO₃ (LCO). The absence of mechanical battery pre-treatments and the high rate of valuable metal components (such as nickel and cobalt) recovery are the key advantages of this process.

Toxco Process

The Toxco process for recycling spent Li-ionBs is based on hydrometallurgy. This process involves pre-treating the battery, separating the components, leaching, purifying the solution, and precipitating the Li (Jinyue Yan 2015; ESMAP 2022). The Toxco battery recycling process flow sheet is depicted in Figure 2-22.

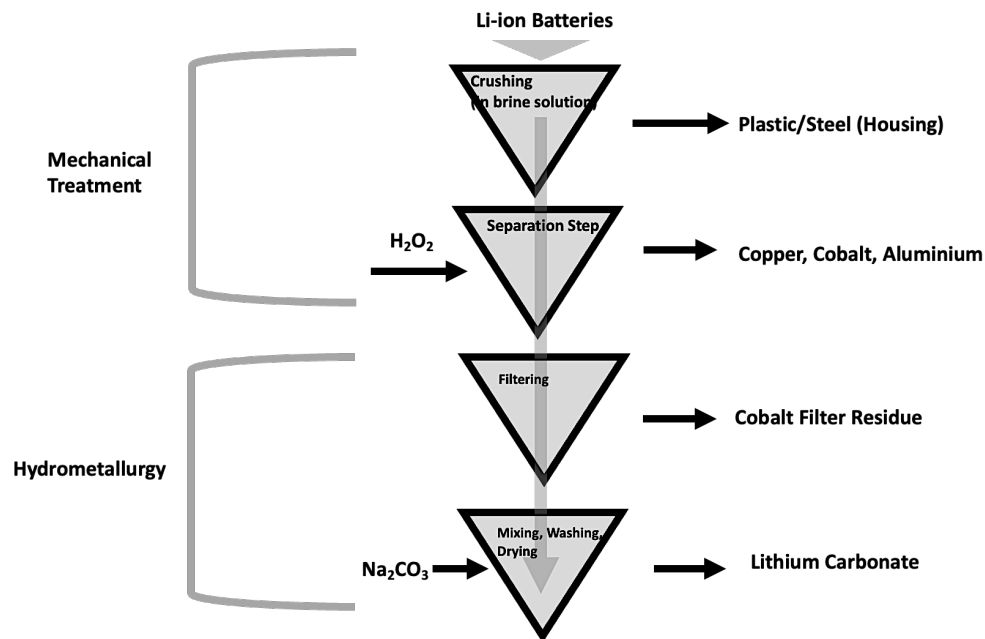


Figure 2-22: Toxco process flow diagram (Jinyue Yan 2015).

Spent batteries are cooled to approximately -175 to -195°C using liquid nitrogen in a proprietary pre-treatment process involving cryogenic cooling (AL Shaqsi et al. 2020; ESMAP 2022). This temperature range effectively brings the reactivity of Li-ionB components below the threshold for an explosion. Additionally, at this cryogenic temperature, the plastic case of spent Li-ionBs becomes brittle, making them susceptible to breakage. The batteries are then crushed in a Li brine after being torn and put through a hammer mill. During hammer milling, the Li component dissolves to produce a solution of LiCl , LiSO_3 and Li_2CO_3 .

The screw press integrated inside the hammer mill separates the Li solution and undissolved products. The so-called fluff and the Li solution's undissolved components, such as fine carbon and metal oxide, necessitate additional treatments. After that, the fluff is sent through a shaking table to separate the high-density Co-Cu mixture from the low-density stainless steel and plastic mixture. All of these products are packaged and available for purchase. Before filtration, the Li solution is kept in a holding tank. In order to prevent contamination of the Li product with Na, $\text{Li}(\text{OH})_2$ is used to modify the pH of the solution rather than sodium hydroxide. To produce the finished product, Li_2CO_3 , the solution in the holding tank is dewatered, compressed with filters, and purified.

INMETCO Process

The International Metals Reclamation Company (INMETCO) battery recycling process applies a pyrometallurgical process for recovering valuable metallic material from spent batteries (Jinyue Yan 2015; AL Shaqsi et al. 2020; ESMAP 2022). The process entails three stages: (1) feedstock preparation, mixing and pelletising, (2) component reduction; and (3) melting and alloy casting.

The spent Li-ionBs are first discharged, dismantled, stripped of the plastic casing, drained of their electrolytes, and the remaining components shredded. The remaining solid waste is assorted with a carbonaceous reductant. The liquid wastes of Ni and Cd are added to the solid waste mixture as it is pelletized. These pellets are then combined with shredded spent battery components before being channelled into the reduction stage. The reduction stage is carried out at 1260 °C for approximately 0.5 hours to reduce metal oxides to their pure metallic state. The gas emitted from this reduction phase is scrubbed and the outlet scrubbing liquid is then fed to the wastewater treatment facility. The treated water from the wastewater treatment facility is circulated back to the scrubbing process for reuse. The reduced solid mixture is smelted to produce an alloy containing Ni, Fe, Cr, and Mn. The alloy is cast to make pig alloy, which is then further processed to make stainless steel in the stainless-steel industry.

Overall, these hybrid processes plant setups, recycling research, and strict recycling laws (e.g., in China, and Europe) show major efforts to recycle spent batteries. The current recycling rate for spent Li-ionBs is just about 5%, as was previously stated (CSIRO 2022; ESMAP 2022), this means current battery recycling processes for recycling are incapacitated to handle disposed Li-ionBs amount especially in the coming years when the battery waste is expected to reach enormous figures as pr(Lander et al., 2021; Islam & Iyer-Raniga, 2022; Velázquez-Martínez et al., 2019)Velázquez-Martínez et al., 2019).

Furthermore, the amount of alloy metals that can be recovered using the above-stipulated process routes from spent Li-ionBs is relatively minimal (e.g., Ni, Co, Cu). The resultant slag still has a significant proportion of unrecovered valuable components and is sold at low costs as construction materials. Attributable to their high energy requirements, as well as their high costs for collection and transportation, INMETCO recycling processes are less economically attractive (Zheng et al. 2018; de Oliveira Demarco et al. 2019; CSIRO 2022). In order to upsurge

revenue and draw additional investment for the recycling of the spent Li-ionB waste, it is important to improve the quality of recovered products from the recycling process (i.e., recycling spent Li-ionBs into pure, effective, and valuable components). Because of the enormous amount of spent Li-ionBs projected in the coming years, more capacitated recycling facilities will be required. As a result, developing a comprehensive and efficient recycling system for extracting and recovering valuable metals from spent Li-ionBs is critical to achieving global sustainability.

2.6 Electrometallurgy

2.6.1 Overview

In contrast to pyro- and hydrometallurgy, which have a long history, electrometallurgy is a relatively underdeveloped technology that was born just after the discovery of electric current in the nineteenth century. In 1800, Alessandro Volta made the first electric pile and in the same year, Carlisle and Nicholson used Volta's pile to decompose water into hydrogen and oxygen. Humphry Davy in 1807 officially was the first one who used the knowledge in electrochemistry for metallurgical aims. He decomposed sodium and potassium from caustic soda and caustic potash in a large battery and, for the first time, identified these two elements as metals.

His assistant, Michael Faraday, in 1830 found relationships between the current and the amount of deposited material. Since then, considerable developments in the purification of metals via electrometallurgical methods have been achieved. Nowadays, it is difficult to imagine the production of aluminium from bauxite using methods other than electrometallurgy. More than 50 percent of copper and zinc are similarly produced and purified by electrometallurgical processes. There is also a huge interest within different metal industries to shift already well-established pyrometallurgical routes to electrometallurgical ones (Mulaudzi and Kotze 2013; Halli et al. 2020).

Generally, there are four main categories under electrometallurgy namely electrowinning, electrorefining, electroplating and electroforming (Abbey 2019). The extraction of metals from aqueous solutions or their salts is called electrowinning while electrorefining is the purification of metals by anodically dissolving the impure metals followed by cathodically depositing the pure metals. Electroplating is used to modify the surface of metals (and in some cases non-

metals) in order to improve appearance or corrosion and abrasion resistivity. A special branch of electroplating, in which the electroplated metal can be removed from the cathode as an entity, is called electroforming.

In this chapter, a short introduction about the principles and concepts of electrowinning, in general, will be given. Then, variable aspects of Co/Ni electrowinning, from theoretical aspects to practical difficulties, will be presented.

2.6.2 Electrowinning Working Principle

In metallic conductors, free electrons are responsible for the transportation of electric charge while in electrolytic conductors the charge is transferred by ions. To be able to charge the current into an electrolyte, two electrodes are needed namely anode and cathode. These two electrodes are connected to a DC power supply. A simple schematic of an electrowinning circuit, consisting of an electrowinning cell, a switch, a resistance, a voltmeter, and an ammeter, is shown in Figure 2-23. This is the simplest approach to building an electrowinning circuit.

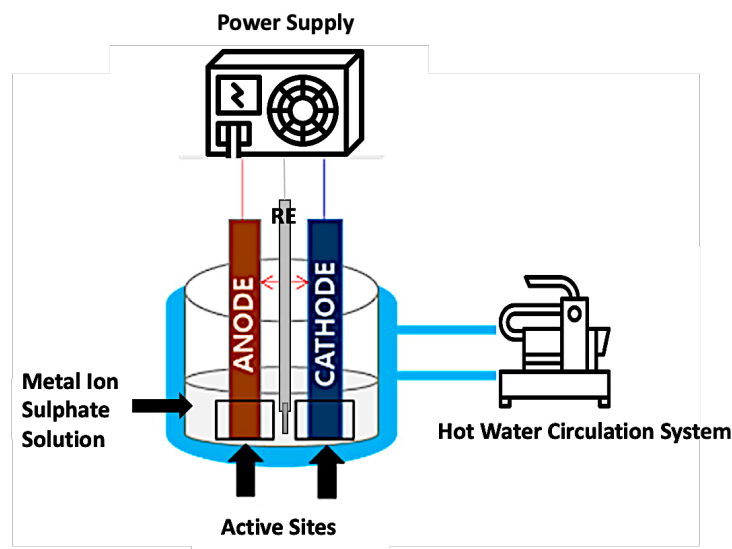


Figure 2-23: Schematic of the simplest electrowinning circuit.

To maintain a steady current in the circuit shown in Figure 2-23, electrochemical reactions should take place at the interfaces of electrolytes and electrodes. These reactions are heterogeneous reduction or oxidation reactions, which consequently result in the reduction or oxidation of compounds. Depending on the type of the electrolyte and the electrodes these

reactions can be varied considerably. However, since inert electrodes are always used in electrowinning (Halli et al. 2020), the reactions can be summarized below:

At the cathode, metal cations are always reduced by the following reaction:



and at the anode, the following reactions take place:



2.6.3 Faraday Law

In 1830, Faraday formulated the relationship between the amount of deposited material, the quantity of electricity and the chemical equivalent weight of the metal which was expressed in the below form (Sharma et al. 2005a; Abbey 2019; Halli et al. 2020):

$$m = \left(\frac{M}{n}\right) \frac{It}{F} \quad 2-18$$

where m is the amount of deposited metal, M is the atomic weight of the metal, n is the valance of the metal, I is the amperage of the electrical current and F is the Faraday constant which is equal to 96485 [A.s] (Seyed Mohammad Khosh Koo Sany 2009).

2.6.4 Current Efficiency

The ratio between the weight of the deposited substance obtained by electrowinning and that calculated by faraday law is known as the current efficiency as annotated by the equations below:

$$\eta = \frac{m_o}{m_e} \times 100 \quad 2-19$$

and:

$$m_e = \frac{Mit}{NF} \quad 2-20$$

Where m_o is mass obtained from electrowinning, m_e is the calculated expected mass, M is molar mass, I is the current in amperes, t is the time in seconds, N is the oxidation state and F is the faradays constant.

Current efficiencies are not always 100 percent, and this does not mean that the application has failed. It only indicates that there are also some other electrochemical reactions that the current takes part in. These reactions, depending on the type of electrolytes and electrodes, are the evolution of hydrogen, the interaction of anode and cathode products, the electrolytic reversal of electrode processes, the interaction of the product with the electrolyte and the interaction of anode components with the electrolyte (Sharma et al. 2005b, 2005a).

2.6.5 Electrode Potential and Nernst's Equation

From a thermodynamic point of view, the change in free energy of reaction 2-15 must be negative in order to forward the reaction towards the production of metal on the cathode (Mulaudzi and Kotze 2013; Abbey 2019).

$$\Delta G = G_{Me} - G_{Me^{n+}} \quad 2-21$$

However, G is positive, and metal always tends to dissolve in the electrolyte. Therefore, a driven force in the form of an electrical current should be applied to make the reaction 2-15 happen.

$$\Delta G = -nEF \quad 2-22$$

E is called electrode potential and in practice, it is the voltage applied to the cell.

Nernst's equation suggests the measurement of electrode potential at any concentration of dissolved metal, Me^{n+} :

$$E = E^0 - \frac{RT}{nF} \ln + |Me^{n+}| \quad 2-23$$

Where E^0 is the standard electrode potential and is defined as the voltage of the reduction reaction of one molar solution at 25 °C against the hydrogen standard electrode.

2.6.6 Cell Voltage and Energy Consumption

Also known as cell potential, cell voltage is the sum of the electrode potential difference between anode and cathode, absolute values of anode and cathode overvoltage's (η_A and η_C) and total ohmic electric resistances (Seyed Mohammad Khosh Koo Sany 2009):

$$V_c = E_A - E_C + \eta_A + \eta_C + I \sum R \quad 2-24$$

Cell voltage has no theoretical significance, and it is only important for the calculation of energy consumption:

$$W = V_c I t \quad 2-25$$

By applying Faraday's law (equation 2-18) and considering current efficiency (eff), specific energy consumption, W , is calculated by equation 2-26:

$$W = \frac{W}{m} = \frac{n F V_c}{M \cdot \eta_{eff}} \quad 2-26$$

Where m is the specific energy consumption, M is the atomic weight of the metal, n is the valance of the metal, I is the amperage of the electrical current, η_{eff} is the current efficiency, V is the cell voltage, and F is the Faraday constant.

2.6.7 Metal Electrodeposition

According to Faraday's law, the only important factor in the determination of metal deposition rate is the quantity of electricity and other factors like temperature, concentration, flow rate, etc. do not play any role in this regard. Nevertheless, these factors along with some others are responsible for the character of the electrowon metal.

Nucleation and crystal growth are two phenomena that take place during metal deposition on the surface of the cathode (Oluwatosin Abegunde et al. 2019). If the nucleation rate is larger than the rate of growth of crystals, the deposited metal will be powdery. Conversely, if the crystal growth rate is high relative to nucleation rate, the metal deposit will be coarse-grained. When the process is diffusion controlled, i.e. the concentration of metal ions at the interface is close to zero, nucleation dominates the metal deposition, and the product will be fine powder.

On the other hand, if the electrochemical reactions are chemically controlled, then the rate of crystal growth will be higher and, again, the coarse-grained metal will be formed on the cathode.

There are a number of factors in electrowinning processes, which affect the concentration of metal ions at the interface (Seyed Mohammad Khosh Koo Sany 2009; Abbey 2019):

Current Density: At low current densities, the electrochemical reactions occur at a slow rate and the process is controlled chemically. Consequently, a coarse-grained crystallization occurs on the cathode. At high current densities, the electrochemical reactions are occurring rapidly, and the process is un-controlled chemically. Consequently, irregular crystallization occurs on the cathode.

Concentration of electrolyte: When the concentration of metal ions in the electrolyte is low, the movement of these ions towards the electrode surface is slow and primarily controlled by diffusion (movement of ions from higher to lower concentrations), resulting in metal deposits that tend to be in granular form rather than forming a solid, continuous layer. Conversely, when the concentration of metal ions is high, the process is not limited by diffusion, allowing for the formation of a more solid or dense product instead of a powder.

Temperature: Temperature has an effect similar to the concentration. When increasing temperature, diffusion increases, and the rate of crystal growth will be greater than the nucleation rate. As a result, coarse-grained deposition is favoured.

Stirring of bath: By stirring the electrolyte, the thickness of the double layer is decreased, and the diffusion rate will rise. This will result in the production of coarser deposited material.

The presence of a non-reactive species: The presence of non-reactive and immobile species, which do not participate in reactions at the cathode, can reduce the diffusion rate, making diffusion the rate-controlling step. As a result, a granular deposit is likely to form.

Presence of colloidal substances: The addition of colloidal reagents such as agar, glue, gums, sugars, etc., in small amounts (0.05 g/l) has a positive effect on obtaining a smooth powdery deposition (Sharma et al. 2005b; Abbey 2019). The reason is that the presence of these particles

on the cathode hinders the crystal growth. Hence, nucleation will be the dominant process, resulting in a fine-grained deposit. More concentration of colloidal reagents causes the production of very loose metal deposition on the cathode.

2.6.8 Electrowinning of Co and Ni

2.6.8.1 Electrolyte Formulation

To formulate the electrolyte medium, the cathode metals, specifically Li, Mn, Co and Ni, can be successfully extracted (leached) from the cathode powder of spent batteries by dissolving these metals into their respective metal-ion rich solution using leaching agents (usually inorganic or organic acids) (Urbańska 2020). The most commonly investigated leaching agents utilised also at the initial stages of hydrometallurgical development of metal recovery from spent Li-ionBs, are inorganic acids—mainly sulphuric acid (H_2SO_4), but also hydrochloric acid (HCl), nitric acid (HNO_3), and phosphoric acid (H_3PO_4) (Wang et al. 2012; Barik et al. 2017b; Pinna et al. 2017b; Golmohammadzadeh et al. 2018; Peng et al. 2018; Urbańska 2020). The utilisation of strong acids yields high leaching efficiency, and hence a high metal recovery degree while maintaining optimal conditions for the process (Peng et al. 2018).

Apart from technological advantages, inorganic acids are also relatively inexpensive reagents, thus they can be used on an industrial scale (Urbańska 2020). However, very low pH levels during leaching may lead to accelerated wear and tear (corrosion) of the equipment. Another issue to be considered is waste management, namely the battery powder contaminated with mineral acids obtained by leaching. Moreover, during inorganic acid leaching, there is a certain probability of the release of gases posing a danger to human health and the environment, particularly, Cl_2 , SO_3 , or NO_x (Wang et al. 2012).

The frequently accrued problems resulting from the utilisation of inorganic acids in the leaching process of spent Li-ionBs have induced a necessary search for effective alternatives whose application won't be hazardous to human health and the environment (Urbańska 2020). The search for a non-hazardous alternative has led to research on the utilisation of organic acids as leaching agents (Golmohammadzadeh et al. 2018). In recent years, citric acid has been the most frequently investigated organic acid-leaching agent (Urbańska 2020).

Additionally, recent research has shown that the following acids have been tested as the leaching agent: succinic, aspartic, lactic, formic, tartaric, oxalic, acetic, malic, maleic, iminodiacetic, adipic, and nitrilotriacetic (Li et al. 2015b, 2017; Zeng et al. 2015b; Nayaka, Pai, Santhosh, et al. 2016b; He et al. 2017b; Golmohammadzadeh et al. 2018; Zheng et al. 2018). It has been shown that it is possible to successfully recover metals from battery powder from spent Li-ionBs using organic compounds as leaching agents, however, the leaching efficiency is still low, the reactions during the process are slower (longer contact time) and organic acids partially ionises compared to the case of experiments where the leaching agents were inorganic acids.

The utilisation of organic acids reduces the corrosion risk to equipment, and they are also safer for the people involved in this process (Golmohammadzadeh et al., 2018). Additionally, during organic acid compound leaching, secondary contamination hardly ever occurs. However, the price of reagents may pose a problem: they are more expensive than the inorganic acids, hence their use may increase the operating costs of industrial installations. Moreover, in the literature, there are frequent indications that it is difficult to precisely determine chemical reactions taking place during leaching with organic acids, and thus also in determining particular products resulting from these reactions, due to the high probability of forming various compound organic complexes and semi-products in the process (Zeng et al. 2015b; Nayaka, Pai, Santhosh, et al. 2016b; He et al. 2017b; Golmohammadzadeh et al. 2018).

Most frequently, the acidic leaching of spent Li-ionBs is enhanced with the introduction of additives, the so-called reducers (Urbańska, 2020). The utilisation of additives transforms the metals, which are part of battery powder, into a divalent form that is soluble in acidic solutions (Wang et al. 2012). In the case of a LiCoO_2 cathode, it has been demonstrated that the addition of a reducer has the highest influence on cobalt ions (i.e., during leaching the cobalt valence state changes from Co(III) to Co(II)) (Urbańska 2020). In effect, metal recovery may be higher (>95%) and the concentration of used acids is lower. The most common compound used as a reducer in the process of battery powder acidic leaching is hydrogen peroxide (H_2O_2), which was repeatedly dosed in experiments where it was combined with acids, both inorganic and organic are used as leaching agents (Wang et al. 2012; Barik et al. 2017b; Pinna et al. 2017b; Peng et al. 2018; Urbańska 2020).

Researchers investigated the reducing properties of sodium bisulphite (0.075 M NaHSO₃), ammonium chloride (0.8 M NH₄Cl), sodium thiosulphate (0.25 M Na₂S₂O₃), and organic compounds like ascorbic acid (0.11 M C₆H₈O₆), glucose, sucrose, and cellulose combined with sulphuric acid as a leaching agent (Wang et al. 2012; Zeng et al. 2015b; Ku et al. 2016b; Meshram et al. 2016a; He et al. 2017b; Chen et al. 2018; Urbańska 2020). In the experiments in which the leaching agent was an organic acid, a commonly used reducer, apart from hydrogen peroxide, was 0.02 M ascorbic acid, whose presence in the leaching process has proved to improve the efficiency (>97%) of metal recovery, especially cobalt (Zheng et al. 2018). Nevertheless, electrowinning or electrorefining of Co and Ni in acidic media has gained traction as an interesting subject for further investigations.

2.6.8.2 Electrochemistry of the Electrowinning Process

In order to optimise the electrowinning process, it is necessary to understand the electrowinning electrochemical behaviour of Li-ion cathode metals (Li/Mn/Ni/Co). Co and Ni are the critical component in most Li-ionB technologies. The main aim of any Co/Ni electrowinning process is to produce a dense high-purity deposit under conditions which optimise the current efficiency and power consumption. Trimmed nickel sheets and stainless-steel have been widely utilised as anodes, however, they are costly and possess a low contact surface area-mass ratio (Mulaudzi and Kotze 2013). Pure Pb has solely been utilised as cathodes in the electrowinning of Co (Sharma et al. 2005a, 2005b; Mulaudzi and Kotze 2013). Besides high toxicity and its costly nature, researchers haven't found alternatives to replace Pb anodes. It is noteworthy that not much work has been done on electrowinning electrodes.

Co/Ni electrowinning has been tried from both alkaline and acidic electrolytic media. There are several researchers who have utilised acidic cobalt solutions as electrolyte mediums (Sharma et al. 2005a; Mulaudzi and Kotze 2013). Reduction potentials for Cu (0.34 V) and Ni (-0.25 V) are also more positive compared to Co (-0.28 V), hence reduction of Cu and Ni is thermodynamically more favourable than that of Co, therefore these metals co-deposit with Co, resulting in low current efficiency for Co metal production and impure Co metal (Sharma et al. 2005b, 2005a; Mulaudzi and Kotze 2013).

Production of Co/Ni from alkali media proceeds according to the following general electrochemical reactions:

Cathode



Anode



Unfortunately, for the cobalt deposition reaction (Eq 2-27), hydrogen evolution (Eq 2-29) almost always accompanies cobalt deposition, resulting in:

- a) Reduced current efficiency and higher power costs.
- b) An increase in pH at the cathode surface, which in turn can cause cobalt hydroxide precipitation.

The precipitate can be incorporated into the deposit and/or can cause blocking of the cathode surface.

- c) Hydrogen incorporation in the deposit. This may cause hydrogen embrittlement of the electrodeposited cobalt; and
- d) The formation of streak marks along the cathode surface.

Consequently, minimising hydrogen evolution is critically important in the cobalt electroplating process.

Another problem with hydrogen evolution is that using standard electrochemical techniques, it is difficult to distinguish between the reduction of Co^{2+} and H^{+} .

The reduction of H⁺ ions at the cathode results in a rise in pH while the generation of H⁺ ions at the anode results in a decrease in pH. If the anolyte and catholyte are allowed to mix, then, in normal Co electro-winning where the current efficiency for Co deposition is in the range of 90%, the pH of the electrolyte will drop (Sharma et al. 2005a). Similarly, the Co strength of the electrolyte will also deplete. If the above three reactions are the only reactions taking place, then the drop in pH is proportional to the Co ion depletion. Therefore, if Co(OH)₂ is added to this solution, then, when the pH of the solution is restored, the Co strength of the solution will also be restored (Sharma et al. 2005b; Mulaudzi and Kotze 2013). Thus, restoring the pH is an effective method of regenerating the bath with respect to both the pH and the Co concentration.

However, other reactions do take place at the electrodes, the prominent amongst these being (Jeffrey et al. 2000a; Sharma et al. 2005b).



Most of the Co³⁺ ions deposit at the anode as a black oxide/hydroxide powder. The probability of a small fraction reaching the cathode cannot be ruled out. The presence of multivalent ions in the electrolyte affects the nature of the deposit. However, in the purified solutions used in this investigation, the activity of other ions was very low and their discharge at the electrodes could be neglected. Similarly, reaction 2-16 could also be neglected because the Co oxide deposited at the anode was only a small fraction of the Co deposited at the cathode (Sharma et al. 2005b).

Parameters for the electrowinning technique are generally categorized into electrochemical and physical parameters. Some electrochemical parameters include the composition of electrolyte, temperature, current density, concentration of soluble impurities, type and amount of additives, presence of suspended solids and electrical conductivities. On the other hand, physical parameters are cell arrangements, anode- cathode distance, current distribution, electrode cleanliness, deposition time and electrolyte flow (Sharma et al. 2005a; Abbey 2019).

Finally, at the end of the process, the performance of electrowinning can be judged by evaluation of different indicators such as purity of the electrowon deposit, current efficiency, morphology of the deposit and so on. For electrowinning of Co in alkaline solutions, the main

parameters are the initial concentration of Co in the solution, concentration of free electrolyte (NaOH, H₂SO₄ etc), batch temperature of the electrolyte, current density, as well as agitation (or flow rate. In some older studies, other parameters like the material of the cathode and anode, and the distance between them have been discussed (Jeffrey et al. 2000a; Seyed Mohammad Khosh Koo Sany 2009; Mulaudzi and Kotze 2013). However, it is presently known that the electrode distance has no effect on the purity of deposited Co. The conventional best cathode material for electrowinning is established to be stainless steel due to its respective ease of stripping.

It is important to find out the relation between each single parameter and a performance indicator. However, owing to the complexity of inter-relationships between the parameters and performance indicators listed above, it would be very difficult to achieve this goal. This complexity is pointed out by Sharma et al. (2005) under two main categories:

- A specific setting for a parameter may improve one performance indicator at the expense of another. For instance, an increase in temperature raises the quality of the deposit, but it also lowers the current efficiency and purity.
- There is an unknown synergetic cause-effect between the parameters. This makes it difficult

The anode is usually titanium oxide, lead or graphite (Jeffrey et al. 2000a; Halli et al. 2020), The electrolyte is the acidic solution of metal ions. The cathode is usually made of stainless-steel sheets and the anode is conventionally made of lead (Pb) sheets (Mulaudzi and Kotze 2013; Halli et al. 2020). The anode made of Pb usually suffers from sludge accumulation and severe corrosion during electrowinning which consequently affects the overall energy formation and cost of operation (Elsherief 2003; Wang 2006; Ferreira et al. 2009b; Lu et al. 2018).

Inorder to fully comprehend the complexity of the influence of multiple input parameters on one or more variables, the techniques of Design of Experiments (DOE) can be used to design a series of goal-oriented experiments, enabling the application of statistical models to analyze the data extracted from these experiments. This will be discussed in the next chapter where some theoretical aspects about the statistical method used in this project to design and analyse the experiments are given.

2.7 Summary of Review

The Li-ionB hydrometallurgical recycling process, as stipulated above, is preferred out of the various available processes because it entails low energy consumption, minimal gas emissions, and most significantly, high product purity and recovery rate (de Oliveira Demarco et al. 2019). These advantages, consequently, outweigh the high chemical usage disadvantage. In addition, the recycling process can also guarantee a good economic return when implemented at the plant level.

A variety of metal ions are also present in leachate after the acid-leaching process. In order to recover, and produce regenerated cathode active materials for commercial sales, it is necessary to separate or isolate these metal ions. Henceforth, liquid-liquid extraction (solvent extraction) and/or selective chemical precipitation are employed for that purpose as previously indicated. They both deliver high metal separation efficiency and material purity (Nayaka, Pai, Santhosh, et al. 2016a; de Oliveira Demarco et al. 2019; Phuc Anh LE 2019). These findings are identified as the starting foundations for the development of spent battery recycling processes based on the context of research outcomes.

The variation of leachant concentration, pulp density (S/L ratio), reductants and their concentration, reaction time, and especially reaction temperature can directly influence the leaching efficiency of valuable metals from spent Li-ionB cathodic materials (de Oliveira Demarco et al. 2019; Halli et al. 2020). As a result, efforts to optimize the leaching stage are required to achieve optimal extractive leaching efficiency for cathodic metals entailing low energy, chemical and time consumption.

Solvent extraction, ion exchange and selective chemical-based precipitation are all employed in the product recovery stage (Aboagye et al. 2021). Solvent extraction utilises toxic chemicals and complex process routes thus selective precipitation and ion exchange requires further investigative exploration, as a possible alternatives to solvent extraction, in order to assess the viability and effectiveness of the selective precipitation process route for metal recovery, as well as to further pursue and develop a recycling process that could easily be scaled up from laboratory scale to pilot scale and ultimately industrial scale (Aboagye et al. 2021; Chandran et al. 2021; Zhao et al. 2021b; Islam and Iyer-Raniga 2022). Solvent extraction, however, requires

the use of toxic organic chemicals as well as complicated experiment sub-process routes (Haiyang Zou 2012; Gratz et al. 2014; Piątek et al. 2021; Islam and Iyer-Raniga 2022).

Hydrometallurgical, pyrometallurgical, bio-metallurgical, electrometallurgy or mechanical unit operations are frequently combined or integrated together in conventional industrial processes to recycle spent batteries (Sharma et al. 2005b; Nayaka, Pai, Santhosh, et al. 2016a; de Oliveira Demarco et al. 2019). In section 2.5.7, well-developed hydrometallurgical and pyrometallurgical recycling processes are briefly discussed namely the Umicore process, INMETCO and Toxco Process.

Chapter 3: Experimental Methodology

3.1 Chapter Overview

This chapter provides a detailed insight into the methodology employed to address the aims and objectives in Chapter 1. This chapter describes the methodology overview (Section 3.2), the process development of valuable metal recovery from spent Li-ionBs (Sections 3.3 until 3.8) and the material and electrochemical characterization techniques (Sections 3.9 and 3.10) employed to assess their respective physical and electrochemical performance.

3.2 Methodology Overview

The extracted spent and discharged NMC (532) cathode material, obtained from the in-house Energy Storage Innovation lab Li-ion Battery Assembly Plant, was ultrasonically treated for 30 minutes after being meticulously sliced into small pieces/fragments, approximately 1 cm² in size, to facilitate the subsequent leaching of valuable metals using an inorganic acid-reductant leachant combination. *Each data point used to calculate the graphs presented in this work is an average derived from three repeated experiments for that specific data point.* Various leaching reagents are employed to address spent Li-ion, predominantly utilizing an inorganic acid as the leaching agent. Examples of such acids include H₂SO₄, HCl, or HNO₃. In comparison to all the alternatives documented in the literature, H₂SO₄ demonstrates significant recovery efficiency in NMC batteries and is more cost-effective (Chen and Ho 2018; Chandran et al. 2021; Kim et al. 2021). Consequently, H₂SO₄ was selected as the leaching agent for processing NMC cathode materials. Hydrogen peroxide (H₂O₂), which is used in this study, is utilized in NMC leaching processes due to its oxidizing properties, which enhance leaching efficiency, accelerate reaction kinetics (Chen and Ho 2018).

During the leaching experimental parameter optimisation phase, the following operating variables were explored: H₂SO₄ concentration, H₂O₂ concentration, temperature, leaching time, and solid-liquid ratio. Following optimisation, precisely 37.5g of NMC 532 cathode material was leached in 500 ml of 6 vol% H₂O₂ and 2M H₂SO₄ acid (75 g/L S/L ratio) leachant for total reaction time of 2 hrs. At leaching reaction time of 20 mins, carbon flakes, which float in the intra-leaching solution, and aluminium fragments (both from the pre-processed cathode

material fragments) were freed (washed) from the cathode matrix using the acid-reductant leachant and filtered out thereafter using a 1 mm gauze sieve before leaching is continued.

The second experimental phase comprised the electrowinning parameter optimisation phase. The single-compartment electrowinning cell consisted of a Pyrex ~350 ml jacketed cylinder with a Perspex cover holding the 3 electrodes. The cathode slot was fitted with a Metrohm rotating motor. Initial electrowinning optimisation tests were conducted in a jacketed reactor vessel using a synthetic 47.5 g/L $\text{Ni}^{2+}_{0.25}\text{Co}^{2+}_{0.1}\text{Mn}^{2+}_{0.15}\text{Li}^{+}_{0.5}$ sometimes presented as 30 g/L $\text{Co}^{2+}_{0.3}\text{Ni}^{2+}_{0.7}$ solution (made from mixing NiSO_4 , Li_2SO_4 , MnSO_4 , and CoSO_4 in 250 ml) to determine the optimal conditions for Co^{2+} and Ni^{2+} deposition. All synthetic solutions contained an unvaried 5.5 g/L of Li^{+} and 12.0 g/L of Mn^{2+} except for cyclic voltammetry experiments, which utilised pure Co^{2+} (15 g/L), Ni^{2+} (15 g/L) and $\text{Ni}^{2+}_{0.25}\text{Co}^{2+}_{0.1}\text{Mn}^{2+}_{0.15}\text{Li}^{+}_{0.5}$ (47.5 g/L) solutions.

An Aluminium plate (5052 aluminium alloy) with 2 cm² active surface area was used as a cathode. An in-house single platinum-plated titanium plate, made by the electroless Pt coating method reported by Rao & Pushpavanam (Rao and Pushpavanam 2001) with a 4 cm² exposed surface area, was used as the anode. The electroless plating method was reported in detail in section 3.5.1.2. The distance between the electrode planes is 2.5 cm, and the tip of the reference electrode is positioned 1.15 cm from the anode and 0.5 cm from the cathode, providing sufficient space for the cathode electrode to rotate. The Ag/AgCl in saturated KCl reference electrode was utilised throughout all electrowinning experiments. The effect of different electrowinning parameters (pH, temperature, potential, concentration, buffer dosage, cathode rotating speed, and Co/Ni ratio) on current efficiency and deposit composition, and quality (purity and morphology) was studied to establish optimal levels. Cyclic voltammetry studies were conducted at a scan rate of 2.5 mV/s from -1.2 to -0.2 V (vs Ag/AgCl), a temperature of 50 °C, and a pH of 4. Aluminium alloy plates with 2 cm² active surface area were used as the working electrode. A single platinum plate with 2 cm² exposed surface area was used as the anode. The anode was positioned on the opposite facial side of the cathode with the reference electrode Ag/AgCl reference electrode) in the middle.

The optimized parameters conditions (-1.15 V vs Ag/AgCl, (47.5 g/L) $\text{Ni}^{2+}_{0.25}\text{Co}^{2+}_{0.1}\text{Mn}^{2+}_{0.15}\text{Li}^{+}_{0.5}$, 50 °C, 15 g/L of monosodium phosphate, 15 g/L Na_2SO_4 , pH 4.5 and Cathode Rotating Speed

(CRS) of 40 rpm) determined using synthetic solutions were utilized in the Co-Ni composite electrowinning studies of the leachate solution obtained using an actual Li-ionB NMC532 cathode. The resulting solution of the leaching stage had a pH of approximately 0.65. After the pH increased up to 4.5 through the addition of 10 M NaOH, Fe, Al and Cu were precipitated as hydroxides. The resultant solution was filtered through 0.45 μm PTFE membrane to recover precipitates. Thereafter, the electrowinning operation, utilising optimised parameters, was conducted in a jacketed reactor vessel using a leachate solution obtained using an actual Li-ionB NMC532 cathode leachate (as electrolyte) to recover Ni-Co composite material.

Titanium was coated by platinum using the electroless deposition method by Rao & Pushpavanam, (2001) (Rao and Pushpavanam 2001). An aluminium plate with a 2 cm^2 active surface area was used as a cathode coupled with a single platinum-coated titanium plate with a 4 cm^2 exposed surface area was used as anode for the 2 $\text{cm}^2/250 \text{ cm}^3$ cathodic surface area to electrolyte volume ratio (AA/EV) set-up. The aluminium plate of (10 \times 3) 30 cm^2 surface area was used as cathodes coupled with two layered platinum-coated titanium sheets measuring 10 \times 3 cm which was used as anodes placed on opposite facial side of the cathode for the 30 $\text{cm}^2/250 \text{ cm}^3$ AA/EV set-up. The Ag/AgCl reference electrode was utilised throughout all upscaled batch electrowinning experiments.

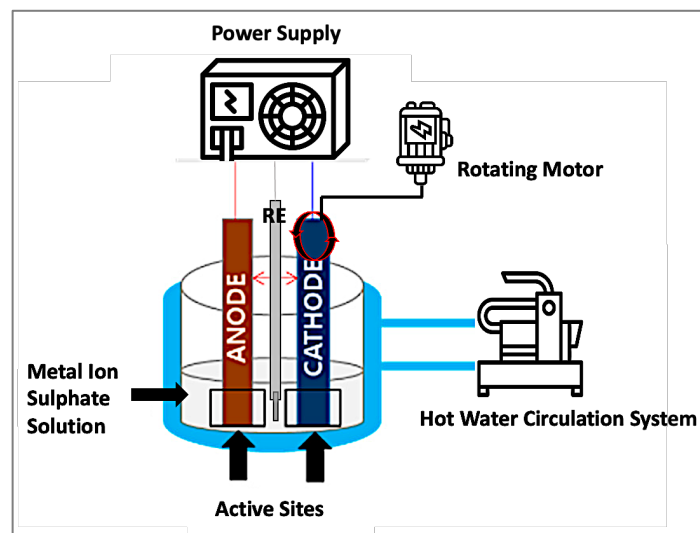


Figure 3-1: Single-compartment cell used in the different electrowinning tests.

To determine the current efficiency, the weight of the Al-cathode was measured before and after each experiment, and the difference in mass represented the mass of the deposited Co-

Ni material. However, to ensure that this mass difference accurately reflected the deposit's mass only, the cathode and the deposit were thoroughly rinsed with acetone. Then air dried using pressurized air to eliminate any traces of residual electrolyte solution adhering to the electrode-deposit matrix. The current efficiency was calculated according to the equations below:

$$\eta = \frac{m_o}{m_e} \times 100 \quad 3-1$$

and:

$$m_e = \frac{Mit}{nF} \quad 3-2$$

Where m_o is mass obtained from electrowinning, m_e is the calculated theoretical mass at 100% faradaic efficiency, M is molar mass, I is the current in amperes, t is the time in seconds, n is the oxidation state, and F is the faradays constant.

The third experimental phase comprised the recovery of valuable metals remaining in the electrowinning effluent using chemical-based precipitation. The resultant electrowinning effluent was treated with NaOH and Na₂CO₃ to recover 0.6[Ni(OH)₂].0.3[Mn(OH)₂].0.1[Co(OH)₂] composite material and Li₂CO₃ respectively. The recovery and separation process of the valuable metals from spent NMC cathode material was achieved by a two-step precipitation method. After electrowinning, the pH of the leachate solution was adjusted from 5.5 to 13 using a 10 M NaOH solution to study the behaviour of Mn, Co, and Ni precipitates at different pH levels. The following operating variables were explored: pH and temperature. During precipitation, aliquots of liquid samples were taken periodically (at every experimental variant) to determine the metal content for elemental analysis. At pH=7.8 and 20 °C, The supernatant liquid was filtered, the residue was hot air dried, and the 0.6[Ni(OH)₂].0.3[Mn(OH)₂].0.1[Co(OH)₂] composite material was obtained and stored in a dry, air-tight and inert atmosphere container. At pH=12.8 and 20 °C, The supernatant liquid was filtered, the residue was hot air dried, and the Mn(OH)₂ composite material was obtained and stored in a dry, air-tight and inert atmosphere container.

Thereafter, the post precipitation leachate was further used to recover the Li by adding 12.6 g of Na₂CO₃ to the resultant supernatant liquid with a Li⁺ concentration of 1.38 M (9.7 g/L) (which

was concentrated from 4.75 g/L through evaporation using hot plate-open beaker set up at 90 °C) and agitated at 500 rpm for 1 h to efficiently precipitate Li_2CO_3 . The Li^+ concentration was raised to 9.7 g/L via evaporation, following the findings by Zhao et al. (2019) that a Li^+ concentration of at least 10 g/L is required to attain a high (>82%) Li^+ recovery efficiency (Zhao et al. 2019). The following operating variables were explored: $\text{Li}^+ : \text{CO}_3^{2-}$ to ratio, pH and temperature). The Li_2CO_3 precipitates were separated from the suspension through filtration followed by washing using deionised water and hot air drying. The sample composition was assessed using EDS, XRD and ICP analysis. The precipitation efficiency (E) (%) was calculated using the equation below:

$$E = (C_i - C_t) / C_i \quad 3-3$$

Where E is the precipitation efficiency (%), C_i is the initial metal content in g/L and C_t is the final metal content in g/L.

The complete hydro-electrometallurgy experimental design of the recovery of Ni-Co composite from spent Li-ionBs is formulated in Figure 3-2.

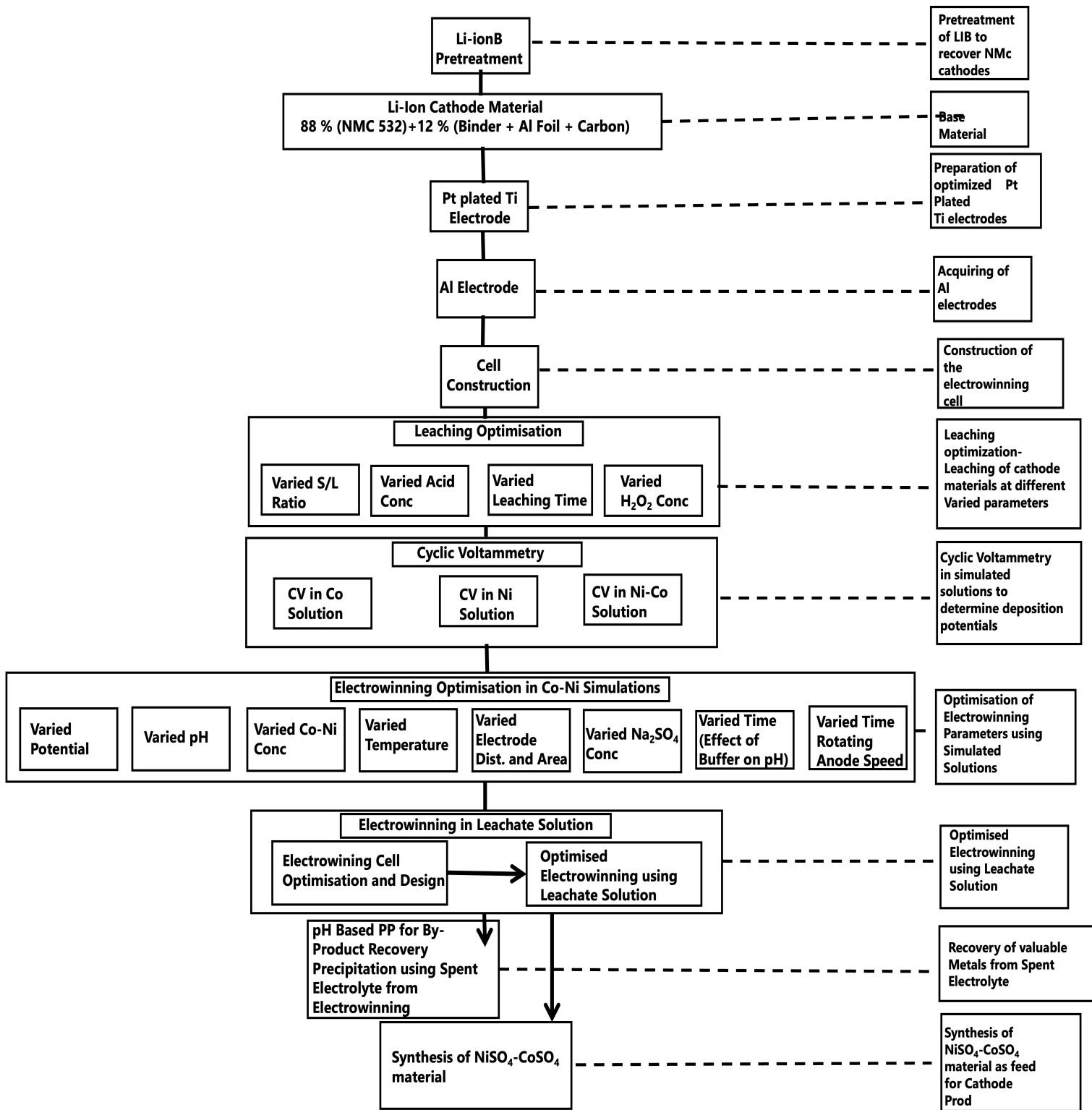


Figure 3-2: The complete hydro-electrometallurgy experimental design of the recovery of Ni-Co composite from spent Li-ionBs.

3.3 Recovery Process Setup

To ensure consistency in the in-house synthesized electrodes, the process was designed to maintain control over the operating parameters such as temperature, pressure, and time were optimally stipulated, and equipment was calibrated before research work commenced.

3.3.1 Material and Chemicals

Table 3-1 provides a list of materials and chemicals (including their details) that were employed during the course of this research.

Table 3-1: Materials and chemicals utilised during the course of this research.

Material/Chemical	Supplier	Comp.	Details
Aluminium	Q-Lite	99.0%	5052 Alloy
Cobalt Sulphate	Kimix Chemicals	99.9%	Reagent Grade
Li-ion Batteries	In-house		
Manganese Sulphate	ACE	99.9%	Reagent Grade
Titanium Electrodes	Sigma Aldrich	99.9%	
Lithium Sulphate	Sigma Aldrich	99.9%	Reagent Grade
Nickel Sulphate	Sigma Aldrich	99.9%	Reagent Grade
Sodium Hydroxide	Kimix Chemicals	99.0 %	Reagent Grade
Sodium Carbonate	Kimix Chemicals	99.0 %	Reagent Grade
Hydrochloric Acid	Alfa Aesar	37.5%	Reagent Grade
Sulphuric Acid	ACE	98.0%	Reagent Grade
Sodium Sulphate	Alfa Aesar	99.9%	Reagent Grade
Monosodium Phosphate	Alfa Aesar	99.9%	Reagent Grade
Deionized Water	WP Municipality		Water deionized by PURELAB® Prima, Elga Veola

3.3.2 Equipment

During the experiments, various machines were utilised to extract Ni-Co alloys.

3.3.2.1 Leaching Set-Up

A custom set-up (Figure 3-3) for the leaching process was used to leach the metals from the NMC cathode.

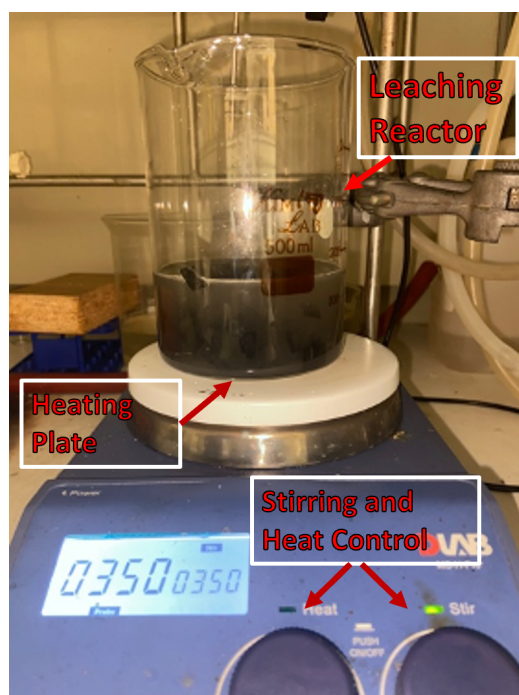


Figure 3-3: Schematic diagram of the leaching set-up.

3.3.2.2 Hot-Air Oven

The oven (Labotec Ecotherm, South Africa), depicted in Figure 3-4, was employed to facilitate the removal of solvent from wet materials.

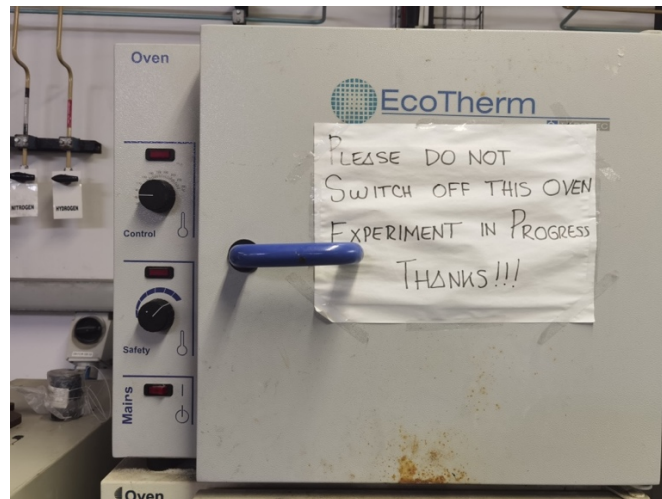


Figure 3-4: The oven employed during material synthesis.

3.3.2.3 Electrowinning Cases

Single-compartment electrowinning process was designed and manufactured by WAKE Engineering, SA. The schematic of the electrowinning process set-up and lab set-up figures are provided in Figure 3-5.

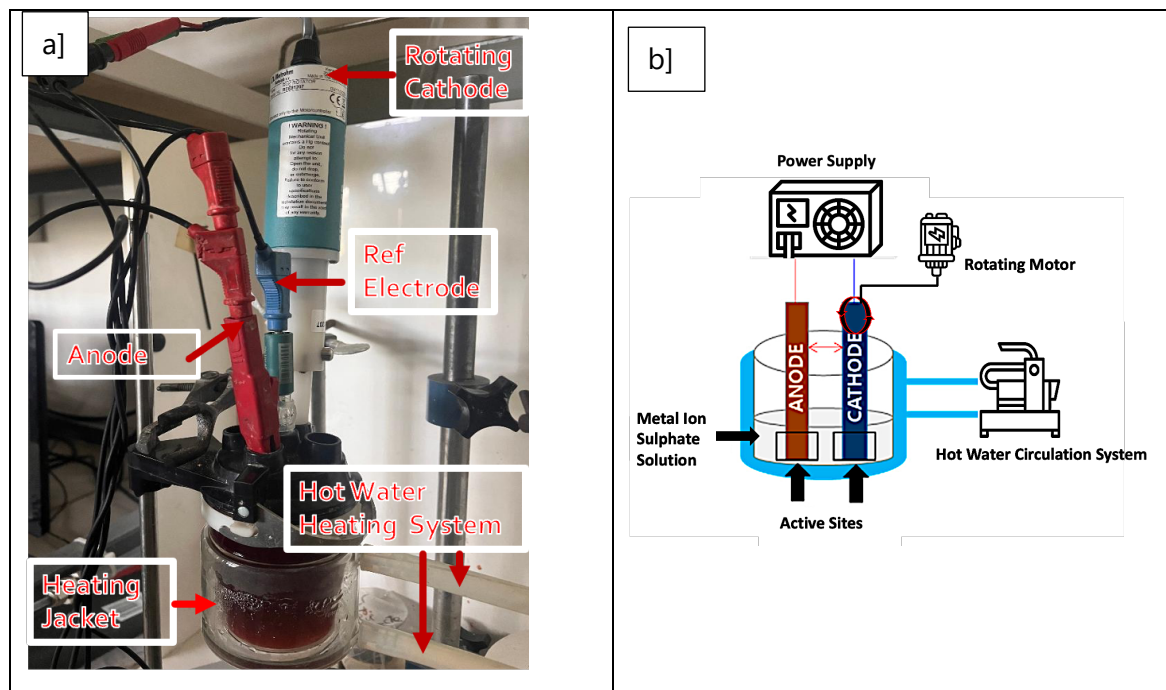


Figure 3-5: a) Electrowinning lab set-up b) schematic of the electrowinning set-up.

3.3.2.4 Overhead Mixer

The overhead mixer (Velp, Netherlands), depicted in Figure 3-6, was employed to facilitate the dissolution of materials in solvents and induce homogeneity in solutions



Figure 3-6: Overhead mixer.

3.3.2.5 Electrochemical Management System

The electrochemical management system (Metrohm, China), depicted in Figure 3-7, was employed to operate electrowinning cells.



Figure 3-7: Electrochemical management setup.

3.3.2.6 Other Equipment

Other small equipment employed during the course of the research are listed in Table 3-2.

Table 3-2: Compilation of all the small equipment used in this project.

Equipment / Item	Make / Model	Details
Spatulas	Flat and spoon spatulas, Lasec Co.	Stainless steel
Stirring Rods	Stainless steel rods, Lasec Co.	15 mm length
Mixing Vessels	Glass vessels, Lasec Co.	1L, 2L
Magnetic Stirrer	Eins Sci	
Water Purification System	PURELAB® Prima, Elga Veola Co.	
Sieves	Air & Vacuum Technologies	

3.3.3 Battery Pre-Treatment

Spent Li-ionBs are chosen due to their abundant quantity and ease of supply connection since in the last decade most technological devices and automated vehicles employ largely Li-ion batteries. To prevent short-circuiting, battery voltage was first measured by a voltmeter to test the remaining capacity of spent batteries. Normal L-ionBs voltage is commonly 3.4-4.1 V (Phuc Anh LE 2019; Manthiram 2020). Hence, a lower measured voltage than this range is required for safe dismantling.

To minimize possible explosion as well as toxic electrolyte risks, spent Li-ionBs were carefully dismantled in a fume hood. A plastic cutting knife was used to remove the plastic outer casing of Li-ionB. The enveloping polymer film and cathode layer were then dismantled. Cathode and anode stacked layers were then uncovered, separated from each other. Cathodes were cut into small fragments ($\sim 1 \text{ cm}^2$) to facilitate metal dissolution during leaching.

This thesis aims at recovering a high quantity and quality of Ni-Co, $\text{Mn}(\text{OH})_2$, and Li_2CO_3 compounds from the spent active cathode material in 3 subsequent stages, acid-reductant leaching, selective electrowinning and chemical based precipitation. In the first step, which is the inorganic acid-reductant leaching step, metallic compounds are dissolved as ions in an

inorganic acid-reductant environment. Optimal acid-reductant leaching can enhance the efficiency of subsequent metal separation steps. Therefore, optimization of acid-reductant leaching is necessary to identify appropriate conditions for the highest efficiency of acid leaching without waste of chemicals or energy.

The leaching step in this thesis was conducted in sulphuric acid (H_2SO_4) medium because, in research work, H_2SO_4 is cost effective and has provided higher leaching efficiency than HCl and HNO_3 (Georgi-Maschler et al. 2012; Chen and Ho 2018; Werner et al. 2020). Acid concentration, leaching temperature, and leaching time contribute to high leaching efficiency. Carbon flakes, which float in the intra-leaching solution, and aluminium fragments (both from the pre-processed cathode material fragments) were freed (washed) from the cathode matrix after 20 minutes ($t=20$ mins) using the acid-reductant leachant and filtered out thereafter using a 1 mm gauze sieve before leaching is continued. In addition, oxidizing agents enhance the reaction kinetics of the formation of highly soluble complexes, decreasing the required inorganic acid quantity and avoiding the risks of handling highly concentrated acid (Meshram et al. 2016a; Cheng 2018). Moreover, pulp density (i.e., the ratio of NMC powder to leaching liquid) is also an important factor contributing to the leaching efficiency of metals (Georgi-Maschler et al. 2012; Zheng et al. 2018). Experiments for leaching condition investigation were conducted in a 100 mL glass beaker on a stirring hot plate.

For each set of experiments, only one factor or parameter is varied while keeping all other factors constant. The goal is to determine the optimal value for this factor to achieve the highest leaching efficiency for Li, Co, Mn and Ni, while minimizing material, energy and time consumption. Refer to Figure 3-8 for the experiment setup for the battery pre-treatment process. The resulting mixture, after leaching, was then electrowon to recover dissolved valuable metals.

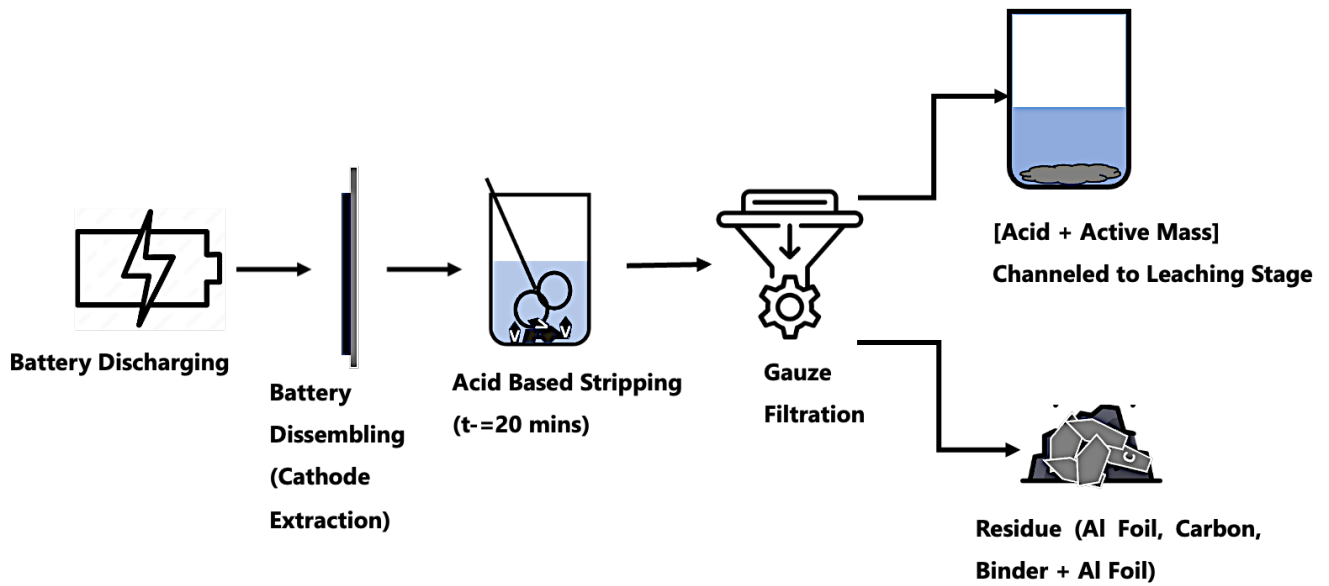


Figure 3-8: Experimental set-up for battery pre-treatment process.

3.3.4 Test Cell Assembly

Following Battery pre-treatment as per section 3.3.3, producing the Pt coated Ti electrode as per 3.5.1.2 and procuring the Al alloy electrode, the electrowinning cell assembly is the final step. For this step, a cylindrical glass reactor was designed and produced. The case housed the commercial Al alloy cathode, electrolyte, reference electrode, and platinum-plated titanium anode. The case has a heating jacket that is utilised for isothermal regulation. A 2D conception of the cell with two electrodes is shown below in Figure 3-9 (b).

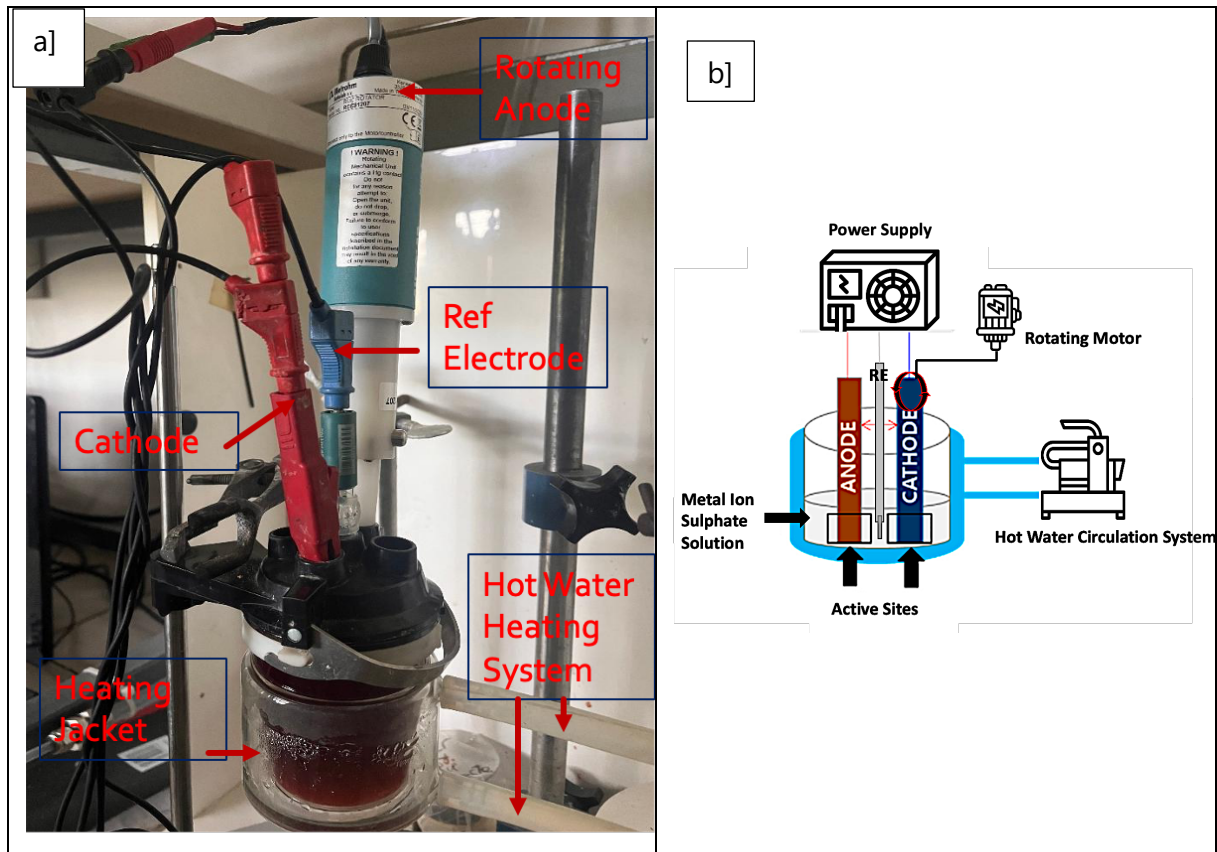


Figure 3-9: a) Electrowinning lab set-up b) 2D conception of the electrowinning cell with three electrodes.

Basically, for this type of cell, only one anode and one cathode could be put inside the cell. The anode should have double the dimensions of the cathode but with double the surface area. The reason for making the anode larger is to ensure that it can handle the same or a greater current density without becoming a limiting factor.

3.3.5 Leaching Process Optimisation

3.3.5.1 Overview

Following pre-treatment, the NMC 532 cathode electrode material was manually homogenized and leached in varied leachant concentration levels (0,5, 1, 2 and 3M) of H_2SO_4 solution and varied hydrogen peroxide concentration levels (2, 4, 6 and 8 %) for varied time levels (30, 60, 120 and 120 mins) and varied S/L ratios (20, 40, 60 and 80 g/L) at 90°C under constant agitation (350 rpm). At leaching reaction time of 20 mins, carbon flakes, which float in the intra-leaching solution, and aluminium fragments (both from the pre-processed cathode material fragments) were freed (washed) from the cathode matrix using the acid-reductant leachant and filtered out thereafter using a 1 mm gauze sieve before leaching is continued.

After leaching was completed, the minute insoluble residue was again filtrated and weighed. The concentrations of Ni, Co, Fe, Zn, and Mn in the leaching solutions were determined by inductively coupled plasma (ICP). Leaching efficiency was determined by the equation below:

$$\eta_L = \frac{C_i}{C_p} \times 100 \quad 3-4$$

Where C_i is the total metal leached per gram of cathode (as calculated from ICP results) and C_p is the initial metal total metal present per gram of cathode.

3.3.5.2 Leaching Optimisation Experimental Design

The 3 most influential leaching parameters were first optimised and therefore, a 3-level-2 factor full factorial experimental design was used to investigate the capabilities of each parameter as well as the effects of each variable on the recovery performance. The leaching tests investigated the H₂O₂ concentration, solid-liquid ratio, acid molarity and temperature. However, only solid liquid ratio, acid molarity, and temperature were modelled on a fractional factorial design whilst H₂O₂ concentration and time were subsequently optimised using sequential experimental (OFAT) design. Each leaching factorial design parameter was explored and tested within a range previously proven effective in literature for similar metals in other matrices (Lee and Rhee 2003a; Wang et al. 2012; Zhu et al. 2012; Meshram et al. 2015b, 2016b; Huang et al. 2016; Barik et al. 2017a; Xiao et al. 2020). A summary of the leaching variable high and low values is summarised below in Table 3-3, while the other variable experimental designs are presented in the next sections.

Table 3-3: Leaching experimental design specifying the high and low values for each variable.

Variables	Low	High	Units
H₂O₂ Vol%	1	8	Vol%
S/L*	30	75	g/L
[H₂SO₄]*	0.5	3	M
Temp*	50	90	°C
Time	15	180	min

*Parameters identified as most influential as per literature.

3.3.5.3 Investigation of the Effect of H₂O₂ on Leaching

This experiment was performed to investigate the effect of H₂O₂ concentration on the leaching process. Firstly, the H₂O₂ concentration was varied while all other parameters such as temperature, pulp density, acid leachant concentration and leaching time were kept constant. The experimental conditions are shown in Table 3-4 for the leaching process.

Table 3-4: leaching conditions at different H₂O₂ concentration levels.

Sample Code	Varied		Constant		
	H ₂ O ₂	H ₂ SO ₄ (mol/L)	S/L (g/L)	Temperature. (°C)	Time (hrs)
H-1	0				
H-2	1				
H-3	2				
H-4	4	3	30	70	3
H-5	6				
H-6	8				

3.3.5.4 Investigation of the Effect of Solid/Liquid Ratio on Leaching Efficiency

This experiment investigated the Solid/Liquid ratio in the leaching process. Following the investigation of the effect of H₂O₂ on Leaching efficiency experiments, the solid/liquid ratio was varied while all other parameters such as temperature, acid leachant and reductant concentration and leaching time were kept constant. The experimental conditions for the leaching process are shown in Table 3-5.

Table 3-5: Leaching conditions at different solid/liquid ratios.

Sample Code	Varied		Constant			
	S/L (g/L)	H ₂ SO ₄ Conc. (M)	Temperature (°C)		Time (hrs)	
SL-1	30					
SL-2	45					
SL-3	60	2	3	70	50	3
SL-4	75					
SL-5	90					

3.3.5.5 Investigation of the Effect of Acid Molarity on Leaching Recovery Efficiency

This experiment was performed to investigate the effect of acid molarity on the leaching recovery efficiency. Firstly, concentration was varied while all other parameters, such as temperature, pulp density and leaching time. The experimental conditions for the leaching process are shown in Table 3-6.

Table 3-6: Leaching conditions at acid concentrations.

Sample Code	Varied		Constant			
	H ₂ SO ₄ (mol/L)	S/L (g/L)	Temperature (°C)		Time (hrs)	
AL-1	0.5					
AL-2	1					
AL-3	2	75	45	70	50	3
AL-4	3					

3.3.5.6 Investigation of the Effect of Temperature on Leaching Recovery Efficiency

This experiment was performed to investigate the effect of temperature on the leaching recovery efficiency. The temperature was varied while all the other parameters, such as S/L ratio, acid and reductant concentration, and time were kept constant. The experimental conditions for the leaching process are shown in Table 3-7.

Table 3-7: leaching conditions at different temperature levels.

Sample Code	Varied		Constant			
	Temp (°C)	S/L (g/L)	Time (min)	H ₂ SO ₄ Conc. (mol/L)		
LT-1	25					
LT-2	30					
LT-3	40	75	45	180	2	3
LT-4	50					
LT-5	60					
LT-6	70					

3.3.5.7 Investigation of the Effect of Time on Leaching Recovery Efficiency

This experiment was performed to investigate the effect of time on the leaching efficiency. The time was varied while all the other parameters, such as temperature, acid concentration, and pulp density were kept constant. The experimental conditions for the leaching process are shown in Table 3-8.

Table 3-8: leaching conditions at different time levels.

Sample Code	Varied		Constant	
	Time (mins)	S/L (g/L)	Temperature (°C)	H ₂ SO ₄ Conc. (mol/L)
Lt-1	15			
Lt-2	30			
Lt-3	60	75	60	3
Lt-4	120			
Lt-5	180			

3.3.6 Cyclic Voltammetry

The equipment used for experiments was as follows:

1. A Potentiostat/Galvanostat Metrohm Autolab PGSTAT302N which is controlled by NOVA software (arranged as depicted in Figure 3-10).
2. Silver/Silver Chloride reference electrode (SCE).

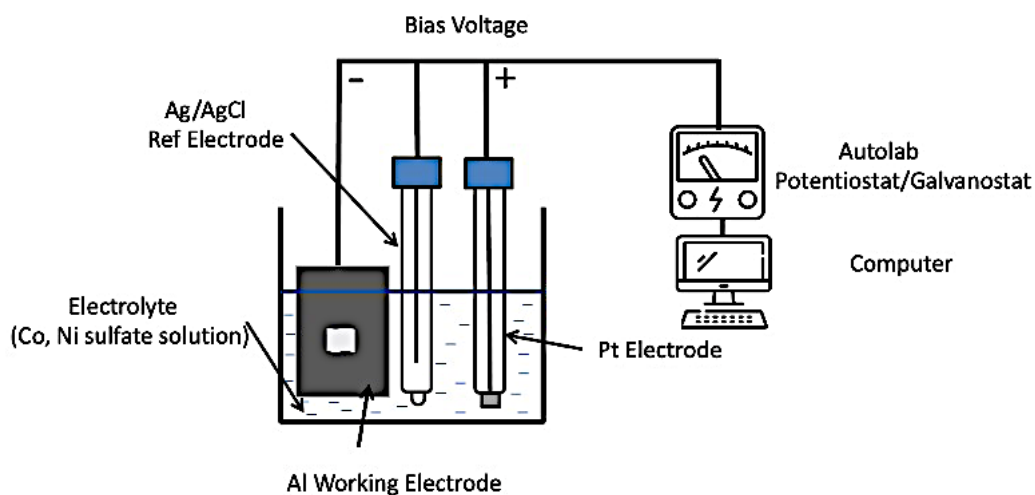


Figure 3-10: The schematic representation of the 3-electrode Autolab system.

Cobalt sulphate and nickel sulphate salts were dissolved in triply distilled water to make 15 g/L Co^{2+} , 15 g/L Ni^{2+} and 47.5 g/L $\text{Ni}^{2+}_{0.25}\text{Co}^{2+}_{0.1}\text{Mn}^{2+}_{0.15}\text{Li}^{+}_{0.5}$ electrolyte solutions. All the chemicals used were reagent grade. The pH of the solution was measured by using an EDT digital pH meter and adjusted to 4 with the addition of sufficient H_2SO_4 or NaOH . The working electrode (substrate) was made of an aluminium plate with a total exposed surface area of 2 cm^2 , and the pure platinum plate anode was utilized with a total surface of about 4 cm^2 , which is twice larger than the cathode surface. All potentials were measured against a saturated calomel electrode (SCE) from Metrohm (USA). The current and voltage were regularly stored in a computer. All investigations were conducted at a scan rate set at 2.5 mv/s , the temperature at $50\text{ }^\circ\text{C}$, and pH at 4.

3.4 Electrowinning Optimisation Using Synthetic Quasi NMC 532 Solutions

3.4.1 Methodology Overview

Aiming to define the ideal optimum potential window for Co and Ni deposition, firstly the tests were accomplished in a beaker using a synthetic $47.5\text{ g/L Ni}^{2+}_{0.25}\text{Co}^{2+}_{0.1}\text{Mn}^{2+}_{0.15}\text{Li}^{+}_{0.5}$ solution denoted as $30\text{ g/L Co}^{2+}_{0.3}\text{Ni}^{2+}_{0.7}$ solution (made from mixing NiSO_4 , Li_2SO_4 , MnSO_4 and CoSO_4). A single-compartment cell was built to allow for reduced mass transfer limitations of ions. Following electrowinning optimisation, the leachate achieved from acid leaching of the cathodic material of spent Li-ionBs will be used as an electrolyte. The leachate has a high number of metal ions; hence, there is an unavoidable requirement for separating and recovering these metals in solid forms. All the electrowinning experiments were run for 180 minutes unless otherwise stated. Unless otherwise stated, the leachate is treated with 15 g/L of Na_2HPO_4 , which acts as a buffer and background electrolyte. This minimises the changes in interfacial pH as a result of hydrogen evolution, which occurs simultaneously with Co and Ni electrodeposition. The bulk pH was adjusted using sodium hydroxide or sulphuric acid to the desired value. In the electrowinning setup, the treated leachate was the designated electrolyte.

An undivided glass EW cell with a solution volume of 0.250 L was used. One platinum anode (with a double surface area to that of the cathode) and one modified blank aluminium cathode were used at constant anode-to-cathode spacing. Titanium was coated by platinum using the electroless deposition method by Rao & Pushpavanam, (2001) (Rao and Pushpavanam 2001). An aluminium plate with a 2 cm^2 active surface area was used as a cathode, coupled with a

single platinum-coated titanium plate with a 4 cm² exposed surface area was used as anode for the 2 cm²/250 cm³ cathodic surface area to electrolyte volume ratio (AA/EV) set-up. The aluminium plate of (10 × 3) 30 cm² surface area was used as cathodes coupled with two layered platinum-coated titanium sheets measuring 10 × 3 cm, which was used as anodes placed on opposite facial side of the cathode for the 30 cm²/ 250 cm³ AA/EV set-up. All upscaled batch electrowinning experiments utilized the Ag/AgCl reference electrode.

The Metrohm Autolab Electrochemical Management System (EMS) supplied the applied potential to the working electrode in an electrowinning cell at predetermined levels. The cell electrolyte temperature was maintained at a desired temperature by an electric water heating circulation chamber. The spent electrolyte was collected in a discharge tank, and the valuable by-products were recovered using low-cost Na-based precipitants. The pH, Ni-Co concentration, applied potential; electrode distance and area, temperature, buffer dosage and cathode rotation speed are investigated to formulate the optimum electrowinning conditions using platinum-plated titanium electrodes and aluminium cathodes. The parameter limits for each variable are fully annotated in the next sections.

The cathode was weighed before and after each experiment for the current efficiency determination, and the mass difference represents the deposit mass. However, to ensure that this mass difference exclusively regarded the deposit, the cathode as well as the deposit were rinsed with acetone and then evaporated using pressurised air to ensure that no solution trace amounts were stuck on the surface. The current efficiency was then determined by dividing the theoretical current to produce the deposit by the real supplied one, as annotated by the equations 2-19 and 2-20.

3.4.2 Electrowinning Optimisation Experimental Design

The 3 most influential electrowinning parameters (pH, temperature and dosage) were only optimised using factorial design and therefore a 3-level-4-factor full factorial experimental design was used to investigate the capabilities of each parameter as well as the effects of each variable on the recovery performance. The electrowinning tests investigated were Co-Ni dosage, applied potential, cathode rotational speed, inter-electrode distance, electrode active area, buffer dosage, Na₂SO₄, pH, and temperature. However, only Ni-Co dosage, pH and

temperature were modelled on a full factorial design whilst the rest of the parameters were optimised using sequential experimental design. Each electrowinning parameter was explored and tested within a range that has proven effective previously in literature for similar applications (Jeffrey et al. 2000b, 2000a; Pradhan et al. 2001; Kargl-Simard et al. 2003; Sharma et al. 2005a; Nusheh and Yoozbashizadeh 2009; Mulaudzi and Kotze 2013; Lu et al. 2018; Abbey 2019; Carvajal Ortiz et al. 2020; Kazem-Ghamsari and Abdollahi 2022; de Castro et al. 2023). A summary of the electrowinning variable values is summarised below in Table 3-9, while the other tabulated experimental designs are presented in the next sections.

Table 3-9: Electrowinning experimental design.

Variables	Low	High	Units
Potential	-0.95	-1.45	V vs Ag/AgCl
pH *	2	6	
Temp *	25	80	M
Co-Ni Dosage *	5	30	g/L
Cathode Rotational Speed	10	40	rpm
Buffer Dosage	5	20	g/L
Na₂SO₄ Dosage	5	20	g/L

*Parameters identified as most influential as per literature

3.4.3 Investigation of the Effect of Co/Ni Ratio on Current Efficiency and Deposit Composition

This experiment was performed to investigate the effect of the Co/Ni ratio on current efficiency and deposit composition. Firstly, the Co/Ni ratio was varied while all other parameters such as total $\text{Co}^{2+}_{0.3}\text{Ni}^{2+}_{0.7}$ concentration applied potential, pH and temperature were constant. The experimental conditions for electrowinning set-up at different Co/Ni ratios are shown in Table 3-10.

Table 3-10: Electrowinning conditions at different Co/Ni ratios.

Sample Code	Varied	Constant			
	Co/Ni Ratio	Applied Potential (E vs Ag/AgCl)	pH	Temperature	Co ²⁺ _x Ni ²⁺ _y (x+y=1) Conc. (g/L)
E-R1	0.025				
E-R2	0.05				
E-R3	0.15				
E-R4	0.20				
E-R5	0.25	-0,95	5	60	30
E-R6	0.3				
E-R7	0.4				
E-R8	0.6				
E-R9	0.8				
E-R10	1.0				

3.4.4 Investigation of the Effect of Applied Potential

This experiment was performed to investigate the effect of current density on the electrowinning process. The applied was varied while all other parameters such as Co²⁺_{0.3}Ni²⁺_{0.7} concentration, pH and temperature were constant. The experimental conditions for electrowinning set-up at different potential levels are shown in Table 3-11.

Table 3-11: Electrowinning conditions at different potential levels.

Sample Code	Varied			Constant		
	Applied Potential (E vs Ag/AgCl)	pH		Temperature		$\text{Co}^{2+}_{0.3}\text{Ni}^{2+}_{0.7}$ Conc. (g/L)
E-AP1	-0.95					
E-AP2	-1.05					
E-AP3	-1.15	4	5	50	60	30
E-AP4	-1.25					
E-AP5	-1.35					
E-AP6	-1.45					

3.4.5 Investigation of the Effect of pH

This experiment was performed to investigate the effect of pH on the electrowinning process. Firstly, PH was varied while all other parameters such as $\text{Co}^{2+}_{0.3}\text{Ni}^{2+}_{0.7}$ concentration, applied potential and temperature were constant. The experimental conditions are shown in Table 3-12. Table 3-12 depicts the electrowinning conditions used to determine the optimised pH level for electrowinning. Different pH levels of 2, 2.5, 3, 4 and 5 were adjusted by the addition of an appropriate amount of NaOH.

Table 3-12: Electrowinning conditions at different pH levels.

Sample Code	Varied pH	Constant			
		$\text{Co}^{2+}_{0.3}\text{Ni}^{2+}_{0.7}$ Conc. (g/L)	Temperature (°C)	Applied Potential (E vs Ag/AgCl)	
E-pH1	2				
E-pH2	2.5				
E-pH3	3	30	50	60	-1.15
E-pH4	4				
E-pH5	5				
E-pH6	6				

3.4.6 Investigation of the Effect of Temperature

This experiment was performed to investigate the effect of Temperature on the electrowinning process. Firstly, the temperature was varied while all other parameters such as $\text{Co}^{2+}_{0.3}\text{Ni}^{2+}_{0.7}$ concentration, pH, and current density, were fixed at constant levels. The experimental conditions for electrowinning at different temperature levels are shown in Table 3-13.

Table 3-13: Electrowinning conditions at different temperature levels.

Sample Code	Varied				Constant		
	Temperature (°C)	pH			Applied Potential (E vs Ag/AgCl)	$\text{Co}^{2+}_{0.3}\text{Ni}^{2+}_{0.7}$ Conc. (g/L)	
E-T1	25						
E-T2	30						
E-T3	40						
E-T4	50	3	4	5	6	-1.15	30
E-T5	60						
E-T6	70						
E-T7	80						

3.4.7 Investigation of the Effect of Co-Ni Concentration

This experiment was performed to investigate the effect of Co-Ni concentration on electrowinning. Co-Ni concentration was varied in this experiment, while all other parameters were constant. The optimised pH level was obtained, as detailed in the previous section. The experimental parameters used in these experiments are listed in Table 3-14.

Table 3-14: Electrowinning conditions at different Ni-Co concentrations.

Sample Code	Varied		Fixed				Applied Potential (E vs Ag/AgCl)
	Co ²⁺ _{0.3} Ni ²⁺ _{0.7} Conc. (g/L)	pH	Temperature (°C)				
E-C1	5	4.5	40	50	60	70	-1.15
E-C2	10						
E-C3	15						
E-C4	20						
E-C5	25						
E-C6	30						

3.4.8 Investigation of the Effect of Distance Between Electrodes

This experiment was performed to investigate the effect of distance between electrodes on electrowinning. In this experiment, the distance between electrodes was varied while all other parameters were constant. The optimised parameters were obtained as detailed in previous sections. The experimental parameters used in these experiments are listed in Table 3-15. Table 3-15 depicts the electrowinning conditions used to determine the optimal electrode distance for Co-Ni electrowinning.

Table 3-15: Electrowinning conditions at different electrode distance levels.

Sample Code	Varied		Fixed		
	Distance (cm)	pH	Temperature (°C)	Applied Potential (E vs Ag/AgCl)	Co ²⁺ _{0.3} Ni ²⁺ _{0.7} c Conc. (g/L)
E-D1	0.5	4.5	50	-1.15	30
E-D2	1				
E-D3	1.5				
E-D4	2				
E-D5	2.5				
E-D6	3				

3.4.9 Investigation of the Effect of Electro-Active Area

This experiment was performed to investigate the effect of electrode active area on electrowinning. In this experiment, the distance between electrodes was varied while all other parameters were constant. The optimised parameters were obtained as detailed in previous sections. The experimental parameters used in these experiments are listed in Table 3-16.

Table 3-16: Electrowinning conditions at different electro-active area levels.

Sample Code	Varied		Fixed		
	Area (cm ²)	pH	Temperature (°C)	Applied Potential (E vs Ag/AgCl)	Co ²⁺ _{0.3} Ni ²⁺ _{0.7} Conc. (g/L)
E-E1	1	4.5	50	-1.15	30
E-E2	2				
E-E3	3				
E-E4	4				

3.4.10 Investigation of the Effect of Monosodium Phosphate on pH as a Function of Time

The effect of NaH₂PO₄ (monosodium phosphate) buffer on pH as a function of time was studied in this experiment. All other parameters were kept constant, as indicated in Table 3-17. The optimised parameters were obtained as detailed in previous sections. Table 3-17 depicts the electrowinning conditions used to determine the effect of buffer dosage on pH as a function of time.

Table 3-17: Electrowinning conditions at different buffer concentrations.

Sample Code	Variable	Fixed			
	Time	Initial pH	Temperature (°C)	Applied Potential (E vs Ag/AgCl)	Co ²⁺ _{0.3} Ni ²⁺ _{0.7} Conc. (g/L)
E-B1	5	4.5	50	-1.15	30
E-B2	10				
E-B3	15				
E-B4	20				

3.4.11 Investigation of the Effect of Na₂SO₄ Concentration

This experiment was performed to investigate the effect of Na₂SO₄ concentration on electrowinning. In this experiment, Na₂SO₄ concentration was varied while all other parameters were constant. The optimised parameters were obtained as detailed in previous sections. The experimental parameters used in these experiments are listed in Table 3-18.

Table 3-18 depicts the electrowinning conditions used to determine the optimised Na₂SO₄ concentrations for electrowinning.

Table 3-18: Electrowinning conditions at different Na₂SO₄ concentrations.

Sample Code	Varied	Fixed			
	Na ₂ SO ₄ Conc. (g/L)	pH	Temperature (°C)	Applied Potential (E vs Ag/AgCl)	Co ²⁺ _{0.3} Ni ²⁺ _{0.7} Conc. (g/L)
E-A1	5	4.5	50	-1.15	30
E-A2	10				
E-A3	15				
E-A4	20				

3.4.12 Investigation of the Effect of the Rotating Cathode Speed

This experiment was performed to investigate the effect of the rotating anode speed on electrowinning. In this experiment, the anode rotating speed was varied while all other parameters were constant. The optimised parameters were obtained as detailed in previous sections. The experimental parameters used in these experiments are listed in Table 3-19.

Table 3-19: Electrowinning conditions at different rotating anode speeds.

Sample Code	Varied		Fixed		
	Rotating Anode Speed (rpm)	pH	Temperature (°C)	Applied Potential (E vs Ag/AgCl)	Co ²⁺ _{0.3} Ni ²⁺ _{0.7} Conc. (g/L)
E-CS1	10	4.5	50	-1.15	30
E-CS2	20				
E-CS3	30				
E-CS4	40				

3.5 Electrowinning Experiments Using Synthetic Ni, Co Sulphate Solution

The aim of this set of experiments was to create a cohesive deposit with high current efficiency by studying a number of electrowinning parameters: cobalt-nickel concentration. The variables under investigation were the pH, temperature, buffer dosage, coenzyme N concentration, and potential. Table 3-20 annotates the composition of the solutions employed in the electrowinning tests.

Table 3-20: Composition of the solutions employed in the electrowinning tests.

Electrolytes	Concentration [g/L]				Purpose
	Ni	Co	Mn	Li	
Ni	15	0	0	0	CV
Co	0	15	0	0	CV
Ni-Co	21.25	8.5	0	0	CV and EW
Ni-Co-Mn-Li	21.25	8.5	12.5	5.5	EW

The optimum electro-winning parameters were:

30 g/L of $\text{Co}^{2+}_{0.7}\text{Ni}^{2+}_{0.3}$ (47.5 g/L [$\text{Ni}^{2+}_{0.25}\text{Co}^{2+}_{0.1}\text{Mn}^{2+}_{0.15}\text{Li}^{+}_{0.5}$]), 50 °C, 15 g/L of buffer dosage, pH 4.5, and -1,15 V against Ag/AgCl.

3.5.1 Anode Selection and Fabrication

3.5.1.1 Methodology Overview

The methodology constitutes the synthesis of platinum electroless plated titanium. The electrode produced is utilised as the anode in assembling the electro-winning test cell. Each step will be discussed in the subsequent sections.

3.5.1.2 Electroless Platinum Plating of Titanium Plate

Platinum was coated on titanium using the electroless deposition technique. Chloroplatinic acid was purchased from Sigma Aldrich. All other chemicals are of analytical grade. The electroless bath solutions are prepared according to the reported procedure with no further modification (Rao and Pushpavanam 2001). A stock solution of chloroplatinic acid was prepared by dissolving 2 g in 100 ml of 4% HCl. An aliquot of 25 ml of 1 g/L platinum bath was prepared by taking 3.2 ml of the stock solution and diluting it to 25 ml with water. Solid hydrazine (as a monohydrochloride) was added (3.7 g/L) to the bath just before the experiment commenced. The deposition was carried out at 65 °C using a hot water circulation system. Titanium plates (1 cm × 5 cm) were cleaned with ethanol before being immersed in the electroless deposition bath for 1 hour. The electro-deposition was carried out on a 1 cm² area of the panel. The thickness of the deposits was measured by the XRF method using coating measurement instruments [CMI] type XRX-XYZ.). The measurements are accurate to within ±0.001 μm for coating thickness.

3.6 Electrowinning Experiment Using Leached Cathode Solutions

The optimised parameters determined in previous sections were used in this section of the experiments. The optimum electro-winning parameters were 50 °C, 15 g/L of buffer dosage, pH 4.5, and -1,15 V against Ag/AgCl. A single-compartment cell was built to allow for uninhibited mass transfer of ions.

Figure 3-11 presents the assembly scheme of a single-compartment cell used in the different electrowinning tests. The anodic plate, made of platinum-plated titanium, was connected to a rotating motor, allowing for improved ionic mass transfer and counteract ion-depleted zones. The Al cathodic plate was fixed in a static position. The Al cathodic plate was fixed in a static position.

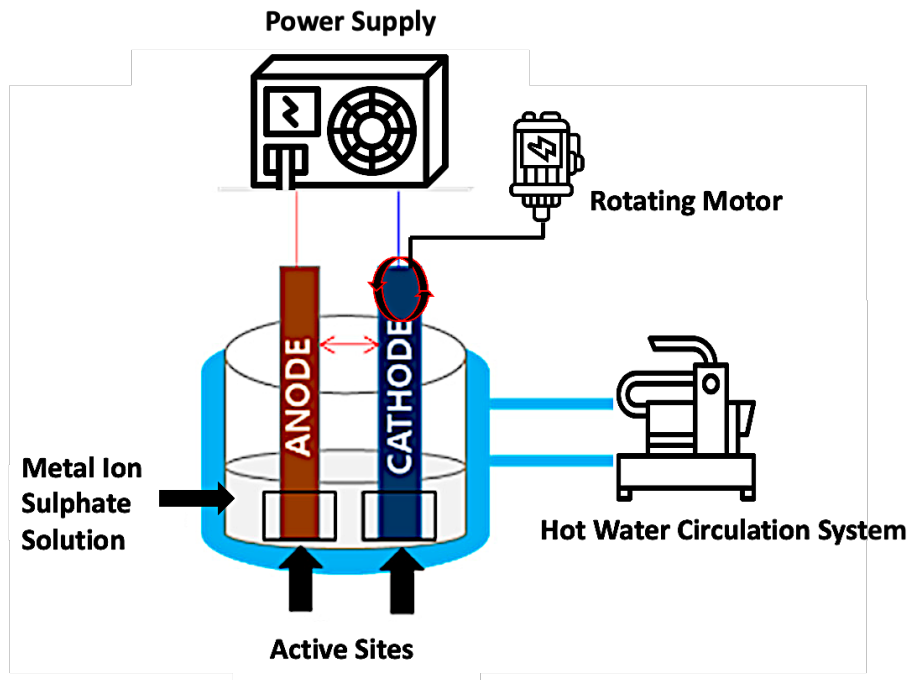


Figure 3-11: Single-compartment cell used in the different electrowinning tests.

The cathode consists of a polished Al sheet with a 2-cm² active area and an anode of titanium coated by platinum with a 4-cm² active area. In all electrowinning optimization tests, a Ni²⁺_xCo²⁺_yMn²⁺_{0.15}Li⁺_{0.5} solution was used in the electrowinning compartment, with the electrolyte solutions circulated every 3 hours, and each electrowinning test having a 3-hour reaction time.

To determine the current efficiency, the weight of the Al cathode was measured before and after each experiment, and the difference in mass represented the mass of the deposited Co-Ni material. However, in order to ensure that this mass difference accurately reflected the mass of the deposit only, both the cathode and the deposit were thoroughly rinsed with acetone and then air dried using pressurized air to eliminate any traces of residual electrolyte solution adhering to the electrode-deposit matrix. The current efficiency was subsequently determined by dividing the obtained deposit mass by the theoretical mass deposit calculated at the same

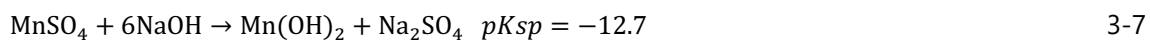
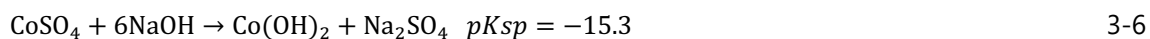
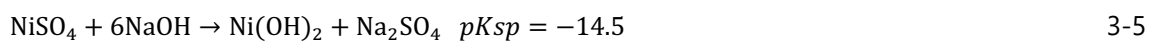
specific current level the electrowinning was operated at. The current efficiency was calculated according to the equations 2-19 and 2-20.

3.7 Recovery of Mn(OH)_2 and $0.6[\text{Ni(OH)}_2].0.3[\text{Mn(OH)}_2].0.1[\text{Co(OH)}_2]$ Precipitates

The resulting solution from electrowinning will be analysed using ICP-OES and the composition will be quantified. The electrowinning resultant solution will still constitute a substantial amount of metals that need to be recovered and integrated back into the spent battery recycling process. The resultant electrowinning effluent was treated with NaOH and Na_2CO_3 to recover $0.6[\text{Ni(OH)}_2].0.3[\text{Mn(OH)}_2].0.1[\text{Co(OH)}_2]$ composite material and Li_2CO_3 respectively. The recovery and separation process of the valuable metals from spent NMC cathode material was achieved by a two-step precipitation method.

After electrowinning, the pH of the leachate solution was adjusted from 5.5 to 13 using a 10 M NaOH solution to study the behaviour of Mn, Co, and Ni precipitates at different pH levels. The following operating variables were explored: pH and temperature. During precipitation, aliquots of liquid samples were taken periodically (at every experimental variant) to determine the metal content for elemental analysis. At pH=7.8 and 20 °C, The supernatant liquid was filtered, the residue was hot air dried, and the $0.6[\text{Ni(OH)}_2].0.3[\text{Mn(OH)}_2].0.1[\text{Co(OH)}_2]$ composite mixture material was obtained and stored in a dry, air-tight and inert atmosphere container. At pH=12.8 and 20 °C, The supernatant liquid was filtered, the residue was hot air dried, and the Mn(OH)_2 composite material was obtained and stored in a dry, air-tight and inert atmosphere container.

Precipitation tests were carried out in 200 mL conical flasks on an overhead-stirrer. The initial solution volume was 200 mL, maintained at a designated temperature and the agitation rate was kept constant at 350 rpm. The conical flask corresponded to a pre-selected target pH value (7.8, 12.8) in the range where $0.6[\text{Ni(OH)}_2].0.3[\text{Mn(OH)}_2].0.1[\text{Co(OH)}_2]$ and Mn(OH)_2 can be precipitated respectively. The chemical reactions of pH adjustment with NaOH are shown below:



The precipitating agent (10M NaOH) was added to the solution stepwise. Once the target pH was attained in each flask, the reaction time was initiated, and the experiments were continued for a total duration of 30 mins. The pH in each flask was monitored hourly and adjustments to maintain the target pH value were undertaken using 10 M NaOH as necessary. Once the reaction time reached 60 mins, the resulting solution was filtered through a 0.45 μm PTFE membrane to recover the precipitate. The precipitate was washed 3 times using deionized water to remove any water-soluble impurities. After washing, the individual filter cakes were collected and analysed. pH and temperature parameters were analysed as stipulated in the below section.

The Effect of pH on Precipitation (at different temp)

This experiment was performed to investigate the effect of pH on precipitation at different temperature levels. In this set of experiments, temperature and pH were varied while all other parameters were constant. The optimised parameters were obtained as detailed in previous sections. The experimental parameters used in these experiments are listed in Table 3-21 and Table 3-22.

Table 3-21: Precipitation conditions at different pH levels (20 °C).

Sample Code	Varied		Fixed	
	pH	Reaction Time (min)	Temperature	NaOH (M)
E-A1	1			
E-A2	3			
E-A3	5			
E-A4	6			
E-A5	7			
E-A6	8	30	20	10
E-A7	9			
E-A8	10			
E-A9	11			
E-A10	12			
E-A11	13			
E-A12	14			

Table 3-22: Precipitation conditions at different pH levels (40 °C).

Sample Code	Varied		Fixed	
	pH	Reaction Time (min)	Temperature (°C)	NaOH (M)
E-AT1	1			
E-AT2	3			
E-AT3	5			
E-AT4	6			
E-AT5	7			
E-AT6	8	30	40	10
E-AT7	9			
E-AT8	10			
E-AT9	11			
E-AT10	12			
E-AT11	13			
E-AT12	14			

3.8 Recovery of Li₂CO₃ Precipitates

The Li⁺ remaining in the solution is precipitated by adding Na₂CO₃ in the CO₃²⁻:Li⁺ mole ratio of at least 1:2 as per the reaction:



The precipitating agent (40 g/L Na₂CO₃) was added to the 9.7 g/L Li⁺ solution stepwise. The Li⁺ concentration was raised to 9.7 g/L via evaporation, following the findings by Zhao et al. (2019) that a Li⁺ concentration of at least 10 g/L is required to attain a high (>82%) Li⁺ recovery efficiency. Once the target mole ratio was attained in each flask, the reaction time was initiated, and the experiments were continued for a total duration of 60 mins. Once the precipitation reaction time reached 60 mins, the resulting solution was filtered through a 0.45 μm PTFE membrane to recover the precipitate. The precipitate was washed 3 times using deionized water to recover and remove any water-soluble impurities. After washing, the individual filter cakes were collected and analysed.

The total cake mass and related metal content (Ni, Co, Mn, Li) were quantified using ICP-OES. The precipitation efficiency (*E*) (%) was calculated using the equation below:

$$E = \frac{C_i - C_t}{C_i} \quad 3-9$$

Where *E* is the precipitation efficiency (%), *C_i* is the initial metal content in g/L and *C_t* is the final metal content in g/L. pH, CO₃²⁻:2Li⁺ ratio and temperature parameters were analysed as stipulated in the below section.

The effect of CO₃²⁻:Li⁺ Ratio on Precipitation

This experiment was performed to investigate the effect of the CO₃²⁻:2Li⁺ Ratio on precipitation. In this set of experiments, CO₃²⁻:2Li⁺ Ratios were varied while all other parameters were constant. The optimised parameters were obtained as detailed in previous sections. The experimental parameters used in these experiments are listed in Table 3-23.

Table 3-23: Precipitation conditions at different $\text{CO}_3^{2-}:\text{Li}^+$ Ratios.

Sample Code	Varied		Fixed		
	$\text{CO}_3^{2-}:\text{Li}^+$ Ratio	pH	Temperature ($^{\circ}\text{C}$)	Mixing Speed (Rpm)	
PP-A1	1.0:1.0				
PP-A2	1.2:1.0				
PP-A3	1.4:1.0	13	20	500	
PP-A4	1.6:1.0				
PP-A5	1.8:1.0				

The effect of Temperature on Precipitation

This experiment was performed to investigate the effect of temp on precipitation. In this set of experiments, temperature levels were varied while all other parameters were constant. The optimised parameters were obtained as detailed in previous sections. The experimental parameters used in these experiments are listed in Table 3-24.

Table 3-24: Precipitation conditions at different temperature levels.

Sample Code	Varied		Fixed		
	Temp	pH	$\text{CO}_3^{2-}:\text{Li}^+$ Ratio	Mixing Speed (Rpm)	
PP-T1	20				
PP-T2	30				
PP-T3	40	13	1.6:1.0	500	
PP-T4	50				
PP-T5	60				

The effect of pH on Precipitation

This experiment was performed to investigate the effect of pH on precipitation. In this set of experiments, pH levels were varied while all other parameters were constant. The optimised parameters were obtained as detailed in previous sections. The experimental parameters used in these experiments are listed in Table 3-25.

Table 3-25: Precipitation conditions at different pH levels.

Sample Code	Varied	Fixed		
	pH	CO²⁻₃:2Li⁺ Ratio	Temperature (°C)	Mixing Speed (Rpm)
PP-P1	13.00	1.6:1.0	20	500
PP-P2	13.35			
PP-P3	13.70			
PP-P4	14.00			

3.9 Material Characterization

3.9.1 X-Ray Diffraction

3.9.1.1 Working Principle

X-ray diffraction is computed from the constructive interference of monochromatic X-rays with a crystalline sample (Guinier 2013). Guinier (2013) added that these X-rays are generated by a cathode ray tube, filtered to produce monochromatic radiation, collimated to concentrate, and projected into the crystalline sample. The interaction of the incident rays with the sample formulates constructive interference signals (diffracted X-ray) which satisfy Bragg's law (Equation 3-1);

$$n\lambda = 2d\sin\theta$$

3-10

where n is a positive integer, λ is the wavelength of the incident ray, θ is the scattering angle and d is the interplanar distance (in Angstroms). Bragg's law establishes a connection between the wavelength of electromagnetic radiation, the diffraction angle, and the lattice spacing (interplanar distance) within the crystalline structure of the sample. The resultant diffracted X-

ray signals are subsequently detected, processed, and quantified. By systematically scanning the sample across a range of 2θ angles, all potential constructive interference signals (diffraction X-rays) arising from the lattice can be acquired, owing to the random orientation of the crystals. Analysing the diffraction peaks and converting them to d-spacings facilitates the identification of compound(s) in the sample, as each compound exhibits a distinctive set of d-spacings. Typically, compound identification involves comparing these d-spacings with standard reference patterns.

3.9.1.2 Procedure for XRD Analysis

The electrode materials, as well as the charged and discharged electrode materials, were characterized by X-ray diffraction (XRD) using a D8 Diffractometer with a theta-theta goniometer (HySA, South Africa). Cu $K\alpha$ radiation ($\lambda \approx 1.541874 \text{ \AA}$) was utilized, covering a 2θ range (from 5° to 90°) at a scan rate of 5° per minute. Rietveld refinement was not conducted. Phase identification was done in DIFFRAC.EVA software and the plane reflection were indexed using a powder diffraction file (PDF). A qualified lab technician conducted the analysis and provided the results.

3.9.1 Scanning Electron Microscopy

3.9.1.1 Working Principle

Stokes (2008) characterized a scanning electron microscope (SEM) as an electron microscope variant that produces images by scanning the surface of the specimen with a focused beam of high-energy electrons. This electron beam interacts with atoms in the specimen, eliciting various signals that provide information about the surface topography, morphology, and composition of the specimen (Debbie J Stokes, 2008). The electron beam follows a raster scan pattern, and the image is formed by correlating the position of the electron beam with the frequency of the detected signal. The detection of secondary electrons emitted by atoms excited through the electron beam represents the most commonly utilized SEM mode, as indicated by Suryanarayana (2016). Figure 3-12 depicts a schematic diagram of a typical SEM.

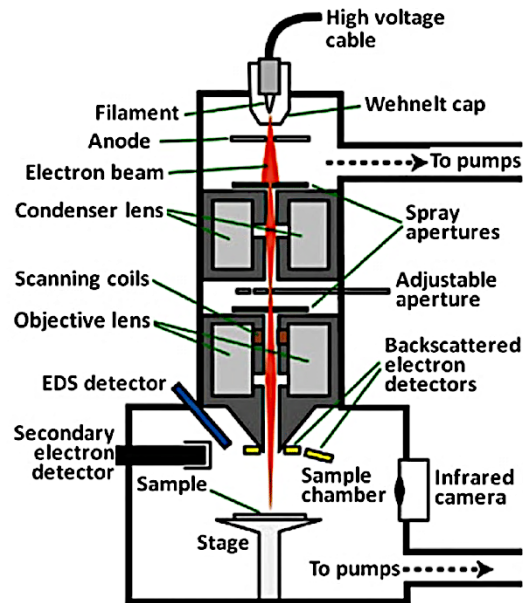


Figure 3-12: Schematic diagram of a SEM machine (Figure derived from (Suryanarayana 2016)).

3.9.1.2 Procedure for SEM Analysis

The morphologies of all Ni-Co alloys were taken by a TESCAN MIRA SEM with a Raman confocal system (EMU-University of Cape Town, South Africa). A qualified lab technician conducted the analysis and provided the results.

3.9.1 Inductively Coupled Plasma-Optical Emission Spectroscopy (ICP-OES)

3.9.1.1 Working Principle

In ICP-OES, samples are typically introduced as acid solutions and subsequently nebulized to generate a fine aerosol. This aerosol is then transported into the plasma, where it undergoes desiccation, vaporization into molecular gases, and dissociation into atoms that are capable of being ionized. Both atoms and ions become excited in the plasma, returning to their ground state while emitting light, which is quantified using an optical spectrometer. All elements present in the radiation source emit their characteristic spectra concurrently. Consequently, based on the principles of OES, it is evident that this is a multi-element method, capable of operating in either a simultaneous or sequential mode (de la Guardia and Armenta 2011).

3.9.1.2 Procedure for ICP-OES

ICP-OES was used to determine the concentration of metal ions. Elemental analysis of the metal solution collected before and after the adsorption experiments was done in order to gain a better understanding of the metal species and concentrations in the filtrates obtained from the adsorption experiments. The instrument used for determining the metal ions was a Varian Radial ICP-OES using a High Matrix Introduction (HMI) accessory and He as collision gas. External calibration of the instrument was performed daily, and a quality control standard verifying accuracy was included with every batch of samples analysed. During the ICP-OES analysis, internal standards were used to correct the matrix effects and instrument drift. Samples were diluted by a factor of a hundred depending on the concentration solution that was available since some samples contained high metal concentrations. Triplicate samples were considered in order to achieve reproducibility of the analysis results.

3.10 Electrochemical Characterization

3.10.1 Cycling Voltammetry

3.10.1.1 Working Principal

Cyclic voltammetry (CV) is a technique the expansively utilised for acquiring quantitative and qualitative information about electrochemical reactions and reactivity. It offers the instantaneous identification of redox potentials relative to the electro-active species under investigation, substantial information about the thermodynamics and kinetics of the redox reactions and analysis of electron transfer-initiated chemical reactions, which includes adsorption reactions (catalysis) (Davies et al. 2005).

Cyclic voltammetry consists of linearly scanning the potential of the working electrode through a zigzag potential waveform. Figure 3-13 below depicts the typical potential-time profiles generated during linear sweep and cyclic voltammetry.

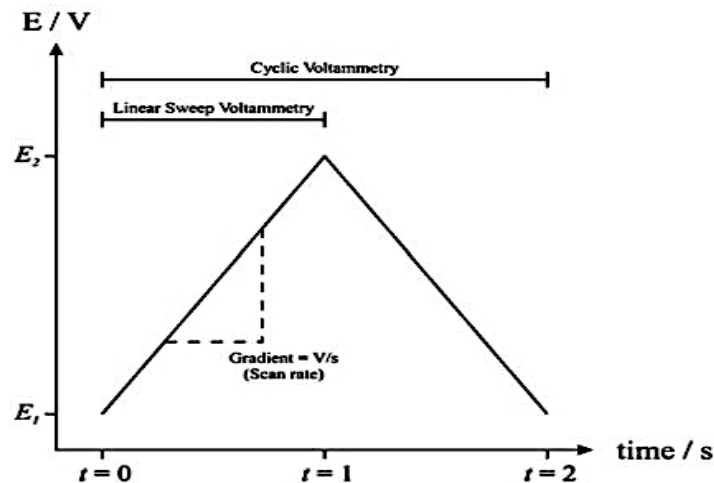


Figure 3-13: Potential-time profiles generated during the linear sweep and cyclic voltammetry (concept adapted from (Figure derived from (Figure derived from (Davies et al., 2005))).

The rate at which the potential is swept from E_1 to E_2 is termed the voltammetry scan rate (mV/s). In the case where the potential sweep is stopped at E_2 , this is regarded as linear sweep voltammetry (Davies *et al.*, 2005).

If the potential is swept back to E_1 , a full potential cycle is generated; this is identified as cyclic voltammetry. Single or multiple cycles can be enacted depending on the information being sought. The potentiostat measures the resulting current that emanates during the full duration of the potential sweep when potential (voltage) is applied.

The current versus potential (voltage) plot depicted in Figure 3-14 is termed a "cyclic voltammogram". A cyclic voltammogram (CV) is multifaceted and dependent on multiple factors, including time and the sample's chemical and physical properties.

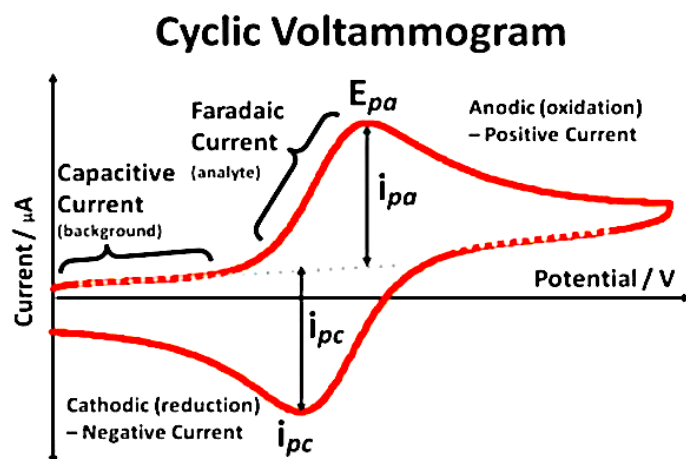


Figure 3-14: Cyclic voltammogram (Figure derived from (Davies et al., 2005)).

As shown in Figure 3-14, the voltammogram consists of mainly two current peaks: the oxidation peak (anodic peak) and the reduction peak (cathodic peak). The potential window is fixed before testing, taking into consideration that all the standard potential of species' electrochemical reactions involved should fall within the specified potential range.

3.10.1.2 Procedure for Cycling Voltammetry

Figure 3-15 presents the experimental testing configuration for cycling voltammetry.

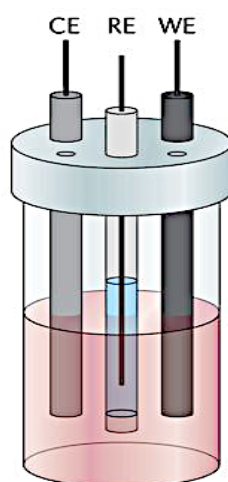


Figure 3-15: Experimental testing configuration for conventional cycling voltammetry (Figure adapted from (Tawonezvi, 2020)).

The experimental testing configuration for cyclic voltammetry consists of three electrodes immersed in an acidic electrolyte solution. The three electrodes, namely the working electrode (Al electrode), the counter electrode (Pt coated Ti electrode) and the reference electrode (Ag/AgCl electrode), are connected to the N series Autolab potentiostat/galvanostat system.

All the electrodes were immersed totally in the electrolyte to obtain accurate data results. This configuration serves just for electrochemical testing purposes. However, during the experiment, it must be ensured that there is no side reaction going on inside the testing cell. Gas tightness is important since CO₂ present in the air that fills the laboratory, reacts with NaOH to form Na₂CO₃ and H₂O as shown in the reaction below:



This reaction was curbed by gas-tightening the apparatus. If the apparatus is not gas-tight, the concentration of electrolyte falls further and decreases the measuring results. The reason for even temperature control is that the electrolyte has a different conductivity depending on the temperature and thus, a comparability of the measuring results at different temperatures is difficult.

The temperature control also helps to ensure that the internal pressure in the apparatus does not become smaller than the ambient pressure since the temperature thus no longer has a disturbing effect on the cell's internal pressure.

The pieces of equipment used for experiments were as follows:

1. A Metrohm Autolab PGSTAT302N potentiostat/galvanostat that is managed by NOVA software (arranged as depicted in Figure 3-17).
2. Silver/Silver Chloride reference electrode (SCE).

Figure 3-16 depicts the on-ground schematic representation of the test environment.

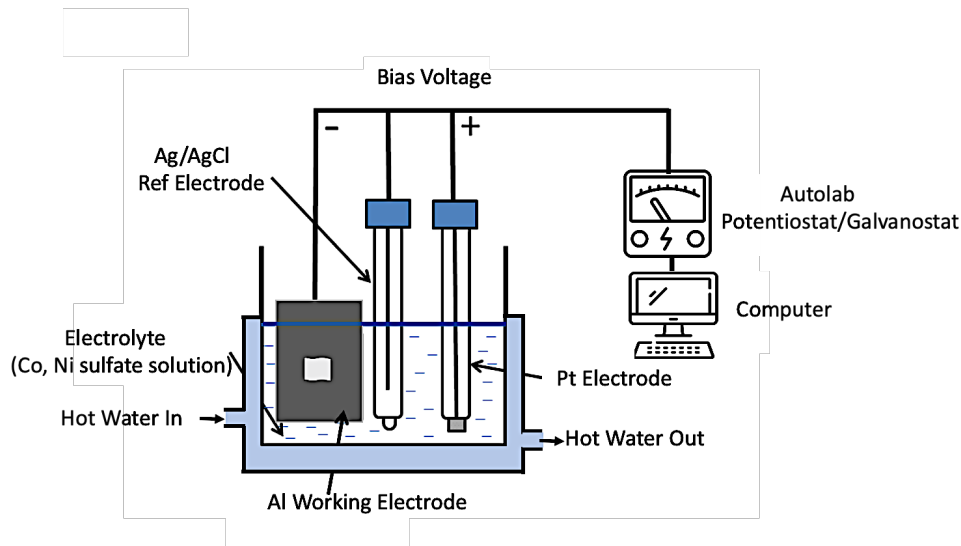


Figure 3-16: Schematic representation of the on-ground test environment.

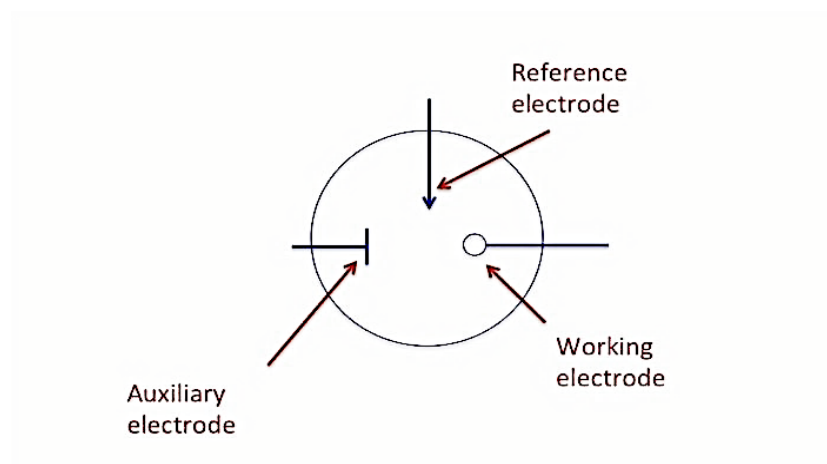


Figure 3-17: Schematic representation of the on-ground test environment (Top view).

Nitrogen was filled into the apparatus via the rubber stopper, in which a fermenting tube was attached to the apparatus during the execution of the test run. This nitrogen is supposed to displace the O_2 and CO_2 from the apparatus so that it is not absorbed by the electrolyte and thus no unwanted precipitates form in the electrolyte.

Cobalt sulphate and nickel sulphate salts were dissolved in triply distilled water to make 15 g/L Co^{2+} , 15 g/L Ni^{2+} and 47.5 g/L $Ni^{2+}_{0.25}Co^{2+}_{0.1}Mn^{2+}_{0.15}Li^{+}_{0.5}$ electrolyte solutions. The 10 x 10 mm active area aluminium working electrode was immersed in the electrolyte (Co/Ni Leachate solution) with a Pt counter electrode and Ag/AgCl reference electrode (Figure 3-17). All three electrodes are fit with correspondingly sized O-rings so they can rest upon a Teflon

cap set into a glass electrowinning cell. All electrodes were submerged in electrolyte solution and were ideally level with each other. The electrodes were contacted with alligator clips outside of the cell (as depicted in Figure 3-9) at the electrode tip not submerged in the electrolyte solution. The active area of the electrode is immersed in the electrolyte, while the non-active area is covered with polyfilm to prevent exposure of the electrode material to the electrolyte. These measuring cables were connected to the Autolab potentiostat via cable glands through the cover of the apparatus. The measurements were recorded at a sweep rate of 2.5 mV/s and within a potential range from -0.2 to -1.2 V.

3.10.2 Potentiostatic Electrochemical Operation

3.10.2.1 Working Principle

In constant voltage, the working electrode is subjected to constant voltage until the electrode potential reaches the pre-set voltage (Pyun *et al.*, 2012). Pyun et al (2012) iterated that constant voltage charging, also known as constant potential charging, is usually performed on a battery testing system (BMS). The BMS produces current to charge the battery whereby the voltage in this type of system is usually held constant. With a constant voltage, the charging rate to a low battery will be high. But as the battery approaches full charge, the opposing voltage of the battery goes up, so it more strongly opposes the charging current. This opposition to the charging current indicates that a smaller charge is needed. As the battery approaches full charge, the charging voltage decreases. This condition decreases the ability to maintain a charging current to the battery. As a result, the charging current tapers off to a very low value by the time the battery is fully charged. This principle of operation is the same as that of the voltage regulator on a vehicle. The two available charging programs are depicted in Figure 3-18.

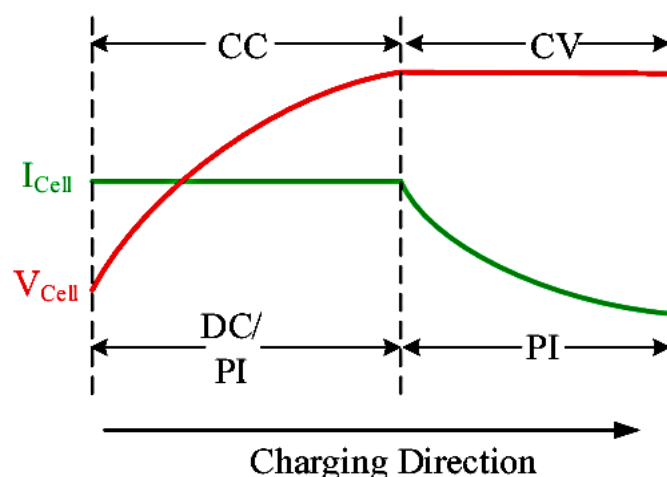


Figure 3-18: Constant current and constant voltage charging (concept adapted from (Pyun et al., 2012)).

The standard charging programs (presented in Figure 3-18) can be readily utilised to comprehensively characterize the electrochemical properties of electroactive materials.

3.10.2.2 Equipment for Constant Potential Electrowinning Test

- **Equipment and Software for Galvanostatic Analysis**

In order to undertake potentiostatic and galvanostatic tests and operations, a Metrohm Autolab testing system PGSTAT302N (depicted in Figure 3-19) was used.



Figure 3-19: Front panel of the metrohm autolab electrochemical testing station.

- **Software**

The host computer of metrohm autolab testing system PGSTAT302N is equipped with NOVA software that assists with custom writing of potentiostatic and galvanostatic programs.

3.10.2.3 Procedure for Constant Voltage/Current Operation

- **Start-up and Operation**

Start-up: set steps on the electrochemical channel, start channels work according to the setting step: including constant current discharge, constant current charge, constant voltage charge, constant current constant voltage charge, constant power discharge, rest, cycle, etc.

1. Open Nova.
2. Click and Select Method: CV, IV, Linear Sweep, Chronopotentiometry, Potentiostatic etc.
3. Define relevant parameters:
 - Current (Galvanostatic)
 - Potential (Potentiostatic)
 - Start Potential
 - Stop Potential
 - Step Potential
 - Time
 - Scan Rate
4. Press Start.
5. Open Data: for working channel data (Voltage, current, capacity, and cycles) for real-time display.

- **Potentiostatic Operation**

Throughout the whole test period, the cells were placed in a water bath at a specified temperature. Cells were connected to a device where they undergo of charge phase comprised of:

1. A rest step of 30 minutes
2. A charge step at constant voltage (potentiostatic), $V=V_x$ for 3 hours

3. A rest step for 30 minutes

- **Galvanostatic Operation**

Throughout the whole test period, the cells were placed in a water bath at a specified temperature. Cells were connected to a device where they undergo of charge phase comprised of:

1. A rest step of 30 minutes
2. A charge step at constant current (galvanostatic), $I=I_x$ for 3 hours
3. A rest step for 30 minute

Chapter 4: Inorganic Acid-Reductant Leaching of Valuable Metals from NMC 532 Cathodes

4.1 Overview

The results presented in this chapter are the outcomes of numerous experiments that were conducted during the study. Several investigations were carried out, in order, involving NMC cathode composition analysis and inorganic acid-reductant leaching. The leaching parameters such as solid/liquid ratio, temperature, acid and reductant concentration and leaching time were successfully optimized to recover effectively the valuable metals (Ni, Co, Mn, Li) from $\text{LiN}_{0.5}\text{Mn}_{0.3}\text{Co}_{0.2}\text{O}_2$ (NMC 532) cathode material. The composition of the solids was meticulously quantified using ICP-OES and SEM-EDS, while the liquids were analysed by ICP. Additionally, the phase composition was evaluated through XRD analysis, and the morphology of the solids was examined using SEM. The findings demonstrated the technical feasibility of high metal recovery through inorganic acid-reductant leaching.

4.2 NMC Material Characterisation and Analysis

To assess the elemental composition of the cathode (88.5% active material + 11.5 % of binder, Al foil, and Carbon), ICP-OES and EDS were utilized. In this work, X-ray diffraction (XRD) was utilized to determine the phase composition—including phase identification—and to analyse orientation. The XRD pattern of the NMC cathode material, shown in Figure 4-1, reveals that the valuable metals (Ni, Co, Mn, and Li) are predominantly present in the $\text{LiN}_{0.5}\text{Mn}_{0.3}\text{Co}_{0.2}\text{O}_2$ (NMC 532) crystalline phase (PDF #01-084-4264). This phase corresponds to the layered $\alpha\text{-NaFeO}_2$ structure with the space group $R\bar{3}m$, as described by Noh et al. (2013). The sharp peaks and distinct peak splitting observed in the (006)/(012) and (018)/(110) diffraction pairs confirm a well ordered crystalline layered structure for NMC 532 (Noh et al. 2013).. XRD analysis indicates no formation of new phases during the cathode storage period or pretreatment, as the XRD patterns of the

NMC material align well with the reference spectrum. However, some very small peaks could not be precisely identified, suggesting the possible presence of trace amounts of additional phases. Phases with concentrations below 3 wt.% are beyond the detection limit of the XRD analysis and were thus not included in the analysis results.

Based on the phase composition analysis and elemental composition analysis, the analysis further showed that 99.9% of the cathode material originated from NMC batteries. Moreover, the absence of detected carbon, typically in the cathode matrix, indicates that the pre-treatment process for Li-ion component separation effectively prevented contamination of the black mass powder.

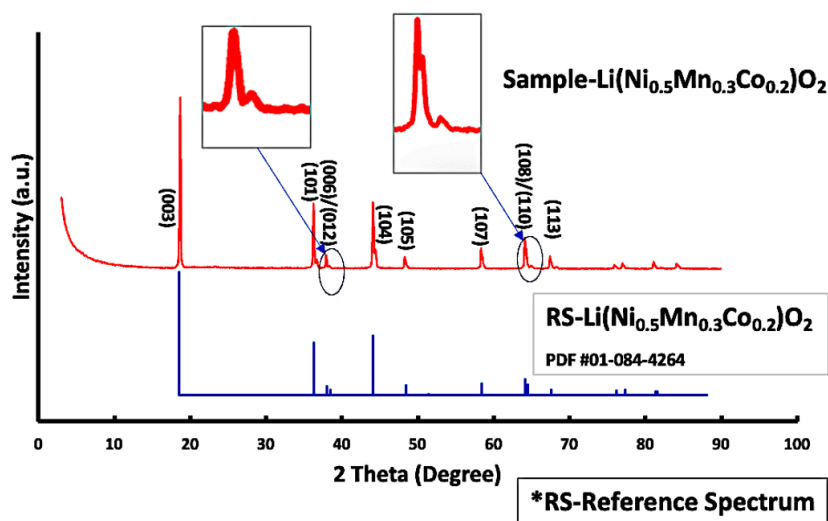


Figure 4-1: The X-ray diffraction (XRD) pattern of spent lithium nickel manganese cobalt oxide (NMC 532) cathode materials.

Figure 4-2 shows the microscopy and spectroscopy analysis of the cathode material by SEM and EDS, respectively. The analysis indicated the presence of metals Ni, Co, O, and Mn, the elements that are distributed throughout the sample, indicating a high level of homogeneity. In conclusion, the analysis successfully detected the presence of valuable metals Ni, Co, and Mn but not for Li since equipment cannot detect Li. ICP-OES and EDS, were used to analyse and quantify the chemical and material composition of the Li-ionB cathode materials. All ICP analysis results

presented in this work, which are used for primary composition analysis, show a standard deviation ranging from 0.4% to 1.3% across the triplicate experiments. SEM was used to assess the morphology and approximate particle size. The results indicated that the NMC metals (Li, Mn, Co, and Ni) were present in the following compositions: 18.2% Co, 44.4% Ni, 26.2% Mn, 10.9% Li, and traces of Al contaminants (from pre-treatment), which did not exceed 0.68% ($0.4 \pm 0.28\%$), as shown in Table 4-1. The SEM imaging shows spherical morphology and average particle size of $12.5 \mu\text{m}$, as assessed from SEM images using the ImageJ program.

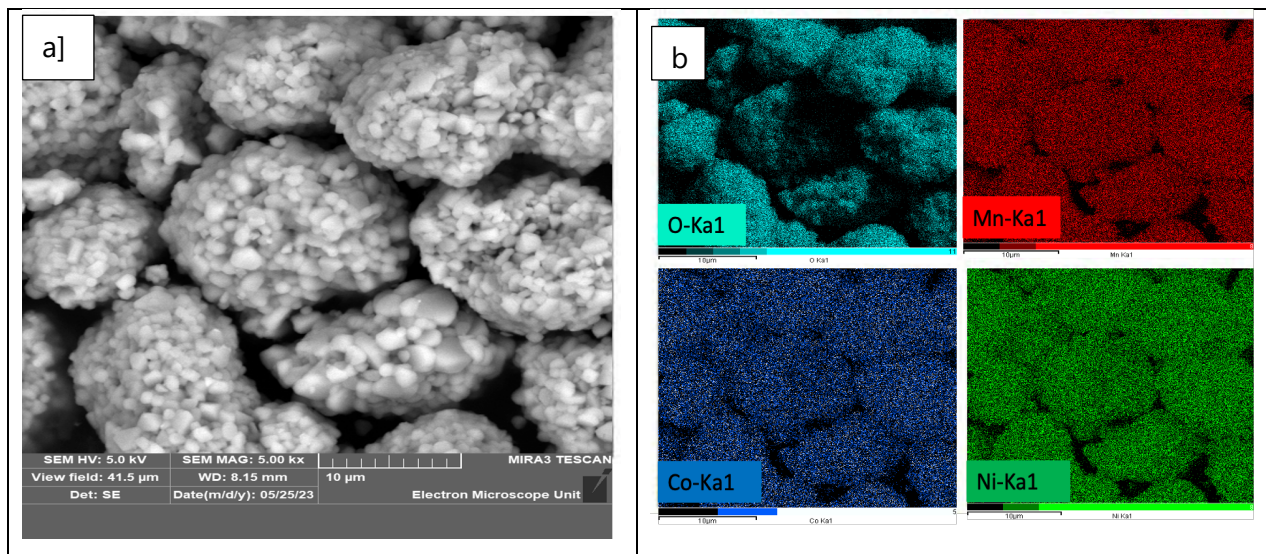


Figure 4-2: (a) The scanning electron microscopy (SEM) analysis of cathode materials; (b) the energy-dispersive X-ray spectroscopy (EDS) analysis of NMC cathode materials.

The significant similarity in the physicochemical and electrochemical properties of Co and Ni contributes to the co-precipitation and co-extraction of the two elements (Flett 2004). Ultimately, since the Co and Ni separation processes are costly, an alternative process route to extract high-purity Ni-Co alloys is developed and presented in this work but in order to electro-extract the Ni-Co alloys, the Ni, Co, Li and Mn metals have to be leached first from the NMC active material.

4.3 Leaching Process Optimization

4.3.1 NMC 532 Composition Analysis

In order to calculate the amount of metal extracted during leaching, samples of the Li-ionB cathode material were analysed, and the metal composition of Ni, Mn, Co, and Li the starting cathode material was quantified. Table 4-1 shows the metal composition of the cathode material obtained at the end of the pre-treatment stage.

Table 4-1: Characterization of the sample using ICP-OES obtained after pre-treatment of the NMC battery cathode used for the acid leaching tests.

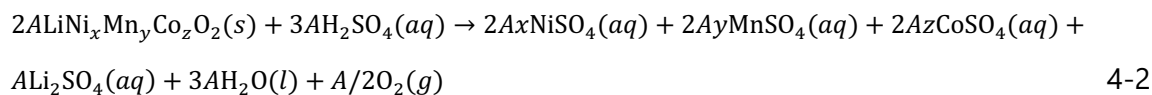
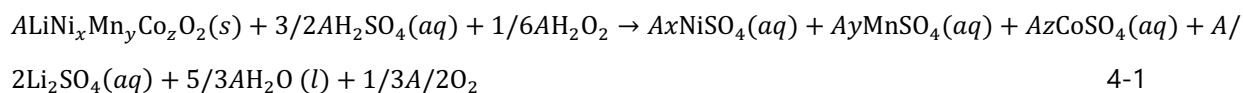
Metals	Composition Weight Percentage (%)
Co	18.3
Ni	44.6
Mn	26.2
Li	10.9
Al	0.4

4.3.2 Effect of H₂O₂ on Leaching Efficiency

In the first step, the effect of H₂O₂ concentration on the leaching recovery efficiency of the spent cathode active materials was investigated. The spent LiNi_{0.5}Co_{0.2}Mn_{0.3}O₂ material was leached with 3 M H₂SO₄ acid solution at an solid to liquid (S/L) ratio of 25 and 45 g/L and impeller speed (IS) of 350 rpm. In addition, the temperature was maintained at 70°C and the leaching time was 180 min during the metal leaching process. The effect of H₂O₂ on leaching efficiency results (depicted in Figure 4-3) indicate that the concentration of H₂O₂ increases proportionally with leaching recovery efficiency at both S/L of 25 g/L and 45 g/L.

The addition of H₂O₂ or similar reducing agents during leaching serves the purpose of reducing transition metals found in spent Li-ionB cathodes (such as Co³⁺ to Co²⁺) into lower and more readily leachable valence states (Lee and Rhee 2003a; Meshram et al. 2016b), thus enhancing

leaching recovery efficiency while also mitigating the necessity for utilisation of highly concentrated acid solutions (Ferreira et al. 2009b). The chemical reactions involving the leaching of the metals from Li-ionB NMC cathodes with sulfuric acid, both with and without the addition of hydrogen peroxide, are annotated by equations 4-1 and 4-2 respectively, where $x + y + z = 1$, and A symbolizes the molar quantities of reactants and products in the reactions (Vieceli et al. 2023). Notably, when sulfuric acid serves as the leaching agent and hydrogen peroxide functions as the reducing agent, the predominant gas produced during the leaching process is oxygen.



When 8% v/v H_2O_2 and a 45 g/L S/L ratio were used, the terminal leaching recovery efficiency was 99.3% for Co, 98.4% for Ni, and 97.4% for Mn. The highest terminal recovery efficiency among the four metals was for Li, recorded at 99.8%. The leaching recovery efficiency when no reductant was utilised was generally lower than 65%, which is expected when leaching is carried out without a reductant since the leaching recovery efficiency is enhanced at lower valence states (Vieceli et al. 2023). The leaching behaviour of Co and Ni exhibited similar trends during their respective leaching from NMC 532 at different H_2O_2 concentration levels. Mn had the lowest leaching recovery among the four metals (Li, Ni, Co, and Mn) from the NMC 532 cathodes, with Mn dissolution gradually increasing until it peaked at 97.1% with 6% H_2O_2 . The leaching yield after 180 min of Li, Co, and Ni from NMC 532 was slightly higher at higher S/L ratio (45 g/L) than at lower S/L ratio (25 g/L).

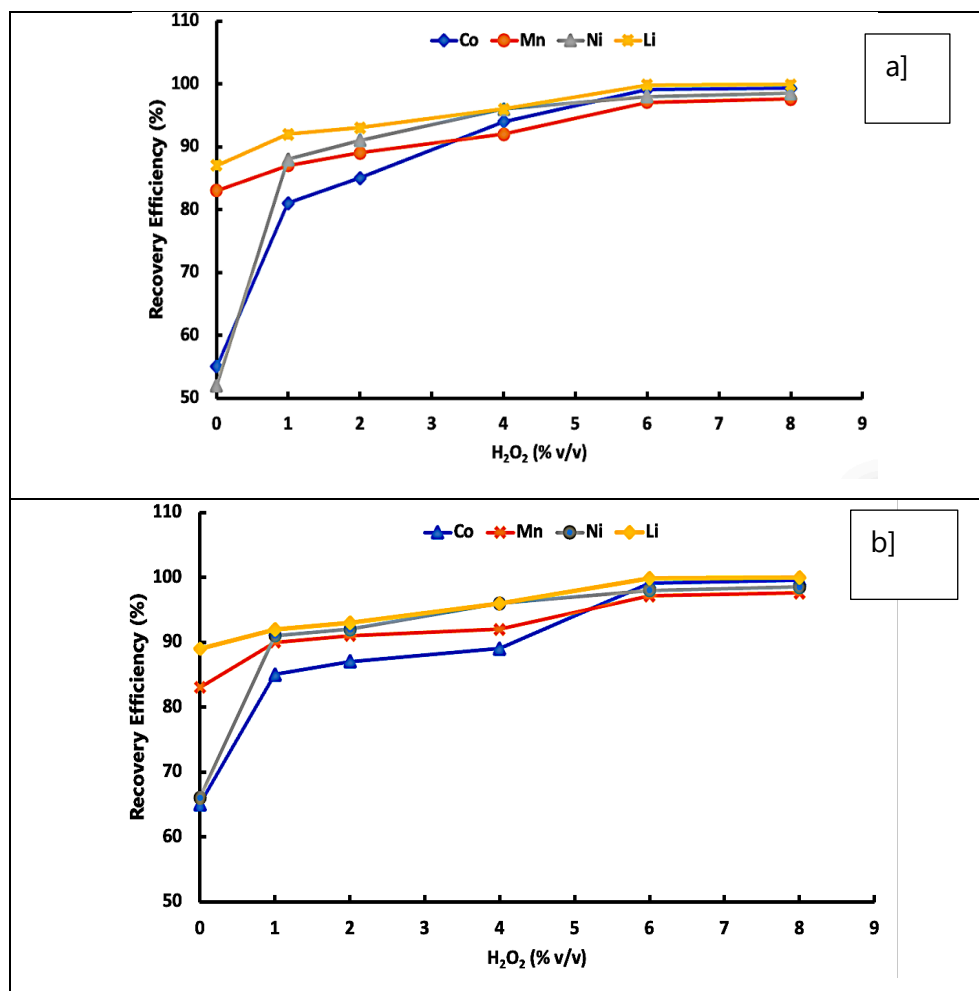


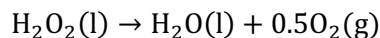
Figure 4-3: Effect of H₂O₂ concentration on leaching recovery efficiency at a) S/L=25 g/L and b) 45 g/L (H₂SO₄ =3M, Time=3 hrs, T=70 °C, IS=350 rpm).

In the absence of H₂O₂, at 25 g/L, the leaching efficiency of the spent LiNi_{0.5}Co_{0.2}Mn_{0.3}O₂ was 87 %, 55 %, 52 %, and 83% for Li, Co, Ni, and Mn, respectively (Figure 4-3 a). In the absence of H₂O₂, at higher S/L ratio of 45 g/L, the leaching efficiency of the spent LiNi_{0.5}Co_{0.2}Mn_{0.3}O₂ was 89 %, 65 %, 66 %, and 84 % for Li, Co, Ni, and Mn, respectively (Figure 4-3 b). This relatively high leaching recovery efficiency can be attributed to the fact that Li⁺, Ni²⁺, and Co²⁺ ions can be readily and effectively leached in the mere contact presence of the H⁺ protons from the acid leachate through reductive leaching while Ni³⁺, Ni⁴⁺, Co³⁺, and Mn⁴⁺ ions require a reductant to

convert them to more stable and readily leachable M^{2+} valance state ($M=> Co, Li, Mn$ and Ni) ionic form (Sun et al., 2018; Lee & Rhee, 2003).

In addition, the inclusion of reductant H_2O_2 in the leaching media converts the metal in the cathode material to more soluble ions at lower oxidation states (Rafsanjani-Abbasi et al. 2018). Therefore, more metal (from NMC) is leached per unit of time than when leaching media without H_2O_2 is utilised. The addition of H_2O_2 effectuated an increase in the leaching recovery efficiency, which consequently increased remarkably and reached above 98 % for all (Li, Ni and Co) but Mn (97 %) when the H_2O_2 content was 6 vol.% at all S/L ratios. Increasing the S/L ratio when adding hydrogen peroxide (from 0% to 6 %) during the leaching of NMC cathodes enhances leaching recovery due to the phenomenon that higher S/L ratios promote increased surface contact between the leaching reagent solution (Inorganic acid-reductant) and the NMC cathode material, facilitating particle interaction and dissolution. The improved mass transfer allows the leaching solution to efficiently reach the cathode material, enhancing dissolution of target components. Additionally, higher S/L ratios enhance reaction kinetics by increasing the availability of reactants and preventing agglomeration, ensuring more uniform contact between the solution and the cathode material. Consequently, these combined effects lead to improved leaching efficiency and higher recovery rates at higher S/L ratios.

In the leaching reaction phase where H_2O_2 is present, hydrogen peroxide could be oxidised by high-valent transition metal ions. The leaching efficiency did not exhibit any significant variation when the concentration of H_2O_2 was further increased to 8 vol.%. It is worth noting that the reductant H_2O_2 can disintegrate at high temperatures because of its low thermal stability. The decomposition reaction proceeds as annotated by the equation below: (Lee and Rhee 2003b; Meshram et al. 2016a; Cheng 2018).



4-3

It is worth noting that the decomposition of H_2O_2 will consequently affect its effective concentration during leaching hence why the leaching was operated at optimal temperatures and closed reactor environment.

4.3.3 Effect of S/L Ratio on Leaching Recovery Efficiency

In order to achieve optimal leaching results, it is generally preferable to utilise a higher solid-to-liquid (S/L) ratio, as it tends to enhance the recovery efficiency of the leaching process. In order to establish the optimal S/L ratio, the effect of the S/L ratio on leaching recovery efficiency was studied. The solid/liquid ratio (S/L) varied from 30 to 90 g/L and its respective effect on the leaching recovery efficiency of Co, Ni, Mn, and Li was studied under experimental conditions of 70 °C, 1 & 3 M H_2SO_4 , 3 hours leaching reaction time and Impeller speed (IS) of 350 rpm. Figure 4-4 (a) indicates that the leaching recovery efficiencies of Li, Co, Ni, and Mn using 3M decrease negligibly as the S/L ratio increases and then drop sharply after the 75 g/L S/L ratio.

At an S/L ratio of 75 g/L, more than 97% of the Li, 94 % of the Co, 95% of the Ni, and 91% of the Mn was leached. Figure 4-4 (b) indicates that the leaching recovery efficiencies of Li, Co, Ni, and Mn using 1M decrease negligibly as the S/L ratio increases and then drop sharply after the 45 g/L S/L ratio. At an S/L ratio of 75 g/L, more than 89.6% of the Li, 85.2% of the Co, 86.1% of the Ni, and 82.2 % of the Mn was leached which is significantly lower compared to the leaching recovery efficiencies at 3M. This is due to the increased reactivity of hydrogen ions in the acidic solution which facilitates the dissolution of metals. In addition, the higher solubility of metal compounds in more concentrated acid solutions allows for better separation of metal ions from the solid NMC matrix.

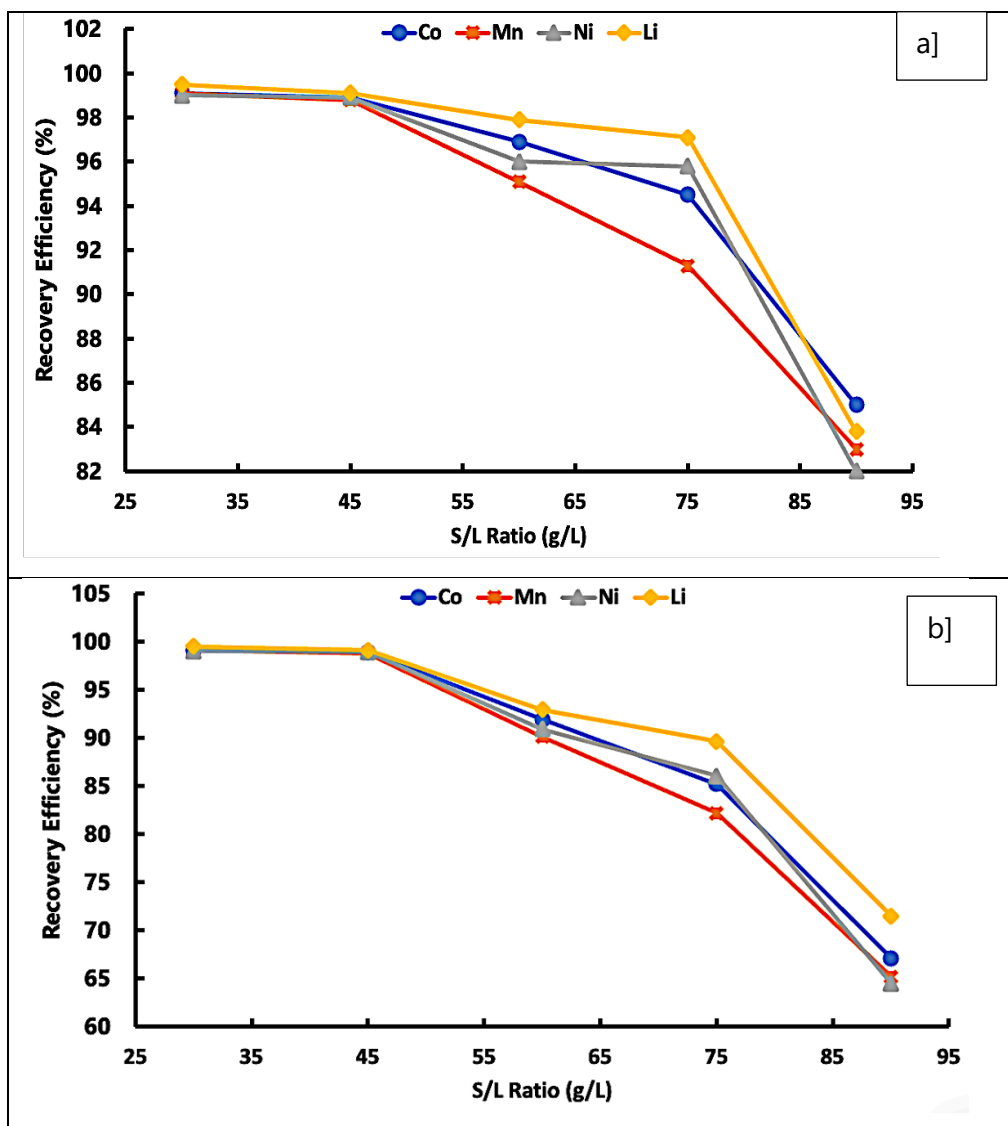


Figure 4-4: Effect of solid-to-liquid ratio on the leaching recovery efficiency at different acid concentrations a) 1 M and b) 3M (6 % v/v H₂O₂, t=180 min, T=70 °C, IS=350 rpm).

The leaching recovery efficiency dramatically dropped when the S/L ratio went above 75 g/L. At a low S/L ratio, there are more acid leachant molecules surrounding solid molecules during leaching therefore the recovery efficiency will be higher compared to when there is a higher S/L ratio, in this case, the solid becomes the limiting reagent consequently resulting in a reduced recovery efficiency. The increase in leaching recovery efficiency, with time, is due to increased collisions between solid material sub-particles and reductant H⁺ ions from the acid leachant.

However, when the solid concentration exceeds the saturation concentration point further increase of the solid concentration will exhibit no effect on the leaching reaction kinetics. The ideal solid/liquid ratio was consequently identified to be 75 g/L after accounting for both chemical consumption and leaching recovery efficiency.

4.3.4 Effect of H₂SO₄ Acid Concentration on Leaching Recovery Efficiency

The effect of H₂SO₄ acid concentration on the leaching recovery efficiency was studied under the conditions of an S/L ratio of 75 g/L, leaching reaction time of 3 hrs, Impeller Speed of 350 rpm, and reaction temperature of 50 °C and 70 °C. As depicted Figure 4-5, the leaching recovery efficiencies of various metals (Li, Ni, Mn, and Co) demonstrated a positive correlative trend with increasing H₂SO₄ acid concentration from 0.5 to 2 M and 50 to 70 °C. At 2 M H₂SO₄ concentration and 70 °C temperature, the leaching process achieved satisfactory recovery efficiencies of over 96 % for Li, 94 % for Co, 95 % for Ni, and 91 % for Mn. Leaching recovery efficiency increased significantly as the H₂SO₄ acid concentration increased from 0.5 M to 1 M, then gradually increased between 1-2 M. Further increase of the H₂SO₄ acid concentration (at over 2 M) does not effectuate any significant increase in leaching recovery efficiency.

At 2 M H₂SO₄ concentration and 50 °C temperature, the leaching process achieved satisfactory recovery efficiencies of over 95.5% for Li, 93.4% for Co, 94.6% for Ni, and 90.2% for Mn. This trend indicates that higher recovery efficiencies can only be attained at higher concentrations (≥ 2 M) and at higher temperature (≥ 70 °C), however adequate recovery efficiencies $>85\%$ are also achieved at moderate concentration (1M) and temperature (50 to 70 °C). This is due to the correlation that higher temperatures and acid concentrations effectuate increased reaction rates and enhanced solubility, promoting more efficient dissolution of metals from solid materials. Elevated thermal energy facilitates mass transfer, aiding the movement of the leachant through the porous NMC structure. Temperature also influences the viscosity of the solution and the selectivity of leaching for different metals.

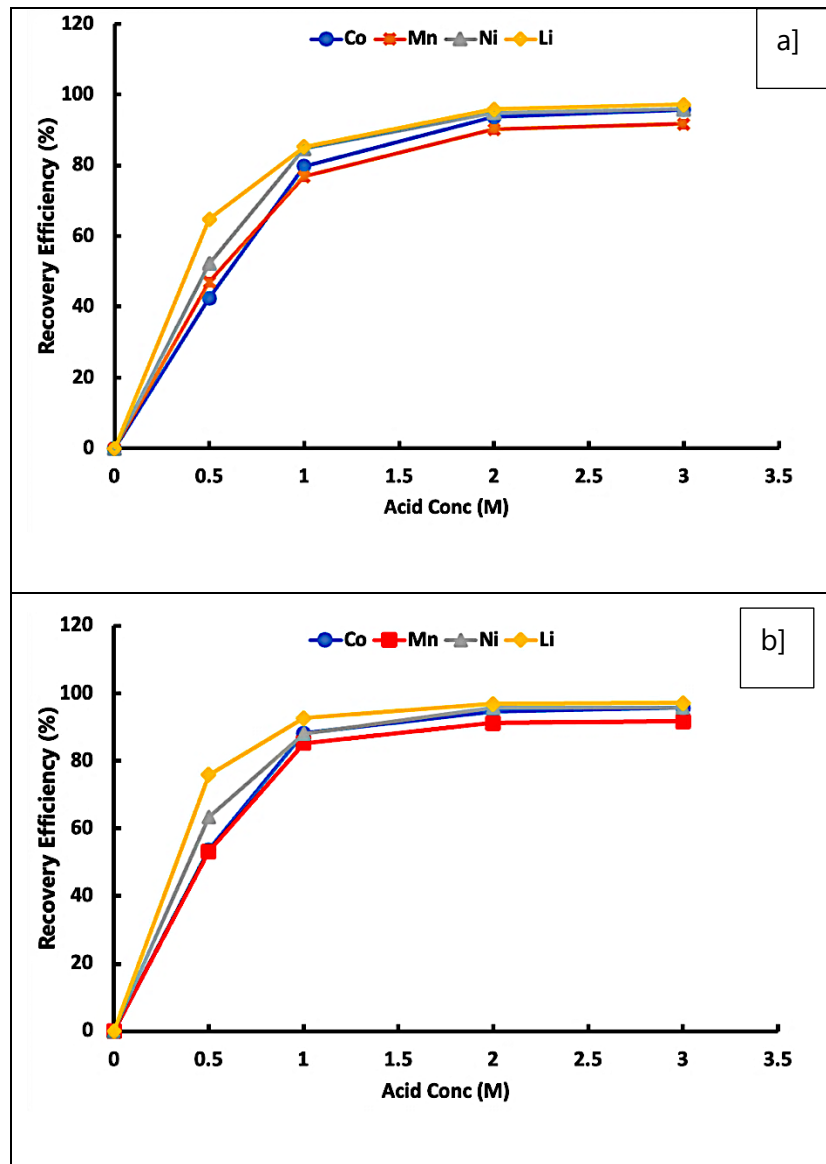


Figure 4-5: Effect of H₂SO₄ acid concentration on leaching recovery efficiency at different temperatures a) 50 °C and b) 70 °C (6 % v/v H₂O₂, t = 180 min, S:L=75 g/L, IS=350 rpm).

Leaching recovery efficiency at 70 °C increased significantly as the H₂SO₄ acid concentration increased from 0.5 M to 1 M, then gradually increased between 1-2 M. Further increase of the H₂SO₄ acid concentration (at over 2 M) does not effectuate any significant increase in leaching recovery efficiency. The increase in leaching efficiency is due to increased collisions between solid material sub-particles and reductant H⁺ ions from the acid leachant. However, when the

reductant H^+ ions concentration exceeds the saturation concentration point further increase of the acid concentration will exhibit no effect on the leaching reaction kinetics. Hence, the optimal H_2SO_4 acid concentration for the leaching process is locked at 2 M after taking into account both chemical consumption and leaching recovery efficiency.

4.3.5 Effect of Leaching Temperature on Leaching Recovery Efficiency

The effect of the temperature on the leaching recovery efficiency is illustrated in Figure 4-6. The leaching recovery efficiency increased with the increasing temperature due to the significant kinetic effect temperature has on the metal leaching reaction. The increase in temperature increases the ionic, electronic and molecular movement frequency and leaching chemical reaction rate, thus accelerating the molecular and ionic migration and diffusion and mass transfer rate in the metal-leaching system, and ultimately favouring the metal-leaching kinetic process.

At lower S/L ratio (Figure 4-6 b), the metal leaching recovery efficiencies are higher compared to the higher S/L ratio (Figure 4-6 a). This is due to the correlation that a lower solid-to-liquid ratio in leaching processes contributes to the increased efficiency of metal leaching from solid materials. This is primarily attributed to the increased contact surface area between the solid material and the leachant, facilitating improved interaction and dissolution of metals. The reduction in diffusion resistance allows the leachant to more easily reach the surface of the solid NMC material, promoting efficient metal leaching through enhanced mass transfer. Additionally, the concentrated leachant in a moderated S/L ratio can exhibit a more potent effect in breaking down the solid material, creating optimal conditions for leaching reactions. At an S/L ratio of 75 g/L (60 °C), more than 97% of the Li, 94 % of the Co, 95% of the Ni, and 91% of the Mn was leached.

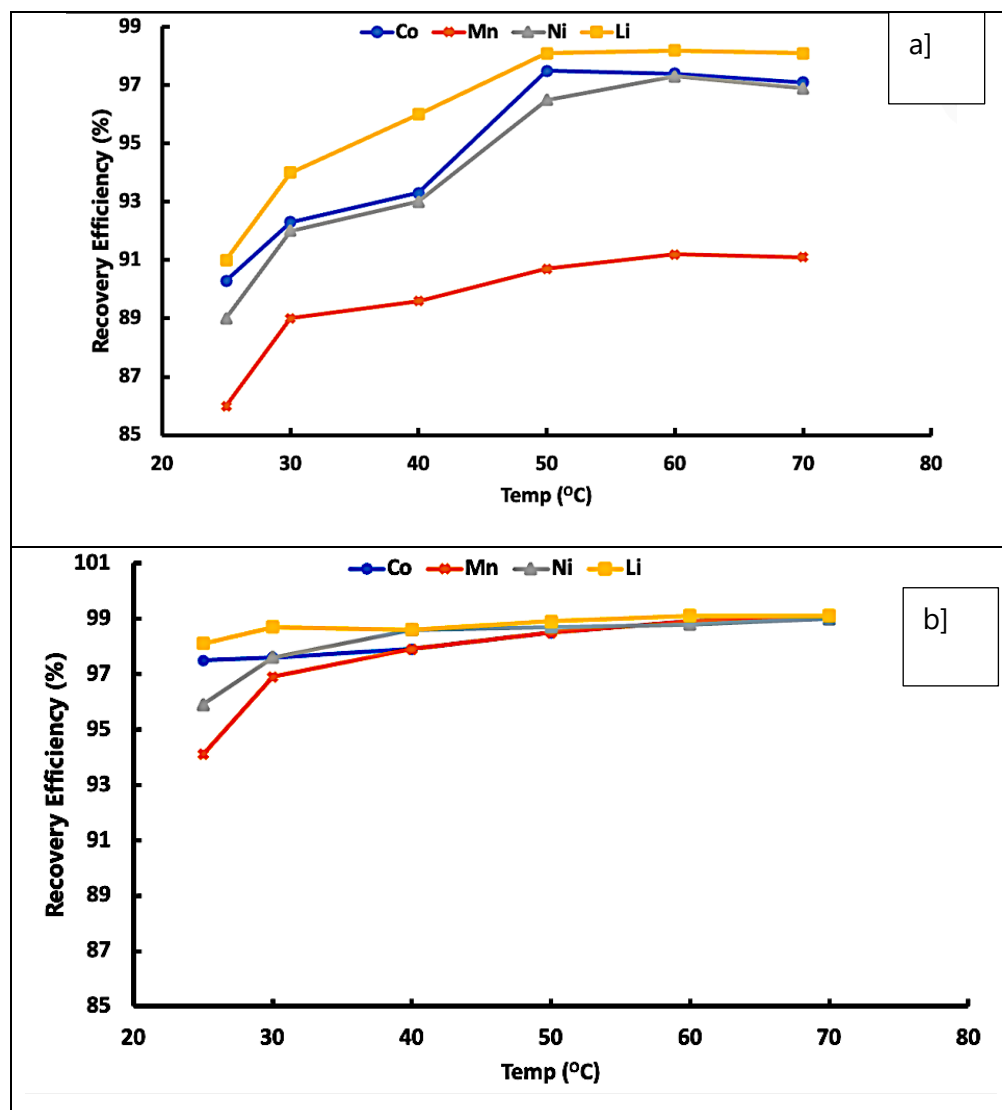


Figure 4-6: Effect of temperature on leaching recovery efficiency at different S/L ratios a) 75 g/L and b) 45 g/L (6 % v/v H₂O₂, H₂SO₄ =2M, S/L=75 g/L, Time=180 mins, IS=350 rpm).

4.3.6 Effect of Leaching Reaction time on Leaching Recovery Efficiency

The effect of leaching reaction time (0-180 minutes) on the leaching of Co, Ni, Mn, and Li was examined using specific constant conditions: H₂SO₄ acid concentration of 2 M, solid-to-liquid (S/L) ratio of 75 g/L, reaction temperature of 60 °C, and an agitation speed (IS) of 350 rpm. As illustrated in Figure 4-7, the leaching reaction time significantly affects the leaching recovery

efficiency for all the metals leached. The leaching recovery efficiencies of Co, Li, Ni, and Mn substantially increased by about 41%, 21%, 36%, and 62% when the leaching reaction time was increased from 15 to 180 min. The effect was attributed to the fact that with the increase in the leaching time, a greater and greater surface area of the unreacted particle cores collided and reacted with the reductant H^+ ions from the sulphuric acid leachant. The largest increase in leaching efficiency per unit of time was apparent in the first 30 min. As the reaction proceeded at times more than 30 minutes, the leaching recovery efficiency-time slope became less steep. The leaching recovery efficiency peaked at 120 minutes, with efficiencies of over 97.1%, 96.1%, 96.1%, and 95.7% for Li, Co, Ni, and Mn, respectively. Thereafter, the recovery efficiency remained relatively stable without significant changes. Consequently, a 120-minute leaching reaction was identified as the optimal leaching time.

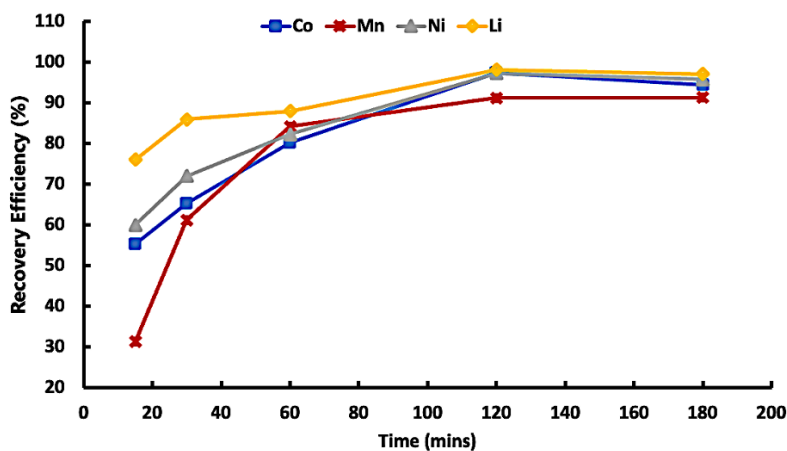


Figure 4-7: Effect of time on leaching recovery efficiency (6 % v/v H_2O_2 , $H_2SO_4 = 2M$, $S/L = 75$ g/L, $T = 60$ °C, $IS = 350$ rpm).

4.3.7 Leaching Kinetics

In light of the discussion above, the optimal conditions for the leaching of Co, Ni, Mn, and Li from waste $\text{LiNi}_{0.5}\text{Co}_{0.3}\text{Mn}_{0.2}\text{O}_2$ can be determined. Through the utilisation of leachant solutions comprising 2M H_2SO_4 + 6 vol.% H_2O_2 , and a 75 g/L S/L ratio and conducting leaching for 120 minutes at a temperature of 60°C, peak leaching recovery efficiency of 98.9% for Li, 97.1% for Co, 96.9% for Ni, and 95.7% for Mn can be attained as shown in Table 4-2. The maximum metal recovery that was attained is $0.595 \text{ g}_{\text{total metal}}/\text{g}_{\text{cathode}}$.

Table 4-2: Leaching yields obtained using a 75 g/L S/L, 2M H_2SO_4 + 6 H_2O_2 v/v % solution, at 60 °C for 2h.

Element	Composition (All Elements in Cathode)		Composition (NMC Elements Cathode)	Expected Leachate Conc. [g/L]	Real Leachate Conc. [g/L]	Recovery [%]	Recovery rate ($\text{g}_{\text{metal}}/\text{g}_{\text{cathode}}$)
	Mv.*	Tv.*	Mv.	Mv.*	Mv.*		
Li	6.7	6.4	10.9	5.04	4.98	98.9	0.066
Ni	27.2	27	44.4	20.58	19.94	96.9	0.264
Co	11.3	10.8	18.2	8.46	8.21	97.1	0.110
Mn	16.2	15.1	26.1	12.10	11.59	95.7	0.155
O	27.1	29.3					
Non NMC 532 Elements	11.5	11.5					
Total							0.595 g/g

***Mv**=Measured values (All measure compositions were determined using ICP-OES)

***Tv**=Theoretical values (Calculated using stoichiometry equations)

The leaching reaction kinetics of metal dissolution from the spent Li-ionBs cathodic material have been calculated and quantified using the data correlations obtained by varying the reaction temperature and leaching residence time. Leaching reactions were performed at a constant S/L ratio of 75 g/L and leachant concentration of 2 M H₂SO₄ + 6 vol% H₂O₂. The first-order reaction kinetics equations of the shrinking core model and Avrami model were examined for the reductive leaching (dissolution) reaction for Co, Mn, Ni and Li (Zhou et al. 2018; Meng et al. 2020; Xiao et al. 2020; Sahu and Devi 2023; Bhagaskara et al. 2024; Wang et al. 2024). The constant values of K_c at different temperatures were quantified using a carefully selected theoretical kinetic model. The experimental leaching kinetic models for Co, Mn, Li and Ni dissolution fit well with the three kinetic models "spherical particles under reaction control", "spherical particles under product layer diffusion control" and "Avrami" as annotated in the equation below (Liddell 2005; Zhou et al. 2018; Meng et al. 2020; Xiao et al. 2020; Sahu and Devi 2023; Bhagaskara et al. 2024; Wang et al. 2024):

Model I, spherical particles under reaction control;

$$1 - (1 - X)^{1/3} = K_c t. \quad 4-4$$

Model II, spherical particles under product layer diffusion control;

$$1 - 3(1 - X)^{2/3} + 2(1 - X) = K_c t \quad 4-5$$

Model III, Avrami model;

$$\ln(-\ln(1 - X)) = \ln K_c + n \ln t \quad 4-6$$

where K_c is the reaction rate constant (1/min), t is time (min), n is the Avrami exponent and X is recovery efficiency of metal (%).

On the basis of these equations, the highest value time reaction rate constant product ($K_c t$), i.e. the regression coefficient and the constant value of $K_c t$ were calculated. The best-fit model was selected based on the regression value (R^2) for each metal matrix at different temperatures.

Graphical plots for each equation using experimental data were computed: Model I is shown in Figure 4-8, Model II in Figure 4-9, and Avrami Model in Figure 4-10. These plots illustrate the effect of temperature on the leaching reaction kinetics.

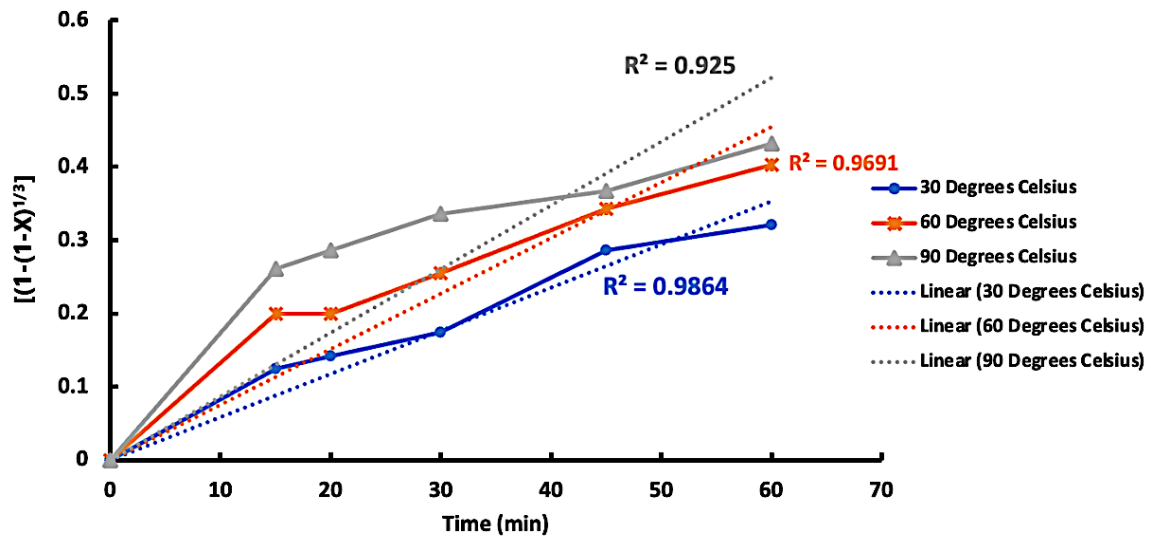


Figure 4-8: Experimental fit for Model I: Spherical particles under reaction control.

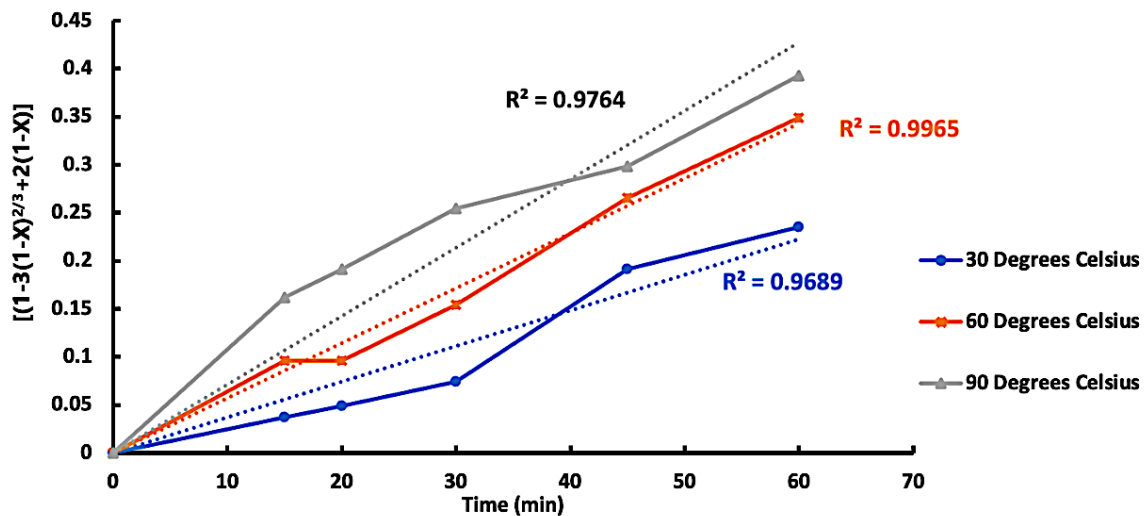


Figure 4-9: Experimental fit for Model II: Spherical particles under product layer diffusion control.

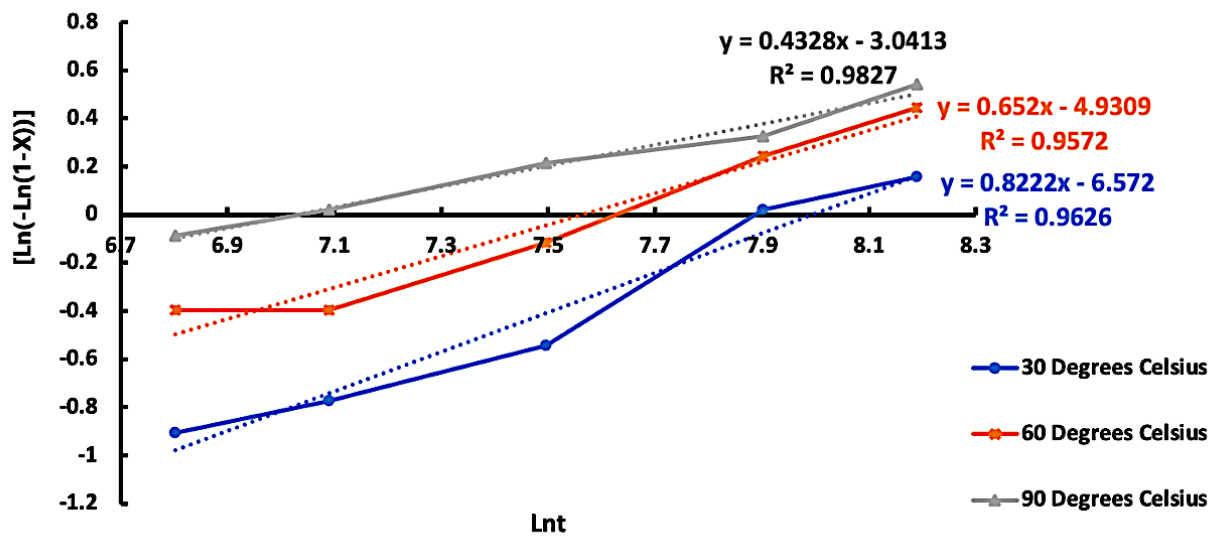


Figure 4-10: Experimental fit for Model III: Avrami model.

Table 4-3: Kinetic parameters for leaching of Li, Co, Ni, and Mn under different temperature Model I, Model II and by Avrami model.

	30 °C		60 °C		90 °C	
	K_c (min^{-1})	R^2	K_c (min^{-1})	R^2	K_c (min^{-1})	R^2
Model						
Model I	0.0059	0.9864	0.0076	0.9691	0.0087	0.9250
Model II	0.0037	0.9689	0.0057	0.9965	0.0071	0.9764
Avrami	0.0014	0.9626	0.0072	0.9527	0.0478	0.9827

Based on the data in Table 4-3, Model I, the 'Spherical particles under reaction control' model, fits the leaching reaction satisfactorily at 30 °C, while Model II, which describes 'spherical particles under product layer diffusion control,' fits best at 60 °C. The Avrami model fits best at 90 °C. Overall, however, the leaching reaction aligns more closely with model II which describes 'spherical particles under product layer diffusion control' ($R^2 > 0.9680$ for all temperatures as shown

in Table 4-3). The results indicate that the increase in the residence time and temperature results in an increase in metal recovery efficiency as highlighted and discussed in previous sections.

The kinetic constant (K_c) values obtained from the slope analysis of the time versus reaction rate constant-time product for Model II at different temperatures were used to create the Arrhenius plot. The calculation to evaluate activation energy using the Arrhenius equation which has been adapted to linear line equation as follows:

$$\ln[Kc] = \ln[A] - \frac{E_a}{R} \cdot \frac{1}{T} \quad 4-7$$

Where A is the frequency factor, E_a is the activation energy, R is the universal gas constant, K_c is the reaction rate constant, and T is the absolute temperature.

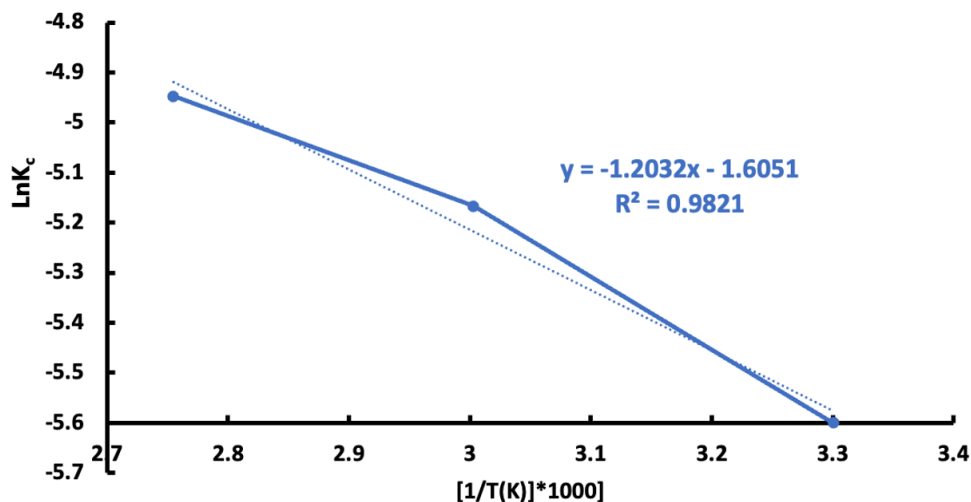


Figure 4-11: Arrhenius plot for leaching of metals from Li-ionBs.

The activation energy (E_a) was quantified, using a modified linear line equation generated from the Arrhenius plot (Figure 4-11), to be +12.1 kJ/mol as shown in Figure 4-11. A lower activation energy implies that leaching reaction can occur more easily and at lower temperatures. The activation energy value, which indicates improved kinetics, is significantly lower than the

published E_a values for the leaching of NMC metals, which range between 30 and 65 kJ/mol (Meng et al. 2020; Sahu and Devi 2023; Bhagaskara et al. 2024; Wang et al. 2024).

The positive E_a indicates that the reaction rate increases with temperature, as expected for thermally activated leaching processes (Lee and Rhee 2003a; Wang et al. 2012; Li et al. 2014, 2017; Zhou et al. 2018). This is consistent with the principles of the Arrhenius equation, which suggests that higher temperatures provide the necessary energy to overcome the activation barrier, thus accelerating the reaction. Furthermore, the experimental data for the leaching reaction closely follow Model II, which describes the rate of a chemical reaction occurring on spherical particles, where the reaction is limited by the diffusion of products through a surrounding layer. This alignment suggests that the leaching process may involve similar mechanisms that are temperature-dependent, further corroborating the observed effects of temperature on the reaction rate.

Chapter 5: Electrowinning Optimization Using Synthetic Quasi NMC 532 Solutions

5.1 Overview

This chapter is hinged on research that is centred on the recovery of Ni and Co (as Ni_xCo_y) from synthetic Ni, Co, Mn and Li sulphate solutions mimicking the NMC 532 ratio of elements using a hydro-electrometallurgy process route that integrates hydrometallurgy and potentiostatic electrometallurgy techniques. This quasi-model is done to elucidate the effect of multiple influencing parameters, through isolation and varying, on the selective electrodeposition of Co-Ni from multi-ion (Li, Ni, Mn and Co) complex solutions before applying it using real cathode leachates. The selective electrowinning metal recovery process route is a cost-effective alternative to the energy, cost and material-intensive hydrometallurgy intermediate purification processes such as solvent extraction, selective precipitation, and ion-exchange.

The study delves into the effects of various electrowinning parameters, including applied potential, temperature, pH, Co, Ni, Na_2SO_4 , NaH_2PO_4 buffer concentration, and cathode rotational speed. All electrowinning experiments were conducted for 120 minutes unless otherwise stated. These parameters were thoroughly investigated and effectively optimised to achieve the recovery of $Ni_{0.65}Co_{0.35}$ at a minimum rate of $0.060 \text{ g}/(\text{cm}^2 \cdot \text{hr})$ with an impressive 89.25% current efficiency and recovery rate of 90 % and 75 % for Co and Ni respectively. The composition of the deposit was meticulously quantified using ICP-OES and SEM-EDS, the phase composition was evaluated through XRD analysis, and the morphology was examined using SEM. The results successfully demonstrate the technical feasibility of recovering Ni-Co alloys, yielding high quantities of industrial-grade pure Ni-Co alloys.

5.2 Cyclic Voltammetry (For Co and Ni Deposition)

The potentiostatic electrowinning process is operated at a constant potential corresponding to the desired reaction. Therefore, it is imperative to determine the appropriate and optimal potential for the deposition of the desired species, Ni and Co, in their respective pure solutions. Additionally, it is also crucial to assess whether any undesired species deposit at this potential in a multi ion synthetic cathode (NMC 532, $\text{Ni}^{2+}_{0.25}\text{Co}^{2+}_{0.1}\text{Mn}^{2+}_{0.15}\text{Li}^{+}_{0.5}$) solution before proceeding with the Ni-Co electrowinning process using real Li-ionB cathode leachates.

The practice quickly assesses the current versus voltage using a voltammogram for a specific electrochemical system, determined at a particular concentration of electrolyte, pH, and temperature. The voltammetry analysis (Depicted in Figure 5-1) was done pH= 4, 50 °C and cathodic surface area to electrolyte volume ratio (AA/EV) of 2 cm²/250 cm³. For the Al alloy working electrode, voltammograms were created for the reactions of Co to Co²⁺, Ni to Ni²⁺, and oxygen evolution in their respective 15 g/L metal sulphate solutions spanning potential ranges of -1.2 to -0.2 and -0.2 to -1.2 V (vs Ag/AgCl). Figure 5-1 (a) shows the characterization of the electrochemical behaviour of Co and Ni in synthetic Co and Ni electrolytes using Al cathodes at a scan rate of 2 mV/s. Figure 5-1 (b) shows the electrochemical behaviour analysis of the Ni and Co behaviour in a synthetic 532 leachate solution (47.5 g/L $\text{Ni}^{2+}_{0.25}\text{Co}^{2+}_{0.1}\text{Mn}^{2+}_{0.15}\text{Li}^{+}_{0.5}$) solution using Al cathodes.

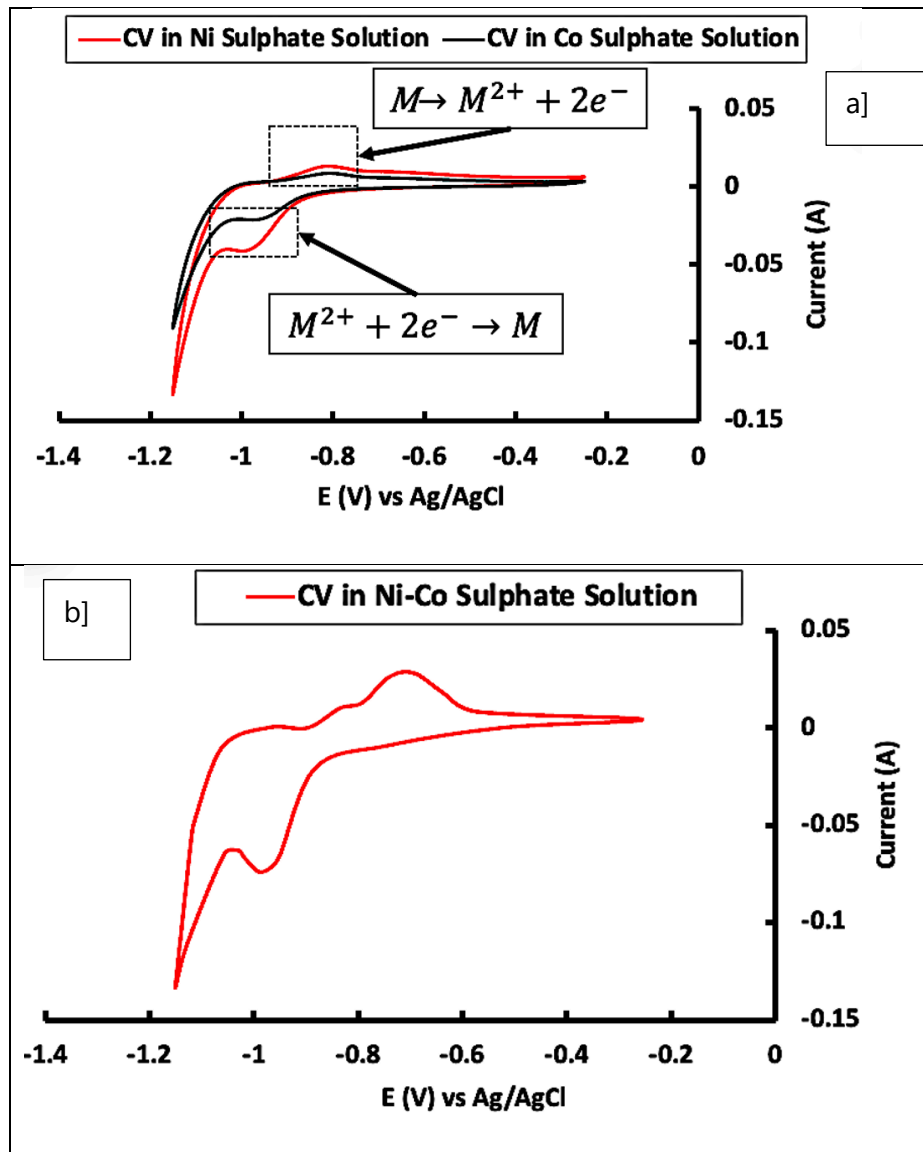


Figure 5-1: Voltammograms of a) Co and Ni deposition on Al alloy cathode in 15 g/L metal ion solution at pH= 4 and 50 °C and b) Co-Ni deposition on Al cathode in 47.5 g/L $Ni^{2+}_{0.25}Co^{2+}_{0.1}Mn^{2+}_{0.15}Li^{+}_{0.5}$ solution at pH= 4.

Figure 5-1 (a) shows two anodic peaks when scanned in the positive direction for both the Co and the Ni voltammograms. In addition, Co exhibited one defined cathodic peak when scanning in a negative direction similar to the Ni voltammogram that shows one defined cathodic peak in the same potential window while demonstrating slightly higher current intensity. The trend is similar

to what is reported in the literature (Matsushima et al. 2006; Kozhina et al. 2009; Nusheh and Yoozbashizadeh 2009; de Castro et al. 2023). The anodic peaks on the Ni and Co voltammogram, when scanning in the positive direction, also occur in the same potential window (Matsushima et al. 2006; Kozhina et al. 2009; Nusheh and Yoozbashizadeh 2009). The deposition peak currents were found to be increasing in the order of Ni<Co<Ni-Co, similar to the trends reported in literature (Lew et al. 2008). It should be noted that an increase in the deposition current is indicative of higher deposition kinetics.

On the Co voltammogram, the first anodic peak (at -0.8 V), which occurs when scanning in the positive direction, is the anodic dissolution of Co (0) to Co (II), and the broad peak (at -0.6 V) is the further oxidation of Co (II) to Co (III) (leading to the formation of Co₂O₃ layer), which has passivating properties, followed by a broad passive region (Matsushima et al. 2006; Kozhina et al. 2009; Nusheh and Yoozbashizadeh 2009; de Castro et al. 2023). As the anodic potential increases to more positive values (over -0.4 V), Co dissolution continues, and with a further increase in the potential, O₂ evolution commences from around -0.2 V (Matsushima et al. 2006; Kozhina et al. 2009; Nusheh and Yoozbashizadeh 2009). Oxygen evolution intensifies with the increase in cycle number (Kozhina et al., 2009; Nusheh & Yoozbashizadeh, 2009). The cathodic peak, which appeared at -0.95 V in the reverse scan (negative scan), could be attributed to the reduction of Co (II) to Co (0) formed on the Al surface interface (Matsushima et al. 2006; Nusheh and Yoozbashizadeh 2009; de Castro et al. 2023).

On the Ni voltammogram, the first anodic peak (at -0.75 V), which occurs when scanning in the positive direction, is the anodic dissolution of Ni to Ni(II), and the broad peak (at -0.55 V) is the further oxidation of Ni(II) to Ni(III) (leading to the formation of Ni₂O₃ layer), which has passivating properties. As the anodic potential increases to more positive values (over -0.4 V), Co dissolution continues, and with a further increase in the potential, O₂ evolution commences in the region of over -0.2 V (Brousse et al. 2015). Oxygen evolution intensifies as the cycle number increases (Brousse et al. 2015; Reyes-Valderrama et al. 2017). The cathodic peak, which appeared at -0.95 V in the reverse

scan (negative scan), could be attributed to the reduction of Ni (II) to Ni (0) formed on the Al surface interface (Brousse et al. 2015).

Based on the above results, it is evident that Ni and Co exhibit similar electrochemical behaviour as shown by very broad peaks (as can be seen in Figure 5-1 (b)) when CV was done in multi ion (Li, Mn, Co and Ni) solution. It is worth noting that the higher cathodic and anodic currents observed in a multi-ion solution containing Li, Mn, Co, and Ni, compared to pure Ni or Co solutions, can be attributed to several factors. The presence of multiple metal ions increases the ionic strength, enhancing the conductivity of the electrolyte and leading to higher currents. Additionally, interactions between the different metal species, such as complex formation or enhanced adsorption on the electrode, can facilitate electron transfer, further boosting current.

The results also indicate that Li and Mn activity is excluded from the chosen potential window, as the voltammogram shows only one defined cathodic peak and one defined anodic peak. These peaks are attributable to the similar reduction and oxidation potentials of both Ni and Co, which overlap to form broad yet distinct cathodic and anodic peaks. These results indicate that Co and Ni can selectively deposit from a $\text{Co}^{2+}/\text{Ni}^{2+}/\text{Li}^+/\text{Mn}^{2+}$ sulphate electrolyte at deposition potentials between -0.85 and -1.15 V (vs. Ag/AgCl), as shown in Figure 5-1 b).

5.3 Effect of Co/Ni Ratio on Current Efficiency and Deposit Composition

Following the composition analysis of the deposit from the cyclic voltammetry of 47.5 g/L $\text{Ni}^{2+}_{0.25}\text{Co}^{2+}_{0.1}\text{Mn}^{2+}_{0.15}\text{Li}^{+}_{0.5}$, the deposit constituted a Co/Ni ratio of 2.45 whilst the electrolyte constituted a Co/Ni ratio of 0.4. The anomalous behaviour of iron-triad metals was examined through studying the effect Co/Ni ratio in the electrolyte on Co/Ni co-deposition. Figure 5-2 illustrates the effect of the Co/Ni ratio on current efficiency and deposit composition.

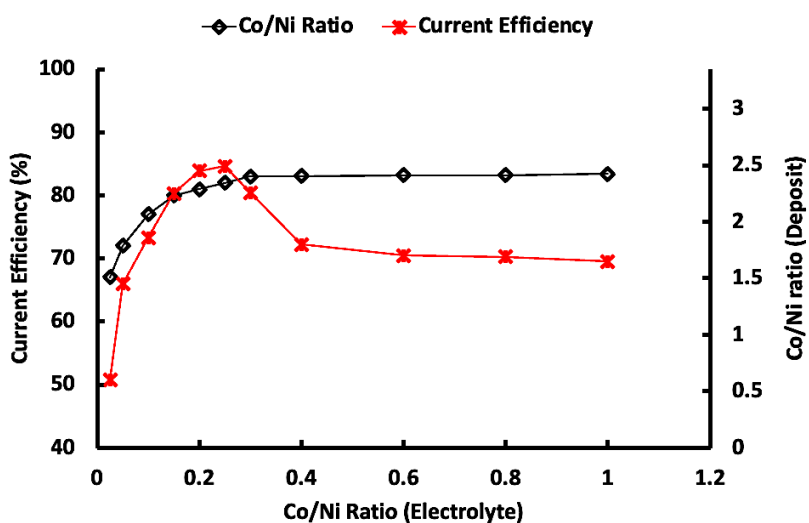


Figure 5-2: the effect of Co/Ni ratio on current efficiency and deposit composition (-0.95 V, pH =4, 60 °C, 47.5 g/L $\text{Ni}^{2+}_x\text{Co}^{2+}_y\text{Mn}^{2+}_{0.15}\text{Li}^{+}_{0.5}$ (where $x+y=0.35$), Cathodic Active Area/Electrolyte Volume (AA/EV) of 2 $\text{cm}^2/250 \text{ cm}^3$).

From Figure 5-2 it is evident that the content of cobalt in the deposit is always higher than that extrapolated from the cobalt concentration in the electrolyte bath. The slight increase in the Co/Ni ratio in the electrolyte results in an exponential increase of Co content in the deposit, for example, at an electrolyte Co/Ni ratio of 0.1 the deposit constituted a Co/Ni ratio of 1.86, while at a Co/Ni ratio of 0.5 the Co/Ni ratio of the deposit was 2.5 (71 % Co) at pH of 4 and -0.95 V vs Ag/AgCl. Thus, we have, for the Ni-Co composite, an unambiguous indication of the inhibition of the electro-deposition of the more noble metal (Ni) and promotion of the electro-deposition of the less noble metal (Co). A similar trend was observed by Golodnitsky *et al.* (2019) (Golodnitsky et al. 1998). Aside from the evident effect of the Co/Ni ratio on the anomalous co-deposition of Ni and Co, it was found that the electrowon Ni/Co deposit composition of the Ni-Co electrowinning systems was also sensitive to the applied potential (illustrated and discussed in section 5.4).

The extent to which the current efficiency and cobalt content is affected by applied potential depends strongly on the Co/Ni ratio in the electrolyte. This intricate nature of the dependence is presumably related to diffusion limitations and changes in the composition of metal complexes,

which are formed in the bulk of the electrolyte and electrical double layer at the electrode-electrolyte interface (Golodnitsky et al. 1998). Golodnitsky et al. (1998) added that the inhibiting effect on the code position of the more noble metal is generally strongest when the reaction rate of the less noble metal is kinetically controlled, and it diminishes as the limiting current is reached.

The Co-Ni composite current efficiency reaches a maximum at a Co-Ni ratio in the electrolyte equal to 0.25 ± 0.05 , which corresponds to approximately 22 - 28% of cobalt content in the Co-Ni composite. The maximum of the current efficiency is coincident with the formation of the more sophisticated structure of the Ni-Co composite. The further decrease of current efficiency as a function of Co^{2+} concentration in sulphate electrolyte may be attributed to the decrease in hydrogen evolution overpotential on the cobalt-rich alloys resulting in hydrogen evolution side reaction.

Partial polarization curves of Ni^{2+} and Co^{2+} co-deposition presented by Golodnitsky et al. (1998) indicated that after an increase of cobalt (II) concentration in the electrolyte by a factor of 16, the curve is accompanied by the positive (0.2 V) shift of the cobalt reduction potential whilst the opposite effect (-0.5 V) was found for Ni (II) co-deposition (Golodnitsky et al. 1998). This shift indicates that Co deposition is more favoured as the concentration of Co^{2+} in the electrolyte increases. Changes in temperature, pH and bath composition do not influence the Tafel slope (Golodnitsky et al. 1998; Zech et al. 1999). The cathode reactions were found to be first order with respect to Ni^{2+} and Co^{2+} concentrations which entails a two-stage process, where the rate-determining step is the acquisition of the first electron (Golodnitsky et al. 1998). Additional support for this assumption is the large apparent activation energy of alloy deposition (15.5 kcal/mol) (Golodnitsky et al. 1998; Zech et al. 1999).

To elucidate the anomalous co-deposition of Ni^{2+} and Co^{2+} , it is worth considering the formation of the individual complexes from the standpoint of crystal-field theory. In light of this theory, Ni^{2+} and Co^{2+} complexes can be related to coordinative substances, whose structures show little sublevel splitting and are high-spin complexes. This possible deduction points to the fact that the

inhibiting of the discharge rate of the nobler component is likely to depend on the internal structural features of Ni^{2+} and Co^{2+} species involved in the reduction process.

To further explain the anomalous co-deposition of Ni^{2+} and Co^{2+} , it is pre-eminent to consider the individual metal ion complexes from the standpoint of the crystal-field theory. Cobalt possesses the electronic structure $3d^74s^2$. Nickel has the electronic structure $3d^84s^2$. In the light of this theory, aquo- and protonated sulphate Ni^{2+} and Co^{2+} complexes can be related to coordinative substances, whose structures show little sublevel splitting, namely, high spin complexes (Golodnitsky et al. 1998; Zech et al. 1999). The calculated crystal field stabilization energy for Ni^{2+} in octahedral complexes is 29.3 and 17.1 kcal for Co^{2+} .

High-spin octahedral Co^{2+} complexes with three unpaired electrons are more labile than that of Ni^{2+} . Therefore, the formation of high-spin Co^{2+} complexes is more feasible (than high-spin Ni^{2+} complexes) and is expected to react rapidly. It is believed that the formation of labile high-spin cobalt complexes would explain the preferential reduction of Co^{2+} as compared with Ni^{2+} . Moreover, high-spin complexes involved in the reaction would permit a two-step reduction mechanism, which is in complete agreement with the experimentally modelled Tafel slopes by Golodnitsky et al. (1998). Notwithstanding the fact that the actual electrode reactions of electrochemical alloying of the iron-group metals may include additional intermediate steps, the author believes that in a first approach, the crystal-field theory permits generalization for anomalous co-deposition of Co^{2+} and Ni^{2+} from different electrolytes. Along with competitive adsorption and underpotential deposition, the crystal-field theory can be considered as one possible explanation of the anomalous behaviour of electrochemical alloying of the iron-triad metals.

5.4 Effect of Applied Potential on Current Efficiency and Rate of Deposition

The investigation of potential against the rate of deposition revealed that there was an increase in the rates of deposition for an increase in applied potential (Figure 5-4 a). In addition, the current

density ramps up as the potential is increased (Figure 5-3). The highest deposition rate was found to be 0.0382 g/hr.cm² at -1.45 V (vs Ag/AgCl) and 1 cm cathode-anode distance. As the potential increases, more electrons are available for the deposition reaction (metal ion reduction reaction) leading to an increased amount of deposit formed. The deposition rate is highest (0.0382 g/hr.cm²) at -1.45 V. Since the surface of the deposit on the cathode became irregular at high deposition rates and the supplementary deposited mass could not stick to the cathode, the impurities could easily be deposited along with Co and Ni, therefore, it is not advisable to operate at high potentials. Figure 5-3 illustrates the effect of applied potential on the current as a function of time. There was no significant current density and efficiency response difference between 50 and 60 °C and pH of 4 and 5.

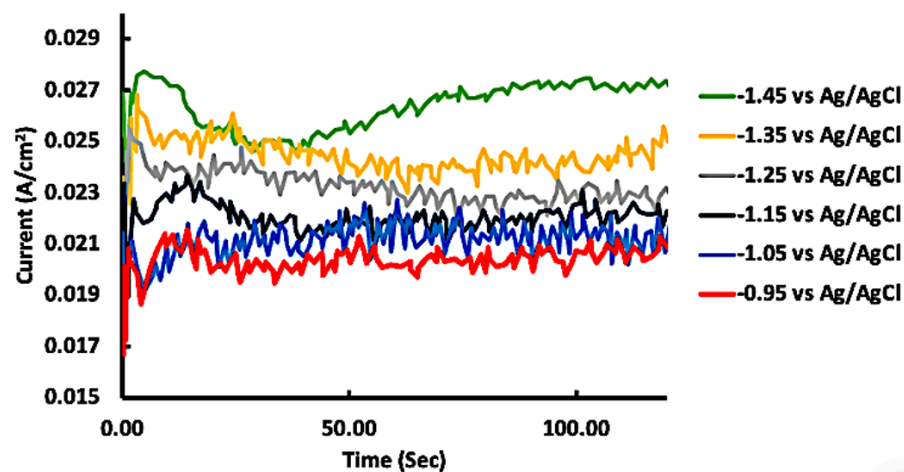


Figure 5-3: Effect of applied potential on the current as a function of time (tests done in 47.5 g/L of Ni²⁺_{0.25}Co²⁺_{0.1}Mn²⁺_{0.15}Li⁺_{0.5} solution at pH=5, 60 °C and 2 cm²/250 cm³ AA/EV).

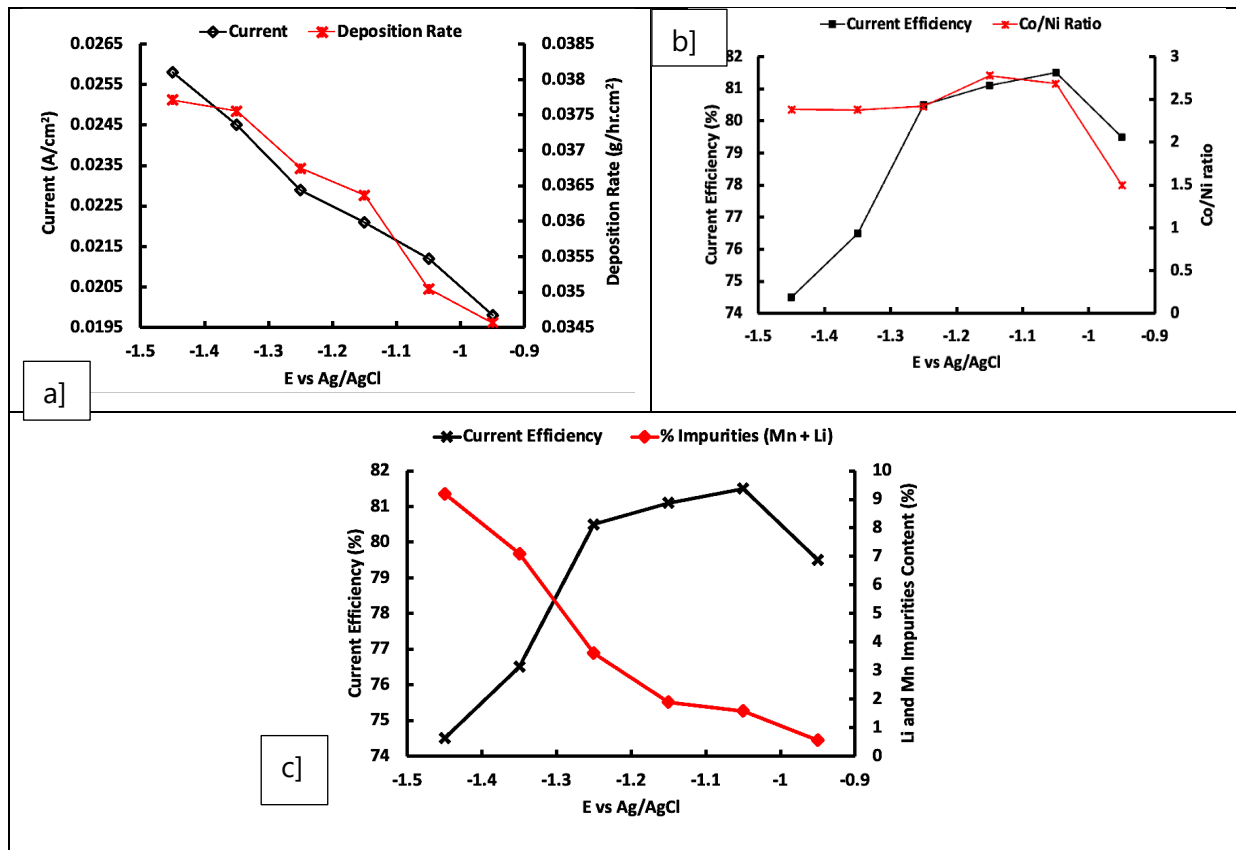


Figure 5-4: Effect of applied potential on a) the mean current and rate of deposition b) current efficiency and Co/Ni ratio and c) current efficiency and % Li and Mn impurity (tests done at pH=5, 60 °C and 2 cm²/250 cm³ AA/EV in 47.5 g/L Ni²⁺_{0.25}Co²⁺_{0.1}Mn²⁺_{0.15}Li⁺_{0.5}).

The deposition rate-potential curves exhibit similar trends to current-potential curves, as seen in Figure 5 4 a), since more active electrons are availed for the Co²⁺ reduction at higher applied potentials and currents. In the region where the curves are steep (between -1.25 to -1.45 V vs Ag/AgCl), after the limiting overvoltage (-0.95 V vs Ag/AgCl), the system becomes unstable (as indicated by the high voltage fluctuations in Figure 5-3), and the liberation of hydrogen produces a spongy-cobalt deposit onto the cathode as depicted by Figure 5-5. Figure 5-4(c) indicates that the impurities composition increases with applied potential due to the non-selective reduction of impurity species on the cathode at higher applied potentials. At -1.15 V vs Ag/AgCl, the composition of impurities was 1.8 %, while at -1.45 V versus Ag/AgCl, the composition of impurities reached a substantial 9 %. It is also possible that the impurities are getting trapped

within the pores on the surface since at the degree of non-uniform morphology increases with applied potential.

Figure 5-4 (b) shows that the Co/Ni ratio increases from 2.0 to 2.75 when the potential decreases from -0.95 to -1.05; hereafter the Co/Ni ratio remains virtually constant at approximately 2.5. The anomalous Ni-Co deposition is discussed in the previous section 5.3. The Co-Ni composite current efficiency reaches a maximum (81 %) at -1.05 V vs Ag/AgCl. The liberation of hydrogen and non-selective reduction of impurity species is intensified as the potential increases, this leads to a subsequent decrease in current efficiency (Figure 5-4 b). The maximum of the current efficiency coincides with the formation of the stable, coherent and more orderly and uniform structure of Ni-Co composite at higher potentials. The decrease in current efficiency as a function of Co^{2+} concentration in a sulphate electrolyte could be attributed to the reduction in hydrogen evolution overpotential on cobalt-rich composites. This reduction means that the cobalt-rich composites become more effective at catalysing the hydrogen evolution reaction (HER), leading to an increased rate of HER and, consequently, a decrease in current efficiency for the desired electrochemical process (see Figure 5-5).

Partial polarization curves of Ni^{2+} and Co^{2+} co-deposition presented by Golodnitsky et al. (1998) indicated that at high Co concentrations, the curve is accompanied by the positive (0.2 V) shift of the cobalt reduction potential whilst the opposite effect (-0.5 V) was established for Ni (II) co-deposition (Golodnitsky et al. 1998). This shift indicates that Co deposition is more favoured at high concentrations of Co. At lower potentials, the Ni is favoured, whilst at higher potentials, the reaction kinetics, enhanced by higher potential, favour Co over Ni.

Figure 5-5 depicts the SEM imaging of the cathode surface at different applied potential levels.

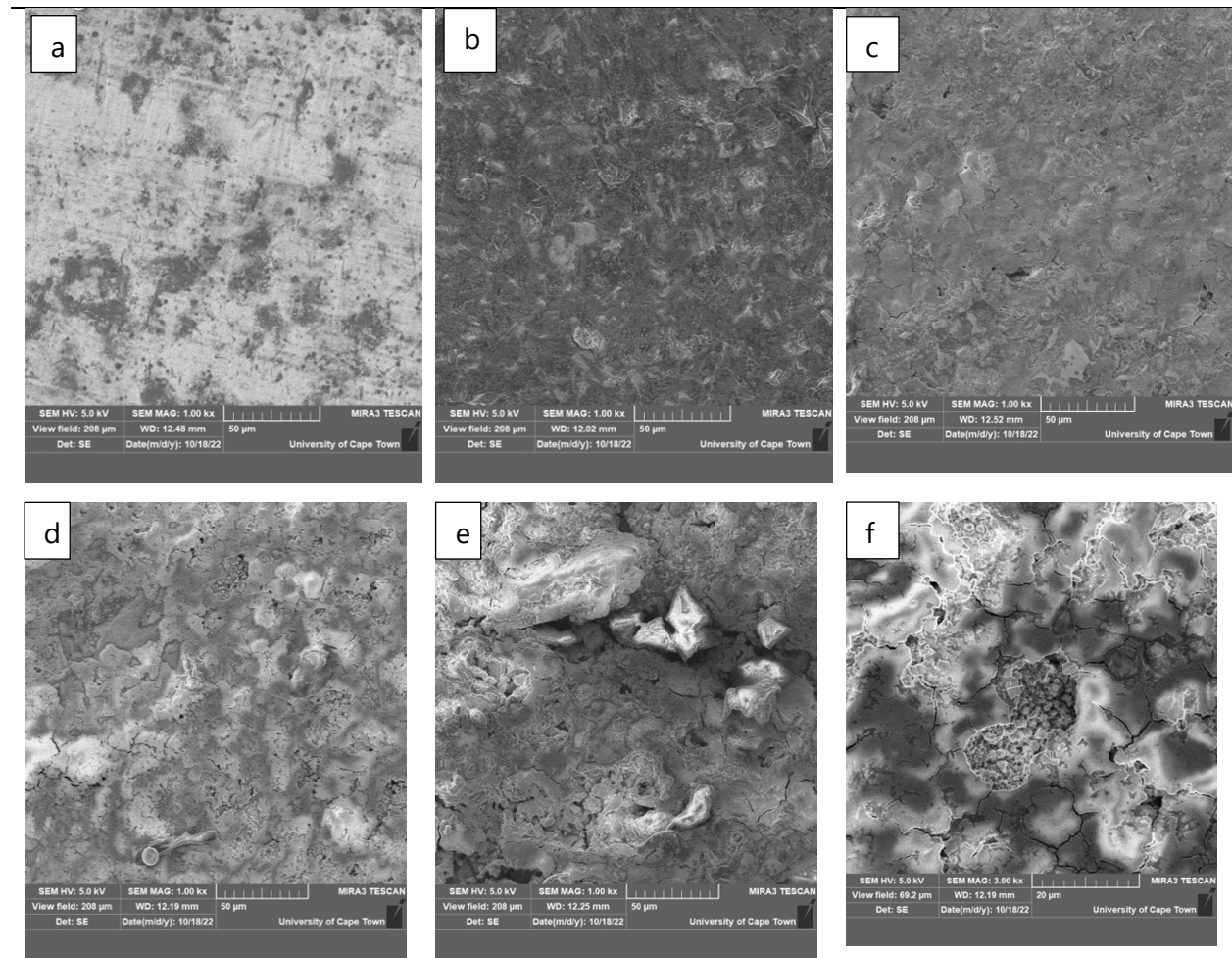


Figure 5-5: SEM images of cathode surface after applying different potentials a) 0 V (Fresh electrode), b) - 1.15 V, c) -1.25 V, d) -1.35 V, e) and f) -1.45 V vs Ag/AgCl (Deposit obtained in 47.5 g/L of $\text{Ni}^{2+}_{0.25}\text{Co}^{2+}_{0.1}\text{Mn}^{2+}_{0.15}\text{Li}^{+}_{0.5}$ solutions at pH=5, 60 °C and 2 cm²/250 cm³ AA/EV).

The cathode plate was found to have a non-sticking, spongy deposit at potentials higher than - 1.25 Volts (Figure 5-5 c-f). Cleaning the cathodes was challenging since the porous layer of Co could be lost during cleaning, increasing the likelihood of an efficiency mistake. Electrowon deposit obtained when the applied potential was below or at the limiting potential (-1.15 V vs Ag/AgCl) resulted in a smooth, greyish and adherent deposit as shown in Figure 5-5 (b). However, applying potential above the limiting potential produced an uneven, non-adherent, and nodular electrowon deposit, which denoted an unstable electrowinning system. The irregular-spongy

deposit could be lost during washing, which would raise errors in the deposition rate and, as a result, reduce the apparent efficiency as it is now. In light of this, the limiting potential was established as $-1.15\text{ V vs Ag/AgCl}$ for the next section of studies.

As the applied potential increased, the thickness of the film increased, and the electrode surface became more homogeneous, as the hemispherical grains growing on each crystal overlapped into larger agglomerates (Figure 5-5 c – e). The width of the cracks, now more linear in shape, seemed to increase with increasing film thickness, and some of them followed the grain boundaries. For -1.35 V and -1.45 V in particular, some deposits had been detached from the cathode surface. The existence of thin layers of Co-Ni in some of the pits caused by deposit exfoliation demonstrates that some material was lost from the anode surface during electrolysis (Figure 5-5 f).

The cathode plate was found to have a non-sticking, spongy deposit at potentials higher than -1.25 Volts (Figure 5-5 c-f). Cleaning the cathodes was challenging since the porous layer of Co could be lost during cleaning, increasing the likelihood of an efficiency mistake. Electrowon deposit obtained when the applied potential was below or at the limiting potential ($-1.15\text{ V vs Ag/AgCl}$) resulted in a smooth, greyish and adherent deposit (Figure 5-5 b). However, applying potential above the limiting potential produced an uneven, non-adherent, and nodular electrowon deposit, which denoted an unstable electrowinning system (Figure 5-3). The irregular-spongy deposit could be lost during washing, which would raise errors in the deposition rate and, as a result, reduce the efficiency as it is now. In light of this, the limiting potential was established as $-1.15\text{ V vs Ag/AgCl}$ for the next section of studies.

5.5 Effect of pH on Current Efficiency

The correlation in Figure 5-6 depicts the influence of the pH of the electrolyte on the Co-Ni electro-deposition current efficiency at different temperatures. The current efficiency rises sharply as the pH rises to around $\text{pH}=4$ (81%); then it stabilizes between 4 and 5 and then decreases sharply beyond 5. A similar trend was observed for the current efficiency and temp correlation at

pH=4. It is also noteworthy that the average current efficiency is slightly lower at 60 °C than at 50 °C due to increased Co-Ni deposition kinetics that can lead to an increased rate of the hydrogen evolution reaction, potentially lowering the selectivity for Co and Ni deposition.

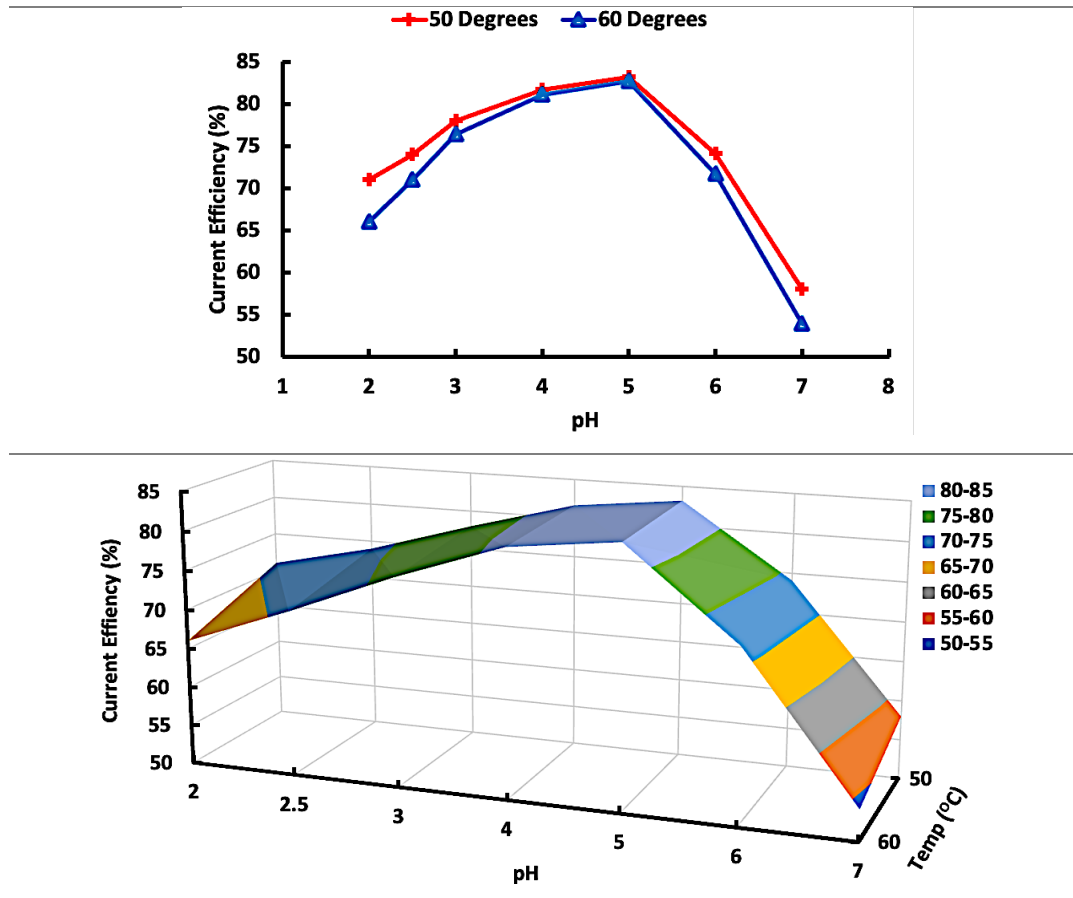


Figure 5-6: Influence of pH of the electrolyte on Co-Ni electro-deposition at different temperatures (47.5 g/L of $\text{Ni}^{2+}_{0.25}\text{Co}^{2+}_{0.1}\text{Mn}^{2+}_{0.15}\text{Li}^{+}_{0.5}$, 50 °C and 60 °C and , -1,15 V vs Ag/AgCl and AA/E of 2 cm²/250 cm³).

At lower pH, the higher H⁺ ion concentration results in substantial H₂ gas evolution at the cathode resulting in porous and poor morphology electro-won deposits that are poorly adherent to the Al cathode substrate. This subsequently results in poor current efficiency of the electro-won deposit. When pH is adjusted to levels higher than 5, the continuous consumption of H⁺ ions (through H₂ gas evolution) and increased OH⁻ ions (from NaOH) at the cathode results in increased pH in the catholyte initiating Co(OH)₂ and Ni(OH)₂ precipitation (Jeffrey et al. 2000b). At high pH levels (>5), Ni and Co hydroxides precipitate and become incorporated into the electro-won deposit, resulting

in a very poor adhesion and suboptimal deposit morphology (Altamirano-Garcia et al. 2021). It is noteworthy that below pH 2.5 and more than 4.5 the current efficiency steeply drops. Hence a pH range of 3 to 4.5 appears to be reasonably optimal and satisfactory for good quality and adherent deposit, as further supported by enhanced current efficiency within the range.

5.6 Effect of Temperature on Current Efficiency

The correlation in Figure 5-7 depicts the effect of temperature on the current efficiency at an applied potential of -1.15 V vs Ag/AgCl, pH=3, pH=4, pH=5 and pH=6 using an electrolyte composition of 47.5 g/L [$\text{Ni}^{2+}_{0.25}\text{Co}^{2+}_{0.1}\text{Mn}^{2+}_{0.15}\text{Li}^{+}_{0.5}$]. Generally, an increase in temperature leads to an increase in current efficiency across all pH levels up to 60 °C, indicating a positive temperature dependence. However, at higher temperatures (70 °C and 80 °C), the current efficiency begins to exhibit a decline, suggesting a potential temperature threshold beyond which the current efficiency diminishes, possibly due to unfavourable side reactions i.e. hydrogen evolution reaction and formation of cobalt oxide. Furthermore, the efficiency of the current is influenced by pH levels, and variations in the degree of change are evident across different pH values. The peak efficiency for each pH level occurs at different temperatures, emphasizing the interdependence between temperature, pH, and current efficiency in the electrochemical system studied.

The electrowinning data for cobalt deposition reveals compelling trends. The positive correlation between increasing temperature and current efficiency up to 60 °C is consistent with expectations in electrowinning, indicating enhanced kinetics at higher temperatures. However, the subsequent decline at 70 °C and 80 °C suggests a critical temperature threshold beyond which the benefits diminish, possibly due to unfavourable side reactions (hydrogen evolution reaction and metallic hydroxide formation reaction). The mean current efficiency is significantly higher at pH=5 than pH =3 due to the decreased rate of the hydrogen evolution reaction, potentially improving the selectivity for cobalt deposition. The mean current efficiency is notably reduced at pH levels below 3 and above 6. This is because, at pH < 3, the increased rate of hydrogen evolution competes with

metal deposition, while at $\text{pH} > 6$, the formation of cobalt and nickel hydroxides predominates. Both conditions can decrease the selectivity for cobalt and nickel deposition. As depicted Figure 5-7 b), the highest current efficiency levels were recorded at temperatures between $50\text{ }^\circ\text{C}$ and $60\text{ }^\circ\text{C}$ and $\text{pH}=4$ and $\text{pH}=5$. The optimal values were chosen as $50\text{ }^\circ\text{C}$ (to reduce the thermal factor related energy consumption) and $\text{pH}=4.5$ (to reduce chemical consumption).

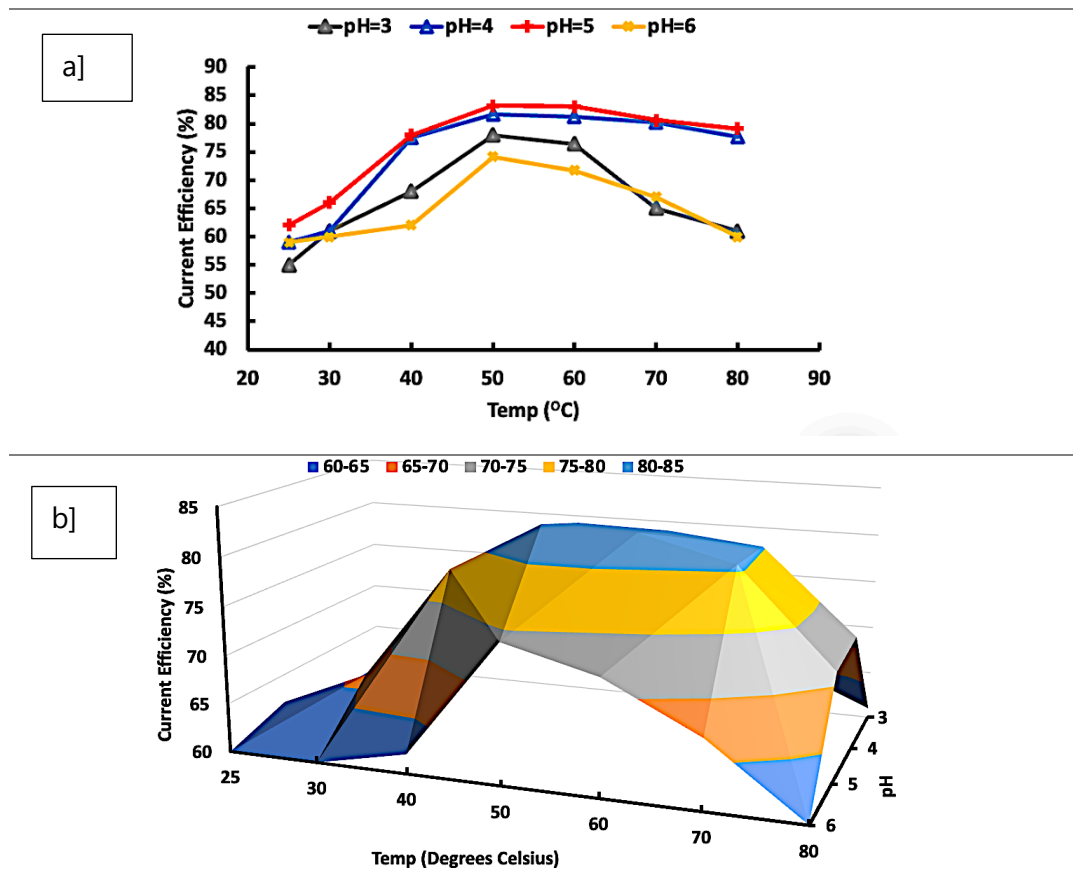


Figure 5-7: The effect of temperature on the current efficiency at an applied potential of -1.15 V , $\text{pH}=3, 4, 5$ and 6 using an electrolyte composition of $47.5\text{ g/L } [\text{Ni}^{2+}_{0.25}\text{Co}^{2+}_{0.1}\text{Mn}^{2+}_{0.15}\text{Li}^{+}_{0.5}]$ and AA/EV of $2\text{ cm}^2/250\text{ cm}^3$.

Electrowinning of Co-Ni alloys at higher temperatures (50 and 60 °C at pH=5) enhanced both deposit quality and adherence, although the deposit generated at temperatures up to 40 °C was non-uniform and non-adherent. The enhanced ionic mobility at higher temperatures is what effectuates an increased current efficiency. The rapid fall of current efficiency from 70 °C is attributed to the decrease in hydrogen evolution overpotential on the cobalt-rich alloys, resulting in a hydrogen evolution side reaction. This trend is also iterated with correlations by Lu et al. (2018), who demonstrated that the voltage needed to achieve the specified current density falls as the temperature rises (Lu et al. 2018). The rapid availability of Co ions at the cathode can also result in less stressed, better-quality deposits (Sharma et al. 2005a; Lu et al. 2018). Other factors, such as phase composition, affect the quality of the deposit as further detailed as follows:

- Cobalt can be found in both a and h forms, but the h form is favoured since it is face-centred and the a form is hexagonally close-packed and not typically deposited in an electrochemical cell (Pradhan et al. 2001; Cohen-Hyams et al. 2002).

It is asserted that the Co deposit will be h if made at higher temperatures and a mixture of a and h if made at lower temperatures. The latter composition exerts stress on the deposit and lead to its dissociation from the electrode substrate (Mehmood et al. 2015). Another issue with cobalt deposits is that in addition to cobalt (II), which is produced at the anode, cobalt (III) is also present in the electrolyte (Lakshminarayanan et al. 1976). Lakshminarayanan et al. (1976) examined Co_2O_3 deposit collected at the anode in an oxidation-reduction process using ferrous-cobalt sulphate solutions. Lakshminarayanan et al. (1976) noted that the presence of multivalent cations in the electrolyte causes a decrease in the efficiency and dendritic character of the deposit, even if the effects of Co (III) in the electrolyte are unknown, a trend that was also noted in this work when Ni-Co-Li-Mn sulphate solutions (containing mono and multivalent cations) were used as depicted in Figure 5-8. However, it must be noted that the effects were not detrimental to the objectives of this work. Figure 5-8 depicts the SEM images of cathode surface (with Ni-Co alloy deposit) after electrowinning in a solution containing pure (a) 30 g/L of $\text{Co}^{2+}_{0.3}\text{Ni}^{2+}_{0.7}$ and (b) 47.5 g/L $\text{Ni}^{2+}_{0.25}\text{Co}^{2+}_{0.1}\text{Mn}^{2+}_{0.15}\text{Li}^{+}_{0.5}$.

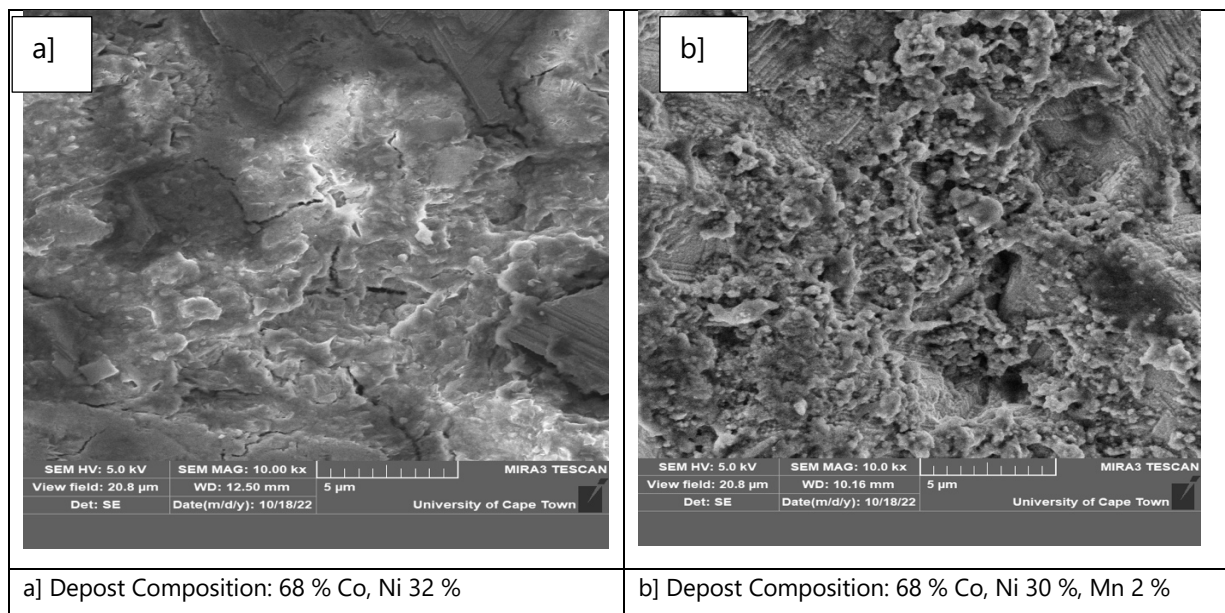


Figure 5-8: SEM images of cathode surface (with Ni-Co alloy) after electrowinning in an electrolyte solution containing a) pure 30 g/L of $\text{Co}^{2+}_{0.3}\text{Ni}^{2+}_{0.7}$ and b) 47.5 g/L $\text{Ni}^{2+}_{0.25}\text{Co}^{2+}_{0.1}\text{Mn}^{2+}_{0.15}\text{Li}^{+}_{0.5}$ (tests done at 1.15 V vs Ag/AgCl, 50 °C, pH = 4.5 for 180 minutes).

In order to generate Co-Ni alloys at optimal current efficiency, a higher temperature of 50 °C was chosen as optimal for next set of experiments.

5.7 Effect of Concentration on Co-Ni Concentration on Current Efficiency

Electrolysis was conducted by varying the Ni-Co concentration from 0 g/L to 30 g/L in the 2 $\text{cm}^2/250 \text{ cm}^3$ AA/EV set-up, at a temperature of 40 °C, 50 °C, 60 °C and 70 °C, pH 4.5 and applied potential of -1.15 V (vs Ag/AgCl). The results are summarized in Figure 5-9, show that the current efficiency increases with an increase in cobalt concentration and temperature of the electrolyte.

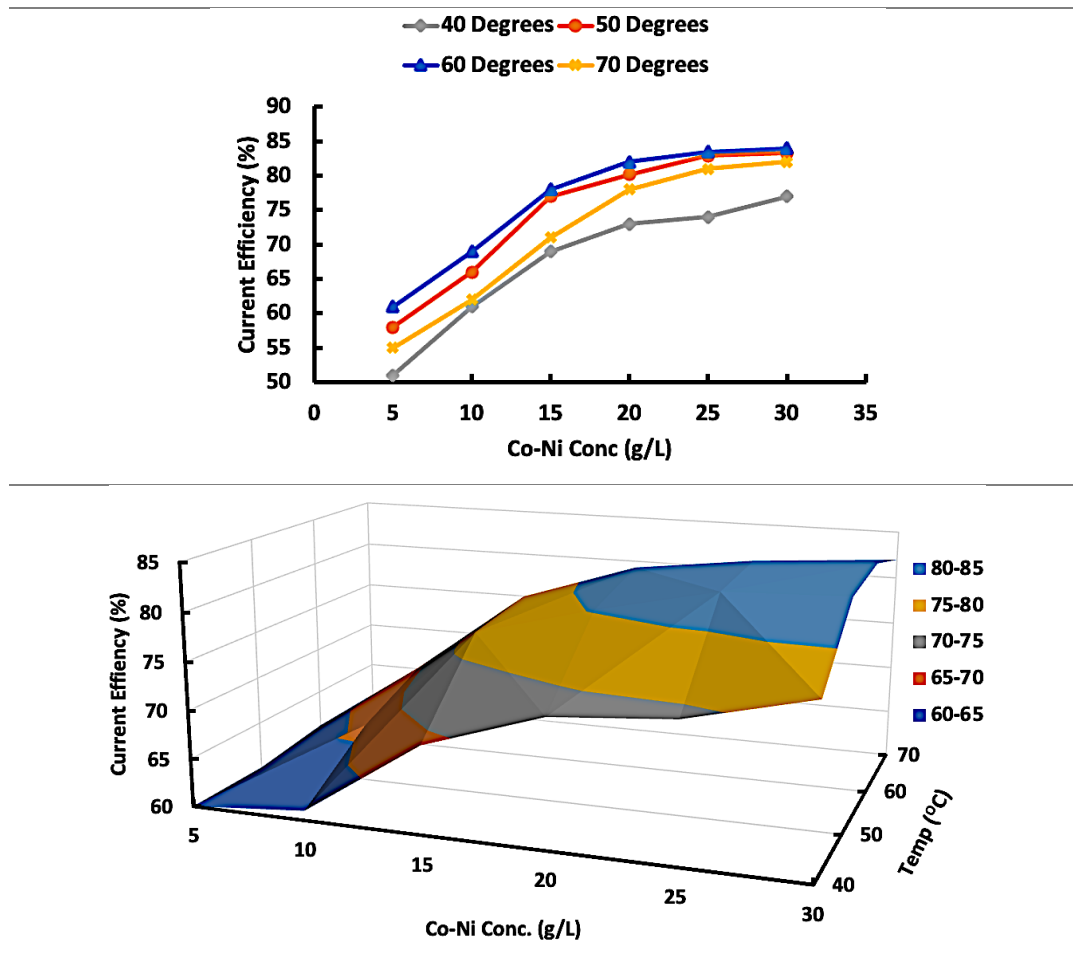


Figure 5-9: Effect of Co-Ni concentration $[\text{Co}^{2+}_{0.25}\text{Ni}^{2+}_{0.1}]$ in a multi-ion $[\text{Co}^{2+}_{0.25}\text{Ni}^{2+}_{0.1}]\text{Mn}^{2+}_{0.15}\text{Li}^{+}_{0.5}$ solution on the current efficiency at -1.15 V vs Ag/AgCl , $\text{pH}=4.5$, Temperatures= $40\text{ }^{\circ}\text{C}$, $50\text{ }^{\circ}\text{C}$, $60\text{ }^{\circ}\text{C}$ and $70\text{ }^{\circ}\text{C}$ using a varied electrolyte composition up to 30 g/L $[\text{Co}^{2+}_{0.25}\text{Ni}^{2+}_{0.1}]$ solution and AA/EV of $2\text{ cm}^2/250\text{ cm}^3$.

Additionally, it was noted that electrowinning at low Co^{2+} - Ni^{2+} concentrations ($<15\text{ g/L}$) produces Co-Ni deposits that are stressed and brittle and ultimately stick loosely, therefore easily falling off from the Al cathode during electrowinning. This trend results in a reduced current efficiency. Electrowinning at higher Co^{2+} - Ni^{2+} ($>15\text{ g/L}$) concentrations produces Co-Ni deposits that are smoother and less brittle and ultimately don't fall off easily from the Al cathode during electrowinning. This correlation is indisputably due to the more abundant availability of Ni^{2+} and Co^{2+} ions, vis-a-vis hydrogen ions (H^{+}), at the higher Co^{2+} concentrations, while at lower cobalt concentrations, relatively higher H_2 evolution, and its consequent incorporation into the

electrowon Ni-Co deposit, results not only in lower current efficiencies but also in brittle and stressed deposits. Since no additional benefit is derived in going beyond 25 g/L, a higher 30 g/L Co-Ni concentration value was chosen as the optimum Co-Ni concentration. The energy required to deposit cobalt also drops as the Co concentration increases. This is an obvious consequence of the lower voltage requirement (due to higher conductivity at the higher Ni-Co concentration levels) and the increased current efficiency.

As seen in Figure 5-9, Ni and Co electrowinning activity is favoured between 50 and 60 °C since higher current efficiency (83 % to 84 %) is recorded at high Ni-Co concentrations (30 g/L) compared to temperatures out of this range (77 % for 40 °C and 81.5 % for 70 °C). In-between the optimal temperature range, electrowinning at a higher temperature (60 °C) evidently yields slightly higher current efficiency (84.2 %) than low temperature (50 °C) which yields 83.1 %. This is due to the correlation that elevated temperatures accelerate Ni-Co electrodeposition reaction rates and enhance ion mobility, leading to faster electrodeposition of Co-Ni metallic deposits. The increased thermal energy can reduce the activation energy barriers for the Ni-Co electrowinning reactions, promoting a more efficient metal recovery. Moreover, higher temperatures may impact the physical properties of the electrolyte, such as its conductivity and viscosity, which can influence the overall performance of the electrowinning cell. However, it's essential to strike a balance, as excessively high temperatures pose challenges, including increased energy consumption, potential electrode passivation, and concerns about the stability of the electrolyte (hence why 60 °C is the limit, but 50 °C is the optimal).

5.8 Effect of Inter-Electrode Distance on Developed Current

The effect of inter-electrode distance was investigated against the developed current density in the electrowinning cell circuit for a fixed potential level. The results, depicted in Figure 5-10, indicated that the 0.5 cm inter-electrode distance had the highest developed current density compared to all the distance levels. As per current-distance correlation Figure 5-10, the highest

developed current density is 0.03 A/cm^2 (at 0.5 cm interelectrode) and the lowest is 0.01 A/cm^2 at 3 cm inter-electrode distance.

The results also indicate that increasing the inter-electrode distance increases the resistance across the electrowinning cell as electron and ionic species have to be transported over longer distances for electrochemical reactions to occur. As a result, transportation of electron and ionic species over longer distances requires a higher electromotive force (to mobilise the species) for the desired reactions to occur. This phenomenon ultimately increases the voltage whilst reducing the current field strength and the current density on the active areas of the electrodes. As a consequence, of the slower rate of deposition that occurs at lower current density levels, the reduced current density will lengthen the time required for the deposition process to be completed.

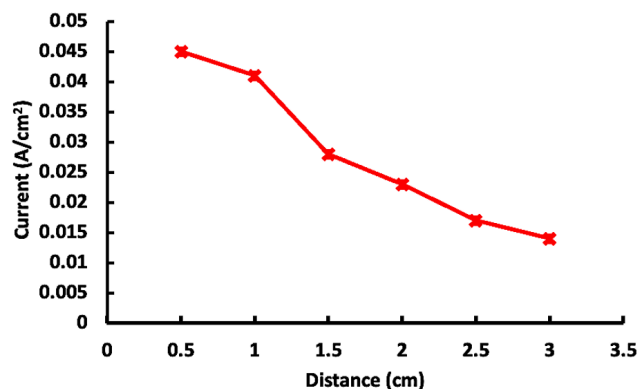


Figure 5-10: The effect of distance between electrodes on the developed current density at -1.15 V vs Ag/AgCl , 47.5 g/L [$\text{Ni}^{2+}_{0.25}\text{Co}^{2+}_{0.1}\text{Mn}^{2+}_{0.15}\text{Li}^{+}_{0.5}$], $\text{pH}=4.5$, $50 \text{ }^\circ\text{C}$ and AA/EV of $2 \text{ cm}^2/250 \text{ cm}^3$.

The inter-electrode distance-resistance trend, depicted in Figure 5-10, suggest that the developed current density decreases with an increase in inter electrode distance and increases with a decrease in inter electrode distance. This correlation is attributed to the increased electron and ionic species mass transfer kinetics between the cathode and anode. Increasing the distance between electrodes increases the ohmic resistance (voltage) and consequently reduces the

current density leading to a reduced rate of metal deposition due to decreased inter electrode electric field strength on the electrode-active area and active species mass transfer kinetics (Chen, Mojica, et al. 2017) .

5.9 Effect of Electrode Active Area on the Developed Current

The active area of the electrode affected the developed current as indicated in Figure 5-11. Four different active areas were used during the investigation (1, 2, 3 and 4 cm²). The results show that the developed current for a small active area (1 cm²) was lower (0.022 A) when compared to those of the other active areas. The highest active area (4 cm²) exhibited the highest limiting current (0.1 A). The values for the 2 cm² and 3 cm² distances were found to be 0.042 and 0.064 A respectively.

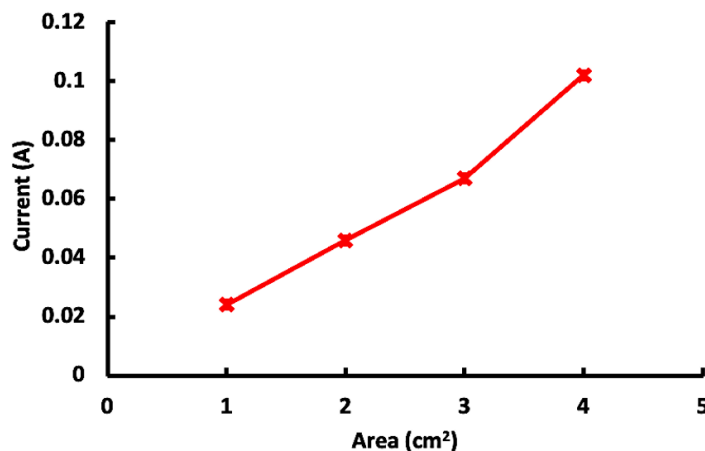


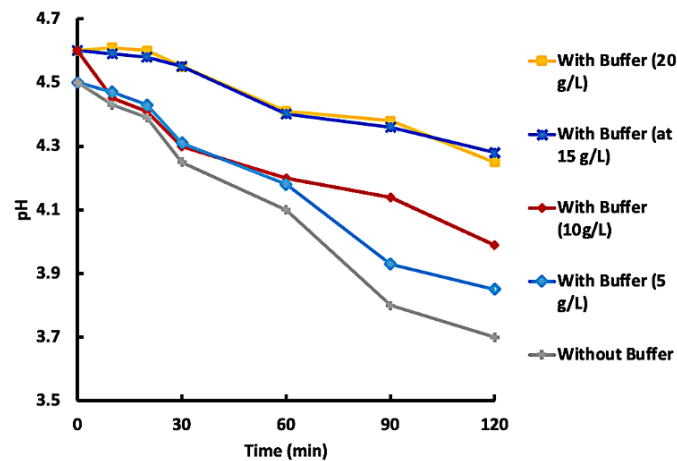
Figure 5-11: Effect of Electrode-active Area on the developed Current density at -1.15 V vs Ag/AgCl, 47.5 g/L [Ni²⁺_{0.25}Co²⁺_{0.1}Mn²⁺_{0.15}Li⁺_{0.5}], pH=4.5, 50 °C and AA/EV of 2 cm²/250 cm³.

Figure 5-11 indicates that an increase in the active area increased the limiting current because a higher active area provides more area for electron transfer resulting in a higher developed current. The rate of reaction and therefore the rate of deposition of Co will be affected by this correlation. If there is a drop of current, there is a corresponding drop of mass deposited at the cathode.

5.10 Effect of Monosodium Phosphate on pH Fluctuation

The tests were performed in a jacketed single-compartment reactor; however, there was significant pH variation during the experiments. A buffer was incorporated into the electrolyte solution to obtain higher current efficiency and an optimal way to limit the pH variation. Figure 5-12 (a) demonstrates the pH variation of the catholyte-anolyte solution during the course of the experiment. It can be observed that, except for the correlation related to a system with buffer, the pH tends to decline during the course of the experiment. Excluding the effect of electrochemical reaction mechanisms and kinetics, these correlations also indicate that a higher solution temperature effectuates an increase in the proton migration and consumption rate as the pH decrease is much lesser in a higher temperature solution than in a lower temperature solution. The pH decreases rapidly from 4.5 to 3.7 after 120 minutes without the use of a monosodium phosphate buffer solution and less rapidly from 4.6 to 3.95 when monosodium phosphate is incorporated into the electrolyte solution.

a)



b)

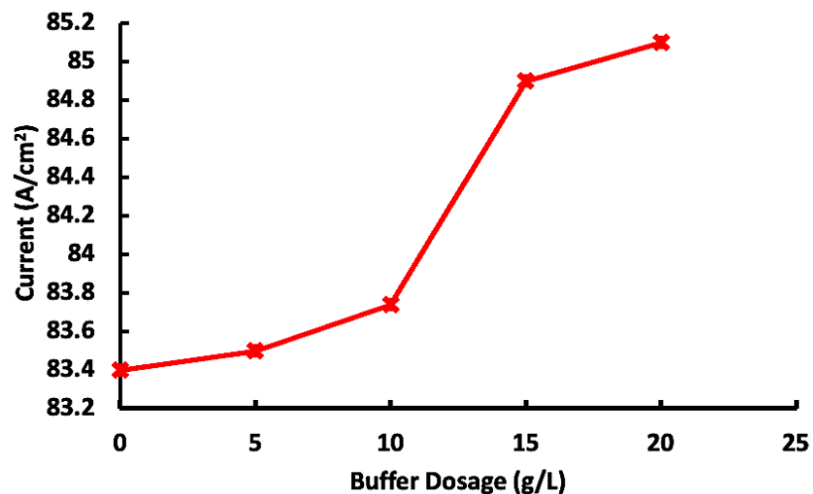


Figure 5-12: a) pH variation with time at different buffer dosages and effect of buffer dosage on the current efficiency in the electrowinning set-up at -1.15 V vs Ag/AgCl, 47.5 g/L $[\text{Ni}^{2+}_{0.25}\text{Co}^{2+}_{0.1}\text{Mn}^{2+}_{0.15}\text{Li}^{+}_{0.5}]$, Starting pH=4.5, 50 °C and AA/EV of 2 cm²/250 cm³.

The pH stabilizes (decreases negligibly) over a 120-minute electrowinning period as the dose of monosodium phosphate increases. The pH decreased slightly from 4.6 to 4.2 after 120 minutes when monosodium phosphate buffer solution was utilised at 15 g/L. In the corresponding correlation, when electrowinning was conducted at 50 °C, it was observed that the pH decreased at a significantly faster rate compared to when monosodium phosphate was not used. This effect

confirms the buffer utilization efficiency in pH control and contributes to cost reduction since it reduces the amount of chemical reactants necessary for continuous pH adjustment.

This pH variation may occur due to the water decomposition reaction on the anode electrode surface that yields oxygen gas and H^+ ions, which tend to migrate to the cathodic plate, where they accept electrons to produce H_2 gas. The continuous generation of H^+ at the anode results in a decrease in pH and current efficiency as the H^+ concentration in the electrolyte continues to increase. The buffer counteracts the rapid decrease in the pH (increase in H^+ ions) (Figure 5-12 a) and consequently the current efficiency (Figure 5-12 a) by neutralising the generated H^+ ions. As seen in Figure 5-12 an increase in the buffer dosage results in pH stabilisation and current efficiency increase. Thus, the pH increases for the test done at 50 °C could be explained as a function of the reaction rate gradient between the rate of H^+ ions generation (from water electrolysis) at the anode and the rate of H^+ rate of consumption (H_2 evolution).

It is important to note that at lower temperatures (<40 °C), due to the low molecular kinetic energy, the rate of the proton mobility and consequently migration from the anolyte phase to the catholyte phase is consequently reduced (Sharma et al. 2005a). Regarding electrowinning at very low temperatures (<30 °C), a negligible change could be observed in the pH variation when monosodium phosphate was added since little Co/Ni is expected to be deposited (Santos et al. 2007). However, at higher temperatures, the proton (H^+). migration is significantly increased due to heightened kinetic mobility, thereby intensifying the effect of the pH increase due to H_2 evolution, making the pH decrease less rapid during the course of the tests since this effect counteracts the effect of pH decrease due to H^+ generation (Bertuol et al. 2016). Evidently, monosodium phosphate addition, when acting as a buffer, effectuated improvements regarding the pH variation and current efficiency for the results obtained at 50 °C.

5.11 Effect of Na_2SO_4 on the Current Efficiency

The incorporation of an alkaline metal sulphate additive into the electrolyte solution increases the conductivity of the electrolyte solution medium (Sharma et al. 2005a). Experiments were performed by the addition of alkaline sulphates of sodium. The addition of a small amount of sodium sulphate resulted in an adherent and uniform morphology Co-Ni composite deposit. The effect of sodium sulphate concentration on the current efficiency is depicted in Figure 5-13.

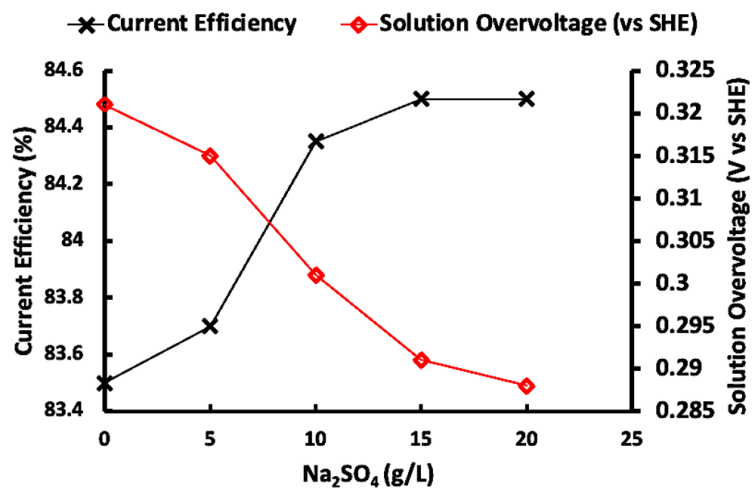


Figure 5-13: Effect of Na_2SO_4 in an electrowinning set-up (-1.15 V, pH =4.5, 15 g/L of buffer, 50 °C, 47.5 g/L of $\text{Ni}^{2+}_{0.25}\text{Co}^{2+}_{0.1}\text{Mn}^{2+}_{0.15}\text{Li}^{+}_{0.5}$, AA/EV of 2 cm²/250 cm³).

As can be observed, the current efficiency increases from 83.48 to 84.47 with Na_2SO_4 addition up to 15 g/L, beyond which further addition of the salt exhibits insignificant effect since current efficiency was stagnate at ~84.47 after 15 g/L. The trend is largely due to solution electroconductivity induced by the free sulphate and sodium ions which act as charge carriers, therefore the more the amount of free and mobile ions, the higher the conductivity. The correlation is explicitly depicted by trends presented by Schalenbach et al. (2022), which depicts the parametrisation of the molar conductivity of Na_2SO_4 as a function of concentration (Schalenbach et al. 2022). The increased molar conductivity results in lower H_2 evolution and higher efficiency for Co recovery. When the Na_2SO_4 concentration is increased above 15 g/L, there

is a negligible drop in overpotential and a negligible increase in current efficiency. The lowering of the applied potential and the increased current efficiency also results in lower energy requirement.

5.12 Effect of Rotating Cathode Speed on Current Efficiency and Current

The effects of cathode electrode rotation on the EW electrowinning performance were investigated by varying the cathode rotating speed from 0 to 40 rpm. As shown in Figure 5-14, the operating current density of the EW process increased from 0.018 ± 0.001 A/cm² (0 rpm) to 0.024 ± 0.001 A/cm² (20 rpm) and eventually to 0.35 ± 0.001 A/cm² (40 rpm).

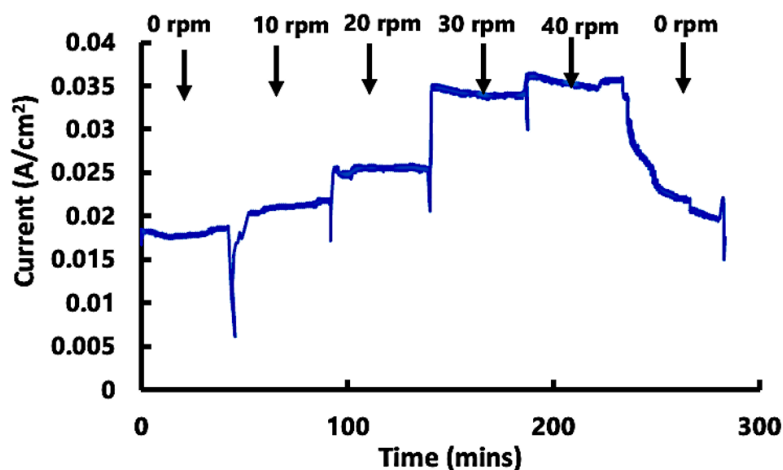


Figure 5-14: Current as a function of rotating cathode speed (-1.15 V, pH =4.5, 15 g/L of buffer, 15 g/L Na₂SO₄, 50 °C, 47.5 g/L of Ni²⁺_{0.25}Co²⁺_{0.1}Mn²⁺_{0.15}Li⁺_{0.5}, AA/EV of 2 cm²/250 cm³).

This correlation in Figure 5-14 indicates a significant 74% surge in the current density from 0 to 40 rpm. The deposition rate at 40 rpm was denoted to be 0.062 g/cm².hr), which increased by 76 % from the deposition rate at 0 rpm (0.035 g/cm².hr). In addition, the cathode rotation speed played a significant role in effectuating turbulence in the electrolyte flow. This is reflected in the estimated Reynolds number (Re) that increased from 465 (10 rpm) to 1850 (40 rpm) using the equation:

$$N_{Re} = \frac{nDe^2\rho_{sg}}{\mu_k}$$

5-1

Where n is impeller rotational speed (rev/s), De is plate effective diameter (0.08 m), ρ_{sg} is the specific gravity (1.3) and μ_k is the kinematic viscosity (0.000003 m²/s).

The turbulence in the electrolyte flow, indicated by a higher Reynolds number, can effectuate higher ionic and electronic mobility, resulting in accelerated reduction reaction kinetics and less species build-up on the electrode-electrolyte interface per each level of potential. Meanwhile, the constant turbulent fluid motion also accelerates the diffusion and transfer of protons and anions from the anode surface film, thereby minimizing a localized pH gradient within the electrolyte-anode interphase. In addition, increased turbulence within the electrolyte flow can decrease the anodic and transport resistance for ionic species through to the cathode side, resulting in a higher current density (Sleutels et al. 2009; Pan et al. 2019). When the cathode rotation speed was set to 0rpm, current density quickly decreased to 0.055 ± 0.02 A/cm², demonstrating that the cathode rotation speed played a significant role in the increase of the current density. The Levich plot analysis of the set of electrowinning experiments conducted at different rotational speeds is depicted in Figure 5-15 b).

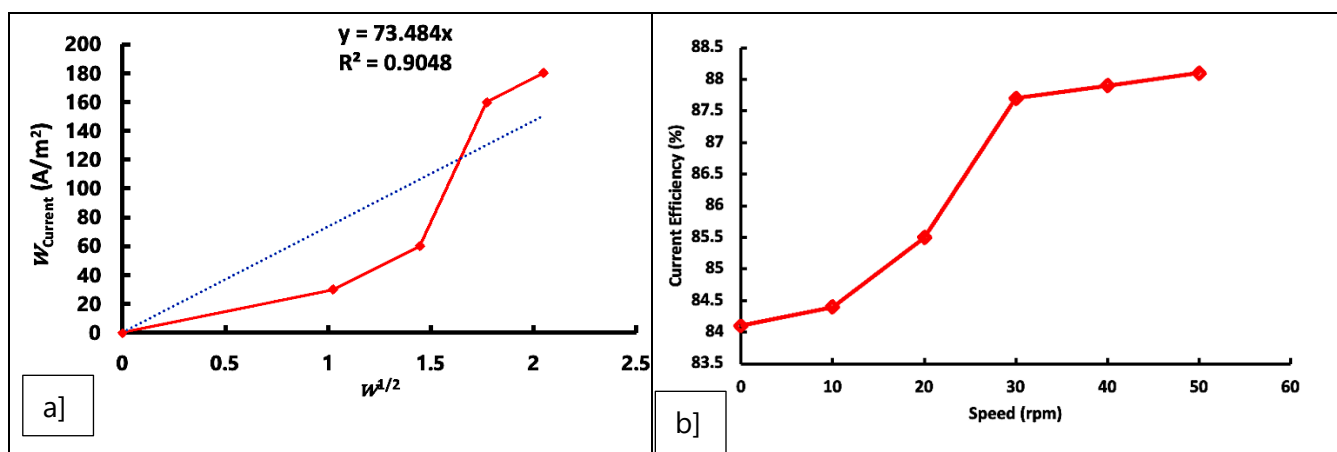


Figure 5-15: a) The Levich plot analysis and b) the effect of cathode rotational speed on current efficiency and (-1.15 V, pH =4.5, 50 °C, 47.5 g/L of Ni²⁺_{0.25}Co²⁺_{0.1}Mn²⁺_{0.15}Li⁺_{0.5}, AA/E of 2 cm²/250 cm³).

The rotation speed of the electrowinning set-up also affected the current efficiency of Ni-Co deposition, as depicted in Figure 5-15 b). Although the effect of rotating cathode speed on current efficiency was not immediately apparent between 0 rpm (84%) and 10 rpm (84.5%) since the current efficiency negligibly increased, further increasing the rotating speed gradually increased current efficiency to 85.5% (20 rpm), 87.5% (30 rpm), 87.9% (40 rpm) and 88.1% (40 rpm) and 88.2% (50 rpm). The correlational trend distinctly indicates that the increasing cathode rotating speed results in a significant surge in the current efficiency. It is worth noting that the current efficiency increased significantly from 84% at 0 rpm to 87.7% at 30 rpm, and then only slightly to 88.2% between 30 and 50 rpm. Meanwhile, the increase in current density was minimal (between 30 and 40 rpm), indicating that power consumption per unit of mass decreased. This was possibly due to the verity that the anode electrode rotation enhances the ionic, electron and bulk species mass transfer, thereby increasing the activities of electrochemically active ionic and electronic species in the solution.

5.13 Cobalt/Nickel Electrowinning Using Synthetic Solution

Following completion of the electrowinning optimization experiments with synthetic solutions, which aimed to determine the ideal and optimal electrowinning conditions (-1.15 V vs Ag/AgCl, 47.5 g/L $\text{Ni}^{2+}_{0.25}\text{Co}^{2+}_{0.1}\text{Mn}^{2+}_{0.15}\text{Li}^{+}_{0.5}$, 50 °C, 15 g/L of NaH_2PO_4 , 15 g/L Na_2SO_4 , pH 4.5 and 40 rpm cathode speed (CS)), final electrowinning of Co-Ni was performed using the previously optimized conditions and parameters. The aluminium plate electrode was utilized as the cathode, and Pt coated Ti electrode as the anode. The stripped electrowon Co-Ni deposit exhibited smooth morphology and evenly distributed particle size and shape, as shown in Figure 5-19 a), and a significant part of it adhered to the cathode surface; therefore, it was quite possible to easily calculate the accurate, current efficiency.

In order to assess the best separation technique between constant current electrowinning and constant voltage electrowinning, the deposit quality and composition were assessed. Optimal level for constant current (0.035 A/cm²) for constant current electrowinning were noted from the

approximated current response at the -1.15 V vs Ag/AgCl potential level whilst optimal potentiostatic electrowinning parameters were experimentally determined in this work. As illustrated by Figure 5-16, constant current electrowinning at optimal current (0.035 A/cm^2) (galvanostatic electrowinning) produced a deposit with lower purity (82 % Ni-Co) than at constant potential (potentiostatic electrowinning), which produced 98 % pure Ni_xCo_y . Constant potential electrowinning is more selective to specific reactions (Co and Ni reduction at -1.15V vs Ag/AgCl) at a specific potential compared to constant current, which reduces relatively most of the cations in the solution. The lower purity of constant current electrowinning is primarily due to the deposited Mn, Li and Al and other impurities as confirmed by ICP and EDS analysis.

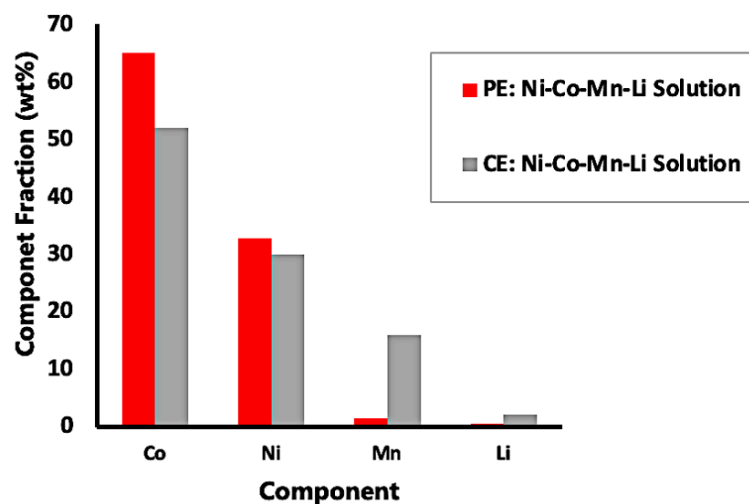


Figure 5-16: Composition of deposit from constant current electrowinning (CE) vs constant potential electrowinning (PE) (PE= -1.15 V vs Ag/AgCl, CE= 0.035 A/cm^2 , 180 minutes, $2\text{cm}^2/250 \text{ cm}^3 \text{ AA/EV}$ in $47.5 \text{ Ni}^{2+}_{0.25}\text{Co}^{2+}_{0.1}\text{Mn}^{2+}_{0.15}\text{Li}^{+}_{0.5}$ Solution).

A graphical representation of how current efficiency varies over time is depicted in Figure 5-17. The figure indicates that current efficiency decreases over time, it decreases insignificantly between 0-180 minutes then rapidly after 180 minutes. This trend is attributed to the build-up of the non-conductive cobalt oxide layer on the aluminium cathode plate and the decrease in the pH, which promotes the hydrogen evolution side reaction.

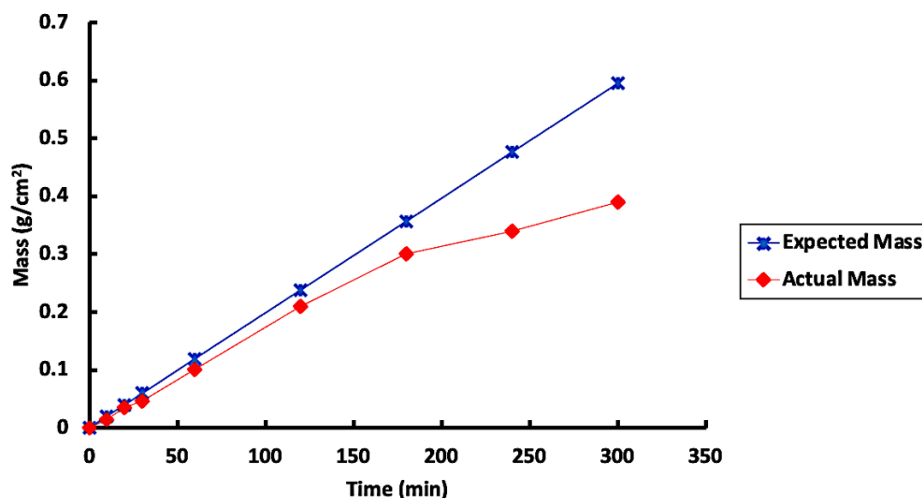


Figure 5-17: Expected mass deposited vs actual mass deposited over a 120 minute period (-1.15 V, pH =4.5, 50 °C, 47.5 g/L of $\text{Ni}^{2+}_{0.25}\text{Co}^{2+}_{0.1}\text{Mn}^{2+}_{0.15}\text{Li}^{+}_{0.5}$, AA/E of $2 \text{ cm}^2/250 \text{ cm}^3$).

In addition, Figure 5-18 indicated that electrowinning of Ni-Co in a 30 g/L $[\text{Co}^{2+}_{0.3}\text{Ni}^{2+}_{0.7}]$ solution can be depleted to approximately 4.75 g/L $\text{Co}_{0.35}\text{Ni}_{0.65}$ solution over a period of 180 minutes using a two layered $3 \times 10 \text{ cm}^2$ Pt coated Ti anodes and a rotating $3 \times 10 \text{ cm}^2$ aluminium plate electrode (active area-electrolyte volume (AA/EV) ratio of $30 \text{ cm}^2/250 \text{ ml}$). Through the implementation of an optimised electrowinning process 75% and 90% of Ni and Co respectively were effectively recovered from the leachate as presented in The EW process was halted when the electrolyte concentration dropped below 4.85 g/L since the current efficiency starts dropping rapidly (from 88 % at 180 minutes to 66 % at 250 minutes). Since the reaction rate is solely dependent on one composite reactant (Co:Ni) as evident from Figure 5-18 a) and the linear plot of $\ln[A]$ vs time in Figure 5-18 (a), the electrowinning Co-Ni is deemed to be first order. The electrowinning first-order reaction proceeds according to the following reaction:

$$\ln[C_t] - \ln[C_0] = -kt$$

5-2

Where C_t is concentration at any time t , C_0 is the initial concentration, k is reaction constant, and t is time. The reaction constant, k , is calculated to be 0.016 1/min as depicted in Figure 5-18 (b) bringing the first-order equation to the expression:

$$\ln[C_t] - \ln[C_0] = -0.016t \quad 5-3$$

As per the kinetics correlation in Figure 5-18 a), the reaction kinetics correlation indicates a negative linear correlation between time and concentration, thereafter the electrodeposition stalls as indicated in Figure 5-18 (a). This inactivity is attributed to less mass transfer gradient between the electrolyte and cathode surface, due to depleted metal ion species in the electrolyte, resulting in less metal ion transfer from the electrolyte to the cathode electrode. In light of this, there is a need for continuous electrolyte replenishment therefore after 180 minutes of electrowinning, fresh new electrolyte is added to the electrowinning chamber.

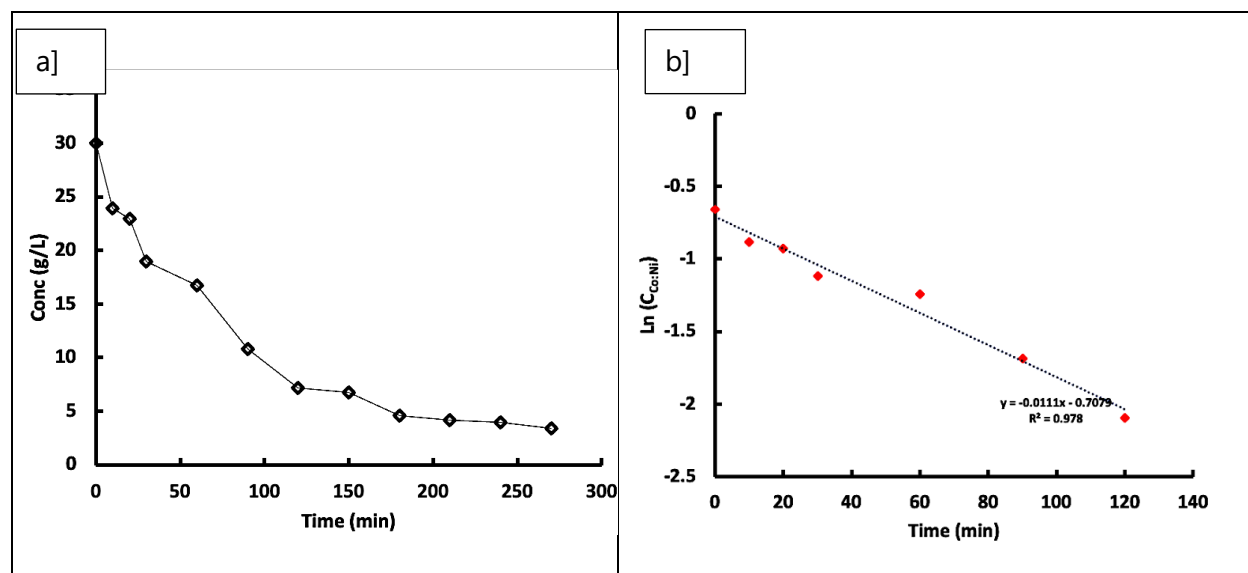


Figure 5-18: a) Concentration variation of a 30 g/L $[\text{Co}^{2+}_{0.3}\text{Ni}^{2+}_{0.7}]$ mixture within a multi-ion synthetic solution (47.5 g/L of $\text{Ni}^{2+}_{0.25}\text{Co}^{2+}_{0.1}\text{Mn}^{2+}_{0.15}\text{Li}^{+}_{0.5}$) over 250 minutes of electrowinning and b) kinetics of Co-Ni electrodeposition during the first 120 minutes (at -1.15 V, pH 4.5 and 50 °C in 30 g/L $[\text{Co}^{2+}_{0.3}\text{Ni}^{2+}_{0.7}]$).

Table 5-1 presents the elemental composition of the electrowon deposit, as obtained by ICP-OES, which evidently shows that the deposit largely constitutes Ni and Co (98 wt.%). The results indicate that post electrowinning, 77% and 90% of Ni and Co respectively were effectively recovered from the synthetic leachate. However, only 0.8% of Li and 4.05% of Mn was recovered during the selective electrodeposition process. This indicates the optimised process is highly selective to Ni and Co. The EW process was halted when the electrolyte concentration dropped below 4.85 g/L since the current efficiency starts dropping rapidly (from 88% at 180 minutes to 66% at 250 minutes) as highlighted in Figure 5-17. As shown in Table 5-1, at low AA/EV ratios, the electrowon Ni-Co alloy deposit contains more Co than Ni, despite the solution being predominantly Ni^{2+} . This anomalous phenomenon of preferential Co deposition over Ni is discussed in detail in Section 5.3. However, at high AA/EV ratios, the larger electrode surface area enhances reaction kinetics, particularly for Ni, due to its significantly higher concentration of Ni^{2+} in the electrolyte solution. This results in a higher Ni content in the deposit at high AA/EV ratios, mitigating the initial preferential deposition phenomenon of Co.

Table 5-1: Chemical composition, determined by ICP-OES, of the Ni-Co deposit obtained in the electrowinning process (47.5 g/L of $\text{Ni}^{2+}_{0.25}\text{Co}^{2+}_{0.1}\text{Mn}^{2+}_{0.15}\text{Li}^{+}_{0.5}$, -1.15 V vs Ag/AgCl, 50 °C, 15 g/L of buffer, 15 g/L of Na_2SO_4 , pH 4.5, 40 rpm).

Component	Weight % (After EW) [AA/EV of 2cm²/250 cm³]	Weight % (After EW) [AA/EV of 30cm²/250 cm³]	Synthetic Leachate (Before EW) [g/l]	% Recovered AA/EV [30cm²/250 cm³]
Co	68.09±0.67	34.07±0.33	8.5	92
Ni	30.18±0.31	65.45±0.72	21.25	78
Na	0.35±0.01	0.39±0.01	-	-
Al	0.12±0.01	0.09±0.01	-	-
Mn	1.58±0.02	1.71±0.02	12.5	4.2
Li	0.01±0.001	0.02±0.001	5.5	0.95

As expected, Na traces ($0.35 \pm 0.01\%$, from NaOH and Na_2SO_4) and Al traces ($0.12 \pm 0.01\%$, from Al cathode and cathode material) were co-deposited with Ni and Co as impurities and possibly the deposit's relatively rough morphology qualities were caused by the presence of such impurities (as shown in SEM imaging in Figure 5-19 a). To determine whether the electrowon deposit was solely constituting metals listed Table 5-1, an analysis by microprobe (EDX), presented in Figure 5-19 (b), was performed.

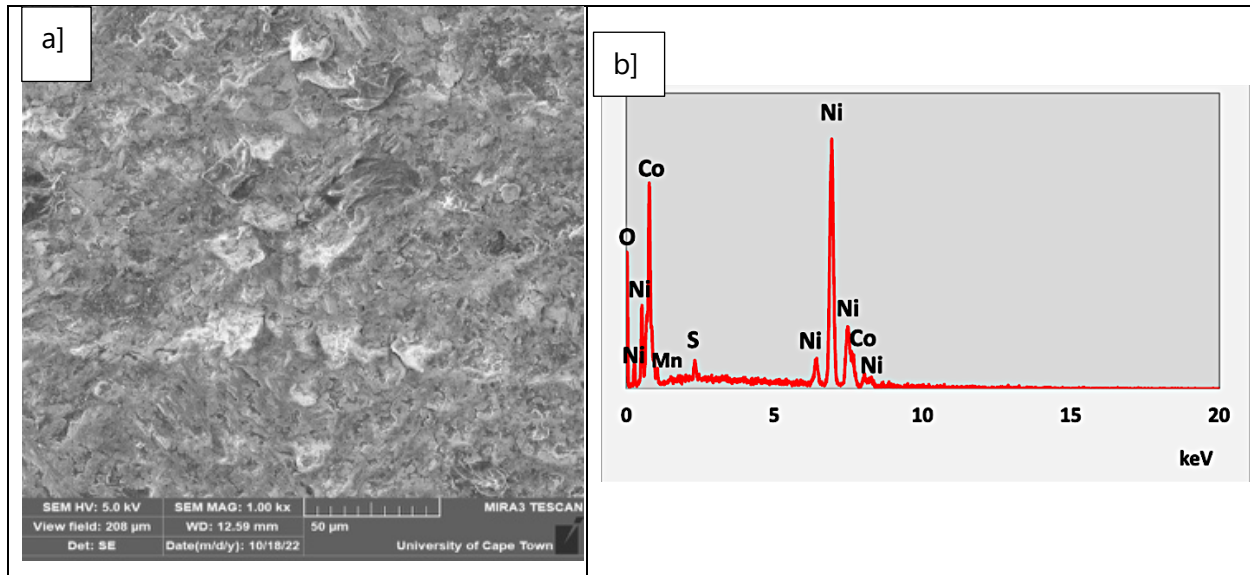


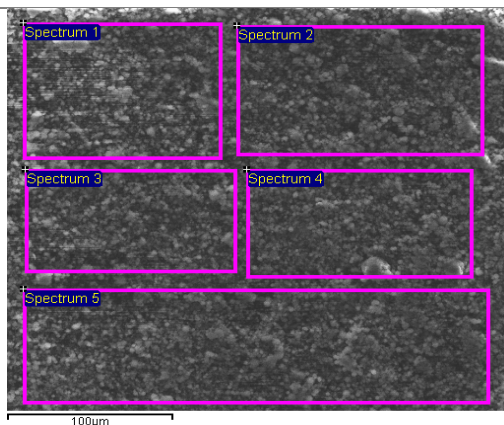
Figure 5-19: a) Micrograph of the deposit morphology, deposit obtained from the synthetic solution electrowinning and b) EDX spectrum of the deposit (47.5 g/L of $\text{Ni}^{2+}_{0.25}\text{Co}^{2+}_{0.1}\text{Mn}^{2+}_{0.15}\text{Li}^{+}_{0.5}$, -1.15 V vs Ag/AgCl , $50 \text{ }^\circ\text{C}$, 15 g/L of buffer, 15 g/L Na_2SO_4 , pH 4.5, AA/E of $2 \text{ cm}^2/250 \text{ cm}^3$).

The results, EDS results summarized in Table 5-2, demonstrate that no other metal was detected, however, they indicate the presence of other elements such as oxygen (O), sulphur (S), and sodium (Na). The presence of these impurities is probably associated with the contamination by from unwanted side reactions or species from the electrolyte solution. The oxygen evolved at the anode or if there are side reactions involving oxygen, the oxygen can get incorporated into the deposit in small amounts. However, it is also worth noting that EDS, the results being referred to are a surface limited analysis, so the figures dose not the reflect the matrix composition and regarded as relatively inaccurate.

The presence of sulphur in the deposit is also an indirect indicator of sulphur based anion involvement in the cathodic reaction (Golodnitsky et al. 1998). In spite of the deposit, as presented in Figure 5-19 a), being rinsed and dried before the analysis, the cleaning process was possibly not effective in promoting the total removal of the solution contaminants.

Table 5-2: Chemical composition, determined by EDS, of the deposit obtained in the electrowinning (47.5 g/L of $\text{Ni}^{2+}_{0.25}\text{Co}^{2+}_{0.1}\text{Mn}^{2+}_{0.15}\text{Li}^{+}_{0.5}$, -1.15 V vs Ag/AgCl, 50 °C, 15 g/L of buffer, 15 g/L Na_2SO_4 , pH 4.5, AA/E of $30\text{ cm}^2/250\text{ cm}^3$).

Component	Weight % (After EW)
Co	61.09±4.76
Ni	26.19±2.41
S	0.56±0.2
O	9.94±1.2
Al	0.31±0.1
Na	0.22±0.1
Mn	1.67±0.3



When the weight composition of nonmetal species (S and O) detected by the EDS analysis are excluded from the alloy purity calculation, the Ni-Co composition is determined to be 97.8 wt.%. This result is further corroborated by ICP-OES, which reports a Ni-Co concentration of 98.2 wt.%. ICP-OES is considered a more reliable analytical method due to its lower standard deviation compared to EDS as shown in Table 5-2 and Table 5-1. Excluding nonmetal concentrations from the alloy purity calculation focuses on the primary metallic components, providing a more accurate assessment of the composition of key elements like Ni, Co, Li, and Mn, which are crucial for evaluating the alloy's quality and performance. Nonmetal elements, being less critical, can be easily separated from the alloy through simple reduction processes to improve purity. The proposed method of using a reductive atmosphere to remove oxygen from the alloys is not included in this work, as it falls outside the scope and is mentioned only as a recommendation for potential future use if necessary.

Chapter 6: Electrowinning Cell Voltage Optimization

6.1 Overview

In the Co and Ni production industrial sectors, the preeminent facet of operational expenditure lies in the cost of electrolysis. Acknowledged by Tawonezvi et al. (2023), there exists an ongoing and concerted scholarly effort directed towards the reduction of costs and energy consumption associated with electrochemical processes integral to the extraction of Co and Ni. The imperative to optimize this cost and energy consumption is of paramount importance, as it exerts a substantial impact on the economic feasibility of the overall production process. The optimisation of the electrowinning voltage, which is function input of both the electrowinning cost and energy consumption, is the focus of this chapter.

Imperative to the comprehension of electrowinning cost is the nuanced recognition that the total cell voltage (E), which is a function input of both the energy consumption and cost factor, is a summation of several contributing component potentials. This chapter delves into a rigorous exploration of the intricate network of factors influencing the operational dynamics inherent to Co and Ni production. The aim of the chapter is to reduce the overall voltage consequently reducing the overall voltage.

6.2 Cell Voltage Optimisation

As highlighted above, the cost of electrolysis constitutes the largest fragment of the total operational cost involved in the Co and Ni production. Therefore, great efforts are continuously being made in research to obtain the Co and Ni at a lower cost (Tawonezvi et al. 2023). The total voltage of the cell (E) is a sum of the potential of various components, which include reaction potential (E_R), as well as contributions from the anode potential (E_a), the anode overpotential (η_a), cathode potential (E_c), the cathode overpotential (η_c), and the ohmic resistance of the electrolyte (R_{ohm}).

solution (E_{OE}), and the contact resistance (E_{CS}). The overall voltage is quantified as per the reaction equation:

$$E_E = E_a + |\eta_a| - (E_c + |\eta_c|) + E_{OE} + E_{CS} \quad 6-1$$

For the electrolysis of Co and Ni with a conventional couple of Pb and stainless-steel electrodes, the total calculated E is 2.8, and in practice, it ranges in the interval of 2.75 to 4 V (Pradhan et al. 2001; Sharma et al. 2005a; Mulaudzi and Kotze 2013; Lu et al. 2018; Kazem-Ghamsari and Abdollahi 2022). 5 Electrodes were selected as potential anodes for the electrowinning process, namely, glass carbon (C), graphite (GC), platinum (Pt), lead (Pb) and Titanium (Ti). Anodic overvoltage for the conventional Pb anode is 0.65V vs Ag/AgCl, for glass carbon (C) is 1.6 V vs Ag/AgCl, for graphite (GC) 1.4 V vs Ag/AgCl, platinum (Pt) 0.25 V vs Ag/AgCl, and for Titanium (Ti) is 0.8 V vs Ag/AgCl. Pt exhibit the lowest overvoltage compared to other electrodes whilst Pb exhibit the highest instability over the course of electrowinning. Figure 6-1 denotes the anodic overvoltage for the 5 electrodes.

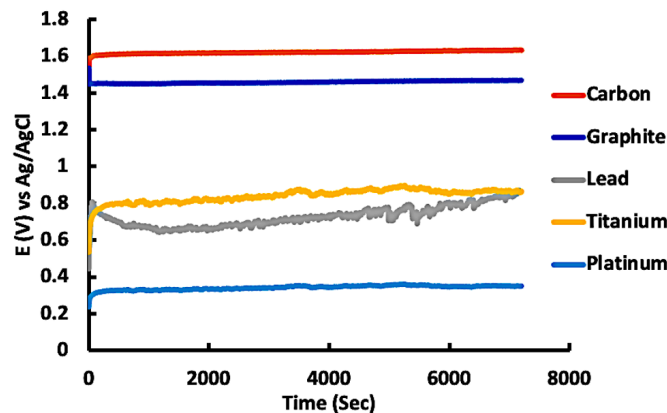


Figure 6-1: Anodic overvoltage for Pt, C, GC, Ti and Pb (0.035 A/cm², pH =4.5, 50 °C, 47.5 g/L of Ni²⁺_{0.25}Co²⁺_{0.1}Mn²⁺_{0.15}Li⁺_{0.5}).

The cost factor, service life factor, corrosion factor (mass loss during operation), and anodic overvoltage for all five electrodes (Carbon, Graphite, Lead, Titanium, and Platinum) were integrated for a comprehensive comparative analysis, as illustrated in Figure 6-2. Titanium appears

to exhibit optimal well-rounded performance compared to other anodes. The capital cost of titanium is way lower than platinum yet its service life and corrosion factor (mass lost per cm^2 per hour) is relatively equal to that of platinum. Therefore, Pt plating of Ti which uses a relatively small amount of Pt can increase the service life whilst reducing the anodic overvoltage.

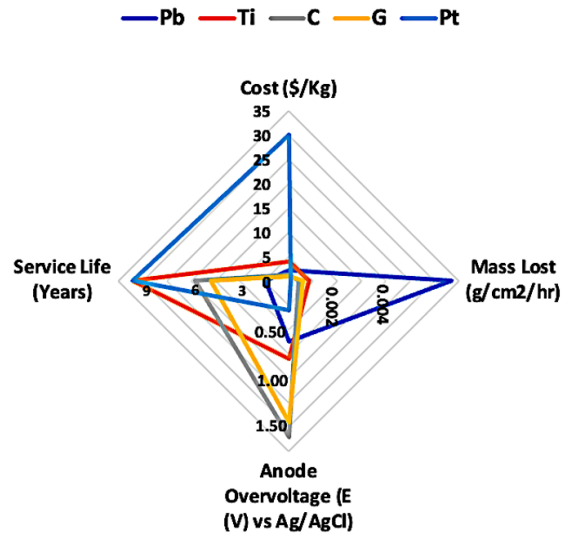


Figure 6-2: Comprehensive performance analysis of pure Pb, Ti, Pt, C and GC electrodes based on anode overvoltage, cost, service life and corrosion factor (mass lost during operation) (Partial Data derived from ref (Moradi et al. 2020; Bloomberg 2022)).

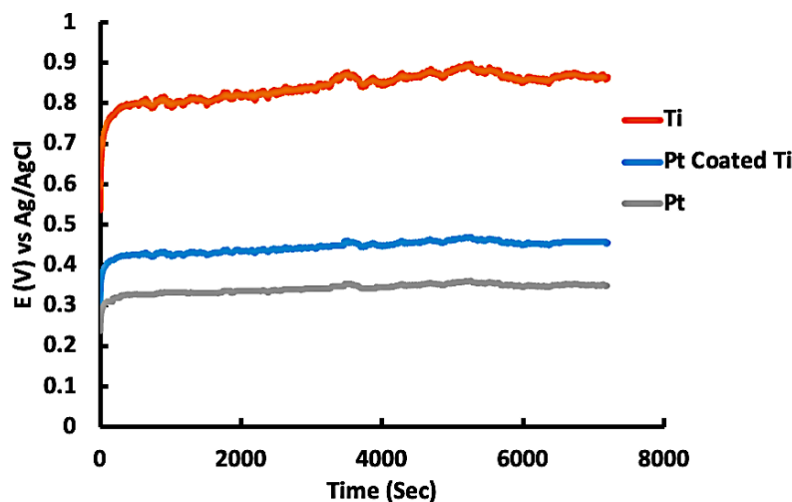


Figure 6-3: Anodic voltage of Ti and Pt Coated Ti (at 0.035 A/cm^2 , $\text{pH} = 4.5$, $50 \text{ }^\circ\text{C}$ in 47.5 g/L of $\text{Ni}^{2+}_{0.25}\text{Co}^{2+}_{0.1}\text{Mn}^{2+}_{0.15}\text{Li}^{+}_{0.5}$).

The Pt-coated Ti electrodes were prepared according to the reported procedure with no further modification (Rao and Pushpavanam 2001). Following this method, the estimated amount of Pt on the surface of the electrode would be 2 mg/cm² according to Rao and Pushpavanam (2001). The actual deposited amount was not verified and outside the scope of the thesis. For platinum-coated titanium DSA, the anodic over-voltage decreased by 0.35 V when tested in 47.5 g/L of Ni²⁺_{0.25}Co²⁺_{0.1}Mn²⁺_{0.15}Li⁺_{0.5}, at a pH of 4.5, and temperature of 50 °C as depicted in Figure 6-3. Through the utilisation of Pt-coated titanium, only the conventional Pb anode will be replaced, but not the main oxidation reaction of water to produce oxygen, H⁺ protons and free electrons. This transition leads to significant savings in specific energy consumption of the overall process and eliminates the classic conventional problem of acid mist formation in electrowinning cells. The results demonstrate that the proposed process exhibit 40% less anodic potential (~0.42 V vs Ag/AgCl) compared to the anodic potential (0.72 V vs Ag/AgCl) of conventional electrowinning cells. Per Ohm's law, this will reduce the power consumption of the cell by 30 % and consequently the cost of operation. The oxygen evolution reaction (OER) reaction potential at pH=4.5 is 1V vs SHE therefore the anodic potential is determined to be 1.705 vs SHE.

$E_c + \eta_c$ is the cathode potential. $E_c + \eta_c$ (-0.812 V vs SHE) was obtained from data obtained from cyclic voltammograms produced using a 50 °C electrolyte with 30 g/L [Ni²⁺_{0.7}Co²⁺_{0.3}], 2M H₂SO₄ at pH=4. The cathode overpotential of plating Co-Ni on Al was obtained by the potential difference between the backward sweep and the standard potential at cobalt deposition. The voltage drop caused by solution resistance can be calculated using current density and electrolyte conductivity. A suitable empirical equation [Eq. 6-2] for electrolyte conductivity was presented by Kargl-Simard et al. (2003).

$$\varepsilon = 103.86 - 0.29464[Co/Ni] + 0.82661T + 0.91000 [H_2SO_4] \quad 6-2$$

Where ε is the electroconductivity (mS/cm), T is the temperature in degrees Celsius and [H₂SO₄] is the H₂SO₄ concentration in g/L (Kargl-Simard et al. 2003). The conductivity of a 30 g/L (Co_{0.3}Ni_{0.7}) in 2M H₂SO₄ (200 g/L), 50°C electrolyte was calculated to be 305 mS/cm (consistent with the

measured value of 312 mS/cm). Current density of 350 A/m², electrode areas of 5cm² and a face-to-face anode to cathode separation of 0.025 m, the E_{OE} was calculated to be 0.287 V using the below equation.

$$E_{OE} = 1/\varepsilon \times L \times I \quad 6-3$$

where ε is the specific conductivity of the electrolyte, L is the electrode gap, and I is the current density. The voltage component related to the contact resistance between electrode header bars and the cell busbars was also calculated to have a resistance of 58 $\mu\Omega$ for spool contacts (Battle et al. 2016). Combining this with a 350 A/m² current density (5 cm² per electrode) at two contact points per cell (one anode and one cathode) produces a potential drop of 0.001V.

$$E_{OE} = \Omega \times L \times I \quad 6-4$$

where Ω is the specific conductivity of the electrolyte, L is the electrode effective length, and I is the current density.

Summating all the individual voltage components as shown in Table 6-1 produces a cell voltage of about 2.745 V which is significantly lower than commonly reported values which range between 3-4 V (Mulaudzi and Kotze 2013; Carvajal Ortiz et al. 2020; Kazem-Ghamsari and Abdollahi 2022). The calculated energy consumption assumes no short circuits and does not include electrical consumption due to rectification and resistances in the electrical bus system.

Table 6-1: Cell voltage contributions from anode potential, cathode potential, solution voltage and contact voltage.

Component	Value (V vs SHE)	Percentage Contribution (%)
Anodic Potential ($E_a + \eta_a $)	1.605	57
Cathodic Potential ($E_c - \eta_c $)	-0.895	32
Solution Resistance Potential (E_{OE})	0.287	10
Contact Resistance Potential (E_{CS})	0.001	0.0004
Total Voltage	2.785	

In the scope of the parameters explored and optimised in this investigation, the energy consumption (2.72 kWh/kg), as indicated in Figure 6-4, was derived utilizing the optimised cell voltage of 2.785 V and a current density of 0.035 A/cm² (350 A/m²). The electrodeposition rate used to calculate energy consumption is 0.06 g/cm²·hr, as computed in Section 5.12, and the comprehensive mass balance for the entire process is presented in Figure 9-2.

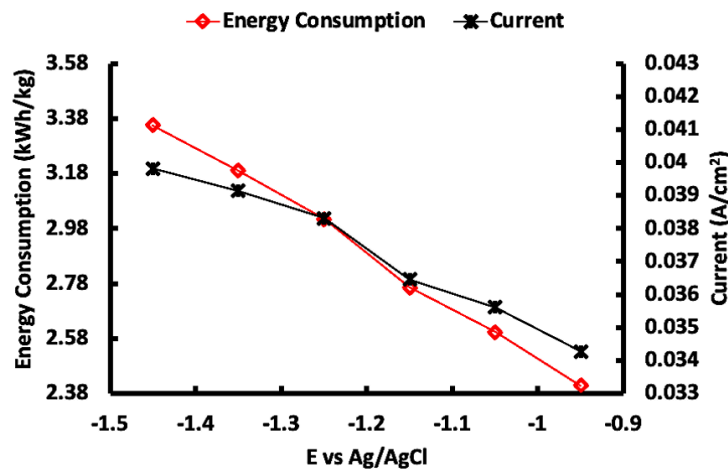


Figure 6-4: Cell potential vs energy consumption and current density for the electrowinning of Co-Ni deposits.

Please note the data used to compute energy consumption in Figure 6-4 is derived from Figure 5-4 data and the total electrowinning cell potential from Table 6-1. The Co-Ni deposit was deposited at the rate of 0.06 g/cm².hr at current efficiency of 88%. The results also indicate that post electrowinning, 77% and 90% of Ni and Co respectively were effectively recovered from the synthetic leachate. However, only 0.8 % of Li and 4.05 % of Mn was recovered during the selective electrodeposition process. A more comprehensive mass balance is presented in Chapter 9: The equation below was used to calculate energy consumption.

$$E = IVt/m \quad 6-5$$

Where E represents the energy consumption (kWh/kg), I is the current (A/m²), V is the electrowinning cell potential (V), t is the duration of electrowinning (hours), and m is the mass (kg) of the Ni-Co over the time t . The relatively minimized energy consumption does not consider corrosion, production rate and other operational limitations. On average, the total energy consumption during Ni-Co electrowinning is typically around 3 kWh/kg, varying within the range of 2.8 to 3.4 kWh/kg, while utilising a current density of 300 A/m². This work presents an approximately 14 % decrease in energy consumption whilst operating at approximately 16 % more current density and 88 % current efficiency. Based on the production capacities of the primary cobalt electrowinning operations worldwide, which summed up to around 185,000–195,000 tons per year in 2019, the energy consumption for the electrowinning stage of electrolytically refined cobalt was estimated to be about 580–650 million kWh annually (Talan and Huang 2022). In light of this, reducing the total energy demand by 1% would lead to energy savings of approximately 6 million kWh within a year.

Chapter 7: Co-Ni Electrowinning using Real NMC Leachate Electrolyte

7.1 Overview

This chapter is centred on the recovery of Ni and Co from NMC 532 leachate solutions using a hydro-electrometallurgy process route that integrates hydrometallurgy and potentiostatic electrometallurgy techniques. This real leachate electrowinning model utilises the optimised leaching and electrowinning parameters from the previous chapters. The selective electrowinning metal recovery process route is a cost-effective alternative to the energy, cost and material-intensive hydrometallurgy intermediate purification processes such as solvent extraction, selective precipitation, and ion-exchange. The study delves into the deposit composition, impurities composition and reaction kinetics. The composition of the precipitates was meticulously quantified using ICP-OES and SEM-EDS, the phase composition was evaluated through XRD analysis, and the morphology was examined using SEM. The results in this chapter successfully demonstrate the technical feasibility of recovering Ni-Co alloys from real NMC 532 leachates, yielding high quantities of industrial-grade pure Ni-Co alloys.

7.2 Co-Ni Electrowinning using real NMC Leachate Electrolyte

Following the completion of the optimisation tests with synthetic solutions, which aimed at the determination of ideal electrowinning conditions (-1.15 V vs Ag/AgCl, 50 °C, 15 g/L of buffer, 15 g/L Na₂SO₄, pH 4.5), new tests were performed using a solution obtained through the Li-ionB battery cathode leaching with sulphuric acid with added H₂O₂. Aluminium was used as the cathode and Pt coated Ti as the anode. The obtained deposit did exhibit good quality, and a great part of it adhered to the cathode, therefore, it was quite possible to easily calculate the current efficiency.

Table 7-1 presents the current efficiency levels attained using the different solution compositions. The current efficiency of Ni-Co reduction is higher when electrowinning is done in electrolytes

containing pure metal species. However, as additional species are introduced to the electrowinning electrolyte, the current efficiency experiences a slight decline. This decrease is attributed to side reactions, specifically the reduction of metals other than Ni and Co. These side reactions occur, albeit at a restricted rate due to potential limitations.

Table 7-1: Current efficiency obtained using different synthetic solution compositions electrowinning (-1.15 V vs Ag/AgCl, 50 °C, 15 g/L of buffer, 15 g/L Na₂SO₄, pH 4.5).

Electrolytes	Concentration [g/L]				Current Efficiency (%)
	Ni	Co	Mn	Li	
Ni	15	0	0	0	88.5
Co	0	15	0	0	89.2
Ni-Co	21.25	8.5	0	0	88.2
Ni-Co-Mn-Li	21.25	8.5	12.5	5.5	87.9

Table 7-2 presents the elemental composition of the electrowon deposit as obtained by ICP-OES; it is evident that the composition of the electrowon deposit largely constitutes Ni and Co (98 wt. %). However, the presence of Mn is still detected, despite its deposition potential window being selectively phased out indicating that Mn was depositing but at a limited rate. As expected, Na traces (from NaOH and Na₂SO₄), Mn (from cathode material) and Al traces (from Al cathode and cathode material) were co-deposited with Ni and Co as impurities and possibly the deposit's relatively rough morphology qualities were attributed to the presence of such impurities. As expected, Al traces were deposited and possibly the deposit's relatively rough morphology qualities were attributed to its presence. As shown in Table 7-2, at low AA/EV ratios, the electrowon Ni-Co alloy deposit contains more Co than Ni, despite the solution being predominantly Ni²⁺. This anomalous phenomenon of preferential Co deposition over Ni is discussed in detail in Section 5.3. However, at high AA/EV ratios, the larger electrode surface area enhances reaction kinetics, particularly for Ni, due to its significantly higher concentration of Ni²⁺

in the electrolyte solution. This results in a higher Ni content in the deposit at high AA/EV ratios, mitigating the initial preferential deposition phenomenon of Co.

Through the utilization of optimized parameters during the electrowinning process, 77% of Ni and 90% of Co were effectively recovered from the leachate, as presented in Table 7-2. However, only 0.8 % of Li and 4.05 % of Mn was recovered during the selective electrodeposition process. The EW process was halted when the deposition rate dropped below 4.85 g/L since the current efficiency starts dropping rapidly (from 88 % at 180 minutes to 66 % at 250 minutes) as highlighted in Figure 5-17. The current efficiency of the deposit obtained from the real leachate was $87.5 \pm 0.08\%$, which is comparable to $87.9 \pm 0.05\%$ from the synthetic leachate. This similarity in efficiency indicates that the electrochemical processes are consistent across both real and synthetic leachates. The minor difference of 0.4% could be attributed to slight variations in composition or impurities, but overall, both types of leachates exhibit similar performance in terms of current efficiency.

Table 7-2: Composition of the cathode before electrowinning, and EW Ni-Co deposit after the electrowinning process as determined by ICP-OES (-1.15 V vs Ag/AgCl, 50 °C, 15 g/L of buffer, 15 g/L Na₂SO₄, pH 4.5).

Component	Weight % (Before EW)	Weight% (After EW) [AA/EV of 2cm²/250 cm³]	Weight % (After EW) [AA/EV of 30cm²/200 cm³]	Leachate before EW [g/L]	% Recovered [AA/EV of 30cm²/200 cm³]
Li	10.9	0.01	0.02	4.98	0.8
Co	18.17	68.05	33.31	19.94	90
Ni	44.6	29.81	64.46	8.21	77
Na	-	0.21	0.28	11.59	-
Al	-	0.11	0.10	-	-
Mn	26.2	1.61	1.71	-	4.05

To verify whether the deposit was composed exclusively of the metals listed in Table 7-1, a microprobe (EDX) analysis was conducted, and the results are presented in Figure 7-1 b) and Table 7-3. Additionally, to assess the phase composition and crystalline nature of the Ni-Co deposit, X-ray diffraction (XRD) analysis was conducted, with findings shown in Figure 7-1 d). The XRD pattern for the Ni-Co alloy confirms the presence of poorly crystalline Ni (JCPDS Card# 00-003-1051) and Co (JCPDS Card# 00-015-0806) phases, while no Li or Mn based phases were detected.

The XRD diffraction peaks are characterized by low intensity and broadness, indicative of poor crystallinity, small crystallite size, and significant disorder in the material. Specifically, a very broad hump observed between 2θ values of 70° and 80° , along with moderately broad peaks between 43° and 48° and between 50° and 55° , corresponds to the poorly crystalline Ni-Co alloy phase.

The $\text{Ni}_{0.65}\text{Co}_{0.35}$ alloy displays characteristic reflections at the (111), (200), and (220) planes, as shown in Figure 7-1d). XRD analysis reveals that the Ni-Co deposits have a face-centered cubic (fcc) structure with a preferential [111] orientation. The diffraction peaks align well with those of pure fcc-Ni and fcc-Co, as illustrated in Figure 7-1 d). The deposition was conducted at a relatively low pH of 4.5. According to Myung et al. (2003) and Park et al. (2002), solution pH significantly impacts the crystal structure of Co-Ni electrodeposits; specifically, a low pH (less than 5) favours the fcc phase, whereas a high pH (greater than 5) promotes the hexagonal close-packed (hcp) phase (Park et al. 2002; Myung et al. 2003).

Additionally, very small peaks that could not be accurately identified suggest the possible presence of trace amounts of additional phases like Mn and Li. These Mn and Li traces, which could originate from the leachate electrolyte solution, may be co-deposited with Co and Ni; however, this is speculative. Phases with concentrations below 3 wt.% are below the detection limit of the XRD analysis and, therefore, were not included in the results. Furthermore, no $\text{Ni}(\text{OH})_2$ or $\text{Co}(\text{OH})_2$ phases were detected. This is consistent with the literature, which indicates that these hydroxide phases are typically formed during electrowinning at high pH (>5) (Altamirano-Garcia

et al. 2021). The absence of these phases supports the conclusion that the process is highly selective for metal deposition rather than hydroxide formation.

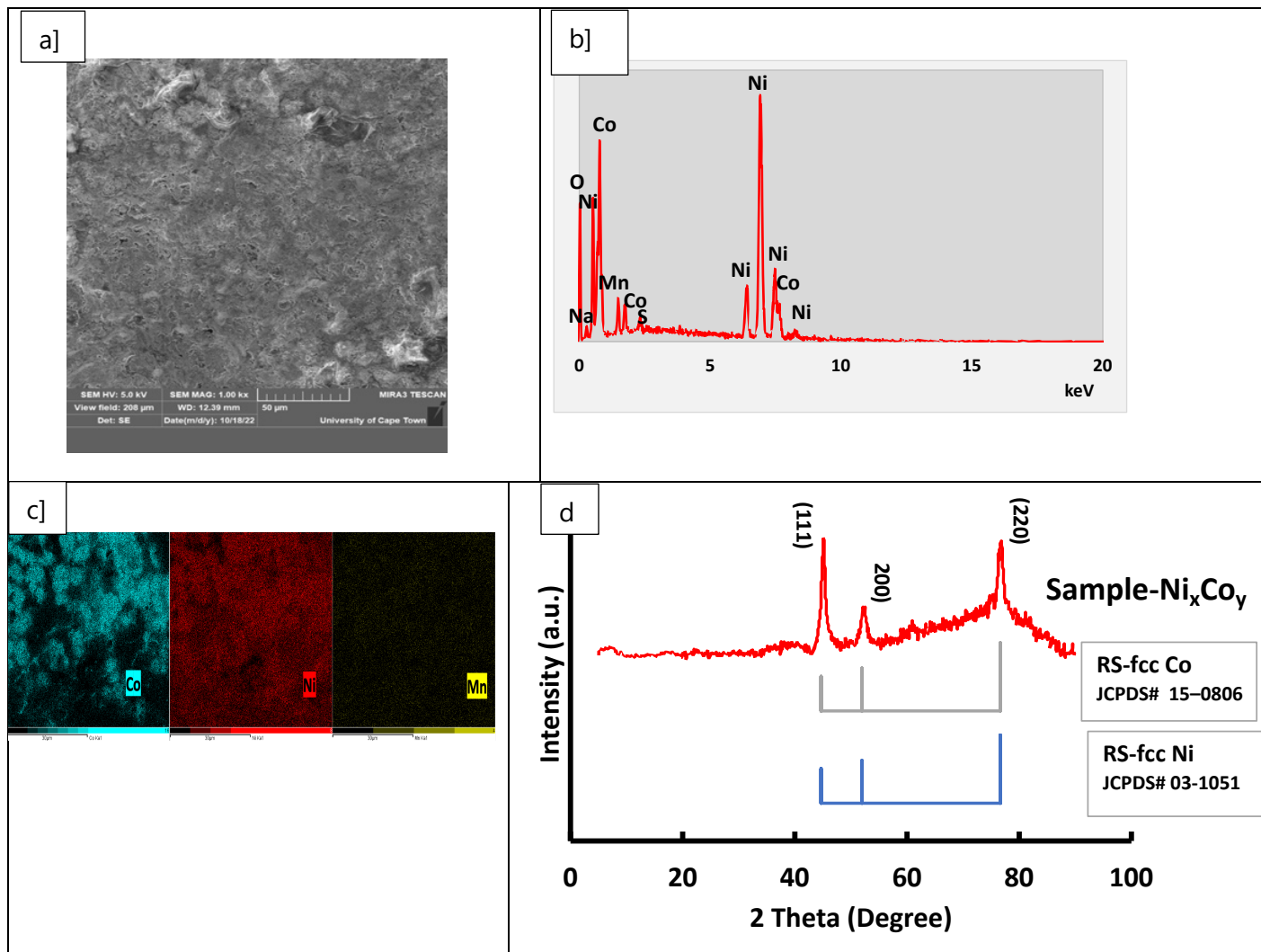


Figure 7-1: a) Micrograph of the deposit obtained from the cathode leachate solution electrowinning, b) EDX spectrum of the electrowon deposit and c) EDS mapping of the electrowon deposit (-1.15 V vs Ag/AgCl, 50 °C, 15 g/L of buffer solution, 15 g/L Na₂SO₄, pH 4, AA/E of 2 cm²/250 cm³).

The results of ICP-OES and SEM-EDS summarized in Table 7-3 and EDS spectrum summarized in Figure 7-1 b) demonstrate that no other metal was detected; however, EDS in particular, they indicate the presence of impurity elements such as O, S, and Cu in trace amounts.

Table 7-3: Chemical composition of Ni-Co deposit, determined by EDS, of the deposit obtained in the electrowinning (-1.15 V vs Ag/AgCl, 50 °C, 15 g/L of buffer, 15 g/L Na₂SO₄, pH 4.5).

Component	Weight % (Before EW)	Weight % (After EW) [AA/EV of 2 cm ² /250 cm ³]	Weight % (After EW) [AA/EV of 30 cm ² /250 cm ³]
Co	14.58	61.64	29.01
Ni	37.05	26.26	59.48
S	-	0.56	0.61
O	31.14	10.21	9.35
Na	-	0.31	0.41
Al	-	0.14	0.11
Mn	15.82	1.81	1.88
Al	1.45	-	-

EDS Spots

The presence of O and S is probably associated with the contamination by unwanted side reactions and species from the electrolyte solution. . The oxygen evolved at the anode or if there are side reactions involving oxygen, the oxygen can get incorporated into the deposit in small amounts. However, it is also worth noting that EDS, the results being referred to are a surface limited analysis, so the figures dose not the reflect the matrix composition and regarded as relatively inaccurate.

In spite of the deposit, as presented in Figure 7-1 (a), being rinsed and dried before the analysis, the cleaning process was possibly ineffective in promoting the total removal of the solution contaminants. When the weight composition of nonmetal species (S and O) detected by the EDS analysis are excluded from the alloy purity calculation, the Ni-Co composition is determined to be 97.5 wt.%. This result is further corroborated by ICP-OES, which reports a Ni-Co concentration of 98.1 wt.%. ICP-OES is considered a more reliable analytical method due to its lower standard deviation compared to EDS as shown in Table 5-2 and Table 5-1.

Excluding nonmetal concentrations from the alloy purity calculation focuses on the primary metallic components, providing a more accurate assessment of the composition of key elements like Ni, Co, Li, and Mn, which are crucial for evaluating the alloy's quality and performance. Nonmetal elements, being less critical, can be easily separated from the alloy through simple reduction processes to improve purity. The proposed method of using a reductive atmosphere to remove oxygen from the alloys is not included in this work, as it falls outside the scope and is mentioned only as a recommendation for potential future use if necessary.

The primary objective of extracting Ni-Co composite with >97 % purity was achieved despite the deposit not exhibiting ideally good quality in terms of morphology and purity. When the obtained results are compared to those found in the literature for the conventional processes of Ni and Co-production, as the ones that use carbonyl or hydrogen reduction, it is observed that the obtained product from these conventional processes is in the form of a powder that should still be pre or post subjected to a subsequent treatment stage to achieve ultra-purity whereas the work presented in this work can attain >95% Ni-Co composite purity which meets the industrial-grade standard excludes such processes (Wang 2006; Moats and Davenport 2014; Farjana et al. 2019).

The powder deposit that is formed on the cathode is easily recovered by stripping and afterwards directed to a washing and drying process to produce an impurity-free Ni-Co alloy. As approximately 10 wt.% of the deposit is composed of oxygen, the powder can be effectively recovered by roasting in a reductive atmosphere to release the oxygen and thus, the composition

of the ingot obtained will be approximately 98 wt.% of Ni-Co composite (Lin and Chen 2004). The proposed method of using a reductive atmosphere to remove oxygen from the alloys is not included in this work, as it falls outside the scope and is mentioned only as a recommendation for potential future use if necessary.

Chapter 8: Recovery of Mn(OH)_2 , Li_2CO_3 and $0.6[\text{Ni(OH)}_2].0.3[\text{Mn(OH)}_2].0.1[\text{Co(OH)}_2]$ Precipitates

8.1 Overview

Following the successful recovery of Ni-Co from spent NMC 532 battery leachates, the valuable by-products such as Li_2CO_3 and Mn(OH)_2 and $0.6[\text{Ni(OH)}_2].0.3[\text{Mn(OH)}_2].0.1[\text{Co(OH)}_2]$ composite were recovered from spent electrolytes through chemical precipitation. This chapter focuses on the recovery of valuable metals from the electrowinning resultant leachate. The resultant leachate was treated with NaOH to specific pH levels to selectively recover mixed Ni, Mn and Co hydroxides and Mn(OH)_2 . The resultant electrolyte is followed up by Na_2CO_3 chemical-based precipitation to recover Li_2CO_3 through filtration.

The combination of pH-based and chemical precipitation was utilised to recover Ni, Co, Mn, Li in metal sulphate solutions as $0.6[\text{Ni(OH)}_2].0.3[\text{Mn(OH)}_2].0.1[\text{Co(OH)}_2]$, Mn(OH)_2 and Li_2CO_3 in separate streams. The recovered $0.6[\text{Ni(OH)}_2].0.3[\text{Mn(OH)}_2].0.1[\text{Co(OH)}_2]$ and Li_2CO_3 are synthesised to be used as precursors in the NMC cathode production facilities. The composition of the solids was meticulously quantified using ICP-OES and SEM-EDS, while the liquids were analysed by ICP. Additionally, the phase composition was evaluated through XRD analysis, and the morphology of the solids was examined using SEM. The results in this chapter successfully demonstrate the technical feasibility of recovering $0.6[\text{Ni(OH)}_2].0.3[\text{Mn(OH)}_2].0.1[\text{Co(OH)}_2]$, Mn(OH)_2 and Li_2CO_3 from real NMC 532 leachates, yielding high quantities of industrial-grade pure materials.

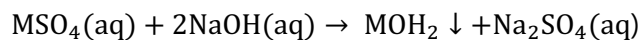
8.2 Spent Electrowinning Electrolyte Analysis

The waste spent leachate from electrowinning was analysed using ICP-OES, and the composition of the leachate before and after the electrowinning process is tabulated in Table 8-1. The optimised EW conditions applied resulted in the removal of 90% of Co and 77% of Ni, while 98.8% of Li and 96% of Mn remained in the leachate after EW. It is evident that the electrowinning resulting solution still constitutes a substantial number of metals that need to be recovered and integrated back into the spent battery recycling process or sold as pure by-products.

Table 8-1: Composition of the leachate before and after the electrowinning process using ICP-OES.

Element	Leachate before EW [g/L]	Leachate after EW [g/L]	Removed [%]
Li	4.98	4.92	1.2
Ni	19.94	4.54	77
Co	8.21	0.82	90
Mn	11.59	11.12	4.05

Precipitation tests were then carried out in a 250 mL reaction vessel on an overhead stirrer, and the effects of temperature and pH on the precipitation efficiency of Co, Li, Ni, and Mn were investigated. Following the filtration of the pH-adjusted post electrowinning leachate solution to remove any Fe, Al, and Cu impurities as their respective hydroxides, Ni, Co, and Ni were precipitated as hydroxides by adding 10 M NaOH to the leachate filtrate. The precipitating process could be expressed by:



8-1

8.3 Mn(OH)_2 and $0.6[\text{Ni(OH)}_2].0.3[\text{Mn(OH)}_2].0.1[\text{Co(OH)}_2]$ Precipitates Recovery: Effect of pH and Temperature on the Elemental Recovery

Precipitation is greatly affected by pH and temperature according to Chen et al. (2022). Figure 8-1 illustrates the concentration variation of the Li, Ni, Co and Mn metals with pH at temperature levels (20 °C and 40 °C). The experimental results illustrated in Figure 8-1 indicate and confirm that the precipitation process is significantly affected by pH and temperature. The recovery rate and efficiency of Ni, Mn, and Co decreased with temperature (from 20 to 40 °C). This phenomenon was effectuated by the correlation between the formation of $0.6[\text{Ni(OH)}_2].0.3[\text{Mn(OH)}_2].0.1[\text{Co(OH)}_2]$ and its respective solubility with temperature.

Since the precipitation of $0.6[\text{Ni(OH)}_2].0.3[\text{Mn(OH)}_2].0.1[\text{Co(OH)}_2]$ is an exothermic process, the increase in temperature (from 20 °C) facilitated the reverse reaction of the precipitation of $0.6[\text{Ni(OH)}_2].0.3[\text{Mn(OH)}_2].0.1[\text{Co(OH)}_2]$, resulting in the decrease in the recovery rate of Co, Mn and Ni. On the other hand, the increase in temperature also increases the solubility of the precipitated $0.6[\text{Ni(OH)}_2].0.3[\text{Mn(OH)}_2].0.1[\text{Co(OH)}_2]$, effectuating a decrease in the metal recovery rate. When the temperature was low (20 °C), the precipitation of $0.6[\text{Ni(OH)}_2].0.3[\text{Mn(OH)}_2].0.1[\text{Co(OH)}_2]$ was a favoured reaction, as the above equation depicts. Therefore, with the increase in temperature from 20 °C to 40 °C, the recovery efficiency of Co, Li, and Mn decreased from over 99.2 % to an approximated value of 84.5 % at the pH of 13.5. With further increasing the reaction temperature (to 40 °C), the dissolution of precipitate eventually becomes the prevailing factor, effectuating the decrease in the recovery rate of Ni, Co, and Mn at a higher reaction temperature.

When the pH value was low (less than 4), the increase in equilibrium pH exhibited a negligible effect on the Li, Ni, and Mn in the leachate solution, as indicated in Figure 8-1(b). From Figure 8-1(b), the precipitation rate of Ni and Co rapidly increases (from pH=5 to 7) and suddenly decreases (after 7) with the equilibrium pH. The precipitation of Mn also exhibited a similar trend of rapid initial increase (from pH= 7-10) and then sudden decrease (after pH=10) with the

equilibrium pH. At temperature $20\text{ }^\circ\text{C}$, 99% of the remaining Co and Ni co-precipitated out of solution between pH $\text{pH}= 8$. At the same pH, 33 % of the remaining Mn precipitated, the remaining 66 % precipitated by pH = 13.

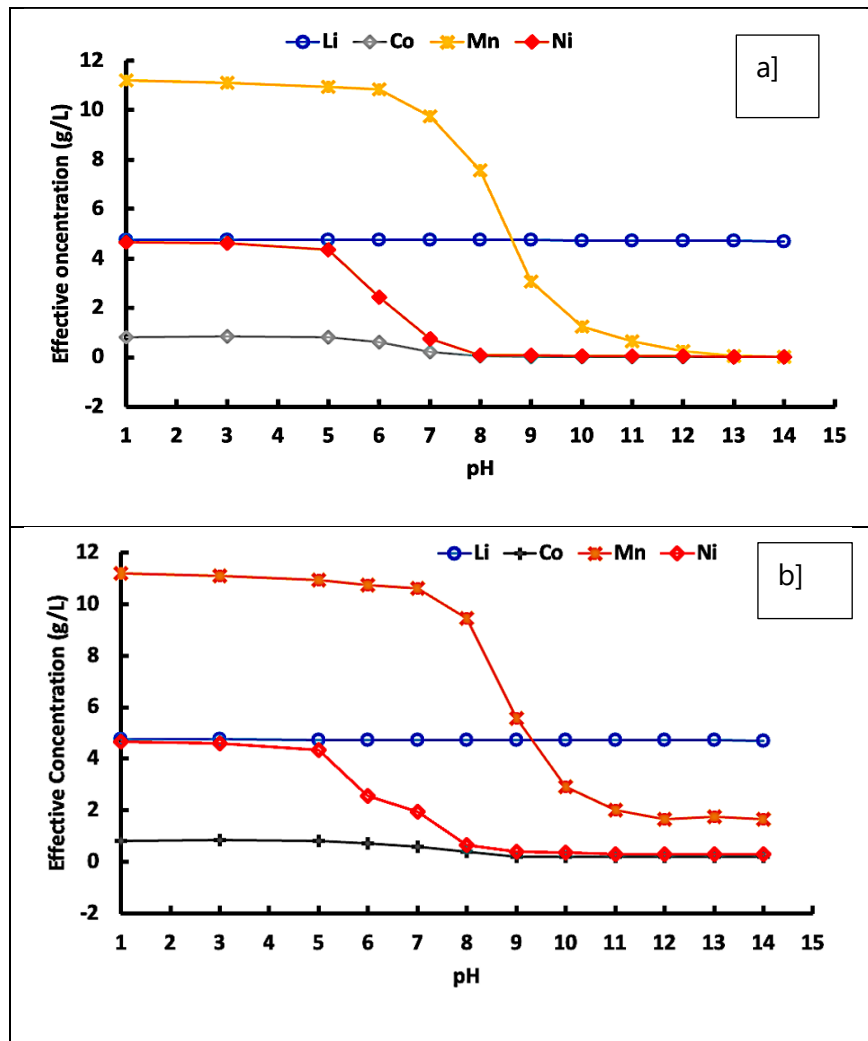


Figure 8-1: Concentration of the Li, Ni, Co and Mn metals at different pH levels (a) Temperature = $20\text{ }^\circ\text{C}$ b) Temperature = $40\text{ }^\circ\text{C}$.

Figure 8-2 depicts the recovery efficiency of the NMC metals at different pH levels at temperature of $20\text{ }^\circ\text{C}$.

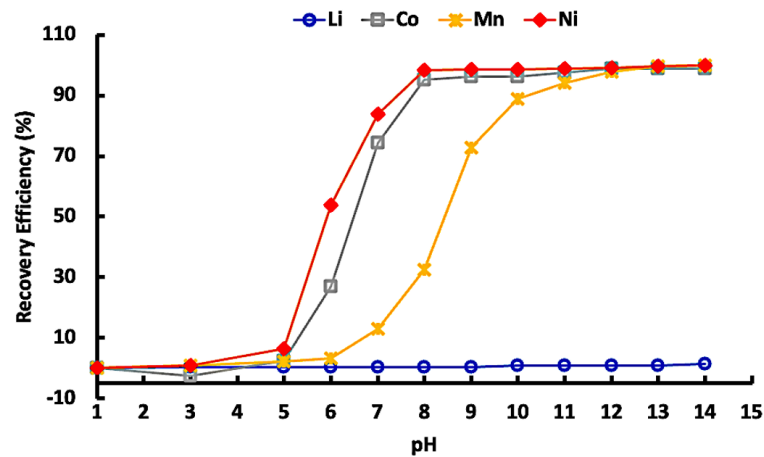
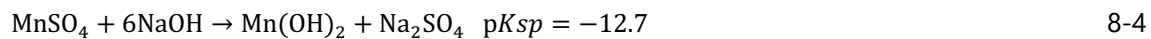
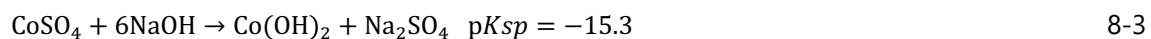
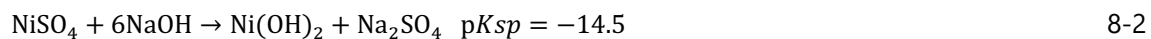


Figure 8-2: Recovery efficiency of the NMC metals at different pH levels (Temp=20 °C).

The majority of the metal ions in the typical spent NMC solution can be precipitated by OH⁻, while Li⁺ cannot. LiOH cannot be precipitated due to its respective higher solubility (higher K_{sp}) at any pH level. Mn, Ni and Co can precipitate at different pH levels because of their respective saturation point, the point at which the concentration of the respective metal ions (Mn²⁺, Ni²⁺, or Co²⁺) and hydroxide ions (OH⁻) in the solution reaches a level where the compound starts to precipitate and form a solid phase, can be reached before pH level of 14. It is worth noting, that the precipitation behaviour of Li, Ni, Mn and Co depends on their respective solubility products (K_{sp}) and the pH-dependent formation of hydroxide or other complex ions (Zhu et al. 2012; Chen et al. 2022; Entwistle et al. 2022). The K_{sp} values are noted below (Ding et al. 2020):



Mn(OH)₂ has the highest K_{sp} value among these three compounds, indicating relatively higher solubility in water. This means that Mn(OH)₂ requires a higher concentration of Mn²⁺ and OH⁻ ions (higher pH) than Ni²⁺ and Co²⁺ in the solution before it reaches its saturation point and begins to

precipitate. As shown in Figure 2-9, the precipitation efficiency of Li, Ni and Co metal ions increased with pH, while that of Li did not change basically. When the pH increases to 5.5, Al^{3+} , Fe^{2+} , and Cu^{2+} ions are precipitated rapidly since they form less soluble hydroxides at low pH values, leading to precipitation at lower pH (below 4.5) (Song and Zhao 2018). Significant amounts of Ni^{2+} and Co^{2+} ions and small amounts of Mn^{2+} were precipitated as the pH increased from 5.5 to 7, and Mn^{2+} ions were also precipitated completely when the pH rose to 12. The Ni, Mn and Co metal ions were removed effectively (above 99%) and a low-level loss of Li (4%) was obtained when the solution pH value was maintained around 12.

The solution precipitated under different experiment conditions were shown in Figure 8-1 and Figure 8-2. The results demonstrate the proposed method as a highly efficient and stable metal precipitation recovery method. Based on the experiment results above, the optimum condition of recovering $0.6[\text{Ni(OH)}_2].0.3[\text{Mn(OH)}_2].0.1[\text{Co(OH)}_2]$ is determined as follows: the optimum equilibrium pH is 13.5, temperature is 20 °C, reaction time is 60 mins, and agitation speed is 300 rpm. Table 8-1 lists the elemental composition of the product. It is shown that about 99.9 % Ni, Co and Mn were deposited as their respective hydroxides with less than 0.5% impurities. Negligible Li was detected in samples recovered samples.

The composition analysis was quantified using ICP and EDS, with the results presented in Table 8-2 and Table 8-3. 98.7% of Ni, 99.2% of Co, and 34.2% of Mn were recovered as $0.6[\text{Ni(OH)}_2].0.3[\text{Mn(OH)}_2].0.1[\text{Co(OH)}_2]$ precipitate from the post-electrowinning (EW) leachate, with a precipitation efficiency of 99% and a purity of 99.8%. The remaining 1.3% of Ni, 0.8% of Co, and 65.8% of Mn were recovered at pH 12.85, primarily compound being Mn(OH)_2 precipitate, with a precipitation efficiency of 99% and a purity of 99.9%.

Table 8-2: ICP-OES analysis of the resultant precipitate at pH 7.85.

Element	Composition [%]	% Recovered (From Pre-EW Leachate)	% Recovered (From Post-EW Leachate)
Li	0.009	0.1	0.4
Ni	61.33	23.6	98.7
Co	10.22	10.2	99.2
Mn	28.48	26.4	34.2

The Mn(OH)₂ precipitate had 99.6 % purity at a precipitation efficiency of 99.25 %.

Table 8-3: ICP-OES analysis of the resultant precipitate at pH 12.85.

Element	Composition [%]	% Recovered (From Pre EW-Leachate)	% Recovered (From Post-EW Leachate)
Li	0.01	0.15	0.7
Ni	0.02	0.8	1.3
Co	0.01	0.1	0.8
Mn	99.6	62.2	65.8

Based on the experiment results above, the optimum condition of recovering 0.6[Ni(OH)₂].0.3[Mn(OH)₂].0.1[Co(OH)₂] is determined as follows: the optimum equilibrium pH is 7.85 and 12.85, temperature is 20 °C, reaction time is 60 mins, and agitation speed is 300 rpm. The XRD pattern of the 0.6[Ni(OH)₂].0.3[Mn(OH)₂].0.1[Co(OH)₂] powder phase is shown in Figure 8-3, which confirms the presence of highly crystalline Ni(OH)₂ (JCPDS Card# 00-014-0117), Mn(OH)₂ (JCPDS Card# 00-030-0443) and Co(OH)₂ (JCPDS Card# 00-038-0715) phases in the precipitate. The presence of distinct phases suggests that the precipitate consists of a mixture of different phases. The XRD diffraction peaks are characterized by high intensity and sharpness, indicative of well-ordered crystallinity and large crystallite size, which suggests a highly ordered crystal

structure with well-defined lattice planes All of the diffraction lines are indexed to a hexagonal structure with a space group of $P\bar{3}m1$.

Table 8-2 and Table 8-3 lists the elemental composition of the $0.6[\text{Ni(OH)}_2].0.3[\text{Mn(OH)}_2].0.1[\text{Co(OH)}_2]$ and Mn(OH)_2 materials respectively. It is shown that about 99.9 % Ni, Co and Mn were deposited as their respective hydroxides with less than 0.5% impurities for both materials. In addition, Li was not detected in the recovered samples.

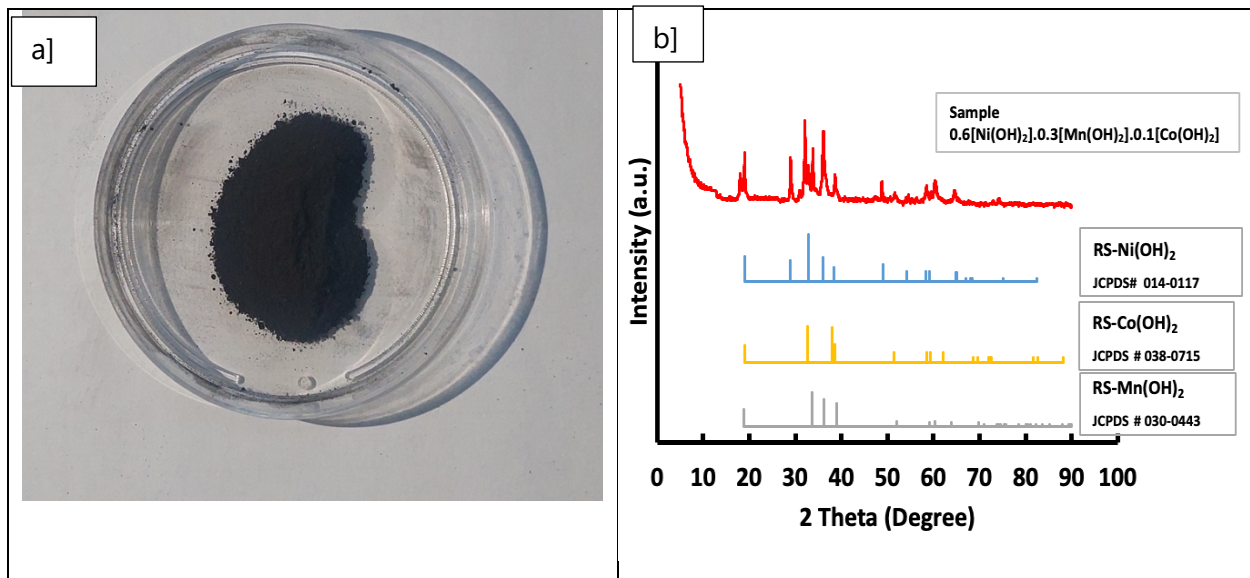
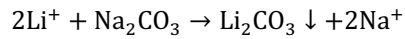


Figure 8-3: Photo (a) and XRD pattern (b) of $0.6[\text{Ni(OH)}_2].0.3[\text{Mn(OH)}_2].0.1[\text{Co(OH)}_2]$ material obtained by precipitation.

8.4 Recovery of the Li_2CO_3 Precipitate

8.4.1 Effect of $\text{CO}_3^{2-}:\text{Li}^+$ Ratio on the Lithium Recovery Efficiency (Li_2CO_3 Recovery)

After recovering Mn(OH)_2 , $0.6[\text{Ni(OH)}_2].0.3[\text{Mn(OH)}_2].0.1[\text{Co(OH)}_2]$ precipitates, Li_2CO_3 was precipitated by adding in excess an amount of sodium carbonate in the left filtrate. The reaction in this system is shown as follows:



8-5

Due to the low concentration of Li⁺ (4.75 g/L) in the resultant solution after 0.6[Ni(OH)₂].0.3[Mn(OH)₂].0.1[Co(OH)₂] precipitation, the remaining filtrate was subjected to concentration through evaporation (4.75 to 9.7 g/L), through high-speed agitation (500 rpm) and excess carbonate reactant. The Li⁺ concentration was raised to 9.7 g/L via evaporation, following the findings by Zhao et al. (2019) that a Li⁺ concentration of at least 10 g/L is required to attain a high (>82%) Li⁺ recovery efficiency. This process methodology aimed to maximize the precipitation of Li₂CO₃ through the addition of Na₂CO₃ into the solution. Figure 8-4 shows the effect of CO₃²⁻:Li⁺ molar ratio on the Li⁺ elemental recovery efficiency.

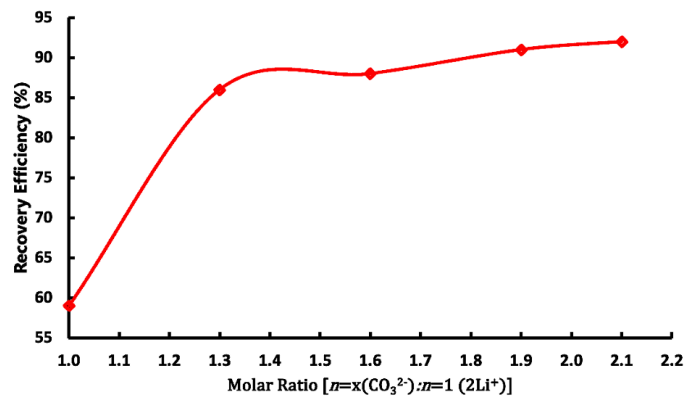


Figure 8-4: The effect of CO₃²⁻:2Li⁺ molar ratio on Li⁺ recovery efficiency (reaction time=1hr).

In the experiment to investigate the influence of temperature, pH and the amount of sodium carbonate on the precipitation efficiency of Li₂CO₃, the Li⁺ concentration was quantified to be 9.7 g/L. Taking the common ion effect into consideration, excess Na₂CO₃ should be added to precipitate the Li₂CO₃. Figure 8-4 shows that the Li-recovery rate increased from 58 % to 87 % when the molar ratio of Na₂CO₃ to Li⁺ was increased from 1.0:1.0 to 1.6:1.0. With a further increase in the molar ratio of Na₂CO₃ to Li⁺ from 1.6:1.0 to 2.1:1.0, the Li recovery efficiency did not increase markedly, therefore 1.6:1.0 was marked as optimal since at this point precipitant consumption can be limited whilst the recovery efficiency is remarkably high.

8.4.2 Effect of Temp on the Elemental Recovery Efficiency (Li₂CO₃ Recovery)

Similar to the formation of NMC532, the precipitation of Li₂CO₃ is also an exothermic reaction therefore increasing the temperature is negligibly beneficial to the precipitation of Li₂CO₃ and inadvertently favours the dissolution of precipitated Li₂CO₃ in the solution (Song and Zhao 2018). Figure 8-5 shows the effect of temperature on the Li⁺ elemental recovery efficiency.

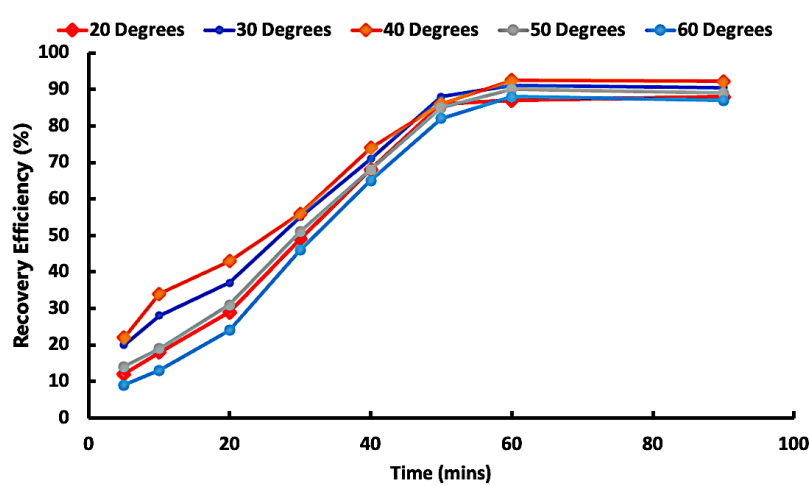


Figure 8-5: The effect of temperature on Li⁺ recovery efficiency.

Figure 8-5 shows that at the condition of temperature lower than 40 °C, the precipitation of the Li₂CO₃ reaction was favoured resulting in a significant increase in the Li recovery rate with the temperature. When the reaction temperature was raised to 40 °C, the dissolution of precipitated Li₂CO₃ turned out to be in equilibrium with the formation of Li₂CO₃ and the recovery rate of Li showed negligible change with the further increase of temperature. This is attributed to the equilibrium shift, on the Li₂CO₃ precipitation reaction (Equation 8-6), effectuated by the temperature increase. The equilibrium reaction is noted below:



Since the forward reaction (8-6) is exothermic, the backward reaction (dissolution of Li₂CO₃) is favoured at higher temperatures.

8.4.3 Effect of pH on the Elemental Recovery Efficiency (Li_2CO_3 Recovery)

Since CO_3^{2-} ions (from Na_2CO_3) can easily combine with H^+ to form HCO_3^- , the reduction of H^+ is beneficial to the precipitation of Li_2CO_3 , i.e., the Li^+ recovery rate showed a slight increase with the increase in equilibrium pH (from 13 to 14) since there is little to no H^+ at higher pH values. Meanwhile, increasing Li_2CO_3 precipitated in solution can enhance its dissolution. Figure 8-6 shows the effect of pH on the Li^+ elemental recovery efficiency over 90 mins.

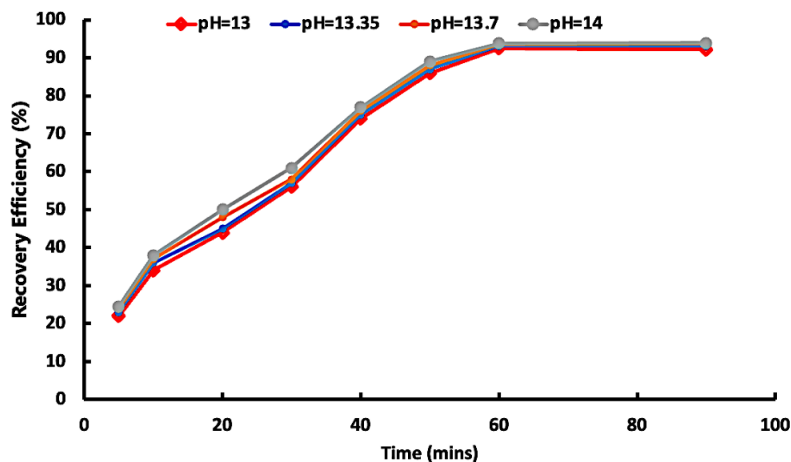


Figure 8-6: The effect of pH on Li^+ recovery efficiency over time.

Therefore, when the equilibrium pH was increased to a certain value (about pH 13.5 in Figure 8-6), the precipitation of Li_2CO_3 turned out to be equilibrating with the dissolution of it. Consequently, the Li^+ recovery rate did not increase significantly with the pH. From the description above, the optimum condition of recovering Li_2CO_3 is as follows: the molar ratio of Na_2CO_3 to Li^+ is 1.2:1.0, equilibrium pH is 13.5, temperature is 40 °C, Li^+ concentration is 9.5 g/L, reaction time is 1 h, and agitation speed is 500 rpm. The crystalline Li_2CO_3 phase (PDF# 96-231-0704) is clearly identified by XRD analysis shown in Figure 8-7. The presence of sharp peaks indicate a highly crystalline layer structure (Noh et al. 2013). From the XRD analysis, no new phases appear to have formed during the precipitation process, as the XRD patterns of Li_2CO_3 align well with the reference spectrum.

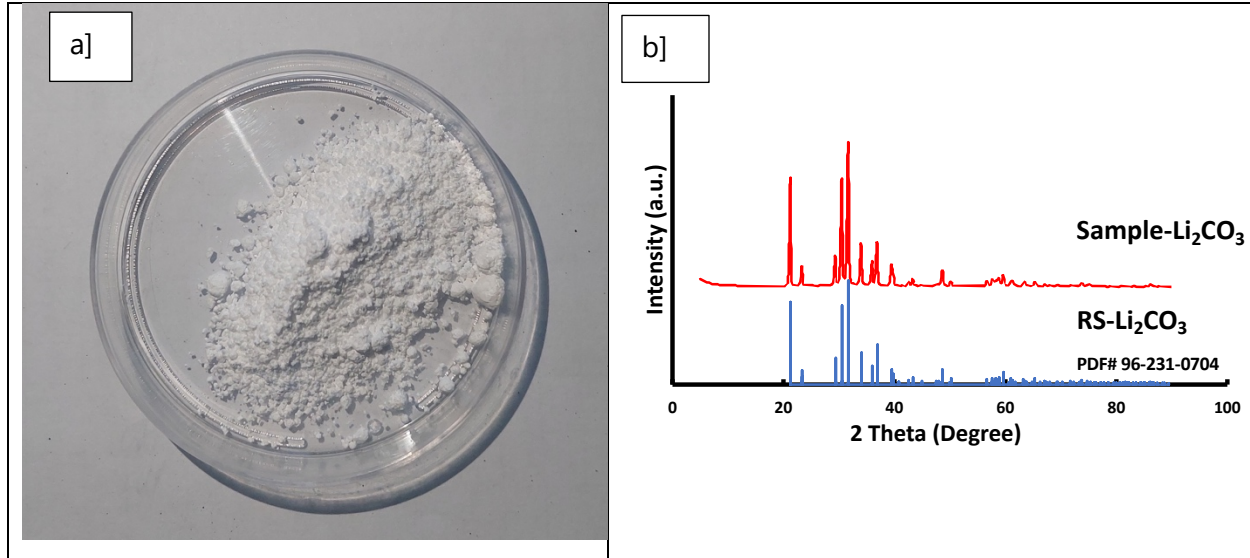


Figure 8-7: a) Photo and b) XRD pattern of Li_2CO_3 material recovered through precipitation.

The experimental results showed that around 93% of Li^+ was precipitated as carbonate with less than 0.5 % impurities. Co and Ni were not detected in the obtained samples.

The Mn(OH)_2 precipitate had 99 % purity at a precipitation efficiency of 99 %. The Mn(OH)_2 can potentially be sold to Mn production companies for further processing. The Li_2CO_3 will be used in the hydrous cathode production process as annotated in the section below. The $0.6[\text{Ni(OH)}_2].0.3[\text{Mn(OH)}_2].0.1[\text{Co(OH)}_2]$ precipitate will be recycled back to the leaching chamber for the leaching process.

After Co, Ni, Mn, and Li precipitation the resultant solution was collected and analysed with ICP-OES and the elemental composition analysis is tabulated in Table 8-4.

Table 8-4: ICP-OES analysis of the resultant solution after electrowinning and multistage precipitation.

	[g/L]	ppm	ppm (disposal limit-EPA)
Li	0.021	21	-
Ni	0.016	16	100
Co	0.012	12	50
Mn	0.018	18	50
pH	-	14	10
SO₄²⁻	308	300 000	250
Na	32	32 000	250

Half of the resulting Na⁺ and OH⁻ rich solution will be used to adjust the pH of the leachate at the pre-electrowinning stage. The other half will be stored for treatment with Ca(OH)₂ to make CaSO₄ which have various uses especially in the fertiliser and health industry or electro dialysis to remove anions (SO₄²⁻) and cations (Na⁺). This process unit will help remove the hazardous SO₄²⁻ and Na⁺ ions remaining in the process effluent and ultimately make the wastewater eligible for disposal and reuse in the presented process. *Please note that this water treatment stage is only a recommendation and was not included in this work, as it falls outside the scope of this study.* The results indicate that the resultant solution is not safe for disposal, if not further treated, according to the U.S. Environmental Protection Agency (EPA) (2023).

Chapter 9: Process Flow Mass Balance

9.1 Overview

In the preceding chapters, the work delved into the intricacies of optimizing the Ni-Co recovery process, examining findings and methodologies. The focus of this chapter sharpens on the critical elements of material balance and the broader considerations anchored in the laws of physics. It is essential to understand the mass and energy outputs within the constraints dictated by the fundamental principles of conservation of mass. Material balance and energy act as a linchpin in this pursuit, serving as a prerequisite for a comprehensive account of the raw materials input and the resultant final products. This chapter serves as a pivotal bridge, linking the theoretical findings of the Ni-Co electrowinning recovery process to the pragmatic component and material balance physicochemical intricacies that define its implementation.

The Li-ionB recycling process developed in this study was illustrated with a process flow diagram and mass balance to gain insight into what the purity and overall recovery will be for each process unit and stream using the optimum conditions identified in this study. The sample preparation mass balance was first completed with the data and information collected during the sample preparation steps of this study. The mass and composition of the cathode powder produced from the sample preparation mass balance was therefore used as the feed conditions to the hydrometallurgical recovery circuit mass balance.

Assumptions made for the mass balances:

1. A constant feed of 18.75 g spent Li-ionB cathodes per 3 hours (105 mg/min) was used for the electro-hydrometallurgical metal separation process.
2. The same type of Li-ionB cathode material is continuously fed to the process system, producing a cathode powder with a constant composition as determined with the ICP analysis.

3. Only the process steps and their optimal conditions determined experimentally in this study were used for the sample preparation, leaching, electrowinning, and precipitation in the mass balance.
4. The optimum leaching, electrowinning, and precipitation conditions as obtained in Chapter 4 to Chapter 8 were used for metal separation processing.

9.2 Process Flow and Material Balance

In order to account for mass and energy outputs for this process, certain constraints imposed by physics need to be considered when developing a new process like the one executed in this study. The material balance is a prerequisite to account for the input raw material and final products. Figure 9-1 outlines the boundary of the overall material and component balance of the Ni-Co composite material production. All the calculations were done at a steady state, meaning mass and energy entering the system equals mass leaving the system. In order to provide a clear understanding of the overall Ni-Co recovery process, a summated process description is provided in the next paragraph.

The Li-ionBs were dismantled and pre-treated to recover the spent Li-ionB cathode material NMC532 sheets. The NMC 532 was leached using an inorganic acid (H_2SO_4)-reductant (H_2O_2) leachant as described in section 3.3.5. In one experimental run, 18.75 g of cathode material was utilised as process feedstock (Stream 1). Through utilising leachant solutions comprising 2M H_2SO_4 + 6 vol.% H_2O_2 , and a 75 g/L S/L ratio (Stream 2) and conducting leaching for 120 minutes at a temperature of 60°C, peak leaching extraction efficiency of 98.1% for Li, 97.1% for Co, 96.1% for Ni, and 95.7% for Mn were attained in Stream 3. It is imperative to note, at leaching reaction time of 20 mins, carbon flakes, which float in the intra-leaching solution, and aluminium fragments (both from the pre-processed cathode material fragments) were freed (washed) from the cathode matrix using the acid-reductant leachant and filtered out thereafter using a 1 mm gauze sieve before leaching is continued. The recovered aluminium-carbon mixture (1.725 g/18.75 g_{cathode})

was collected in Stream X and stored for further processing, the processing which is not reported in this work. The maximum metal recovery that was attained is $0.595 \text{ g}_{\text{total metal}}/\text{g}_{\text{cathode}}$.

The pH of the leachate solution was adjusted using 80 ml of 10 M NaOH (in Stream 4) to 4.5 to recover any Fe, Al and Cu impurities as their respective precipitates. The resultant solution (in stream 6) was filtered to remove any solid residue. The filtered resultant leachate solution (Stream 7) was then utilised in a Co-Ni electrowinning process to recover Ni-Co deposit at a minimum rate of $0.06 \text{ g}/\text{cm}^2 \cdot \text{hr}$ and 88% current efficiency. The unwanted filter cake is recovered in Stream 8. 5.8 g of $\text{Ni}_{0.65}\text{Co}_{0.35}$ was recovered (in Stream 10) during the electrowinning process that utilised the aforementioned process conditions. The optimal conditions that produced 98% pure Ni-Co and ideal deposit cohesion for Ni-Co deposition conditions were: -1.15 V vs Ag/AgCl, 30 g/L Co-Ni, 50 °C, 15 g/L of Na_2HPO_4 , 15 g/L Na_2SO_4 and pH 4.5. 89.5 % of Co, 77.5 % of Ni, 0.8 % of Li and 4.05 % of Mn were recovered during the potentiostatic electrowinning process.

The recovered Co-Ni material can be used as feedstock to make various valuable materials including to make NMC cathodes in the anhydrous NMC cathode production plants. Alternatively, the recovered Co-Ni can be reacted with H_2SO_4 to synthesise sulphates of Ni and Co which can be utilised in hydrous NMC cathode production plants. The post electrowinning resultant or spent solution (in stream 10) was treated with 25 ml of 10 M NaOH to adjust pH to 7.85 and 12.75 so that Co, Ni and Mn hydroxide composite and Mn hydroxide could be extracted respectively. The $0.6[\text{Ni}(\text{OH})_2] \cdot 0.3[\text{Mn}(\text{OH})_2] \cdot 0.1[\text{Co}(\text{OH})_2]$ and $\text{Mn}(\text{OH})_2$ were extracted in stream 19 and 15 respectively. During this stage 7.6 % of Co, 19.1 % of Ni, 0.2 % of Li and 89.2 % of Mn was recovered. The $\text{Mn}(\text{OH})_2$ was extracted and stored for possible; commercial purposes. The Co, Ni and Mn hydroxides mixture was recycled back to the leaching chamber (in stream 19). The resultant Li^+ rich solution (in stream 16) from the precipitation reaction vessel was heat treated (100 °C) to evaporate 50 % of the water and then subsequently treated with 11.85 g Na_2CO_3 (stream 25) to produce 5.8 g of Li_2CO_3 (99.85 % pure) which can be used directly in anhydrous NMC production plants among other purposes. 95.35 % of the Li^+ is recovered during this stage. Overall, 97.1 % of Co, 96.9 % of Ni, 98.9 % of Li and 95.7 % of Mn were recovered.

Half of the resulting 160 ml/3 hr batch of Na^+ and OH^- rich solution (in stream 22) will be mixed with NaOH pellets to produce 10M NaOH which will be used to adjust the pH of the leachate. The other half will be stored for treatment using electrodialysis or precipitation using $\text{Ca}(\text{OH})_2$ to make CaSO_4 which have various uses especially in the fertiliser industry. This process unit will help remove the SO_4^{2-} ions and Na^+ remaining in the process effluent and ultimately make the wastewater eligible for disposal. *Please note that this water treatment stage is only a recommendation and was not included in this work, as it falls outside the scope of this study.* The results indicate that the resultant solution is not safe for disposal, if not further treated, according to the U.S. Environmental Protection Agency (EPA) (2023). Figure 9-2 shows the process flow, material balance and waste management process routes in the whole process of recovering valuable metals and metal-based compounds from 18.75 g cathode material. Figure 9-2 shows the summated and comprehensive metal recovery material balance process block flow diagram for the developed recovery process. Table 9-1 shows the detailed metal recovery material balance for the developed recovery process.

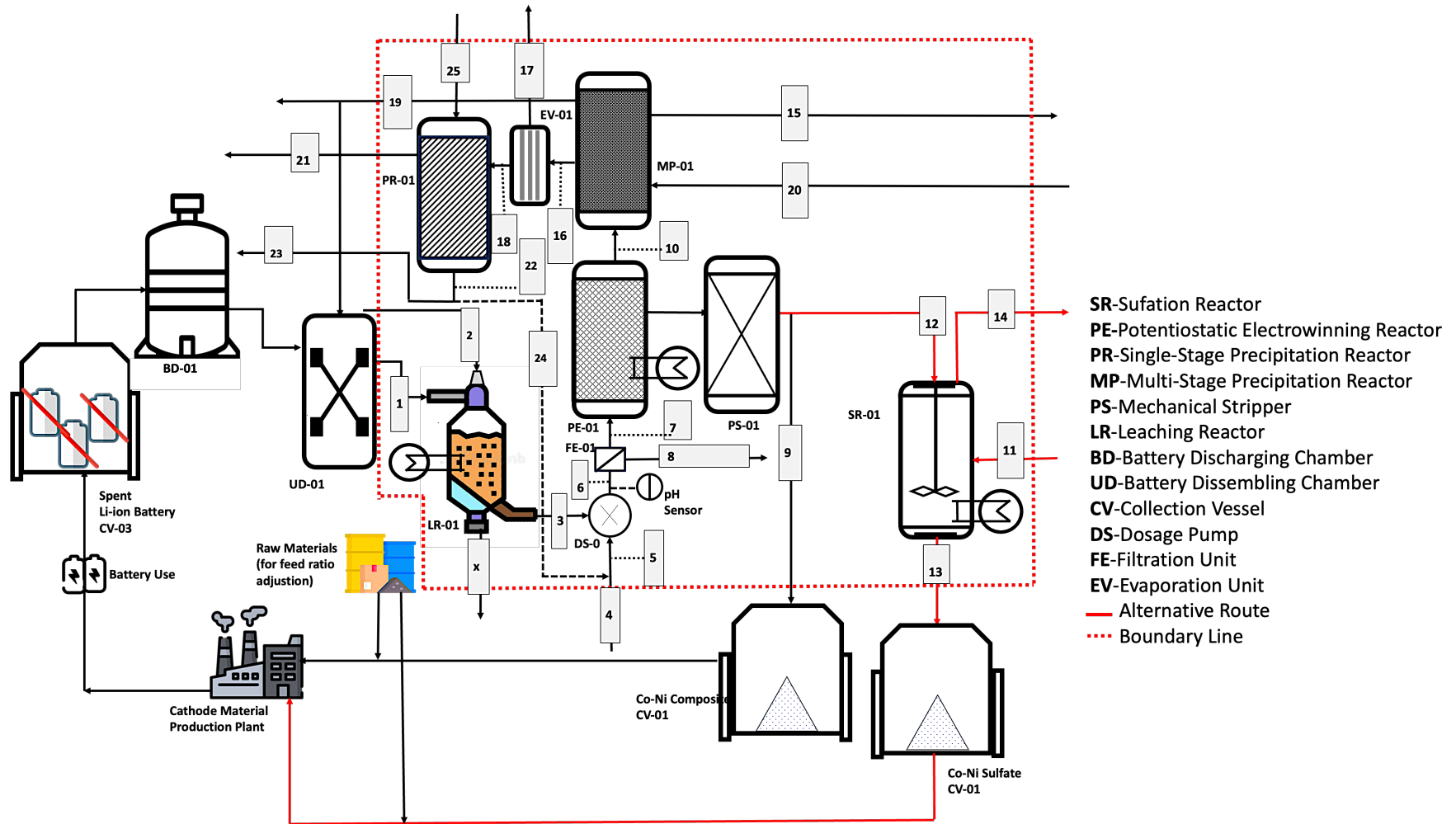


Figure 9-1: Summated process flow diagram (with numbered streams) of the novel process reported in this work.

The equation used in the material balance analysis is annotated below:

$$\sum M_{input} = \sum M_{output} \quad 9-1$$

Where:

M = the total mass of components in a particular stream.

The general material balance equation:

Accumulation = input– output + generation - consumption

The **assumptions** made in the calculations were:

The system is at a steady state, accumulation = 0

Input + generation = Output + Consumption

Sample Calculation: Example of Mass Balance for PR-01

$$\sum M_{input} = \sum M_{output} \quad 9-2$$

$$M_{25} + M_{18} = M_{22} + M_{21} \quad 9-3$$

Since Na_2CO_3 was in excess, conversion, $X_{Li} = 0.99$ (assumed value for calculations)

Since there are generated components in M_{22} and M_{21} , the determination of M_{22} and M_{21} is limited only to the precipitation reactor (PR-01).

For M_{18} (in mg/min)

$$M_{Li} = 7 \text{ mg/min}$$

$$M_{\text{SO}_4^{2-}} = 274 \text{ mg/min}$$

$$M_{Na} = 148 \text{ mg/min}$$

$$M_{H_2O} = 1044 \text{ mg/min}$$

$$M_{NaH_2PO_4} = 20.5 \text{ mg/min}$$

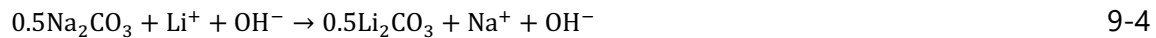
$$M_{OH} = 23 \text{ mg/min}$$

$$M_{18} = 1516.5 \text{ mg/min}$$

For M_{25} (in g/3hrs)

$$M_{Na_2CO_3} = 70 \text{ mg/min}$$

For M_{21} (in g/3hrs)



Since 6.61 mg/min (0.000962 moles/min) of Li^+ is the limiting reagent ($N_{Li}=0.00096$ moles/min), thus.

$$M_{Li_2CO_3} = v_{Li_2CO_3} X_{Li} N_{Li} Mr_{Li_2CO_3} \quad 9-5$$

$$M_{Li_2CO_3} = 0.5 \times 0.99 \times 0.000952 \times 74 = 0.0352 \text{ g/min} = 34.9 \text{ mg/min}$$

For M_{21} (in g/3hrs)

$$\sum M_{input} = \sum M_{output}$$

$$M_{22} = M_{25} + M_{18} - M_{21}$$

$M_{22} = 70 + 1516.5 - 34.9 = 1551.6 \text{ mg/min}$ (which is close to the weighed value (1552.7 mg/min) as noted in the detailed experimental mass balance below). The value is not exact because the conversion factor used was an assumed overstated value not the actual value.

Table 9-1: Detailed mass balance of the novel recovery process reported in this work.

Comp.	Streams (in mg/min)																								
	1	2	3	4	5	6	7	8	9	10	11	12	13	14	15	16	17	18	19	20	21	22	23	24	25
Li	6.94	0.00	6.82	0.00	0.00	6.82	6.81	0.01	0.17	6.64	0.00	0.17	0.00	0.00	0.00	6.61	0.00	6.61	0.00	0.00	0.00	0.24	0.12	0.12	0.00
Ni	27.72	0.00	26.92	0.00	0.00	26.92	26.84	0.08	20.28	6.95	0.00	19.89	0.00	0.00	0.00	0.00	0.00	0.00	0.00	0.00	0.00	0.00	0.00	0.00	0.00
Co	11.39	0.00	11.14	0.00	0.00	11.14	11.07	0.07	10.28	1.18	0.00	9.89	0.00	0.00	0.00	0.00	0.00	0.00	0.00	0.00	0.00	0.00	0.00	0.00	0.00
Mn	16.11	0.00	15.61	0.00	0.00	15.61	15.47	0.14	0.67	14.69	0.00	0.79	0.00	0.00	0.00	0.00	0.00	0.00	0.00	0.00	0.00	0.00	0.00	0.00	0.00
H ₂ O	0.00	1388.89	1425.00	0.00	444.44	1948.89	1948.89	0.00	0.00	1948.89	416.67	0.00	0.00	416.67	0.00	2087.78	1043.89	1043.89	0.00	138.89	0.00	1043.89	524.03	519.86	0.00
OH ⁻	0.00	0.00	0.00	75.56	75.55	0.00	0.00	0.00	0.00	0.00	0.00	0.00	0.00	0.00	0.00	23.33	0.00	23.33	0.00	23.39	0.00	23.39	11.74	11.65	0.00
Na	0.00	0.00	0.00	102.22	102.21	116.17	116.11	0.00	0.00	116.17	0.00	0.00	0.00	0.00	0.00	147.78	0.00	147.78	0.00	31.61	0.00	179.28	90.00	89.28	0.00
H ₂ O ₂	0.00	69.44	0.00	0.00	0.00	0.00	0.00	0.00	0.00	0.00	0.00	0.00	0.00	0.00	0.00	0.00	0.00	0.00	0.00	0.00	0.00	0.00	0.00	0.00	0.00
O ₂	0.00	0.00	31.28	0.00	0.00	0.00	0.00	0.00	0.00	0.00	0.00	0.00	0.00	0.00	0.00	0.00	0.00	0.00	0.00	0.00	0.00	0.00	0.00	0.00	0.00
SO ₄ ²⁻	0.00	267.11	267.11	0.00	0.00	273.94	273.94	0.00	0.00	273.89	80.03	0.00	0.00	0.00	0.00	0.00	0.00	273.89	0.00	0.00	0.00	273.89	137.49	136.40	0.00
H ⁺	0.00	4.37	4.37	0.00	0.00	0.00	0.00	0.00	0.00	0.00	1.61	0.00	0.00	0.00	0.00	0.00	0.00	0.00	0.00	0.00	0.00	0.00	0.00	0.00	0.00
NaH ₂ PO ₄	0.00	0.00	0.00	20.83	20.83	20.83	20.83	0.00	0.00	20.83	0.00	0.00	0.00	0.00	0.00	20.83	0.00	20.83	0.00	0.00	0.00	20.83	10.46	10.38	0.00
CoSO ₄	0.00	0.00	0.00	0.00	0.00	0.00	0.00	0.00	0.00	0.00	0.00	0.00	0.00	0.00	0.00	0.00	0.00	0.00	0.00	0.00	0.00	0.00	0.00	0.00	0.00
NiSO ₄	0.00	0.00	0.00	0.00	0.00	0.00	0.00	0.00	0.00	0.00	0.00	0.00	0.00	0.00	0.00	0.00	0.00	0.00	0.00	0.00	0.00	0.00	0.00	0.00	0.00
LiSO ₄	0.00	0.00	0.00	0.00	0.00	0.00	0.00	0.00	0.00	0.00	0.00	0.00	0.00	0.00	0.00	0.00	0.00	0.00	0.00	0.00	0.00	0.00	0.00	0.00	0.00
MnSO ₄	0.00	0.00	0.00	0.00	0.00	0.00	0.00	0.00	0.00	0.00	0.00	0.00	0.00	0.00	0.00	0.00	0.00	0.00	0.00	0.00	0.00	0.00	0.00	0.00	0.00
Mn(OH) ₂	0.00	0.00	0.00	0.00	0.00	0.00	0.00	0.00	0.00	0.00	0.00	0.00	0.00	0.00	0.00	0.00	0.00	0.00	0.00	0.00	0.00	0.00	0.00	0.00	0.00
Li ₂ CO ₃	0.00	0.00	0.00	0.00	0.00	0.00	0.00	0.00	0.00	0.00	0.00	0.00	0.00	0.00	0.00	0.00	0.00	0.00	0.00	0.00	0.00	0.00	32.78	0.00	0.00
Ni(OH) ₂	0.00	0.00	0.00	0.00	0.00	0.00	0.00	0.00	0.00	0.00	0.00	0.00	0.00	0.00	0.22	0.00	0.00	0.00	0.00	8.11	0.00	0.00	0.00	0.00	0.00
Co(OH) ₂	0.00	0.00	0.00	0.00	0.00	0.00	0.00	0.00	0.00	0.00	0.00	0.00	0.00	0.00	0.00	0.00	0.00	0.00	0.00	0.00	0.00	0.00	0.00	0.00	0.00
CO ₃ ²⁻	0.00	0.00	0.00	0.00	0.00	0.00	0.00	0.00	0.00	0.00	0.00	0.00	0.00	0.00	0.00	0.00	0.00	0.00	0.00	0.00	0.00	0.00	11.17	0.00	0.00
Na ₂ CO ₃	0.00	0.00	0.00	0.00	0.00	0.00	0.00	0.00	0.00	0.00	0.00	0.00	0.00	0.00	0.00	0.00	0.00	0.00	0.00	0.00	0.00	0.00	0.00	0.00	70.00
Na ₂ SO ₄	0.00	0.00	0.00	20.83	20.83	20.83	20.83	0.00	0.00	20.83	0.00	0.00	0.00	0.00	0.00	20.83	0.00	20.83	0.00	0.00	0.00	20.83	10.46	10.38	0.00
Total Mass (mg/min)	62.17	1729.81	1788.24	198.61	643.04	2420.33	2419.97	0.30	31.39	2389.24	498.31	30.73	83.33	416.67	16.44	2286.34	1043.89	1516.34	16.44	193.89	32.78	1552.69	773.84	767.68	70.00

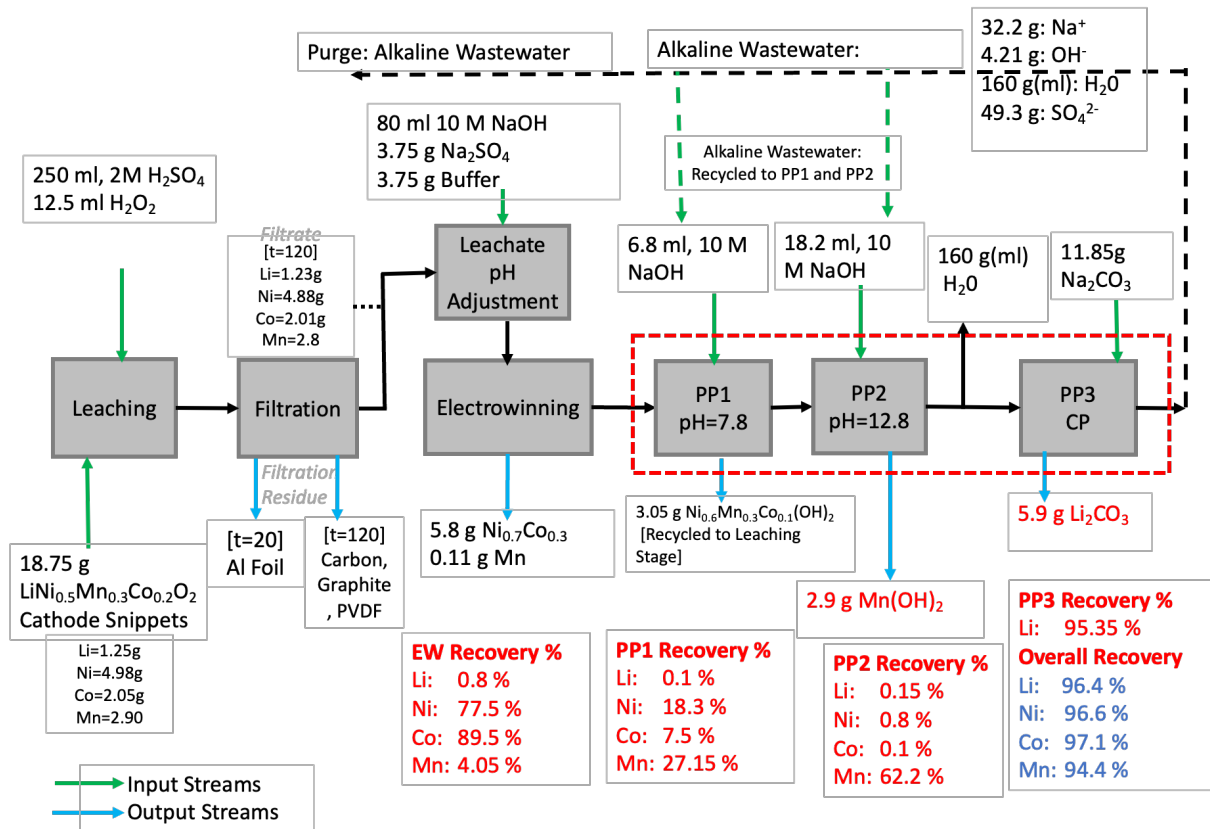


Figure 9-2: Comprehensive metal recovery material balance block flow diagram.

The recovery process has the following characteristics:

- The potentiation electrowinning utilized in this process has high selectivity, which avoids the occurrence of co-precipitation of Co-Ni with unwanted metals.
- Elimination of Co-Ni separation stages saves capital cost and operational costs.
- Optimization of electrowinning reduces energy consumption and leveled the cost of operation.
- The mixed hydroxide precipitates recovered at pH 7.8 could be recycled back to the leachate just prior to the pH adjustment stage which will increase the yield of the more valuable metallic Co-Ni composite.
- Recycling of precipitates from the resulting electrowinning solution saves cost.
- Selling of pure Mn(OH)₂ will counteract the cost of production.
- Recovered Ni-Co meet purity standard class 1 (98 % Ni+Co and 1.9 % Mn to make 99.9 % (Class 1) of battery metals (Ni, Co, Li and Mn)) standard of battery metal precursors to be utilised in conventional cathode production plants.

9.3 Environmental Pseudo-Assessment

The development of cost-cutting, recycling, and environmental preservation strategies will all contribute to the already surging production, usage and integration of Li-ionBs. In the future, the cost of batteries is expected to be significantly impacted by advancements in environmental preservation based recycling technologies and processes. This is because a substantial portion of the demand for Co and Ni in the Li-ion battery sector can potentially be met through efficient recycling processes, thereby influencing the overall pricing dynamics of batteries. There must be attention given to reliability, cost, and the environment.

The appeal of recycling Li-ionB from an economic perspective is influenced by the price of metal on the market as well as the electrode technology and chemistry employed in Li-ionBs. Cobalt recycling is more economically significant than the recovery of lithium, nickel, and copper metals because it costs more per unit mass. Lithium-ion batteries, when inadequately disposed of or recycled, may present potential hazards to both the environment and human health. This is attributed to the inclusion of organic and inorganic components within these batteries, which possess the capacity to undergo explosive reactions at elevated temperatures or introduce harmful substances into the environment, thereby posing risks of contamination.

In light of the above, using suitable economic and environmentally friendly recycling techniques, as presented in this work, is crucial for the environment. This research focuses on a comprehensive electro-hydrometallurgy process for recycling Co-Ni alloys from spent Li-ionB. After pre-treatment, reductive leaching, electrowinning and washing, Co-Ni alloys are recovered. The only by-products in the leaching recovery procedure are, in theory, H₂O and O₂ which are non-hazardous to the environment. Following the recovery and separation the metal ions, the electrowinning spent solution will be treated with sodium hydroxide and sodium carbonate to recover Mn(OH)₂, 0.6[Ni(OH)₂].0.3[Mn(OH)₂].0.1[Co(OH)₂] and Li₂CO₃ respectively. The by-product 0.6[Ni(OH)₂].0.3[Mn(OH)₂].0.1[Co(OH)₂] will be recycled back to be leached again whilst the by-products Li₂CO₃, Mn(OH)₂ are stored for commercial purposes. Portion of the resulting Na and OH⁻ rich solution will be used to adjust the pH of the leachate at the pre-electrowinning stage. The other portion will be stored for treatment with Ca(OH)₂ to make CaSO₄ which have various uses especially in the fertiliser and health industry. This process unit will help remove the hazardous SO₄²⁻ ions remaining in the process effluent and ultimately make the waste-water

eligible for disposal and reuse in the presented process. The A closed-loop method presented in this work for the sustainable recovery of valuable metals from spent Li-ionBs may therefore accrue several cost and environmentally-friendly benefits and attributes.

Chapter 10: Conclusion and Recommendations

10.1 Conclusion

This thesis compiles the results of a research project aimed at recovering Ni-Co composite from NMC Li-ionB cathodes using hydro-electrometallurgy processing. The correlation between hydrometallurgy and electro-metallurgy operational parameters and physicochemical properties of NMC active particles and elements was studied to establish an effective process route to recover Ni-Co composite material. Focusing on the outlook on recovering valuable metal alloys from NMC 532 cathode, the viability of recovering Ni-Co composite material using hydro-electrometallurgy processing was established.

Firstly, this research illustrates the applicability of inorganic acid-reductant leachant-based leaching of NMC 532 to effectively dissolve and recover all valuable metals constituted in the cathode material. This approach provides quantitative recovery data for each element of the entire particle population at different operational parameters: reductant and inorganic acid concentration, S/L ratio, reaction time and temperature. The quantification of elemental recovery data was done through ICP-OES using separate elemental standards for each metal in order to increase the accuracy of the data. Through utilisation leachant solutions comprising 2M H₂SO₄ + 6 vol.% H₂O₂, and a 75 g/L S/L ratio and conducting leaching for 120 minutes at a temperature of 60°C, peak leaching recovery efficiency of 98.9% for Li, 97.1% for Co, 96.9% for Ni, and 95.7% for Mn were attained. The maximum metal recovery that was attained is $0.595 \text{ g}_{\text{total metal}}/\text{g}_{\text{cathode}}$.

The effects of key electrowinning parameters were quantified and studied, and alternative electrodes to suppress the extent of scaling, electrode resistivity, operational and capital costs, and life cycle duration limitation were tested. The key parameters for electrowinning are applied potential, metal ion concentration, pH, temperature, rotating cathode speed, Na₂SO₄ dosage and buffer dosage. The optimal levels of each leaching operational parameter were established and noted for the next experimental phase. In the second phase of experiments, electrowinning of Ni-Co composite from NMC 532 sulphate solutions was investigated in a laboratory cell equipped with electrodes of the same size and design. Most of the electrowinning analysis was done on the deposition of Co-Ni composite on cost-effective and

highly electroconductive Al cathodic plates and highly electroconductive, long-life cycle and low-levelized cost of operation electroconductive Pt-coated Ti anode.

The cathodic deposition of Ni-Co composite material was accelerated at high applied potential, high pH, high active surface area, low inter-electrode distance, high metal ion concentration and high temperature. Anode scaling at optimal electrowinning conditions was totally inhibited when Al cathodes were coupled with Pt-Coated Ti anodes. Due to the presence of the platinum film, the titanium electrode was not passivated. The electrowinning parameters applied potential, temperature, pH, Co-Ni concentration, Na₂SO₄ and buffer concentration, and electrode distance and active area were successfully optimised to recover Ni_{0.65}Co_{0.35} at a minimum rate of 0.06 g/cm².hr at 88% current efficiency. 90 % of the Co and 77 % of the Ni in the leachate was recovered in a 3 hr electrowinning run. 5.8 g of Ni-Co alloy was obtained per 18.75 g of NMC 532 cathode. The optimum process conditions that yielded 88% current efficiency and ideal deposit cohesion for Ni-Co deposition were: conditions (-1.15 V vs Ag/AgCl, 30 g/L Co-Ni, 50 °C, 15 g/L of Na₂HPO₄, 15 g/L Na₂SO₄ and pH 4.5).

Following several tests with synthetic solutions, electrowinning was then accomplished using a real NMC 532 solution obtained after the leaching of cathode material from spent Li-ionBs. The best parameters for deposition were defined in the Co-Ni electrowinning optimisation experiments. However, as the purification stage was not effective in the removal of all contaminants, especially Mn, the obtained deposit was of high but somehow subpar quality; it constituted predominantly a poorly crystalline Ni_{0.65}Co_{0.35} powder with a purity of over 98.05 %. The Ni_{0.65}Co_{0.35} composite was reacted with 2M H₂SO₄ for 3 hrs when contacted at 75 g/L to produce NiSO₄-CoSO₄ salt at 99% yield for the hydrous NMC production plants. The anhydrous NMC production plants can utilise pure Ni-Co powder.

The metals remaining in the spent electrolyte from the electrowinning were recovered through multi-stage precipitation to recover Mn(OH)₂, hydroxide composite formulation of Ni, Mn and Co and Li₂CO₃ at over 99 % precipitation efficiency. The optimum equilibrium pH is 7.85 and 12.85 to recover 0.6[Ni(OH)₂].0.3[Mn(OH)₂].0.1[Co(OH)₂] and Mn(OH)₂ respectively at an optimal temperature of 20 °C, reaction time of 60 mins, and agitation speed of 300 rpm. The optimum equilibrium pH to recover Li₂CO₃ is 13.5 at an optimal temperature of 20 °C, reaction time of 60 mins, and agitation speed of 500 rpm. The Ni-Co composite recovered from spent

Li-ionBs was targeted for closed and open loop recycling since besides Li-ionB cathode production, which is the main target use for the Ni-Co composite, Ni-Co alloys and alloys can be used in magnetic films, electrocatalysis, electronic chips, anti-corrosion systems, micro and nanogears among other various technological applications.

The recovered Li_2CO_3 is a versatile compound with applications ranging from production of Li-ionBs, stabilizing mood in pharmaceuticals to enhancing properties in glass and ceramics, aluminium production, metallurgical processes, chemical synthesis, and absorption refrigeration systems for air conditioning. The recovered $\text{Mn}(\text{OH})_2$ can be employed as a coagulant in water treatment, a cathode material in alkaline batteries, and a micronutrient supplement in agriculture, showcasing its versatility across applications. Lastly, the recovered hydroxide composite formulation of Ni, Mn, and Co ($0.6[\text{Ni}(\text{OH})_2].0.3[\text{Mn}(\text{OH})_2].0.1[\text{Co}(\text{OH})_2]$) is to be used solely for Li-ionB cathode production. The recycling cost (R/kg) of cathode was calculated to be R 153/kg which is at least 50 % lesser than R 360/kg, R 308/kg and R 258/kg recycling costs for direct recycling, pyrometallurgical and hydrometallurgical processes respectively.

Half of the resulting Na^+ and OH^- rich solution will be used to adjust the pH of the leachate at the pre-electrowinning stage. The other half will be stored for treatment with electro dialysis or precipitation with $\text{Ca}(\text{OH})_2$ to make CaSO_4 which have various uses especially in the fertiliser and health industry or electro dialysis to remove anions (SO_4^{2-}) and cations (Na^+). This process unit will help remove the hazardous SO_4^{2-} and Na^+ ions remaining in the process effluent and ultimately make the wastewater eligible for disposal and reuse in the presented process.

The results indicate that the resultant solution is not safe for disposal, if not further treated, according to the disposal standards stipulated by U.S. Environmental Protection Agency (EPA) (2023). The results demonstrate the feasibility of a semi-closed loop spent Li-ionB cathode recycling process comprising battery pre-treatment, single-stage inorganic acid-reductant leaching, single-compartment electrowinning cell, precipitation reactor, and sulphation reactor. The main objective of this work, Ni-Co composite recovery, was successfully reached since the deposit chemical composition presents a rather high concentration of Ni-Co composite, i.e., 98.05wt %.

10.2 The Novelty of the Study

- The presented valuable metal recovery process of NMC 532 Li-ionB cathode.
- The utilisation of rotating plate batch potentiostatic electrowinning to selectively recover pure Ni-Co alloys from Mn^{2+} , Li^+ , Co^{2+} and Ni^{2+} multi-ion solution.
- The utilisation of Pt-plated titanium plate and aluminium plate electrodes and rotating anode mechanism.
- The elimination of conventional pre-purification separation stages (e.g. solvent extraction, ion exchange and selective precipitation).

10.3 Recommendations

Based on the observations and deductions made throughout the process of achieving the aim and objectives of this study, several recommendations can be made that would necessitate further study in order to improve the findings of the present study.

Thus, the recommendations made for future studies are listed below:

- **Functionalizing metallic electrode materials** to exhibit metal selective properties, an approach that involves modifying their surface properties or introducing specific functional groups to enhance performance or enable targeted interactions in various applications. This can be achieved through techniques such as surface modification, coating deposition, functional group attachment, surface activation, self-assembly, template-assisted synthesis, hybrid materials integration, and surface functionalization tailored for specific applications. These approaches allow for the precise control of surface chemistry, morphology, and reactivity, enabling the design of electrodes with optimized properties for applications such as sensing, electrocatalysis, energy storage, and biomedical devices.
- Exploring **utilisation of conductive organic electrolytes** through introduction of different ions into the solution, typically through the addition of conductive salts or solutes. The organic acids as leachants are less costly and exhibit less emissions.
- **Modification of the electrowinning cell design** to accommodate higher surface area per unit volume of electrolyte.

- Exploring more anode alternatives (**Mixed-metal Oxide (MMO) Coated Titanium Electrodes**) (material and design) to reduce the anodic voltage.
- **Utilisation of LiOH as a pH adjusting agent** to avoid the generation of Na-rich wastewater effluent.
- **Precipitation of Li_2CO_3 using CO_2** to avoid generation of Na-rich wastewater process effluent.

References

- Abbey, C. E., 2019. Improving base metal electrowinning. [online]. Available from: https://scholarsmine.mst.edu/doctoral_dissertations/2770.
- Aboagye, E. A., Chea, J. D. and Yenkie, K. M., 2021. Systems level roadmap for solvent recovery and reuse in industries. *iScience*, 24 (10), 103114.
- Ali, H., Khan, H. A. and Pecht, M., 2022. Preprocessing of spent lithium-ion batteries for recycling: Need, methods, and trends. *Renewable and Sustainable Energy Reviews*, 168, 112809.
- Altamirano-Garcia, L., Luna-Sánchez, R. M., Sosa-Rodríguez, F. S., Cabrera-Sierra, R. and Vazquez-Arenas, J., 2021. Co-Ni alloy coatings electrodeposited using real leachates generated from positive electrodes of Ni Cd batteries. *Surface and Coatings Technology*, 425, 127672.
- Apostolakou, A. A., Kookos, I. K., Marazioti, C. and Angelopoulos, K. C., 2009. Techno-economic analysis of a biodiesel production process from vegetable oils. *Fuel Processing Technology*, 90 (7–8), 1023–1031.
- Armstrong, A. R., Lyness, C., Panchmatia, P. M., Islam, M. S. and Bruce, P. G., 2011. The lithium intercalation process in the low-voltage lithium battery anode $\text{Li}_1+\text{xV}_1-\text{xO}_2$. *Nature Materials*, 10 (3), 223–229.
- Asenbauer, J., Eisenmann, T., Kuenzel, M., Kazzazi, A., Chen, Z. and Bresser, D., 2020. The success story of graphite as a lithium-ion anode material – fundamentals, remaining challenges, and recent developments including silicon (oxide) composites. *Sustainable Energy & Fuels*, 4 (11), 5387–5416.
- Aurbach, D., Markovsky, B., Weissman, I., Levi, E. and Ein-Eli, Y., 1999. On the correlation between surface chemistry and performance of graphite negative electrodes for Li ion batteries. *Electrochimica Acta*, 45 (1–2), 67–86.
- Bahaloo-Horeh, N. and Mousavi, S. M., 2017. Enhanced recovery of valuable metals from spent lithium-ion batteries through optimization of organic acids produced by *Aspergillus niger*. *Waste Management*, 60, 666–679.

- Bai, Y., Essehli, R., Jafta, C. J., Livingston, K. M. and Belharouak, I., 2021. Recovery of Cathode Materials and Aluminum Foil Using a Green Solvent. *ACS Sustainable Chemistry & Engineering*, 9 (17), 6048–6055.
- Barik, S. P., Prabakaran, G. and Kumar, L., 2017a. Leaching and separation of Co and Mn from electrode materials of spent lithium-ion batteries using hydrochloric acid: Laboratory and pilot scale study. *Journal of Cleaner Production*, 147, 37–43.
- Barik, S. P., Prabakaran, G. and Kumar, L., 2017b. Leaching and separation of Co and Mn from electrode materials of spent lithium-ion batteries using hydrochloric acid: Laboratory and pilot scale study. *Journal of Cleaner Production*, 147, 37–43.
- Barker, J., Saidi, M. Y. and Swoyer, J. L., 2003. Electrochemical Insertion Properties of the Novel Lithium Vanadium Fluorophosphate, LiVPO₄F. *Journal of The Electrochemical Society*, 150 (10), A1394.
- Battle, T., Moats, M. and Allanore, A., 2016. *Ni-Co 2013*. Cham: Springer International Publishing.
- Baum, Z. J., Bird, R. E., Yu, X. and Ma, J., 2022. Lithium-Ion Battery Recycling—Overview of Techniques and Trends. *ACS Energy Letters*, 7 (2), 712–719.
- Bertuol, D. A., Machado, C. M., Silva, M. L., Calgaro, C. O., Dotto, G. L. and Tanabe, E. H., 2016. Recovery of cobalt from spent lithium-ion batteries using supercritical carbon dioxide extraction. *Waste Management*, 51, 245–251.
- Bhagaskara, A., Saputra, D. A., Saviola, A. J., Wijaya, K., Oh, W.-C., Rahayu, S., Gumelar, M. D., Saudi, A. U., Agustanhakri, A., Budiman, A. H. and Indrijarso, S., 2024. Recycling of nickel metal from spent nickel-manganese-cobalt (NMC) cathode batteries using H₃PO₄–H₂C₂O₄ solution combination as an efficient leaching agent. *Case Studies in Chemical and Environmental Engineering*, 10, 100844.
- Biswal, B. K. and Balasubramanian, R., 2023. Recovery of valuable metals from spent lithium-ion batteries using microbial agents for bioleaching: a review. *Frontiers in Microbiology*, 14.
- Bloom, I., Jones, S. A., Battaglia, V. S., Henriksen, G. L., Christophersen, J. P., Wright, R. B., Ho, C. D., Belt, J. R. and Motloch, C. G., 2003. Effect of cathode composition on capacity fade, impedance rise and power fade in high-power, lithium-ion cells. *Journal of Power Sources*, 124 (2), 538–550.

- Bloomberg, 2022. *Precious and Industrial Metals Markets* [online]. Markets. Available from: <https://www.bloomberg.com/markets/commodities/futures/metals> [Accessed 21 Jan 2023].
- Borah, R., Hughson, F. R., Johnston, J. and Nann, T., 2020. On battery materials and methods. *Materials Today Advances*, 6, 100046.
- Brousse, T., Bélanger, D. and Long, J. W., 2015. To Be or Not To Be Pseudocapacitive? *Journal of The Electrochemical Society*, 162 (5), A5185–A5189.
- Bruce, P. G., Armstrong, A. R. and Gitzendanner, R. L., 1999. New intercalation compounds for lithium batteries: layered LiMnO₂. *Journal of Materials Chemistry*, 9 (1), 193–198.
- Cabana, J., Monconduit, L., Larcher, D. and Palacín, M. R., 2010. Beyond intercalation-based Li-Ion batteries: The state of the art and challenges of electrode materials reacting through conversion reactions. *Advanced Materials*, 22 (35), E170–E192.
- Carvajal Ortiz, R., Amietszajew, T. and Bhagat, R., 2020. Recovery of Nickel and Cobalt By Electrowinning from Spent Lithium-Ion Batteries Using Molten Salt Electrolytes. *ECS Meeting Abstracts*, MA2020-02 (18), 1536–1536.
- de Castro, D., dos Santos, I., Mansur, M. and Dutra, A., 2023. Voltammetric Study on the Electrowinning of Cobalt in the Presence of Additives. *Journal of the Brazilian Chemical Society*.
- Chan, C. K., Peng, H., Liu, G., Mcllwraith, K., Zhang, X. F., Huggins, R. A. and Cui, Y., 2008. High-performance lithium battery anodes using silicon nanowires. *Nature Nanotechnology*, 3 (1), 31–35.
- Chandran, V., Ghosh, A., Patil, C. K., Mohanavel, V., Priya, A. K., Rahim, R., Madavan, R., Muthuraman, U. and Karthick, A., 2021. Comprehensive review on recycling of spent lithium-ion batteries. *Materials Today: Proceedings*, 47, 167–180.
- Chen, C. H., Liu, J., Stoll, M. E., Henriksen, G., Vissers, D. R. and Amine, K., 2004. Aluminum-doped lithium nickel cobalt oxide electrodes for high-power lithium-ion batteries. *Journal of Power Sources*, 128 (2), 278–285.
- Chen, F., Han, J., Kong, D., Yuan, Y., Xiao, J., Wu, S., Tang, D.-M., Deng, Y., Lv, W., Lu, J., Kang, F. and Yang, Q.-H., 2021. 1000 Wh L⁻¹ lithium-ion batteries enabled by crosslink-shrunk tough carbon encapsulated silicon microparticle anodes. *National Science Review*, 8 (9).

- Chen, J., Li, Q., Song, J., Song, D., Zhang, L. and Shi, X., 2016. Environmentally friendly recycling and effective repairing of cathode powders from spent LiFePO_4 batteries. *Green Chemistry*, 18 (8), 2500–2506.
- Chen, J., Zhu, L., Jia, D., Jiang, X., Wu, Y., Hao, Q., Xia, X., Ouyang, Y., Peng, L., Tang, W. and Liu, T., 2019. $\text{LiNi}_{0.8}\text{Co}_{0.15}\text{Al}_{0.05}\text{O}_2$ cathodes exhibiting improved capacity retention and thermal stability due to a lithium iron phosphate coating. *Electrochimica Acta*, 312, 179–187.
- Chen, M., Zheng, Z., Wang, Q., Zhang, Y., Ma, X., Shen, C., Xu, D., Liu, J., Liu, Y., Gionet, P., O'Connor, I., Pinnell, L., Wang, J., Gratz, E., Arsenault, R. and Wang, Y., 2019. Closed Loop Recycling of Electric Vehicle Batteries to Enable Ultra-high Quality Cathode Powder. *Scientific Reports*, 9 (1), 1654.
- Chen, S., Gordin, M. L., Yi, R., Howlett, G., Sohn, H. and Wang, D., 2012. Silicon core–hollow carbon shell nanocomposites with tunable buffer voids for high capacity anodes of lithium-ion batteries. *Physical Chemistry Chemical Physics*, 14 (37), 12741.
- Chen, S.-Y. and Lin, J.-G., 2009. Enhancement of metal bioleaching from contaminated sediment using silver ion. *Journal of Hazardous Materials*, 161 (2–3), 893–899.
- Chen, W.-S. and Ho, H.-J., 2018. Recovery of Valuable Metals from Lithium-Ion Batteries NMC Cathode Waste Materials by Hydrometallurgical Methods. *Metals*, 8 (5), 321.
- Chen, X., Fan, B., Xu, L., Zhou, T. and Kong, J., 2016. An atom-economic process for the recovery of high value-added metals from spent lithium-ion batteries. *Journal of Cleaner Production*, 112, 3562–3570.
- Chen, X., Guo, C., Ma, H., Li, J., Zhou, T., Cao, L. and Kang, D., 2018. Organic reductants based leaching: A sustainable process for the recovery of valuable metals from spent lithium ion batteries. *Waste Management*, 75, 459–468.
- Chen, X., Luo, C., Zhang, J., Kong, J. and Zhou, T., 2015. Sustainable Recovery of Metals from Spent Lithium-Ion Batteries: A Green Process. *ACS Sustainable Chemistry & Engineering*, 3 (12), 3104–3113.
- Chen, X., Ma, H., Luo, C. and Zhou, T., 2017. Recovery of valuable metals from waste cathode materials of spent lithium-ion batteries using mild phosphoric acid. *Journal of Hazardous Materials*, 326, 77–86.

- Chen, X., Yang, C., Yang, Y., Ji, H. and Yang, G., 2022. Co-precipitation preparation of Ni-Co-Mn ternary cathode materials by using the sources extracting directly from spent lithium-ion batteries. *Journal of Alloys and Compounds*, 909, 164691.
- Chen, Y., Mojica, F., Li, G. and Chuang, P.-Y. A., 2017. Experimental study and analytical modeling of an alkaline water electrolysis cell. *International Journal of Energy Research*, 41 (14), 2365–2373.
- Cheng, E. J., Hong, K., Taylor, N. J., Choe, H., Wolfenstine, J. and Sakamoto, J., 2017. Mechanical and physical properties of $\text{LiNi}_{0.33}\text{Mn}_{0.33}\text{Co}_{0.33}\text{O}_2$ (NMC). *Journal of the European Ceramic Society*, 37 (9), 3213–3217.
- Cheng, Q., 2018. Effect of Different Reductants on Leaching Lithium and Cobalt from Lithium Ion Batteries in Tartaric Acid Solution. *IOP Conference Series: Earth and Environmental Science*, 192, 012007.
- Choi, S. and Manthiram, A., 2012. Synthesis and Electrochemical Properties of Spinel LiCo_2O_4 Cathodes. *In: .* 215–224.
- Cohen-Hyams, T., Kaplan, W. D. and Yahalom, J., 2002. Structure of Electrodeposited Cobalt. *Electrochemical and Solid-State Letters*, 5 (8), C75.
- Colin, J.-F., Godbole, V. and Novák, P., 2010. In situ neutron diffraction study of Li insertion in $\text{Li}_4\text{Ti}_5\text{O}_{12}$. *Electrochemistry Communications*, 12 (6), 804–807.
- Cormier, M. M. E., Zhang, N., Liu, A., Li, H., Inglis, J. and Dahn, J. R., 2019. Impact of Dopants (Al, Mg, Mn, Co) on the Reactivity of Li_xNiO_2 with the Electrolyte of Li-Ion Batteries. *Journal of The Electrochemical Society*, 166 (13), A2826–A2833.
- CSIRO, 2022. *CSIRO Annual Report 2021-22* [online]. Canberra. Available from: https://www.csiro.au/-/media/About/AnnualReport/Files/2019-20/20-00135_CORP_AnnualReport2019-20_WEB_201012.pdf [Accessed 21 Jan 2023].
- Dahn, J. R., Fuller, E. W., Obrovac, M. and von Sacken, U., 1994. Thermal stability of Li_xCoO_2 , Li_xNiO_2 and $\lambda\text{-MnO}_2$ and consequences for the safety of Li-ion cells. *Solid State Ionics*, 69 (3–4), 265–270.
- Darvishi, D., Haghshenas, D. F., Alamdari, E. K., Sadrnezhaad, S. K. and Halali, M., 2005. Synergistic effect of Cyanex 272 and Cyanex 302 on separation of cobalt and nickel by D2EHPA. *Hydrometallurgy*, 77 (3–4), 227–238.
- Darwiche, A., Marino, C., Sougrati, M. T., Fraisse, B., Stievano, L. and Monconduit, L., 2012. Better Cycling Performances of Bulk Sb in Na-Ion Batteries Compared to Li-Ion Systems: An

- Unexpected Electrochemical Mechanism. *Journal of the American Chemical Society*, 134 (51), 20805–20811.
- Davies, T. J., Banks, C. E. and Compton, R. G., 2005. Voltammetry at spatially heterogeneous electrodes. *Journal of Solid State Electrochemistry*, 9 (12), 797–808.
- Delacourt, C., Poizot, P., Levasseur, S. and Masquelier, C., 2006. Size Effects on Carbon-Free LiFePO₄ Powders. *Electrochemical and Solid-State Letters*, 9 (7), A352.
- Ding, Y., Mu, D., Wu, B., Zhao, Z. and Wang, R., 2020. Controllable synthesis of spherical precursor Ni_{0.8}Co_{0.1}Mn_{0.1}(OH)₂ for nickel-rich cathode material in Li-ion batteries. *Ceramics International*, 46 (7), 9436–9445.
- Divakaran, A. M., Minakshi, M., Bahri, P. A., Paul, S., Kumari, P., Divakaran, A. M. and Manjunatha, K. N., 2021. Rational design on materials for developing next generation lithium-ion secondary battery. *Progress in Solid State Chemistry*, 62, 100298.
- Dominguez-Benetton, X., Varia, J. C., Pozo, G., Modin, O., Ter Heijne, A., Fransaer, J. and Rabaey, K., 2018. Metal recovery by microbial electro-metallurgy. *Progress in Materials Science*, 94, 435–461.
- Dong, M., Xue, Z., Wang, L. and Xia, Y., 2018. NaOH induced the complete dissolution of ι-carrageenan and the corresponding mechanism. *Polymer*, 151, 334–339.
- Du, K., Ang, E. H., Wu, X. and Liu, Y., 2022. Progresses in Sustainable Recycling Technology of Spent Lithium-Ion Batteries. *Energy & Environmental Materials*, 5 (4), 1012–1036.
- Dunn, J. B., Gaines, L., Sullivan, J. and Wang, M. Q., 2012. Impact of Recycling on Cradle-to-Gate Energy Consumption and Greenhouse Gas Emissions of Automotive Lithium-Ion Batteries. *Environmental Science & Technology*, 46 (22), 12704–12710.
- Dunn, J., Kendall, A. and Slattery, M., 2022. Electric vehicle lithium-ion battery recycled content standards for the US – targets, costs, and environmental impacts. *Resources, Conservation and Recycling*, 185, 106488.
- ECHEMI, 2023. *Product Market Price & Insight* [online]. Available from: <https://www.echemi.com/> [Accessed 22 Jan 2024].
- Elsherief, A. E., 2003. Effects of cobalt, temperature and certain impurities upon cobalt electrowinning from sulfate solutions. *Journal of Applied Electrochemistry*, 33 (1), 43–49.
- Entwistle, T., Sanchez-Perez, E., Murray, G. J., Anthonisamy, N. and Cussen, S. A., 2022. Co-precipitation synthesis of nickel-rich cathodes for Li-ion batteries. *Energy Reports*, 8, 67–73.

- ESI-Africa, 2021. *The Growing Lithium-Ion Battery Recycling Market* [online]. Available from: <https://www.esi-africa.com/regional-news/international/the-growing-lithium-ion-battery-recycling-market/> [Accessed 21 Jan 2023].
- ESMAP, 2022. *Reuse and Recycling: Environmental Sustainability of Lithium-Ion Battery Energy Storage Systems An Energy Storage Partnership Report* [online]. Available from: <https://documents.worldbank.org/en/publication/documents-reports/documentdetail/593961599738208006/reuse-and-recycling-environmental-sustainability-of-lithium-ion-battery-energy-storage-systems> [Accessed 13 Aug 2024].
- Espinosa, D. C. R., Bernardes, A. M. and Tenório, J. A. S., 2004. An overview on the current processes for the recycling of batteries. *Journal of Power Sources*, 135 (1–2), 311–319.
- European Union, 2006. *Directive 2006/66/EC of the European Parliament and of the Council of 6 September 2006 on batteries and accumulators and waste batteries and accumulators and repealing Directive 91/157/EEC (Text with EEA relevance)* [online]. European Union Law. Available from: <https://eur-lex.europa.eu/legal-content/EN/ALL/?uri=CELEX%3A32006L0066> [Accessed 21 Jan 2023].
- Farjana, S. H., Huda, N. and Mahmud, M. A. P., 2019. Life cycle assessment of cobalt extraction process. *Journal of Sustainable Mining*, 18 (3), 150–161.
- Ferreira, D. A., Prados, L. M. Z., Majuste, D. and Mansur, M. B., 2009a. Hydrometallurgical separation of aluminium, cobalt, copper and lithium from spent Li-ion batteries. *Journal of Power Sources*, 187 (1), 238–246.
- Ferreira, D. A., Prados, L. M. Z., Majuste, D. and Mansur, M. B., 2009b. Hydrometallurgical separation of aluminium, cobalt, copper and lithium from spent Li-ion batteries. *Journal of Power Sources*, 187 (1), 238–246.
- Flett, D. S., 2004. Cobalt-nickel separation in hydrometallurgy: a review. *Cobalt-nickel separation in hydrometallurgy: a review*, 12.
- Fu, Z.-W., Li, C.-L., Liu, W.-Y., Ma, J., Wang, Y. and Qin, Q.-Z., 2005. Electrochemical Reaction of Lithium with Cobalt Fluoride Thin Film Electrode. *Journal of The Electrochemical Society*, 152 (2), E50.
- Gaines, L., 2012. To recycle, or not to recycle, that is the question: Insights from life-cycle analysis. *MRS Bulletin*, 37 (4), 333–338.

- Garcia, E. M., Santos, J. S., Pereira, E. C. and Freitas, M. B. J. G., 2008. Electrodeposition of cobalt from spent Li-ion battery cathodes by the electrochemistry quartz crystal microbalance technique. *Journal of Power Sources*, 185 (1), 549–553.
- Garcia, E. M., Tarôco, H. A., Matencio, T., Domingues, R. Z., dos Santos, J. A. F., Ferreira, R. V., Lorençon, E., Lima, D. Q. and de Freitas, M. B. J. G., 2012. Electrochemical recycling of cobalt from spent cathodes of lithium-ion batteries: its application as supercapacitor. *Journal of Applied Electrochemistry*, 42 (6), 361–366.
- Garcia, E. M., Tarôco, H. A., Matencio, T., Domingues, R. Z., dos Santos, J. A. F. and de Freitas, M. B. J. G., 2011. Electrochemical recycling of cobalt from spent cathodes of lithium-ion batteries: its application as coating on SOFC interconnects. *Journal of Applied Electrochemistry*, 41 (11), 1373–1379.
- Georgi-Maschler, T., Friedrich, B., Weyhe, R., Heegn, H. and Rutz, M., 2012. Development of a recycling process for Li-ion batteries. *Journal of Power Sources*, 207, 173–182.
- Global Battery Alliance, 2020. *A Vision for a Sustainable Battery Value Chain in 2030 Unlocking the Full Potential to Power Sustainable Development and Climate Change Mitigation* [online]. Geneva. Available from: https://www3.weforum.org/docs/WEF_A_Vision_for_a_Sustainable_Battery_Value_Chain_in_2030_Report.pdf [Accessed 21 Jan 2023].
- Gmitter, A. J., Badway, F., Rangan, S., Bartynski, R. A., Halajko, A., Pereira, N. and Amatucci, G. G., 2010. Formation, dynamics, and implication of solid electrolyte interphase in high voltage reversible conversion fluoride nanocomposites. *Journal of Materials Chemistry*, 20 (20), 4149.
- Golmohammadzadeh, R., Faraji, F. and Rashchi, F., 2018. Recovery of lithium and cobalt from spent lithium ion batteries (LIBs) using organic acids as leaching reagents: A review. *Resources, Conservation and Recycling*, 136, 418–435.
- Golodnitsky, D., Gudin, N. V. and Volyanuk, G. A., 1998. Cathode Process in Nickel-cobalt Alloy Deposition from Sulfamate Electrolytes - Application to Electroforming. *Plating and Surface Finishing*, 85 (2).
- Goutam, S., Omar, N., Van Den Bossche, P. and Van Mierlo, J., 2017. Review of Nanotechnology for Anode Materials in Batteries. In: *Emerging Nanotechnologies in Rechargeable Energy Storage Systems*. Elsevier, 45–82.

- Gowda, S. R., Gallagher, K. G., Croy, J. R., Bettge, M., Thackeray, M. M. and Balasubramanian, M., 2014. Oxidation state of cross-over manganese species on the graphite electrode of lithium-ion cells. *Physical Chemistry Chemical Physics*, 16 (15), 6898.
- Granata, G., Moscardini, E., Pagnanelli, F., Trabucco, F. and Toro, L., 2012. Product recovery from Li-ion battery wastes coming from an industrial pre-treatment plant: Lab scale tests and process simulations. *Journal of Power Sources*, 206, 393–401.
- Gratz, E., Sa, Q., Apelian, D. and Wang, Y., 2014. A closed loop process for recycling spent lithium ion batteries. *Journal of Power Sources*, 262, 255–262.
- Guan, J., Li, Y., Guo, Y., Su, R., Gao, G., Song, H., Yuan, H., Liang, B. and Guo, Z., 2017. Mechanochemical Process Enhanced Cobalt and Lithium Recycling from Wasted Lithium-Ion Batteries. *ACS Sustainable Chemistry & Engineering*, 5 (1), 1026–1032.
- Guerrini, N., Jin, L., Lozano, J. G., Luo, K., Sobkowiak, A., Tsuruta, K., Massel, F., Duda, L.-C., Roberts, M. R. and Bruce, P. G., 2020. Charging Mechanism of Li_2MnO_3 . *Chemistry of Materials*, 32 (9), 3733–3740.
- Guinier, A., 2013. *X-Ray Diffraction: In crystals, imperfect crystals, and amorphous bodies*.
- Haiyang Zou, 2012. Development of a Recycling Process for Li-Ion Batteries. WORCESTER POLYTECHNIC INSTITUTE, Worcester.
- Halli, P., Wilson, B. P., Hailemariam, T., Latostenmaa, P., Yliniemi, K. and Lundström, M., 2020. Electrochemical recovery of tellurium from metallurgical industrial waste. *Journal of Applied Electrochemistry*, 50 (1).
- Hanisch, C., Loellhoeffel, T., Diekmann, J., Markley, K. J., Haselrieder, W. and Kwade, A., 2015. Recycling of lithium-ion batteries: a novel method to separate coating and foil of electrodes. *Journal of Cleaner Production*, 108, 301–311.
- Harper, G., Sommerville, R., Kendrick, E., Driscoll, L., Slater, P., Stolkin, R., Walton, A., Christensen, P., Heidrich, O., Lambert, S., Abbott, A., Ryder, K., Gaines, L. and Anderson, P., 2019. Recycling lithium-ion batteries from electric vehicles. *Nature*, 575 (7781), 75–86.
- Hassoun, J. and Scrosati, B., 2010. Moving to a Solid-State Configuration: A Valid Approach to Making Lithium-Sulfur Batteries Viable for Practical Applications. *Advanced Materials*, 22 (45), 5198–5201.
- He, L.-P., Sun, S.-Y., Mu, Y.-Y., Song, X.-F. and Yu, J.-G., 2017a. Recovery of Lithium, Nickel, Cobalt, and Manganese from Spent Lithium-Ion Batteries Using I^- -Tartaric Acid as a Leachant. *ACS Sustainable Chemistry & Engineering*, 5 (1), 714–721.

- He, L.-P., Sun, S.-Y., Mu, Y.-Y., Song, X.-F. and Yu, J.-G., 2017b. Recovery of Lithium, Nickel, Cobalt, and Manganese from Spent Lithium-Ion Batteries Using L-Tartaric Acid as a Leachant. *ACS Sustainable Chemistry & Engineering*, 5 (1), 714–721.
- He, L.-P., Sun, S.-Y., Song, X.-F. and Yu, J.-G., 2015. Recovery of cathode materials and Al from spent lithium-ion batteries by ultrasonic cleaning. *Waste Management*, 46, 523–528.
- He, Y.-B., Liu, M., Huang, Z.-D., Zhang, B., Yu, Y., Li, B., Kang, F. and Kim, J.-K., 2013. Effect of solid electrolyte interface (SEI) film on cyclic performance of Li₄Ti₅O₁₂ anodes for Li ion batteries. *Journal of Power Sources*, 239, 269–276.
- Hebert, A. and McCalla, E., 2021. The role of metal substitutions in the development of Li batteries, part I: cathodes. *Materials Advances*, 2 (11), 3474–3518.
- Horeh, N. B., Mousavi, S. M. and Shojaosadati, S. A., 2016. Bioleaching of valuable metals from spent lithium-ion mobile phone batteries using *Aspergillus niger*. *Journal of Power Sources*, 320, 257–266.
- Hosono, E., Kudo, T., Honma, I., Matsuda, H. and Zhou, H., 2009. Synthesis of Single Crystalline Spinel LiMn₂O₄ Nanowires for a Lithium Ion Battery with High Power Density. *Nano Letters*, 9 (3), 1045–1051.
- Huang, B., Pan, Z., Su, X. and An, L., 2018. Recycling of lithium-ion batteries: Recent advances and perspectives. *Journal of Power Sources*, 399, 274–286.
- Huang, H., Yin, S.-C., Kerr, T., Taylor, N. and Nazar, L. F., 2002. Nanostructured Composites: A High Capacity, Fast Rate Li₃V₂(PO₄)₃/Carbon Cathode for Rechargeable Lithium Batteries. *Advanced Materials*, 14 (21), 1525–1528.
- Huang, Y., Han, G., Liu, J., Chai, W., Wang, W., Yang, S. and Su, S., 2016. A stepwise recovery of metals from hybrid cathodes of spent Li-ion batteries with leaching-flotation-precipitation process. *Journal of Power Sources*, 325, 555–564.
- Ijadi Bajestani, M., Mousavi, S. M. and Shojaosadati, S. A., 2014. Bioleaching of heavy metals from spent household batteries using *Acidithiobacillus ferrooxidans*: Statistical evaluation and optimization. *Separation and Purification Technology*, 132, 309–316.
- Intratec Solutions, 2024. *Industrial Commodities | Current and Forecast* [online]. Available from: <https://www.intratec.us/> [Accessed 18 Jan 2024].
- Islam, M. T. and Iyer-Raniga, U., 2022. Lithium-Ion Battery Recycling in the Circular Economy: A Review. *Recycling*, 7 (3), 33.

- Jeffrey, M. I., Choo, W. L. and Breuer, P. L., 2000a. *The effect of additives and impurities on the cobalt electrowinning process*. Minerals Engineering.
- Jeffrey, M. I., Choo, W. L. and Breuer, P. L., 2000b. The effect of additives and impurities on the cobalt electrowinning process. *Minerals Engineering*, 13 (12), 1231–1241.
- Jha, A., Jha, M., Kumari, A., Sahu, S., Kumar, V. and Pandey, B., 2013. Selective separation and recovery of cobalt from leach liquor of discarded Li-ion batteries using thiophosphinic extractant. *Separation and Purification Technology*, 104, 160–166.
- Jiao, F., Bao, J., Hill, A. H. and Bruce, P. G., 2008. Synthesis of Ordered Mesoporous Li-Mn-O Spinel as a Positive Electrode for Rechargeable Lithium Batteries. *Angewandte Chemie*, 120 (50), 9857–9862.
- Jiao, F. and Bruce, P. G., 2007. Mesoporous Crystalline β -MnO₂—a Reversible Positive Electrode for Rechargeable Lithium Batteries. *Advanced Materials*, 19 (5), 657–660.
- Jinyue Yan, 2015. *Handbook of clean energy systems, 6 volume set*. Wiley.
- Joo, S.-H., Shin, D. ju, Oh, C., Wang, J.-P., Senanayake, G. and Shin, S. M., 2016. Selective extraction and separation of nickel from cobalt, manganese and lithium in pre-treated leach liquors of ternary cathode material of spent lithium-ion batteries using synergism caused by Versatic 10 acid and LIX 84-I. *Hydrometallurgy*, 159, 65–74.
- Joo, S.-H., Shin, D., Oh, C., Wang, J.-P. and Shin, S. M., 2016. Extraction of manganese by alkyl monocarboxylic acid in a mixed extractant from a leaching solution of spent lithium-ion battery ternary cathodic material. *Journal of Power Sources*, 305, 175–181.
- Joulié, M., Laucournet, R. and Billy, E., 2014. Hydrometallurgical process for the recovery of high value metals from spent lithium nickel cobalt aluminum oxide based lithium-ion batteries. *Journal of Power Sources*, 247, 551–555.
- Jung, H.-G., Jang, M. W., Hassoun, J., Sun, Y.-K. and Scrosati, B., 2011. A high-rate long-life Li₄Ti₅O₁₂/Li[Ni_{0.45}Co_{0.1}Mn_{1.45}]O₄ lithium-ion battery. *Nature Communications*, 2 (1), 516.
- Kamran, A. Bin, 2023. *Change in Priorities to Alter the Market Share of Different Lithium-Ion Chemistries* [online]. PTR Inc. Available from: Abdullah Bin [Accessed 13 Aug 2024].
- Kang, H.-J., Bari, G. A. K. M. R., Lee, T.-G., Khan, T. T., Park, J.-W., Hwang, H. J., Cho, S. Y. and Jun, Y.-S., 2020. Microporous carbon nanoparticles for lithium–sulfur batteries. *Nanomaterials*, 10 (10), 2012.

- Kang, K., Meng, Y. S., Bréger, J., Grey, C. P. and Ceder, G., 2006. Electrodes with High Power and High Capacity for Rechargeable Lithium Batteries. *Science*, 311 (5763), 977–980.
- Kargl-Simard, C., Huang, J. H. and Alfantazi, A. M., 2003. Electrical conductivity and density of CoSO₄/H₂SO₄ solutions in the range of modern cobalt electrowinning electrolytes. *Minerals Engineering*, 16 (6), 529–535.
- Karimzadeh, A., Aliofkhaezai, M. and Walsh, F. C., 2019. A review of electrodeposited Ni-Co alloy and composite coatings: Microstructure, properties and applications. *Surface and Coatings Technology*, 372, 463–498.
- Kazem-Ghamsari, A. and Abdollahi, H., 2022. Electrowinning of Nickel and Cobalt from Non-circulated Sulfate Electrolyte. *Transactions of the Indian Institute of Metals*, 75 (5), 1141–1151.
- Kiciński, W. and Dyjak, S., 2020. Transition metal impurities in carbon-based materials: Pitfalls, artifacts and deleterious effects. *Carbon*, 168, 748–845.
- Kim, D. K., Muralidharan, P., Lee, H.-W., Ruffo, R., Yang, Y., Chan, C. K., Peng, H., Huggins, R. A. and Cui, Y., 2008. Spinel LiMn₂O₄ Nanorods as Lithium Ion Battery Cathodes. *Nano Letters*, 8 (11), 3948–3952.
- Kim, H., Kim, D. I. and Yoon, W.-S., 2022. Challenges and Design Strategies for Conversion-Based Anode Materials for Lithium- and Sodium-Ion Batteries. *Journal of Electrochemical Science and Technology*, 13 (1), 32–53.
- Kim, J. G., Wang, J. H., Ahn, J. H., Kim, H. J. and Lim, H. C., 2013. Comparison of femoral tunnel length between transportal and retrograde reaming outside-in techniques in anterior cruciate ligament reconstruction. *Knee Surgery, Sports Traumatology, Arthroscopy*, 21 (4), 830–838.
- Kim, M., Jung, Y. and Kang, B., 2015. High electrochemical performance of 3.9 V LiFeSO₄F directly synthesized by a scalable solid-state reaction within 1 h. *Journal of Materials Chemistry A*, 3 (14), 7583–7590.
- Kim, S., Bang, J., Yoo, J., Shin, Y., Bae, J., Jeong, J., Kim, K., Dong, P. and Kwon, K., 2021. A comprehensive review on the pretreatment process in lithium-ion battery recycling. *Journal of Cleaner Production*, 294, 126329.
- Kim, T., Song, W., Son, D.-Y., Ono, L. K. and Qi, Y., 2019. Lithium-ion batteries: outlook on present, future, and hybridized technologies. *Journal of Materials Chemistry A*, 7 (7), 2942–2964.

- Kitsche, D., Schweidler, S., Mazilkin, A., Geßwein, H., Fauth, F., Suard, E., Hartmann, P., Brezesinski, T., Janek, J. and Bianchini, M., 2020. The effect of gallium substitution on the structure and electrochemical performance of LiNiO_2 in lithium-ion batteries. *Materials Advances*, 1 (4), 639–647.
- Knight, J. C., Therese, S. and Manthiram, A., 2015. Delithiation Mechanisms in Acid of Spinel $\text{LiMn}_{2-x}\text{M}_x\text{O}_4$ (M = Cr, Fe, Co, and Ni) Cathodes. *Journal of The Electrochemical Society*, 162 (3), A426–A431.
- Kozhina, G. A., Ermakov, A. N., Fetisov, V. B., Fetisov, A. V. and Shunyaev, K. Yu., 2009. Electrochemical dissolution of Co_3O_4 in acidic solutions. *Russian Journal of Electrochemistry*, 45 (10), 1170–1175.
- Ku, H., Jung, Y., Jo, M., Park, S., Kim, S., Yang, D., Rhee, K., An, E.-M., Sohn, J. and Kwon, K., 2016a. Recycling of spent lithium-ion battery cathode materials by ammoniacal leaching. *Journal of Hazardous Materials*, 313, 138–146.
- Ku, H., Jung, Y., Jo, M., Park, S., Kim, S., Yang, D., Rhee, K., An, E.-M., Sohn, J. and Kwon, K., 2016b. Recycling of spent lithium-ion battery cathode materials by ammoniacal leaching. *Journal of Hazardous Materials*, 313, 138–146.
- Kuhn, M. W. J., 2023. Towards a Business Model For Lithium-Ion Battery Recycling In South Africa. [online]. ESI-Africa. Available from: <https://www.esi-africa.com/africa/unpacking-battery-energy-storage-value-chain-opportunities-in-sa/#:~:text=Currently%2C%20there%20are%20no%20lithium,low%20collection%20rates%20by%20recyclers>. [Accessed 17 Aug 2024].
- de la Guardia, M. and Armenta, S., 2011. Multianalyte Determination Versus One-at-a-Time Methodologies. *In: .* 121–156.
- Lakshminarayanan, G. R., Chen, E. S., Sadak, J. C. and Sautter, F. K., 1976. Electrodeposition of Cobalt Using an Insoluble Anode. *Journal of The Electrochemical Society*, 123 (11), 1612–1616.
- Lander, L., Cleaver, T., Rajaeifar, M. A., Nguyen-Tien, V., Elliott, R. J. R., Heidrich, O., Kendrick, E., Edge, J. S. and Offer, G., 2021. Financial viability of electric vehicle lithium-ion battery recycling. *iScience*, 24 (7), 102787.
- Lee, C. K. and Rhee, K.-I., 2002. Preparation of LiCoO_2 from spent lithium-ion batteries. *Journal of Power Sources*, 109 (1), 17–21.

- Lee, C. K. and Rhee, K.-I., 2003a. Reductive leaching of cathodic active materials from lithium ion battery wastes. *Hydrometallurgy*, 68 (1–3), 5–10.
- Lee, C. K. and Rhee, K.-I., 2003b. Reductive leaching of cathodic active materials from lithium ion battery wastes. *Hydrometallurgy*, 68 (1–3), 5–10.
- Lee, H.-W., Muralidharan, P., Ruffo, R., Mari, C. M., Cui, Y. and Kim, D. K., 2010. Ultrathin Spinel LiMn₂O₄ Nanowires as High Power Cathode Materials for Li-Ion Batteries. *Nano Letters*, 10 (10), 3852–3856.
- Lee, W. J., Maiti, U. N., Lee, J. M., Lim, J., Han, T. H. and Kim, S. O., 2014. Nitrogen-doped carbon nanotubes and graphene composite structures for energy and catalytic applications. *Chemical Communications*, 50 (52), 6818.
- Lee, Y. J., Yi, H., Kim, W.-J., Kang, K., Yun, D. S., Strano, M. S., Ceder, G. and Belcher, A. M., 2009. Fabricating Genetically Engineered High-Power Lithium-Ion Batteries Using Multiple Virus Genes. *Science*, 324 (5930), 1051–1055.
- Lew, K. S., Raja, M., Thanikaikarasan, S., Kim, T., Kim, Y. D. and Mahalingam, T., 2008. Effect of pH and current density in electrodeposited Co–Ni–P alloy thin films. *Materials Chemistry and Physics*, 112 (1), 249–253.
- Li, J. and Ma, Z.-F., 2019. Past and Present of LiFePO₄: From Fundamental Research to Industrial Applications. *Chem*, 5 (1), 3–6.
- Li, J., Shi, P., Wang, Z., Chen, Y. and Chang, C.-C., 2009. A combined recovery process of metals in spent lithium-ion batteries. *Chemosphere*, 77 (8), 1132–1136.
- Li, J., Wang, G. and Xu, Z., 2016. Environmentally-friendly oxygen-free roasting/wet magnetic separation technology for in situ recycling cobalt, lithium carbonate and graphite from spent LiCoO₂/graphite lithium batteries. *Journal of Hazardous Materials*, 302, 97–104.
- Li, L., Dunn, J. B., Zhang, X. X., Gaines, L., Chen, R. J., Wu, F. and Amine, K., 2013. Recovery of metals from spent lithium-ion batteries with organic acids as leaching reagents and environmental assessment. *Journal of Power Sources*, 233, 180–189.
- Li, L., Fan, E., Guan, Y., Zhang, X., Xue, Q., Wei, L., Wu, F. and Chen, R., 2017. Sustainable Recovery of Cathode Materials from Spent Lithium-Ion Batteries Using Lactic Acid Leaching System. *ACS Sustainable Chemistry & Engineering*, 5 (6), 5224–5233.
- Li, L., Lu, J., Ren, Y., Zhang, X. X., Chen, R. J., Wu, F. and Amine, K., 2012. Ascorbic-acid-assisted recovery of cobalt and lithium from spent Li-ion batteries. *Journal of Power Sources*, 218, 21–27.

- Li, L., Qu, W., Zhang, X., Lu, J., Chen, R., Wu, F. and Amine, K., 2015a. Succinic acid-based leaching system: A sustainable process for recovery of valuable metals from spent Li-ion batteries. *Journal of Power Sources*, 282, 544–551.
- Li, L., Qu, W., Zhang, X., Lu, J., Chen, R., Wu, F. and Amine, K., 2015b. Succinic acid-based leaching system: A sustainable process for recovery of valuable metals from spent Li-ion batteries. *Journal of Power Sources*, 282, 544–551.
- Li, L., Zhai, L., Zhang, X., Lu, J., Chen, R., Wu, F. and Amine, K., 2014. Recovery of valuable metals from spent lithium-ion batteries by ultrasonic-assisted leaching process. *Journal of Power Sources*, 262, 380–385.
- Liddell, Kn. C., 2005. Shrinking core models in hydrometallurgy: What students are not being told about the pseudo-steady approximation. *Hydrometallurgy*, 79 (1–2), 62–68.
- Lin, H.-Y. and Chen, Y.-W., 2004. The mechanism of reduction of cobalt by hydrogen. *Materials Chemistry and Physics*, 85 (1), 171–175.
- Lin, Z., Liu, Z., Fu, W., Dudney, N. J. and Liang, C., 2013a. Phosphorous Pentasulfide as a Novel Additive for High-Performance Lithium-Sulfur Batteries. *Advanced Functional Materials*, 23 (8), 1064–1069.
- Lin, Z., Liu, Z., Fu, W., Dudney, N. J. and Liang, C., 2013b. Lithium Polysulfidophosphates: A Family of Lithium-Conducting Sulfur-Rich Compounds for Lithium-Sulfur Batteries. *Angewandte Chemie*, 125 (29), 7608–7611.
- Liu, C., Neale, Z. G. and Cao, G., 2016. Understanding electrochemical potentials of cathode materials in rechargeable batteries. *Materials Today*.
- Liu, K. and Zhang, F.-S., 2016. Innovative leaching of cobalt and lithium from spent lithium-ion batteries and simultaneous dechlorination of polyvinyl chloride in subcritical water. *Journal of Hazardous Materials*, 316, 19–25.
- Liu, N., Lu, Z., Zhao, J., McDowell, M. T., Lee, H.-W., Zhao, W. and Cui, Y., 2014. A pomegranate-inspired nanoscale design for large-volume-change lithium battery anodes. *Nature Nanotechnology*, 9 (3), 187–192.
- Liu, P., Vajo, J. J., Wang, J. S., Li, W. and Liu, J., 2012. Thermodynamics and Kinetics of the Li/FeF₃ Reaction by Electrochemical Analysis. *The Journal of Physical Chemistry C*, 116 (10), 6467–6473.
- Liu, Y., Hudak, N. S., Huber, D. L., Limmer, S. J., Sullivan, J. P. and Huang, J. Y., 2011. In Situ Transmission Electron Microscopy Observation of Pulverization of Aluminum Nanowires

- and Evolution of the Thin Surface Al₂O₃ Layers during Lithiation–Delithiation Cycles. *Nano Letters*, 11 (10), 4188–4194.
- Lu, J., Dreisinger, D. and Glück, T., 2018. Cobalt electrowinning – A systematic investigation for high quality electrolytic cobalt production. *Hydrometallurgy*, 178, 19–29.
- Luo, C., Xu, Y., Zhu, Y., Liu, Y., Zheng, S., Liu, Y., Langrock, A. and Wang, C., 2013. Selenium@Mesoporous Carbon Composite with Superior Lithium and Sodium Storage Capacity. *ACS Nano*, 7 (9), 8003–8010.
- Lv, W., Wang, Z., Cao, H., Sun, Y., Zhang, Y. and Sun, Z., 2018. A Critical Review and Analysis on the Recycling of Spent Lithium-Ion Batteries. *ACS Sustainable Chemistry & Engineering*, 6 (2), 1504–1521.
- Lyu, Y., Wu, X., Wang, K., Feng, Z., Cheng, T., Liu, Y., Wang, M., Chen, R., Xu, L., Zhou, J., Lu, Y. and Guo, B., 2021. An Overview on the Advances of LiCoO₂ Cathodes for Lithium-Ion Batteries. *Advanced Energy Materials*, 11 (2), 2000982.
- Ma, J., Sung, J., Hong, J., Chae, S., Kim, N., Choi, S.-H., Nam, G., Son, Y., Kim, S. Y., Ko, M. and Cho, J., 2019. Towards maximized volumetric capacity via pore-coordinated design for large-volume-change lithium-ion battery anodes. *Nature Communications*, 10 (1), 475.
- Ma, X., Chen, M., Chen, B., Meng, Z. and Wang, Y., 2019. High-Performance Graphite Recovered from Spent Lithium-Ion Batteries. *ACS Sustainable Chemistry & Engineering*, 7 (24), 19732–19738.
- Makuza, B., Tian, Q., Guo, X., Chattopadhyay, K. and Yu, D., 2021a. Pyrometallurgical options for recycling spent lithium-ion batteries: A comprehensive review. *Journal of Power Sources*, 491, 229622.
- Makuza, B., Tian, Q., Guo, X., Chattopadhyay, K. and Yu, D., 2021b. Pyrometallurgical options for recycling spent lithium-ion batteries: A comprehensive review. *Journal of Power Sources*, 491, 229622.
- Manthiram, A., 2020. A reflection on lithium-ion battery cathode chemistry. *Nature Communications* [online], 11 (1550). Available from: <https://doi.org/10.1038/s41467-020-15355-0>.
- Martha, S. K., Haik, O., Zinigrad, E., Exnar, I., Drezen, T., Miners, J. H. and Aurbach, D., 2011. On the Thermal Stability of Olivine Cathode Materials for Lithium-Ion Batteries. *Journal of The Electrochemical Society* [online], 158 (10), A1115. Available from: <https://iopscience.iop.org/article/10.1149/1.3622849>.

- Masquelier, C. and Croguennec, L., 2013. Polyanionic (Phosphates, Silicates, Sulfates) Frameworks as Electrode Materials for Rechargeable Li (or Na) Batteries. *Chemical Reviews*, 113 (8), 6552–6591.
- Matsushima, J. T., Trivinho-Strixino, F. and Pereira, E. C., 2006. Investigation of cobalt deposition using the electrochemical quartz crystal microbalance. *Electrochimica Acta*, 51 (10), 1960–1966.
- Mehmood, T., Khan, B. S., Mukhtar, A. and Tan, M., 2015. Influence of bath temperature and pH on the structure of electrodeposited cobalt nanowires. *International Journal of Materials Research*, 106 (9), 957–961.
- Meng, F., Liu, Q., Kim, R., Wang, J., Liu, G. and Ghahreman, A., 2020. Selective recovery of valuable metals from industrial waste lithium-ion batteries using citric acid under reductive conditions: Leaching optimization and kinetic analysis. *Hydrometallurgy*, 191, 105160.
- Meshram, P., Abhilash, Pandey, B. D., Mankhand, T. R. and Deveci, H., 2016a. Comparison of Different Reductants in Leaching of Spent Lithium Ion Batteries. *JOM*, 68 (10), 2613–2623.
- Meshram, P., Abhilash, Pandey, B. D., Mankhand, T. R. and Deveci, H., 2016b. Comparison of Different Reductants in Leaching of Spent Lithium Ion Batteries. *JOM*, 68 (10), 2613–2623.
- Meshram, P., Pandey, B. D. and Mankhand, T. R., 2014. Extraction of lithium from primary and secondary sources by pre-treatment, leaching and separation: A comprehensive review. *Hydrometallurgy*, 150, 192–208.
- Meshram, P., Pandey, B. D. and Mankhand, T. R., 2015a. Hydrometallurgical processing of spent lithium ion batteries (LIBs) in the presence of a reducing agent with emphasis on kinetics of leaching. *Chemical Engineering Journal*, 281, 418–427.
- Meshram, P., Pandey, B. D. and Mankhand, T. R., 2015b. Recovery of valuable metals from cathodic active material of spent lithium ion batteries: Leaching and kinetic aspects. *Waste Management*, 45, 306–313.
- Mesnier, A. and Manthiram, A., 2020. Synthesis of LiNiO₂ at Moderate Oxygen Pressure and Long-Term Cyclability in Lithium-Ion Full Cells. *ACS Applied Materials & Interfaces*, 12 (47), 52826–52835.
- Miao, Y., Hynan, P., von Jouanne, A. and Yokochi, A., 2019. Current Li-Ion Battery Technologies in Electric Vehicles and Opportunities for Advancements. *Energies*, 12 (6), 1074.

- Mishra, D., Kim, D.-J., Ralph, D. E., Ahn, J.-G. and Rhee, Y.-H., 2008. Bioleaching of metals from spent lithium ion secondary batteries using *Acidithiobacillus ferrooxidans*. *Waste Management*, 28 (2), 333–338.
- Moats, M. S. and Davenport, W. G., 2014. Nickel and Cobalt Production. *In: Treatise on Process Metallurgy*. Elsevier, 625–669.
- Moradi, M., Vasseghian, Y., Khataee, A., Kobya, M., Arabzade, H. and Dragoi, E.-N., 2020. Service life and stability of electrodes applied in electrochemical advanced oxidation processes: A comprehensive review. *Journal of Industrial and Engineering Chemistry*, 87, 18–39.
- Mueller, T., Hautier, G., Jain, A. and Ceder, G., 2011. Evaluation of Tavorite-Structured Cathode Materials for Lithium-Ion Batteries Using High-Throughput Computing. *Chemistry of Materials*, 23 (17), 3854–3862.
- Mulaudzi, N. and Kotze, M. H., 2013. Direct cobalt electrowinning as an alternative to intermediate cobalt mixed hydroxide product. *In: The Southern African Institute of Mining and Metallurgy Base Metals Conference*. Mpumalanga: The Southern African Institute of Mining and Metallurgy .
- Murphy, D. W. and Trumbore, F. A., 1976. The Chemistry of TiS_3 and $NbSe_3$ Cathodes. *Journal of The Electrochemical Society* [online], 123 (7), 960–964. Available from: <https://iopscience.iop.org/article/10.1149/1.2133012>.
- Myoung, J., Jung, Y., Lee, J. and Tak, Y., 2002. Cobalt oxide preparation from waste $LiCoO_2$ by electrochemical–hydrothermal method. *Journal of Power Sources*, 112 (2), 639–642.
- Myung, N. V, Park, D.-Y., Yoo, B.-Y. and Sumodjo, P. T. A., 2003. Development of electroplated magnetic materials for MEMS. *Journal of Magnetism and Magnetic Materials*, 265 (2), 189–198.
- Nan, C., Lin, Z., Liao, H., Song, M.-K., Li, Y. and Cairns, E. J., 2014. Durable Carbon-Coated Li_2S Core–Shell Spheres for High Performance Lithium/Sulfur Cells. *Journal of the American Chemical Society*, 136 (12), 4659–4663.
- Nan, J., Han, D. and Zuo, X., 2005. Recovery of metal values from spent lithium-ion batteries with chemical deposition and solvent extraction. *Journal of Power Sources*, 152, 278–284.
- Nasara, R. N., Ma, W., Tsujimoto, S., Inoue, Y., Yokoyama, Y., Kondo, Y., Miyazaki, K., Miyahara, Y., Fukutsuka, T., Lin, S. and Abe, T., 2021. Electrochemical properties of surface-modified hard carbon electrodes for lithium-ion batteries. *Electrochimica Acta*, 379, 138175.

- Nayaka, G. P., Pai, K. v., Santhosh, G. and Manjanna, J., 2016a. Dissolution of cathode active material of spent Li-ion batteries using tartaric acid and ascorbic acid mixture to recover Co. *Hydrometallurgy*, 161, 54–57.
- Nayaka, G. P., Pai, K. V., Santhosh, G. and Manjanna, J., 2016b. Dissolution of cathode active material of spent Li-ion batteries using tartaric acid and ascorbic acid mixture to recover Co. *Hydrometallurgy*, 161, 54–57.
- Nayaka, G., Pai, K., Manjanna, J. and Keny, S., 2016. Use of mild organic acid reagents to recover the Co and Li from spent Li-ion batteries. *Waste Management*, 51, 234–238.
- Nayaka, G., Pai, K., Santhosh, G. and Manjanna, J., 2016c. Dissolution of cathode active material of spent Li-ion batteries using tartaric acid and ascorbic acid mixture to recover Co. *Hydrometallurgy*, 161, 54–57.
- Nayaka, G., Pai, K., Santhosh, G. and Manjanna, J., 2016d. Recovery of cobalt as cobalt oxalate from spent lithium ion batteries by using glycine as leaching agent. *Journal of Environmental Chemical Engineering*, 4 (2), 2378–2383.
- Nguyen, T. H. and Lee, M. S., 2016. A review on the separation of molybdenum, tungsten, and vanadium from leach liquors of diverse resources by solvent extraction. *Geosystem Engineering*, 19 (5), 247–259.
- Nishi, Y., 2001. Lithium ion secondary batteries; past 10 years and the future. *Journal of Power Sources*, 100 (1–2), 101–106.
- Nishimura, S., Kobayashi, G., Ohoyama, K., Kanno, R., Yashima, M. and Yamada, A., 2008. Experimental visualization of lithium diffusion in Li_xFePO_4 . *Nature Materials*, 7 (9), 707–711.
- Nitta, N., Wu, F., Lee, J. T. and Yushin, G., 2015. Li-ion battery materials: present and future. *Materials Today*, 18 (5), 252–264.
- Niu, Z., Zou, Y., Xin, B., Chen, S., Liu, C. and Li, Y., 2014. Process controls for improving bioleaching performance of both Li and Co from spent lithium ion batteries at high pulp density and its thermodynamics and kinetics exploration. *Chemosphere*, 109, 92–98.
- Noh, H.-J., Youn, S., Yoon, C. S. and Sun, Y.-K., 2013. Comparison of the structural and electrochemical properties of layered $\text{Li}[\text{Ni}_x\text{Co}_y\text{Mn}_z]\text{O}_2$ ($x = 1/3, 0.5, 0.6, 0.7, 0.8$ and 0.85) cathode material for lithium-ion batteries. *Journal of Power Sources*, 233, 121–130.
- Nusheh, M. and Yoozbashizadeh, H., 2009. Study on electrowinning of cobalt by cyclic voltammetry technique. *Iranian Journal of Materials Science & Engineering V*, 7 (2).

- Ohzuku, T., Ueda, A. and Nagayama, M., 1993. Electrochemistry and Structural Chemistry of LiNiO₂ (R3m) for 4 Volt Secondary Lithium Cells. *Journal of The Electrochemical Society* [online], 140 (7), 1862–1870. Available from: <https://iopscience.iop.org/article/10.1149/1.2220730>.
- de Oliveira Demarco, J., Stefanello Cadore, J., da Silveira de Oliveira, F., Hiromitsu Tanabe, E. and Assumpção Bertuol, D., 2019. Recovery of metals from spent lithium-ion batteries using organic acids. *Hydrometallurgy*, 190, 105169.
- Oluwatosin Abegunde, O., Titilayo Akinlabi, E., Philip Oladijo, O., Akinlabi, S. and Uchenna Ude, A., 2019. Overview of thin film deposition techniques. *AIMS Materials Science*, 6 (2), 174–199.
- Ordoñez, J., Gago, E. J. and Girard, A., 2016. Processes and technologies for the recycling and recovery of spent lithium-ion batteries. *Renewable and Sustainable Energy Reviews*, 60, 195–205.
- Othman, E. A., van der Ham, A. G. J., Miedema, H. and Kersten, S. R. A., 2020. Recovery of metals from spent lithium-ion batteries using ionic liquid [P8888][Oleate]. *Separation and Purification Technology*, 252, 117435.
- Oumellal, Y., Rougier, A., Nazri, G. A., Tarascon, J.-M. and Aymard, L., 2008. Metal hydrides for lithium-ion batteries. *Nature Materials*, 7 (11), 916–921.
- Pan, Y., Zhu, T. and He, Z., 2019. Energy advantage of anode electrode rotation over anolyte recirculation for operating a tubular microbial fuel cell. *Electrochemistry Communications*, 106, 106529.
- Pant, D. and Dolker, T., 2017. Green and facile method for the recovery of spent Lithium Nickel Manganese Cobalt Oxide (NMC) based Lithium ion batteries. *Waste Management*, 60, 689–695.
- Park, D.-Y., Myung, N. V., Schwartz, M. and Nobe, K., 2002. Nanostructured magnetic CoNiP electrodeposits: structure–property relationships. *Electrochimica Acta*, 47 (18), 2893–2900.
- Park, Y., Choi, N.-S., Park, S., Woo, S. H., Sim, S., Jang, B. Y., Oh, S. M., Park, S., Cho, J. and Lee, K. T., 2013. Si-Encapsulating Hollow Carbon Electrodes via Electroless Etching for Lithium-Ion Batteries. *Advanced Energy Materials*, 3 (2), 206–212.
- Du Pasquier, A., Plitz, I., Menocal, S. and Amatucci, G., 2003. A comparative study of Li-ion battery, supercapacitor and nonaqueous asymmetric hybrid devices for automotive applications. *Journal of Power Sources*, 115 (1), 171–178.

- Peng, C., Hamuyuni, J., Wilson, B. P. and Lundström, M., 2018. Selective reductive leaching of cobalt and lithium from industrially crushed waste Li-ion batteries in sulfuric acid system. *Waste Management*, 76, 582–590.
- Peter E Roth and Doughty Dan, 2012. A General Discussion on Li-ion Battery Safety. *Electrochem. Soc. Interface*, 2012, pp. 37–44.
- Phadke, S., Cao, M. and Anouti, M., 2018. Approaches to Electrolyte Solvent Selection for Poly-Anthraquinone Sulfide Organic Electrode Material. *ChemSusChem*, 11 (5), 965–974.
- Phuc Anh LE, 2019. The recyclability of lithium-ion battery materials. [online]. The University of Queensland, St Lucia. Available from: <https://core.ac.uk/download/pdf/286812476.pdf> [Accessed 21 Jan 2023].
- Piątek, J., Afyon, S., Budnyak, T. M., Budnyk, S., Sipponen, M. H. and Slabon, A., 2021. Sustainable Li-Ion Batteries: Chemistry and Recycling. *Advanced Energy Materials*, 11 (43), 2003456.
- Pinna, E. G., Ruiz, M. C., Ojeda, M. W. and Rodriguez, M. H., 2017a. Cathodes of spent Li-ion batteries: Dissolution with phosphoric acid and recovery of lithium and cobalt from leach liquors. *Hydrometallurgy*, 167, 66–71.
- Pinna, E. G., Ruiz, M. C., Ojeda, M. W. and Rodriguez, M. H., 2017b. Cathodes of spent Li-ion batteries: Dissolution with phosphoric acid and recovery of lithium and cobalt from leach liquors. *Hydrometallurgy*, 167, 66–71.
- Pradhan, N., Singh, P., Tripathy, B. C. and Das, S. C., 2001. Electrowinning of cobalt from acidic sulphate solutions—effect of chloride ion. *Minerals Engineering*, 14 (7), 775–783.
- Qi, Y., Guo, H., Hector, L. G. and Timmons, A., 2010. Threefold Increase in the Young's Modulus of Graphite Negative Electrode during Lithium Intercalation. *Journal of The Electrochemical Society*, 157 (5), A558.
- Qian, J., Qiao, D., Ai, X., Cao, Y. and Yang, H., 2012. Reversible 3-Li storage reactions of amorphous phosphorus as high capacity and cycling-stable anodes for Li-ion batteries. *Chemical Communications*, 48 (71), 8931.
- Rafsanjani-Abbasi, A., Rahimi, E., Shalchian, H., Vahdati-Khaki, J., Babakhani, A., Hosseinpour, S. and Davoodi, A., 2018. Recycled Cobalt from Spent Li-ion Batteries as a Superhydrophobic Coating for Corrosion Protection of Plain Carbon Steel. *Materials*, 12 (1), 90.
- Ramanan, A., 2019. Nobel Prize in Chemistry 2019. *Resonance*, 24 (12), 1381–1395.
- Rao, C. R. K. and Pushpavanam, M., 2001. Electroless deposition of platinum on titanium substrates. *Materials Chemistry and Physics*, 68 (1–3), 62–65.

- Recham, N., Chotard, J.-N., Dupont, L., Delacourt, C., Walker, W., Armand, M. and Tarascon, J.-M., 2010. A 3.6 V lithium-based fluorosulphate insertion positive electrode for lithium-ion batteries. *Nature Materials*, 9 (1), 68–74.
- Reddy, M. V., Mauger, A., Julien, C. M., Paoletta, A. and Zaghbi, K., 2020. Brief History of Early Lithium-Battery Development. *Materials*, 13 (8), 1884.
- Reddy, M. V., Subba Rao, G. V. and Chowdari, B. V. R., 2013. Metal oxides and oxysalts as anode materials for Li-Ion batteries. *Chemical Reviews*, 113 (7), 5364–5457.
- Ren, G., Xiao, S., Xie, M., Pan, B., Fan, Y., Wang, F. and Xia, X., 2016. *Advances in Molten Slags, Fluxes, and Salts: Proceedings of the 10th International Conference on Molten Slags, Fluxes and Salts 2016*. Cham: Springer International Publishing.
- Ren, W.-X., Li, P.-J., Geng, Y. and Li, X.-J., 2009. Biological leaching of heavy metals from a contaminated soil by *Aspergillus niger*. *Journal of Hazardous Materials*, 167 (1–3), 164–169.
- Reyes-Valderrama, Ma., Salinas-Rodríguez, E., Montiel-Hernández, J., Rivera-Landero, I., Cerecedo-Sáenz, E., Hernándezvila, J. and Arenas-Flores, A., 2017. Urban Mining and Electrochemistry: Cyclic Voltammetry Study of Acidic Solutions from Electronic Wastes (Printed Circuit Boards) for Recovery of Cu, Zn, and Ni. *Metals*, 7 (2), 55.
- Sa, Q., Gratz, E., He, M., Lu, W., Apelian, D. and Wang, Y., 2015. Synthesis of high performance LiNi_{1/3}Mn_{1/3}Co_{1/3}O₂ from lithium ion battery recovery stream. *Journal of Power Sources*, 282, 140–145.
- Saeki, S., Lee, J., Zhang, Q. and Saito, F., 2004. Co-grinding LiCoO₂ with PVC and water leaching of metal chlorides formed in ground product. *International Journal of Mineral Processing*, 74, S373–S378.
- Sahu, S. and Devi, N., 2023. Two-step leaching of spent lithium-ion batteries and effective regeneration of critical metals and graphitic carbon employing hexuronic acid. *RSC Advances*, 13 (11), 7193–7205.
- Santos, J. S., Matos, R., Trivinho-Strixino, F. and Pereira, E. C., 2007. Effect of temperature on Co electrodeposition in the presence of boric acid. *Electrochimica Acta*, 53 (2), 644–649.
- Schalenbach, M., Durmus, Y. E., Tempel, H., Kungl, H. and Eichel, R.-A., 2022. Ion transport and limited currents in supporting electrolytes and ionic liquids. *Scientific Reports*, 12 (1), 6215.
- Sergio, B. and Stefania, 2021. Nanotechnology for Sustainable Energy. *American Chemical Society*, 1140.

- Seyed Mohammad Khosh Koo Sany, 2009. Optimisation of Influential Factors in Electrowinning of Tellurium by Means of PLS Modelling. Lulea University of Technology, Lulea.
- Shakibania, S., Mahmoudi, A. and Mokmeli, M., 2022. Separation of vanadium and iron from the steelmaking slag convertor using Aliquat 336 and D2EHPA: Effect of the aqueous species and the extractant type. *Minerals Engineering*, 181, 107521.
- AL Shaqsi, A. Z., Sopian, K. and Al-Hinai, A., 2020. Review of energy storage services, applications, limitations, and benefits. *Energy Reports*, 6, 288–306.
- Sharma, A. and Das, J., 2019. Small molecules derived carbon dots: Synthesis and applications in sensing, catalysis, imaging, and biomedicine. *Journal of Nanobiotechnology*.
- Sharma, I. G., Alex, P., Bidaye, A. C. and Suri, A. K., 2005a. Electrowinning of cobalt from sulphate solutions. *Hydrometallurgy*, 80 (1–2), 132–138.
- Sharma, I. G., Alex, P., Bidaye, A. C. and Suri, A. K., 2005b. Electrowinning of cobalt from sulphate solutions. *Hydrometallurgy*, 80 (1–2), 132–138.
- Shin, S. M., Kim, N. H., Sohn, J. S., Yang, D. H. and Kim, Y. H., 2005. Development of a metal recovery process from Li-ion battery wastes. *Hydrometallurgy*, 79 (3–4), 172–181.
- Shuguang Zhu, Wenzhi He, Guangming Li, Xu Zhou, Juwen Huang and Xiaojun Zhang, 2011. Recovering copper from spent lithium ion battery by a mechanical separation process. *In: 2011 International Conference on Materials for Renewable Energy & Environment*. IEEE, 1008–1012.
- Sleutels, T. H. J. A., Lodder, R., Hamelers, H. V. M. and Buisman, C. J. N., 2009. Improved performance of porous bio-anodes in microbial electrolysis cells by enhancing mass and charge transport. *International Journal of Hydrogen Energy*, 34 (24), 9655–9661.
- Song, D., Wang, X., Nie, H., Shi, H., Wang, D., Guo, F., Shi, X. and Zhang, L., 2014. Heat treatment of LiCoO₂ recovered from cathode scraps with solvent method. *Journal of Power Sources*, 249, 137–141.
- Song, J. Y., Wang, Y. Y. and Wan, C. C., 1999. Review of gel-type polymer electrolytes for lithium-ion batteries. *Journal of Power Sources*, 77 (2), 183–197.
- Song, M.-S., Kim, R.-H., Baek, S.-W., Lee, K.-S., Park, K. and Benayad, A., 2014. Is Li₄Ti₅O₁₂ a solid-electrolyte-interphase-free electrode material in Li-ion batteries? Reactivity between the Li₄Ti₅O₁₂ electrode and electrolyte. *J. Mater. Chem. A*, 2 (3), 631–636.

- Song, Y. and Zhao, Z., 2018. Recovery of lithium from spent lithium-ion batteries using precipitation and electrodialysis techniques. *Separation and Purification Technology*, 206, 335–342.
- South African Government, 1999. *National Environmental Management Act 107 of 1998*. Government Gazette.
- South African Government, 2009. *Consumer Protection Act 68 of 20* [online]. Government Gazette. Available from: chrome-extension://efaidnbmnnnibpcajpcglclefindmkaj/https://www.gov.za/sites/default/files/gcis_document/201409/321864670.pdf [Accessed 13 Aug 2024].
- Steward, D., Mayyas, A. and Mann, M., 2019. Economics and Challenges of Li-Ion Battery Recycling from End-of-Life Vehicles. *Procedia Manufacturing*, 33, 272–279.
- Su, X., Wu, Q., Li, J., Xiao, X., Lott, A., Lu, W., Sheldon, B. W. and Wu, J., 2014. Silicon-Based Nanomaterials for Lithium-Ion Batteries: A Review. *Advanced Energy Materials*, 4 (1), 1300882.
- Sun, C., Xu, L., Chen, X., Qiu, T. and Zhou, T., 2018. Sustainable recovery of valuable metals from spent lithium-ion batteries using DL-malic acid: Leaching and kinetics aspect. *Waste Management & Research: The Journal for a Sustainable Circular Economy*, 36 (2), 113–120.
- Sun, L. and Qiu, K., 2011. Vacuum pyrolysis and hydrometallurgical process for the recovery of valuable metals from spent lithium-ion batteries. *Journal of Hazardous Materials*, 194, 378–384.
- Sun, L. and Qiu, K., 2012. Organic oxalate as leachant and precipitant for the recovery of valuable metals from spent lithium-ion batteries. *Waste Management*, 32 (8), 1575–1582.
- Sun, Y. K., Yoon, C. S. and Oh, I. H., 2003. Surface structural change of ZnO-coated LiNi_{0.5}Mn_{1.5}O₄ spinel as 5 V cathode materials at elevated temperatures. *Electrochimica Acta*, 48 (5), 503–506.
- Sun, Y.-K., Myung, S.-T., Park, B.-C., Prakash, J., Belharouak, I. and Amine, K., 2009. High-energy cathode material for long-life and safe lithium batteries. *Nature Materials*, 8 (4), 320–324.
- Sun, Z., Cao, H., Xiao, Y., Sietsma, J., Jin, W., Agterhuis, H. and Yang, Y., 2017. Toward Sustainability for Recovery of Critical Metals from Electronic Waste: The Hydrochemistry Processes. *ACS Sustainable Chemistry & Engineering*, 5 (1), 21–40.
- Suryanarayana, C., 2016. *Microstructure: An Introduction*. *Aerospace Materials and Material Technologies*:

- Swain, B., Jeong, J., Lee, J., Lee, G.-H. and Sohn, J.-S., 2007. Hydrometallurgical process for recovery of cobalt from waste cathodic active material generated during manufacturing of lithium ion batteries. *Journal of Power Sources*, 167 (2), 536–544.
- Takacova, Z., Havlik, T., Kukurugya, F. and Orac, D., 2016. Cobalt and lithium recovery from active mass of spent Li-ion batteries: Theoretical and experimental approach. *Hydrometallurgy*, 163, 9–17.
- Talan, D. and Huang, Q., 2022. A review study of rare Earth, Cobalt, Lithium, and Manganese in Coal-based sources and process development for their recovery. *Minerals Engineering*, 189, 107897.
- Tawonezvi, T., Nomnqa, M., Petrik, L. and Bladergroen, B. J., 2023. Recovery and Recycling of Valuable Metals from Spent Lithium-Ion Batteries: A Comprehensive Review and Analysis. *Energies*, 16 (3), 1365.
- Thackeray, M. M. and Amine, K., 2021. LiMn₂O₄ spinel and substituted cathodes. *Nature Energy*, 6 (5), 566–566.
- Tian, L., Xu, J. and Qiang, C., 2011. The electrodeposition behaviors and magnetic properties of Ni–Co films. *Applied Surface Science*, 257 (10), 4689–4694.
- Tycorun, 2021. *What is a lithium-ion battery? How do lithium-ion batteries work?* [online]. Available from: <https://www.tycorun.com/blogs/news/what-is-lithium-ion-battery-how-do-lithium-ion-batteries-work> [Accessed 20 Feb 2024].
- United States Geological Survey, 2020. *Mineral Commodity Summaries 2020*.
- Urbańska, W., 2020. Recovery of Co, Li, and Ni from Spent Li-Ion Batteries by the Inorganic and/or Organic Reducer Assisted Leaching Method. *Minerals*, 10 (6), 555.
- Velázquez-Martínez, Valio, Santasalo-Aarnio, Reuter and Serna-Guerrero, 2019. A Critical Review of Lithium-Ion Battery Recycling Processes from a Circular Economy Perspective. *Batteries*, 5 (4), 68.
- Vieceli, N., Benjamasutin, P., Promphan, R., Hellström, P., Paulsson, M. and Petranikova, M., 2023. Recycling of Lithium-Ion Batteries: Effect of Hydrogen Peroxide and a Dosing Method on the Leaching of LCO, NMC Oxides, and Industrial Black Mass. *ACS Sustainable Chemistry & Engineering*, 11 (26), 9662–9673.
- Virolainen, S., Fallah Fini, M., Laitinen, A. and Sainio, T., 2017. Solvent extraction fractionation of Li-ion battery leachate containing Li, Ni, and Co. *Separation and Purification Technology*, 179, 274–282.

- Vu, N. H., Dao, V.-D., Vu, H. H. T., Van Noi, N., Tran, D. T., Ha, M. N. and Pham, T.-D., 2021. Hydrothermal Synthesis of Li_2MnO_3 -Stabilized LiMnO_2 as a Cathode Material for Li-Ion Battery. *Journal of Nanomaterials*, 2021, 1–6.
- Wagemaker, M., Simon, D. R., Kelder, E. M., Schoonman, J., Ringpfeil, C., Haake, U., Lützenkirchen-Hecht, D., Frahm, R. and Mulder, F. M., 2006. A Kinetic Two-Phase and Equilibrium Solid Solution in Spinel $\text{Li}_{4+x}\text{Ti}_5\text{O}_{12}$. *Advanced Materials*, 18 (23), 3169–3173.
- Wang, F., Robert, R., Chernova, N. A., Pereira, N., Omenya, F., Badway, F., Hua, X., Ruotolo, M., Zhang, R., Wu, L., Volkov, V., Su, D., Key, B., Whittingham, M. S., Grey, C. P., Amatucci, G. G., Zhu, Y. and Graetz, J., 2011. Conversion Reaction Mechanisms in Lithium Ion Batteries: Study of the Binary Metal Fluoride Electrodes. *Journal of the American Chemical Society*, 133 (46), 18828–18836.
- Wang, F., Sun, R., Xu, J., Chen, Z. and Kang, M., 2016. Recovery of cobalt from spent lithium ion batteries using sulphuric acid leaching followed by solid–liquid separation and solvent extraction. *RSC Advances*, 6 (88), 85303–85311.
- Wang, H., Qin, S., Yang, X., Fei, G., Tian, M., Shao, Y. and Zhu, K., 2018. A waterborne uniform graphene-poly(urethane-acrylate) complex with enhanced anticorrosive properties enabled by ionic interaction. *Chemical Engineering Journal*, 351, 939–951.
- Wang, H., Wu, Z., Wang, M., Cheng, Y.-J., Gao, J. and Xia, Y., 2024. “Acid + Oxidant” Treatment Enables Selective Extraction of Lithium from Spent NCM523 Positive Electrode. *Batteries*, 10 (6), 179.
- Wang, J., Chen, M., Chen, H., Luo, T. and Xu, Z., 2012. Leaching Study of Spent Li-ion Batteries. *Procedia Environmental Sciences*, 16, 443–450.
- Wang, J., Chen-Wiegart, Y. K. and Wang, J., 2014. In Situ Three-Dimensional Synchrotron X-Ray Nanotomography of the (De)lithiation Processes in Tin Anodes. *Angewandte Chemie International Edition*, 53 (17), 4460–4464.
- Wang, R., He, X., He, L., Wang, F., Xiao, R., Gu, L., Li, H. and Chen, L., 2013. Atomic Structure of Li_2MnO_3 after Partial Delithiation and Re-Lithiation. *Advanced Energy Materials*, 3 (10), 1358–1367.
- Wang, S., 2006. Cobalt—Its recovery, recycling, and application. *JOM*, 58 (10), 47–50.
- Wang, Y., Sun, Q., Zhao, Q., Cao, J. and Ye, S., 2011. Rechargeable lithium/iodine battery with superior high-rate capability by using iodine–carbon composite as cathode. *Energy & Environmental Science*, 4 (10), 3947.

- Wei, Y., He, J., Zhang, J., Ou, M., Guo, Y., Chen, J., Zeng, C., Xu, J., Han, J., Zhai, T. and Li, H., 2023. Seamlessly Merging the Capacity of P into Sb at Same Voltage with Maintained Superior Cycle Stability and Low-temperature Performance for Li-ion Batteries. *Energy & Environmental Materials*, 6 (2).
- Werner, D., Peuker, U. A. and Mütze, T., 2020. Recycling Chain for Spent Lithium-Ion Batteries. *Metals*, 10 (3), 316.
- Whittingham, M. S., 2004. Lithium Batteries and Cathode Materials. *Chemical Reviews*, 104 (10), 4271–4302.
- Whitworth, A. J., Forbes, E., Verster, I., Jokovic, V., Awatey, B. and Parbhakar-Fox, A., 2022. Review on advances in mineral processing technologies suitable for critical metal recovery from mining and processing wastes. *Cleaner Engineering and Technology*, 7, 100451.
- Williard, N., He, W., Hendricks, C. and Pecht, M., 2013. Lessons Learned from the 787 Dreamliner Issue on Lithium-Ion Battery Reliability. *Energies*, 6 (9), 4682–4695.
- Wu, F., Wang, Z., Li, X., Guo, H., Yue, P., Xiong, X., He, Z. and Zhang, Q., 2012. Characterization of spherical-shaped $\text{Li}_4\text{Ti}_5\text{O}_{12}$ prepared by spray drying. *Electrochimica Acta*, 78, 331–339.
- Wu, J., Zheng, M., Liu, T., Wang, Y., Liu, Y., Nai, J., Zhang, L., Zhang, S. and Tao, X., 2023. Direct recovery: A sustainable recycling technology for spent lithium-ion battery. *Energy Storage Materials*, 54, 120–134.
- Xiao, J., Li, J. and Xu, Z., 2017. Novel Approach for in Situ Recovery of Lithium Carbonate from Spent Lithium Ion Batteries Using Vacuum Metallurgy. *Environmental Science & Technology*, 51 (20), 11960–11966.
- Xiao, W., Liu, X. and Zhao, Z., 2020. Kinetics of nickel leaching from low-nickel matte in sulfuric acid solution under atmospheric pressure. *Hydrometallurgy*, 194, 105353.
- Xin, B., Zhang, D., Zhang, X., Xia, Y., Wu, F., Chen, S. and Li, L., 2009. Bioleaching mechanism of Co and Li from spent lithium-ion battery by the mixed culture of acidophilic sulfur-oxidizing and iron-oxidizing bacteria. *Bioresource Technology*, 100 (24), 6163–6169.
- Xin, Y., Guo, X., Chen, S., Wang, J., Wu, F. and Xin, B., 2016. Bioleaching of valuable metals Li, Co, Ni and Mn from spent electric vehicle Li-ion batteries for the purpose of recovery. *Journal of Cleaner Production*, 116, 249–258.
- Xu, C., Dai, Q., Gaines, L., Hu, M., Tukker, A. and Steubing, B., 2020. Future material demand for automotive lithium-based batteries. *Communications Materials*, 1 (1), 99.

- Xu, Y., Song, D., Li, L., An, C., Wang, Y., Jiao, L. and Yuan, H., 2014. A simple solvent method for the recovery of Li_xCoO_2 and its applications in alkaline rechargeable batteries. *Journal of Power Sources*, 252, 286–291.
- Xue, X., Xu, Y. and Ma, X., 2020. Elevated Energy Density and Cyclic Stability of LiVPO_4F Cathode Material for High-rate Lithium Ion Batteries. *ACS Applied Energy Materials*, 3 (4), 3553–3561.
- Yabuuchi, N. and Ohzuku, T., 2003. Novel lithium insertion material of $\text{LiCo}_{1/3}\text{Ni}_{1/3}\text{Mn}_{1/3}\text{O}_2$ for advanced lithium-ion batteries. *Journal of Power Sources*, 119–121, 171–174.
- Yang, C.-P., Xin, S., Yin, Y.-X., Ye, H., Zhang, J. and Guo, Y.-G., 2013. An Advanced Selenium-Carbon Cathode for Rechargeable Lithium-Selenium Batteries. *Angewandte Chemie International Edition*, 52 (32), 8363–8367.
- Yang, T., Luo, D., Yu, A. and Chen, Z., 2023. Enabling Future Closed-loop Recycling of Spent Lithium-ion Batteries: Direct Cathode Regeneration. *Advanced Materials*.
- Yang, Y., Huang, G., Xie, M., Xu, S. and He, Y., 2016. Synthesis and performance of spherical $\text{LiNi}_x\text{Co}_y\text{Mn}_{1-x-y}\text{O}_2$ regenerated from nickel and cobalt scraps. *Hydrometallurgy*, 165, 358–369.
- Yang, Y., Huang, G., Xu, S., He, Y. and Liu, X., 2016. Thermal treatment process for the recovery of valuable metals from spent lithium-ion batteries. *Hydrometallurgy*, 165, 390–396.
- Yang, Y., Meng, X., Cao, H., Lin, X., Liu, C., Sun, Y., Zhang, Y. and Sun, Z., 2018. Selective recovery of lithium from spent lithium iron phosphate batteries: a sustainable process. *Green Chemistry*, 20 (13), 3121–3133.
- Yang, Y., Zheng, X., Cao, H., Zhao, C., Lin, X., Ning, P., Zhang, Y., Jin, W. and Sun, Z., 2017. A Closed-Loop Process for Selective Metal Recovery from Spent Lithium Iron Phosphate Batteries through Mechanochemical Activation. *ACS Sustainable Chemistry & Engineering*, 5 (11), 9972–9980.
- Yao, L., Yao, H., Xi, G. and Feng, Y., 2016. Recycling and synthesis of $\text{LiNi}_{1/3}\text{Co}_{1/3}\text{Mn}_{1/3}\text{O}_2$ from waste lithium-ion batteries using d,l -malic acid. *RSC Advances*, 6 (22), 17947–17954.
- Younesi, R., Veith, G. M., Johansson, P., Edström, K. and Vegge, T., 2015. Lithium salts for advanced lithium batteries: Li -metal, Li-O_2 , and Li-S . *Energy & Environmental Science*, 8 (7), 1905–1922.

- Yu, H.-C., Ling, C., Bhattacharya, J., Thomas, J. C., Thornton, K. and Van der Ven, A., 2014. Designing the next generation high capacity battery electrodes. *Energy & Environmental Science*, 7 (5), 1760.
- Yu, S.-H., Feng, X., Zhang, N., Seok, J. and Abruña, H. D., 2018. Understanding Conversion-Type Electrodes for Lithium Rechargeable Batteries. *Accounts of Chemical Research*, 51 (2), 273–281.
- Zech, N., Podlaha, E. J. and Landolt, D., 1999. Anomalous Codeposition of Iron Group Metals: I. Experimental Results. *Journal of The Electrochemical Society*, 146 (8), 2886–2891.
- Zeng, G., Luo, S., Deng, X., Li, L. and Au, C., 2013. Influence of silver ions on bioleaching of cobalt from spent lithium batteries. *Minerals Engineering*, 49, 40–44.
- Zeng, X., Li, J. and Shen, B., 2015a. Novel approach to recover cobalt and lithium from spent lithium-ion battery using oxalic acid. *Journal of Hazardous Materials*, 295, 112–118.
- Zeng, X., Li, J. and Shen, B., 2015b. Novel approach to recover cobalt and lithium from spent lithium-ion battery using oxalic acid. *Journal of Hazardous Materials*, 295, 112–118.
- Zeng, X., Li, J. and Singh, N., 2014. Recycling of Spent Lithium-Ion Battery: A Critical Review. *Critical Reviews in Environmental Science and Technology*, 44 (10), 1129–1165.
- Zhang, G., Du, Z., He, Y., Wang, H., Xie, W. and Zhang, T., 2019. A Sustainable Process for the Recovery of Anode and Cathode Materials Derived from Spent Lithium-Ion Batteries. *Sustainability*, 11 (8), 2363.
- Zhang, G., Yuan, X., He, Y., Wang, H., Zhang, T. and Xie, W., 2021. Recent advances in pretreating technology for recycling valuable metals from spent lithium-ion batteries. *Journal of Hazardous Materials*, 406, 124332.
- Zhang, M., Garcia-Araez, N. and Hector, A. L., 2018. Understanding and development of olivine LiCoPO₄ cathode materials for lithium-ion batteries. *Journal of Materials Chemistry A*, 6 (30), 14483–14517.
- Zhang, P., Yokoyama, T., Itabashi, O., Suzuki, T. M. and Inoue, K., 1998. Hydrometallurgical process for recovery of metal values from spent lithium-ion secondary batteries. *Hydrometallurgy*, 47 (2–3), 259–271.
- Zhang, X., Xie, Y., Cao, H., Nawaz, F. and Zhang, Y., 2014. A novel process for recycling and resynthesizing LiNi_{1/3}Co_{1/3}Mn_{1/3}O₂ from the cathode scraps intended for lithium-ion batteries. *Waste Management*, 34 (9), 1715–1724.

- Zhao, C., Zhang, Y., Cao, H., Zheng, X., Van Gerven, T., Hu, Y. and Sun, Z., 2019. Lithium carbonate recovery from lithium-containing solution by ultrasound assisted precipitation. *Ultrasonics Sonochemistry*, 52, 484–492.
- Zhao, J. M., Shen, X. Y., Deng, F. L., Wang, F. C., Wu, Y. and Liu, H. Z., 2011. Synergistic extraction and separation of valuable metals from waste cathodic material of lithium ion batteries using Cyanex272 and PC-88A. *Separation and Purification Technology*, 78 (3), 345–351.
- Zhao, Y., Pohl, O., Bhatt, A. I., Collis, G. E., Mahon, P. J., R  ther, T. and Hollenkamp, A. F., 2021a. A Review on Battery Market Trends, Second-Life Reuse, and Recycling. *Sustainable Chemistry*, 2 (1), 167–205.
- Zhao, Y., Pohl, O., Bhatt, A. I., Collis, G. E., Mahon, P. J., R  ther, T. and Hollenkamp, A. F., 2021b. A Review on Battery Market Trends, Second-Life Reuse, and Recycling. *Sustainable Chemistry*, 2 (1), 167–205.
- Zheng, H., Sun, Q., Liu, G., Song, X. and Battaglia, V. S., 2012. Correlation between dissolution behavior and electrochemical cycling performance for LiNi_{1/3}Co_{1/3}Mn_{1/3}O₂-based cells. *Journal of Power Sources*, 207, 134–140.
- Zheng, X., Gao, W., Zhang, X., He, M., Lin, X., Cao, H., Zhang, Y. and Sun, Z., 2017. Spent lithium-ion battery recycling – Reductive ammonia leaching of metals from cathode scrap by sodium sulphite. *Waste Management*, 60, 680–688.
- Zheng, X., Zhu, Z., Lin, X., Zhang, Y., He, Y., Cao, H. and Sun, Z., 2018. A Mini-Review on Metal Recycling from Spent Lithium Ion Batteries. *Engineering*, 4 (3), 361–370.
- Zheng, Y., Song, W., Mo, W., Zhou, L. and Liu, J.-W., 2018. Lithium fluoride recovery from cathode material of spent lithium-ion battery. *RSC Advances*, 8 (16), 8990–8998.
- Zheng, Y., Zhang, P., Wu, S. Q., Wen, Y. H., Zhu, Z. Z. and Yang, Y., 2012. First-principles studies on the structural and electronic properties of Li-ion battery cathode material CuF₂. *Solid State Communications*, 152 (17), 1703–1706.
- Zhou, L.-F., Yang, D., Du, T., Gong, H. and Luo, W.-B., 2020. The Current Process for the Recycling of Spent Lithium Ion Batteries. *Frontiers in Chemistry*, 8, 1–7.
- Zhou, X., Chen, Y., Yin, J., Xia, W., Yuan, X. and Xiang, X., 2018. Leaching kinetics of cobalt from the scraps of spent aerospace magnetic materials. *Waste Management*, 76, 663–670.
- Zhou, X., He, W., Li, G., Zhang, X., Huang, J. and Zhu, S., 2010. Recycling of Electrode Materials from Spent Lithium-Ion Batteries. In: *2010 4th International Conference on Bioinformatics and Biomedical Engineering*. IEEE, 1–4.

- Zhu, S., He, W., Li, G., Zhou, X., Zhang, X. and Huang, J., 2012. Recovery of Co and Li from spent lithium-ion batteries by combination method of acid leaching and chemical precipitation. *Transactions of Nonferrous Metals Society of China*, 22 (9), 2274–2281.
- Zhu, S., He, W., Li, G., Zhou, X., Zhang, X. and Huang, J., 2012. Recovery of Co and Li from spent lithium-ion batteries by combination method of acid leaching and chemical precipitation. *Transactions of Nonferrous Metals Society of China*, 22 (9), 2274–2281.
- Zhu, X., Meng, F., Zhang, Q., Xue, L., Zhu, H., Lan, S., Liu, Q., Zhao, J., Zhuang, Y., Guo, Q., Liu, B., Gu, L., Lu, X., Ren, Y. and Xia, H., 2021. LiMnO₂ cathode stabilized by interfacial orbital ordering for sustainable lithium-ion batteries. *Nature Sustainability*, 4 (5), 392–401.
- Zou, H., Gratz, E., Apelian, D. and Wang, Y., 2013. A novel method to recycle mixed cathode materials for lithium ion batteries. *Green Chemistry*, 15 (5), 1183.

Appendix A-Process Cost Estimation

A.1 Overview

This section focuses on examining the financial aspects of recovering Ni-Co composite material in a pilot-scale process. It looks beyond scientific and technical aspects to explore the financial details that affect the viability and sustainability of the process. The analysis involves scrutinizing costs, from procurement of raw materials to managing utilities and labour expenses. It includes calculations for various expenses like variable costs, equipment costs, and operational costs. Understanding production costs and the cost per kilogram of Ni-Co provides insights into the economic efficiency of the process. Additionally, it includes a cash flow statement tailored for a pilot scale plant, projecting economic dynamics for a facility processing 4.5 tons of Ni-Co annually. Ultimately, this section aims to assess the economic feasibility and commercial viability of scaling up Ni-Co recovery, offering valuable insights at the intersection of sustainability, technology, and economics from the scientific perspective. All the calculations involved in this section (cost of production of Ni-Co composite material) were determined using formulas and procedures reported by Apostolakou *et al.* (2009).

A.3 Material Production Cost of a Lab Scale Pilot Plant with Capacity of 4500 kgs of Ni-Co Composite/Year

The mass of the Ni-Co composite material produced after a 3-hour run was 5.8 g/0.25 L reactor volume (determined in Section 9.2) which was pseudo-scaled 100 times to 580 g/25 L. When 5 reactors (25 L per reactor) are used concurrently, with each reactor operating at a batch rate of 6 runs per day (3hrs/run), the total Ni-Co produced can total 17 kgs/day, which was the rate of production of Ni-Co composite material in this study. Thus, it must be noted that the production cost of Ni-Co with an upscaled capacity of 17 kgs/day or 4500 kgs per year (where 12 months are equivalent to 260 working days) was investigated in this section. This implied that in one day, 17 kgs of Ni-Co alloy material was produced after 6 batches when five 25 L reactors were operated concurrently for 6 batches a day. The calculations included the cost of raw materials, energy consumption (by the oven, mixer, hot water heating

system, electrowinning management system and oven), lab costs, supervision costs, plant overheads, rental costs, capital charges, operating labour costs and insurance, local taxes and royalties.

In Table A-0-1 the cost of raw materials utilised to recover Ni-Co material from spent Li-ionB is tabulated.

Table A-0-1: Raw materials cost estimation to produce 5.8 g of Ni-Co composite material.

Raw materials	Amount[Kg]	Weight specific Cost[R/Kg]	Cost [R]	Reference (Cost of Materials)
NaOH	0.0420	9.60	0.40	(Intratec Solutions 2024)
NMC Batteries	0.0625	12.42	0.78	(Kuhn 2023)
H ₂ O ₂	0.0125	9.20	0.12	(Kuhn 2023)
H ₂ SO ₄	0.0500	8.30	0.42	(Kuhn 2023)
NaH ₂ PO ₄	0.0038	15.70	0.06	(ECHEMI 2023)
Na ₂ SO ₄	0.0038	7.80	0.03	(Intratec Solutions 2024)
Na ₂ CO ₃	0.0260	6.00	0.16	(Kuhn 2023)
DI H ₂ O	0.5000	0.25	0.13	In-House
Total Mass	0.7005		2.08	
100x Upscaled Mass			207.87	
Cost per annum running Six (5x 25L) batches per day			1621 386	

The total cost to recover 5.8 g of Ni-Co is calculated to be R 2.1/0.25 L (Reactor Volume) (Table A-0-1) therefore in 100 times more volume it translates to R 208/25 L/day (Reactor Volume). In a year, there is 260 working days) therefore cost of raw materials per year translates to R 1 621 386. All the calculations involved in this section (cost of production of Ni-Co composite material per unit mass) were determined using formulas and procedures reported in literature (Apostolakou et al. 2009). Thus, it must be noted that the calculated cost of production of an upscaled capacity of 4500 kgs per year or 17.25 kg per day (where

12 months are equivalent to 260 working days) was investigated in this section. This implied that 4500 kgs/year was the pilot plant capacity of the Ni-Co composite material production.

It was relevant to determine how much money was spent per year using the production rate of 4500 kgs/day. Thus, the cost estimation was carried out as shown next. The cost estimation was initiated by determining the fixed capital investment at the plant capacity of 4500 kgs/year. Fixed capital investment is a vital parameter in computing the production cost, as it estimates the cost of acquisition and maintenance of long-term major equipment utilised in the Ni-Co recovery process. Table A-0-2 presents the sum of installed equipment cost (SIEC), total installed equipment cost (TIEC) and fixed capital investment (FCI).

Table A-0-2: Cost of major equipment utilised in the production of Ni-Co (4500 kgs/year).

Equipment & Size	Price	[R]	Supplier
Hot Water Heating System		4000	Reflecta
Drying Oven (400L)		34000	EcoTherm
Electrowinning Management System (6 V 100 A Transformer with 5 Channels)		140000	Wake Engineering
5 Electrowinning Glass Chambers (with Electrodes) (25 L-with Heating Water Jacket)		19200	Metrohm, In-House
Storage Vessels (2 X 25L)		3000	Labotec
Reaction Vessels (5 X 25L)		4000	Labotec
Filtration Systems (X2)		2000	Labotec
Overhead Mixer		4500	Labotec
Sum of Installed Equipment		210700	
Total installed Equipment Cost		252840	
Fixed Capital Investment		505680	

The calculations were carried out as follows:

$$\text{TIEC} = 1.2 \times \text{SIEC} = 1.2 \times \text{R } 210\,700 = \text{R } 252\,840$$

$$\text{FCI} = 2 \times \text{TIEC} = 2 \times \text{R } 252\,840 = \text{R } 505\,680$$

The fixed capital investment of R 1 505 680 was used to determine the production cost of Ni-Co alloy material recovery. The cost of raw materials/cell was estimated Table A-0-1 The

production scale was scaled from 5.8 g/0.250 L reactor volume to 580 g/25 L reactor volume. The cost of Raw materials per year was calculated as R 1 621 386 (R 2.08/run × 100 × 5 reactors × 6 runs/day × 260 days).

Then, the cost of utilities was estimated as shown below:

Table A-0-3 present the energy consumed (kWh/day) per each major unit involved in the recovery process of 17 kg/day of Ni-Co alloy material from NMC 532 cathode material (discharged state). The Electrochemical Management System account for a substantial portion of the overall energy consumption at 42.7 %, followed by the Hot Water Heating System at 32.4 %, both units of equipment which work in tandem totalling 75.1 %. Sequentially, the Overhead Mixer follows at 13.6 %, and lastly, the Drying Oven follows with a mere contribution of 11.3 %.

Table A-0-3: Energy consumed (kWh/day) per each major unit involved in the recovery process.

Equipment & Size	V (V)	I (A)	t (hrs)	Total Energy (kWh/day)	% contribution
Hot Water Heating System	241.0	2.1	15.0	7.6	32.4
Drying Oven	242.0	2.2	5.0	2.7	11.3
Overhead Mixer	242.0	1.1	12.0	3.2	13.6
Electrowinning Management System (6 V 100 A Transformer with 5 Channels)	240.0	2.8	15.0	10.0	42.7
Total				23.5	

In the present study, the cost of utilities consisted of the cost of electricity. The energy consumed during the Ni-Co production process was estimated from the equipment's specifications (Hot Water Heating System, Drying Oven, Overhead Mixer, and Electrochemical Management System). The mixer consumed 0.266 kW, it was used for 12 hours, and the rate of power was 3.2 kWh per day. The EMS consumed 0.667 kW, it was used for 15 hours, and the rate of power was 10 kWh per day. The oven consumed 0.532 kW, it was used for 5 hours, and the rate of power was 2.7 kWh per day. The hot water circulation system consumed 0.506 kW, it was used for 15 hours, and the rate of power was 7.6 kWh per day. The rate of electricity in South Africa is 183.13c per kWh (R1.83).

(Source: <https://www.capetown.gov.za/Work%20and%20business/Commercial-utility-services/Commercial-electricity-services/the-cost-of-electricity>, Accessed on the 20th August 2023).

Table A-0-4 presents the estimation of the cost of utilities per year.

Table A-0-4: Estimation cost of the plant utilities per year (plant with capacity 4500 kgs Ni-Co/year).

Equipment & Size	KWh/day	KWh/Year	Rand/Year
Hot Water Heating System	7.6	1973.8	3612.0
Drying Oven	2.7	692.1	1266.6
Overheard Mixer	3.2	830.5	1519.9
Electrochemical Management System	10.0	2602.1	4761.8
		Total	11160

Thereafter, the operating labour cost was estimated as shown below.

Two operators were running the battery production process. During this process, the operator was working for 5 hours per day which was equivalent to 1300 hours per year. Each operator was earning R43.05 per hour which was the PayScale for a production operator in South Africa.

(Source: https://www.payscale.com/research/ZA/Skill=Machine_Operation/Hourly_Rate, Accessed on the 20th of August 2023).

Table A-0-5 shows the operating labour cost for 1300 hours per year using a plant capacity for Ni-Co composite material at a rate of 4.5 kgs Ni-Co/year.

Table A-0-5: Operating labour cost for 1300 hours per year using a plant capacity for Ni-Co composite material at a rate of 4500 kgs Ni-Co/year.

Cost Item	R/hr	R/Year
Operator 1	43.05	55 900
Operator 2	43.05	55 900
	Total cost	111 800

Thus, for 1300 hours per year using a plant capacity for Ni-Co composite material at a rate of 4.5 kgs Ni-Co/year, the pay scale showed that a production operator working on the manufacturing of Ni-Co composite material can receive a minimum wage of R55 926 per year. Since two operators were working at the pilot plant; therefore, R 111 852 was the operating labour cost. Thus, the total production cost of Ni-Co composite material was estimated in the next section (Table A-0-6).

Table A-0-6: Manufacturing cost estimation for production of Ni-Co composite material (4500 kgs/year).

Cost Item	Calculations	Rand (ZA)	%
1. Raw Materials	From Material Balance	1621386	67.2
2. Miscellaneous Material	1% of FCI	5057	0.2
3. Utilities	From Utilities Quantification	11160	0.5
(A) Variable Costs	<i>(1)+(2)+(3)</i>	1637603	67.8
4. Maintenance	10% of FCI	50568	2.1
5. Operation labour	Manning Estimates	111800	4.6
6. Lab Costs	30% of (5)	33540	1.4
8. Supervision	40% of (5)	44720	1.9
8. Plant Overheads	50% of (5)	55900	2.3
8. Rentals	40% of FCI	202272	8.4
9. Capital Charges	30% of FCI	151704	6.3
10. Insurance, Local Taxes and Royalties	20% of FCI	101136	4.2
(B) Fixed Costs	<i>(4)+(5)+(6)+...+(10)</i>	751640	31.1
Direct Production Costs	<i>(A)+(B)</i>	2389243	99.0
(C) General Overheads + R&D	<i>5% of FCI of the direct production cost</i>	25284	1.0
Annual Cost of By-Products	Cost of Li ₂ CO ₃ + Mn(OH) ₂ [Cost Calculated at 40 % commercial value]	2311547	
Annual Production Cost	Subtotal (A)+(B)+ (C)	2414527	
Ni-Co Production cost (R/kg)	$[(A)+(B)+ (C)]/4500$ kgs (Ni-Co)	536	
Recycling Cost (R/kg cathode)	Product Cost/15 750 kgs (Cathode)	153	
Ni-Co Production cost (R/kg)	$[(A)+(B)+(C) - \text{Cost of ByProducts}]/4500$ kgs	23	
Potential Revenue (First Year)	Cost of Li ₂ CO ₃ + Mn(OH) ₂ [Cost Calculated at 40 % commercial value]+Cost of Ni-Co (500/kg)	4741547	

The Ni-Co production was performed at lab-scale, the production capacity of Ni-Co material per day estimated during the material balance was 17.3 kgs; this rate of production was projected to a capacity of 4500 kgs/year. Table A-0-6 indicated that R 536 was the production cost estimated for a kilogram of Ni-Co composite. In addition, R 2 414 527 annual production cost and fixed costs of R 751 640 were also reported in Table A-0-6. This indicated that a significant amount of money was spent on raw materials and equipment. The production cost of a Ni-Co composite material was computed to R 537/kg, which is an enormously lower figure than the commercial value of R 638/kg reported for Ni and 810 /kg of Co reported by Bloomberg Org (2023). The production cost of Ni-Co per kg drastically goes lower to R 23/kg if the production of the Li_2CO_3 and $\text{Mn}(\text{OH})_2$ commercially viable material (when sold at 60 % less of the current commercial value) is factored in (ECHEMI 2023; Intratec Solutions 2024). The total revenue that can be generated from materials sales when Ni-Co alloy material is sold at R540/kg, $\text{Mn}(\text{OH})_2$ at R 25.2/kg (60 % less than commercial value) and Li_2CO_3 at R 430/kg (60 % less than commercial value) is R 4 741 547 (ECHEMI 2023; Intratec Solutions 2024). The recycling cost (R/kg) of cathode was calculated to be R 153/kg which is at least 50 % lesser than R 360/kg, R 308/kg and R 258/kg recycling costs for direct recycling, pyrometallurgical and hydrometallurgical processes respectively (Dunn et al. 2022).

The cost of production was inordinate because the process was performed on a small scale. The factors that influenced the process to be costly at a small scale were the operating labour cost, raw materials cost and utilities cost which constituted the energy (per year) consumed by an overheard mixer, hot water heating system, 5 Channel EMS and a hot air oven dryer. These factors do not depend much on the rate of production and are often constant no matter the size of the plant. When a bigger plant is modelled the cost of purchasing the equipment (per unit of capacity) remains steady concurrently with a decrease in the cost of raw materials per kg. Thus, it is relevant to scale up the production capacity in order to reduce the cost of Ni-Co production. Based on the production cost of Ni-Co composite material obtained at the plant capacity of 4500 kg/year, a scale-up is recommended up to a plant capacity of 4500 kg/year.

A-4 Cash Flow of a Plant Capacity of 4500 kg (Ni-Co)/Year

Figure A-0-1 illustrates the cumulative cash flow diagram of a plant with a capacity of 4500 kg (Ni-Co)/year. The full cash flow statement is available in Figure A-0-1.

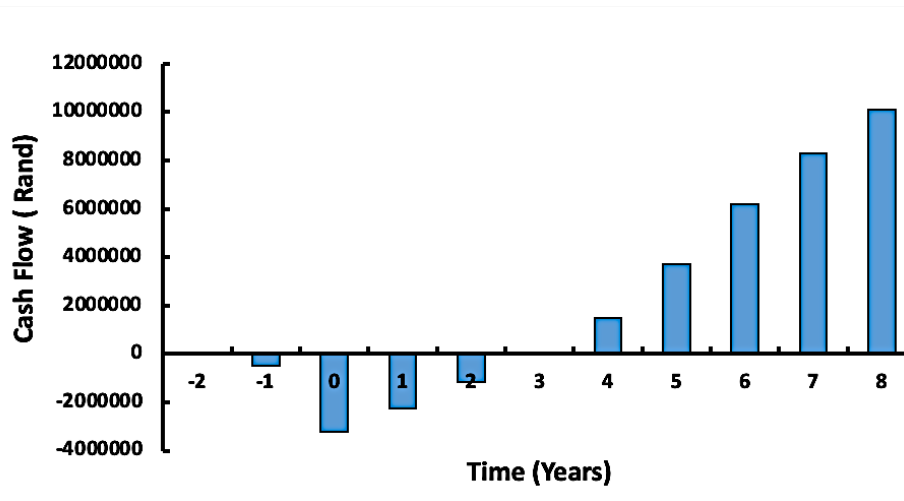


Figure A-0-1: Cash flow of a plant with a capacity of 4500 kgs/year.

$$\text{Total NPV} = \sum_{n=1}^{n=t} \frac{\text{NFW}}{(1+r)^n} = \text{R } 2\,470\,910$$

Where NPV is **the Net Present Value**, NFW is **the Net Future Worth**, r is **the Internal Rate of Return (IRR)**, n is the plant life in years and t is the n th year.

List of assumptions

- The process is run at steady state conditions.
- The plant operates for 260 days a year.
- The sales increase by 20% in the first 3 years after the project has been running for a year, by 30 % in the 4th and 40% in the 5th year, 10 % in the 6th and drop by 10% in the last 2 years of the project.
- The operating expenses increased by 20% in the first 2 years after the project has been running for a year, 20% in the 4th and 5th year, 10% in the 6th year and by 5% until the end of the project life.

- The tax rate is set at 60 %.
- The salvage value of the project is negligible.
- The cost associated with land is negligible.

Different methods are used to analyse the profitability of projects and processes. From the given data the amount that needs to be invested to build the plant and start it up is R 3 203 913. The revenue is attained from the total sales that can be generated from Ni-Co composite material which is sold at R 540/kg, $\text{Mn}(\text{OH})_2$ at R 25.2/kg (60 % less than commercial value) and Li_2CO_3 at R 430/kg (60 % less than commercial value) is R 4 741 547. The trend of both the sales and operating costs throughout the project life was predicted based on sound judgement keeping in mind that in the early years of the project, both operating costs and sales increase and towards the end of the project operating costs continue to increase due to wear and tear of equipment while sales decrease since project completion will be looming.

The payback profitability analysis shows that it takes 3 years (Figure A-0-1) from the inaugural year of the project to recover the money invested and break even. Profit is only made for the last 5 years of the project. Payback analysis does not take the time value of money into account. A better method for profitability analysis is the net present value (NPV) which represents the present value of money of future cash flows. For the company's required interest rate of return of 20%, the NPV is found to be R 2 470 909. A negative NPV indicates that the anticipated expenditure costs in the present rand surpass the projected earnings generated by a project or investment, also in the present rand. In general, a negative NPV means that the project will subtract value from the plant's present value, it has to be rejected. A positive NPV indicates that the projected earnings generated by a project or investment in the present rand exceed the anticipated costs, also in the present rand. In general, a positive NPV is profitable. In order to make the project more profitable, it is suggested that the company drops its required IRR. Calculations done for an assumed IRR of 10%, for example, yield an NPV of R 5 157 433. A lower rate of return means recovering money at a lower rate but the probability of making a profit is higher. The cash flow statement with values and methodology utilised in computing NPV and payback period is embodied in Appendix A-Cash Flow Statement.

Appendix B-Cash Flow Statement (4500 kg Ni-Co Production Plant)

Table B-0-1: Cash Flow Statement (4500 kg Ni-Co Production Plant).

	Total Operating Costs		2414527	IRR	20%						
	Total Operating Cost		2414527	Taxation Rate	60%						
Year	2	-1	0	1	2	3	4	5	6	7	8
Fixed Capital Investment		505680									
Working Capital			-2698233.9								
Total Capital Investment		505680									
Profit - Loss statement											
Revenue			4,741,547	5215701.5	5737271.6	7458453.1	10441834.4	11486017.8	10911716.9	10366131.1	
Cash operating expenses			2414527	2655979.7	2921577.7	3798051.0	4937466.3	5431212.9	5702773.5	5987912.2	
Depreciation			63210.0	63210.0	63210.0	63210.0	63210.0	63210.0	63210.0	63210.0	
Total Operating expenses			2477737.0	2719189.7	2984787.7	3861261.0	5000676.3	5494422.9	5765983.5	6051122.2	
Operating income			2327019.8	2559721.8	2815694.0	3660402.1	5504368.1	6054804.9	5208943.4	4378218.9	
Net income before taxes			2263809.8	2496511.8	2752484.0	3597192.1	5441158.1	5991594.9	5145733.4	4315008.9	
Federal Income Taxes			1358285.9	1497907.1	1651490.4	2158315.3	3264694.9	3594956.9	3087440.0	2589005.3	
Net income after taxes			905523.9	998604.7	1100993.6	1438876.9	2176463.2	2396638.0	2058293.4	1726003.5	
After tax cash flow			-3203913.9	968733.9	1061814.7	1164203.6	1502086.9	2239673.2	2459848.0	2121503.4	1789213.5
Capital recovery											
Cumulative cash flow	0	505680	-3203913.9	-2235180.0	-1173365.3	-9161.7	1492925.2	3732598.4	6192446.4	8313949.7	10103163.2
NPV			-3203913.9	807278.3	737371.3	673728.9	724386.0	900074.4	823798.1	592072.6	416113.9
		NPV	2470909.7								

